UNIVERSIDADE FEDERAL DE PERNAMBUCO
DEPARTAMENTO DE FÍSICA – CCEN
PROGRAMA DE PÓS-GRADUAÇÃO EM FÍSICA

IVÁN RENÉ ROA GONZÁLEZ

THE H-THEORY: UNIVERSALITY CLASSES OF HIERARCHICAL COMPLEX SYSTEMS

Recife
2017

IVÁN RENÉ ROA GONZÁLEZ

THE H-THEORY: UNIVERSALITY CLASSES OF HIERARCHICAL COMPLEX SYSTEMS

Tese apresentada ao Programa de Pós-Graduação em Física da Universidade Federal de Pernambuco, como requisito parcial para a obtenção do título de Doutor em Física.

Orientador:
Prof. Dr. Antônio Murilo Santos Macêdo
Universidade Federal de Pernambuco

Recife
2017

Catalogação na fonte
Bibliotecário Joana D'Arc Leão Salvador CRB 4-572

R628h Roa González, Iván René.
The h-theory: universality classes of hierarchical complex systems / Iván René Roa González . – 2017.
210 f.: fig., tab.

Orientador: Antônio Murilo Santos Macêdo.
Tese (Doutorado) – Universidade Federal de Pernambuco. CCEN. Física, Recife, 2017.
Inclui referências e apêndices.

1. Mecânica estatística. 2. Sistemas complexos. 3. Processos estocásticos. 4. Turbulência. I. Macêdo, Antônio Murilo Santos (Orientador). II. Titulo.

530.15 CDD (22. ed.) UFPE-FQ 2017-36

IVÁN RENÉ ROA GONZÁLEZ

THE H-THEORY: UNIVERSALITY CLASSES OF HIERARCHICAL COMPLEX SYSTEMS

Tese apresentada ao Programa de Pós-Graduação em Física da Universidade Federal de Pernambuco, como requisito parcial para a obtenção do título de Doutor em Física.

Aprovada em: 28/04/2017.

BANCA EXAMINADORA

_____
Prof. Dr. Antônio Murilo Santos Macêdo
Orientador
Universidade Federal de Pernambuco

_____
Prof. Dr. Ernesto Carneiro Pessoa Raposo
Examinador Interno
Universidade Federal de Pernambuco

_____
Prof. Dr. Paulo Roberto de Araújo Campos
Examinador Interno
Universidade Federal de Pernambuco

_____
Prof. Dr. Francisco Anacleto Barros Fidelis de Moura
Examinador Externo
Universidade Federal de Alagoas

_____
Profª Drª Tânia Tomé Martins de Castro
Examinador Externo
Universidade de São Paulo

Abstract

Complex dynamical systems can be characterized through the time series associated with dynamical variables, which yield important information on the underlying stochastic process. The probability density function, the temporal correlation function, the power spectrum, and the memory function are examples of statistical properties that can be extracted from the time series. In this thesis, we are particularly interested in describing complex phenomena in which the stationary distribution of the time series of the main dynamical variable (the signal) exhibits large deviations from Gaussian statistics, possibly showing long and heavy tails. This kind of phenomena is present in many areas of physics, biology, and economics. However, our interest is focused on spectral fluctuations in non-integrable ballistic cavities, intensity fluctuations in random lasers, turbulence in fluids, stock prices fluctuations in financial markets. We shall attempt to describe these phenomena as a composition of distributions with distinct space/time scales which arise from a hierarchical dynamics with a coupling between contiguous scales. The model to be used, denominated H-Theory, was recently proposed by our research group and consists of a set of coupled stochastic differential equations, whose stationary solution leads to a parametric family of distributions represented by Fox H-function. This result unifies and generalizes the universality classes of superstatistics, which is a formalism that has been successfully used to describe systems with two separated time scales.

Keywords: Complex systems. Stochastic dynamics. Time series. Fox H-functions.

Resumo

Sistemas dinâmicos complexos podem ser caracterizados através de séries temporais associadas a variáveis dinâmicas que fornecem importante informação sobre o processo estocástico subjacente. A função densidade de probabilidade, as funções de correlação temporais, a potência espectral e a função memória são exemplos de propriedades estatísticas que podem ser extraídas da série temporal. Nesta tese estamos particularmente interessados na caracterização de sistemas complexos nos quais a distribuição estacionária da série temporal da variável dinâmica principal (o sinal) desvia-se substancialmente da gaussiana, podendo exibir caudas longas e pesadas. Exemplos de sistemas deste tipo podem ser encontrados em diversas áreas da física, da biologia e da economia. Contudo, centraremos nosso foco nos fenômenos de flutuações espectrais em turbulência em fluidos, variações nos preços de ações no mercado financeiro, flutuações de intensidade em lasers aleatórios em fibra óptica e estatística espectral de cavidades balísticas não-integráveis. Caracterizamos esses fenômenos como resultado da composição de distribuições com distintas escalas espaçiais/temporais que resultam de uma dinâmica hierárquica com acoplamento entre escalas contíguas. O modelo a ser usado, denominado teoria H, foi recentemente proposto por nosso grupo de pesquisa e consiste de um sistema de equações diferenciais estocásticas acopladas, cuja solução estacionária produz uma família paramétrica de distribuições representadas por funções H de Fox. Este resultado unifica e estende para múltiplas escalas as classes de universalidade da superestatística, que é um formalismo que tem sido usado com sucesso para descrever sistemas dinâmicos complexos com duas escalas temporais separadas.

Palavras-chave: Sistemas complexos. Dinâmica estocástica. Séries temporais. Funções H de Fox.

List of Figures

1.1 Nearest neighbor spacing distribution (NNSD) of billiards 34
1.2 Limaçon billiard with MPSpack Matlab Toolbox 35
1.3 Example of mesh and dual mesh for Limaçon billiard 36
1.4 GHM applied to Eulerian turbulence with Reynolds number $R = 295000$. 39
1.5 In color dots: normalized PDF for velocity increments u_{δ_i} 41
1.6 Comparative figure between cumulants of experimental data and the SDE model 44

2.1 Large inertia effects decay into smaller eddies in a series of events 50
2.2 Plots of the Gamma distribution as a function of its parameters 56
2.3 Plots of the Inverse-Gamma distribution as a function of its parameters . . 57
2.4 Plots of joint background's distribution $f_N(\varepsilon_N)$ for the Gamma class 61
2.5 Plots of joint background's distribution $f_N(\varepsilon_N)$ for the Inverse-Gamma class 61
2.6 Plots of signal's PDF $P(x)$ for the class stretched exponential 65
2.7 Plots of signal's PDF $P(x)$ for the power-law class 68
2.8 Plots of background's PDF $f(\varepsilon)$ for the beta class 70
2.9 Plots of background's PDF $f(\varepsilon)$ for the inverse beta class 72
2.10 Plots of signal's PDF $P(x)$ for the beta class 73
2.11 Plots of signal's PDF $P(x)$ for the inverse beta class 74
2.12 Plots of background's PDF $f(\varepsilon)$ for the generalized gamma class 75
2.13 Plots of background's PDF $f(\varepsilon)$ for the generalized inverse gamma class . . 76
2.14 Plots of background $f(\varepsilon)$*and*signal's PDF $P(x)$ for the generalized beta class 77

2.15 Plots of background $f(\varepsilon)and$signal's PDF $P(x)$ for the generalized inverse beta class 78
2.16 Plots of signal's PDF $P(x)$ for the generalized gamma class 80
2.17 Plots of signal's PDF $P(x)$ for the generalized inverse gamma class 80

3.1 Background function from random numbers satisfying the PDF (3.8) for the signal 86
3.2 Background function for gamma class from random numbers satisfying the $K-$dist. 87
3.3 Superposition between Gaussian kernel and beta distribution 88
3.4 Beta background's distribution 89
3.5 Background's scale separation of inverse gamma class 90

4.1 Experimental setup and data series for $\delta v_{15}(i)$ 93
4.2 PDF's velocity increments doing crossover from heavy tailed to Gaussian distribution 94
4.3 Crossover from heavy tailed to Gaussian distribution 95
4.4 Fits of signal and background in eulerian turbulence 96
4.5 Histograms for the background of large neighbors 98
4.6 Behavior of kurtosis excess for the signal $x(2^j)$ 99
4.7 Fitting with Meijer G-functions for the turbulence experiment 100
4.8 Signal and background for returns $30s$ Ibovespa index 106

5.1 Conventional lasers and random lasers 109
5.2 Scheme for the Er-RFL experiment 112
5.3 Time series for the output intensities 115
5.4 Power spectrum and turbulence in the intensity dynamics in Er-RFL. . . . 116
5.5 Gaussian distribution of intensity increments 118
5.6 Statistical mixture near the threshold 120

5.7 Statistical mixture of intensity above threshold 124

6.1 Action of operators in discrete exterior calculus 132
6.2 Mesh applied to Mushroom billiard with triangular stem 133
6.3 Spectral exponent for regular and chaotic cavity 135
6.4 Parameter dependence of the Limaçon billiard 139
6.5 NNSD of six of the eight parameters λ of the Limaçon billard 141
6.6 Power spectrum for six of the eight parameters λ of the Limaçon billiard . 142
6.7 Mushroom geometry with characterized parameters 144
6.8 NNSD of six of the nine parameters r/R of the Mushroom billard 145
6.9 Power spectrum of the four smaller r/R parameters 146
6.10 Power spectrum of the four larger r/R parameters 147
6.11 Projection of the curved billiard 148
6.12 NNSD of six of the nine parameters A of the Curved billard 150
6.13 Power spectrum for the parameters $A = 0.1$, $A = 0.2$, and $A = 0.3$, of the Curved billiard 151
6.14 Power spectrum for the parameters $A = 0.4$, $A = 0.5$, and $A = 0.9$, of the Curved billiard 152
6.15 Law of corresponding states between α and $|B|$ 153
6.16 Law of corresponding states between α and δ_{LK} 154

7.1 Distributions of NN increments of level spacings for GDE and GOE 164
7.2 Parametric dependence of the superposition between WD and $\bar{\gamma}$ distribution 168
7.3 Parametric dependence of the superposition between WD and γ distribution 170
7.4 The fits for the NNSD's histograms of the Limaçon billiard 171
7.5 The fits for the NNSD's histograms of the Mushroom billiard 173
7.6 The fits for the NN increments of level spacings histograms of the Limaçon billiard 177

7.7 The fits for the NN increments of level spacings histograms of the Mushroom billiard 178

List of Tables

1.1 First moments in the SS model 40

4.1 Characteristic values for velocity increments 101

5.1 Laboratory elements used for experimental setup 112

6.1 Operators over $p-$forms in the exterior calculus 130

6.2 Numerical values of the three statistical measures for the Limaçon billiard 140

6.3 Numerical values of the three statistical measures for the Mushroom billiard 144

6.4 Numerical values of the three statistical measures for the Curved billiard . 149

List of Abbreviations and Acronyms

GHM	Generalized Hypergeometric Model
SV	Salazar and Vasconcelos theory
K41	Kolmogorov theory 1941
KO62	Kolmogorov-Obukhov theory 1962
SS	Superstatistics
DEC	Discrete exterior calculus
H-Theory	Stationary solution leads to a parametric family of distributions represented by Fox H-function
PDF	Probability density function
CLT	Central Limit Theorem
SDE	Stochastic Differential Equations
FPE	Fokker-Planck equation
PC	percentage changes
BS	Black-Scholes model
RL	Random Lasers
RFL	Random Fiber Lasers
Er-RFL	Erbium Random Fiber Laser
PS	Power Spectrum
NNSD	Nearest Neighbor Spacing Distributions
CDF	Cumulative Distribution Function
KLD	Kullback-Leibler distance

Contents

1 Historical Introduction **16**

1.1 Brief history of turbulence 16

1.1.1 *Reynolds experiment and Navier-Stokes equations* 17

1.2 Statistical approach to turbulence 21

1.3 K41 and KO62 theory 22

1.3.1 *Turbulence's scales* 22

1.3.2 *Kolmogorov 1941 theory* 24

1.3.3 *The Kolmogorov Oboukhov Theory* 28

1.4 A chronological description of the Thesis' project 32

1.4.1 *Stage 1* 32

1.4.2 *Stage 2* 35

1.4.3 *Stage 3* 37

1.4.4 *Stage 4* 38

1.4.5 *Stage 5* 43

1.4.6 *Stage 6* 44

2 The H-Theory **46**

2.1 Introduction 46

2.1.1 *The dynamical hierarchical model* 49

2.2 Parametric Families 52

2.2.1 *Gamma class* 54

2.2.2 *Inverse gamma classes* 56

2.3 The multiscale approach . . . 58
2.3.1 *Marginal distribution* . . . 62
2.3.2 *Probability density functions of the beta classes* . . . 69
2.3.3 *Generalized Gamma and Beta Classes* . . . 74
2.4 Unified Fox H-function representation . . . 78
2.5 Conclusions . . . 81

3 Background series **82**
3.1 Introduction . . . 82
3.2 The background series . . . 83
3.2.1 *Ilustrative examples* . . . 84
3.2.2 *Extracting the inverse gamma distribution* . . . 85
3.2.3 *Extracting the gamma distribution* . . . 86
3.3 Background for beta class . . . 87
3.3.1 *Separating scales into the background* . . . 89

4 Applications of H-theory **91**
4.1 Introduction . . . 91
4.2 Turbulence in classical fluids . . . 92
4.3 Econophysics Aplications . . . 101
4.3.1 *Intraday returns of the Ibovespa* . . . 104
4.4 Conclusions . . . 107

5 Random lasers RL **108**
5.1 Brief introduction . . . 108
5.2 Experimental setup . . . 111
5.3 Power spectum . . . 113
5.4 Mixture of multiscale distributions . . . 117
5.4.1 *$P(x)$ near the threshold* . . . 118

5.4.2 *P(x) above the threshold* . . . 122
5.5 Conclusions . . . 125

6 Ballistic cavities I **126**
6.1 Introduction . . . 126
6.2 Discrete exterior calculus DEC . . . 129
6.3 Statistics for billiards with mixed dynamics . . . 135
6.3.1 *Measures for P(s) crossover* . . . 138

7 Ballistic cavities II **155**
7.1 Abstract . . . 155
7.2 Introduction . . . 156
7.3 Dynamic model applied to NNSD . . . 165
7.3.1 *Inverse-Gamma Class* . . . 165
7.3.2 *Gamma Class* . . . 168
7.4 Fits for NNSD of Limaçon Billiard . . . 170
7.5 Fits for NNSD of Mushroom Billiard . . . 172
7.6 Nearest neighbor increments of level spacings . . . 174
7.7 Conclusions . . . 178

8 Conclusions and perpectives **180**
8.1 Conclusions . . . 180
8.2 Perpectives . . . 182

References **182**

Appendices **196**

A Coupled SDEs for spacing energy levels **196**
A.1 Milstein method . . . 197

B Dissipation rate of Navier Stokes equations **199**

C Connection between Langevin and Fokker-Planck equations **201**

D Mellin Transform **205**

D.1 Mellin Transform 205

E Laplace-Beltrami operator **207**

1 Historical Introduction

1.1 Brief history of turbulence

As a species, we began a recorded history of questions about turbulence in fluids at the time of the ancient Greece, cradle of the western civilization. However, turbulence has proved to be such a complex phenomenon that even after centuries trying to describe its features, we do not yet have a complete understanding. After the initial efforts a long gap followed, which included the Middle Ages, and the West had to wait several centuries to have again the opportunity to inquire about turbulence. As a matter of fact, it was not until the fifteenth century when Leonardo Da Vinci made sketches and described several visual features of turbulence in fluids, that the subject came to the fore once again. In the modern age, after the masterful work done by Galileo and amplified at a level far beyond the extraordinary by Newton, the foundations were laid for a European legion of brilliant men to establish the elasticity theory that later became the standard language for describing fluids and hence turbulence. This was the opening scene in 1880s and 1890s. In this period Osborne Reynolds (Reynolds (1894)), based on Navier and Stokes' research (Batchelor (1953)) and Poiseulle's law (Sutera and Skalak (1977)), used modern scientific methods to determine the relevant quantities to characterize the phenomenon of turbulence and to quantify, for the first time, the different regimes that may occur in the dynamics of a fluid.

1.1.1 *Reynolds experiment and Navier-Stokes equations*

Reynolds tank experiment

The experiment performed by Reynolds broadly consisted of injecting dye into a liquid that flowed through a long tube of constant circular cross-section and attempting to characterize the behavior of the velocity field within it. Two types of motions were observed. In the first, called laminar, the dye forms a well-defined streamline whose contour shows that there is only a small diffusion in the radial direction due to molecular transport and the current lines are parallel to the tube's walls. In this regime, which occurs only if the flow's velocity and the tube's diameter are small enough, any perturbation that appears in the fluid is quickly damped (Batchelor (1953)). On the other hand, if the velocity or diameter of the tube is large enough, the fluid's motion becomes very sensitive to any perturbation, which can be rapidly amplified causing the fluid to become irregular and lose its stationary character. In this scenario, the thickness of the dye grows rapidly and its contour fades into an irregular shape until it becomes a cloud. This is the second type of motion observed by Reynolds, called turbulent (Frisch (1995)). The turbulence phenomenon is universal, which means that it is the same in all fluids, be it a liquid or a gas. A central quantity is the Reynold's number (Re), defined as

$$Re = \frac{VL}{\nu} = \frac{(\text{characteristic velocity})(\text{characteristic length})}{(\text{kinematic viscosity})} = \frac{\text{inertial forces}}{\text{viscous forces}}. \quad (1.1)$$

In turbulent flow, which occurs when Re is above a certain critical number (Temam (1976)), the perturbations can grow to a certain extent and reach a new state. This new state may become unstable in the face of other perturbations and grow into another new state, and the process goes on until finally the flow becomes a superposition of numerous random perturbations (Livi and Vulpiani (2003); McDonough (2004)). The characterization of turbulent flow through a dimensionless number that corresponds to the ratio of the inertial forces and viscous forces is the main legacy left by the Reynolds' tank experiment.

In the next section, we shall summarize some connections between the Reynolds number and the constitutive equations of fluids.

Navier Stokes equations

Building on the famous memoir by Coulomb presented in 1773 about the fundamental equations of elasticity, Navier establishes in 1827 the constitutive equations of fluids. However, its final form was introduced only in the period between 1845-1851 by Gabriel Stokes, who used the tensorial notation developed by Cauchy in 1829 and the Lamé constraints (Tanner and Waiters (1998)). The union of all these works led to the modern form of the Navier-Stokes (NS) equations

$$\frac{\partial \vec{v}}{\partial t} + (\vec{v} \cdot \vec{\nabla})\vec{v} = -\frac{\vec{\nabla} p}{\rho} + \nu \nabla^2 \vec{v}, \tag{1.2}$$

where $\vec{v}$ is the velocity field of the fluid, p is the pressure, ρ is the mass density and ν is the kinematic viscosity. It is usual to impose the no-volume-change constraint

$$\vec{\nabla} \cdot \vec{v} = 0, \tag{1.3}$$

which is essentially the mass conservation law for an incompressible fluid. The NS equations are a consequence of elasticity theory, which in turn are based on Newtonian mechanics. Therefore, these equations must satisfy several dynamical symmetries, which have been summarized very clearly by Frisch (Frisch (1995)). They are listed below

- Space translations: $(t, \mathbf{r}, \mathbf{v}) \rightarrow (t, \mathbf{r} + \mathbf{a}, \mathbf{v}), \quad \mathbf{a} \in \Re^3$.
- Time-translations: $(t, \mathbf{r}, \mathbf{v}) \rightarrow (t + \tau, \mathbf{r}, \mathbf{v}) \quad \tau \in \Re$
- Galilean transformations: $(t, \mathbf{r}, \mathbf{v}) \rightarrow (t, \mathbf{r} + \mathbf{u}t, \mathbf{v} + \mathbf{u}) \quad \mathbf{u} \in \Re^3$.
- Parity: $(t, \mathbf{r}, \mathbf{v}) \rightarrow (t, -\mathbf{r}, -\mathbf{v})$
- Rotations $(t, \mathbf{r}, \mathbf{v}) \rightarrow (t, \mathbf{A}\mathbf{r}, \mathbf{A}\mathbf{v}) \quad \mathbf{A} \in SO(\Re^3)$

- Scaling: $(t, \mathbf{r}, \mathbf{v}) \rightarrow (\lambda^{1-h}t, \lambda\mathbf{r}, \lambda^{h}\mathbf{v}), \quad \lambda \in \Re_{+},\ h \in \Re.$

Using the conditions set by the above transformations it is possible to rescale the Navier Stokes equation with respect to time, length, velocity and pressure. This approach is known as dimensional analysis and allows the generation of dimensionless numbers representing ratios between the types of forces that characterizes a given phenomenon. For example, the NS equation can be written as

$$[St]\frac{\partial \vec{v^*}}{\partial t^*} + (\vec{v^*} \cdot \vec{\nabla^*})\vec{v^*} = -[Eu]\vec{\nabla^*}p^* + \left[\frac{1}{Re}\right]\nabla^{*2}\vec{v^*}. \tag{1.4}$$

where

- **the Strouhal number** St indicates when rotation motion or a periodic motion plays a important role in a flow;
- **the Euler number** Eu indicates when energy losses are relevant;
- **the Reynolds number** Re indicates when viscous effects are important.

Dimensional analysis is supported by the Buckingham π theorem (Bluman and Anco (2002)), which creates dimensionless relations of a primary variable x_1 as a function of the others

$$x_1 = f_1(x_2, ..., x_n), \tag{1.5}$$

where n is the total number of variables. If m is the number of basic dimensions, usually three, the Buckingham π theorem demands that $(n-m)$ dimensionless groups of variables Zohuri (2016), the π terms, are related by

$$\pi_1 = f_1(\pi_2, \ldots, \pi_{n-m}). \tag{1.6}$$

As a method, dimensional analysis is a useful complementary tool in the study of turbulence because it provides functional relationships without the need to solve the dynamical

equations. We show in the following sections that dimensional analysis is a fundamental part of Kolmogorov's theory, which is a statistical approach that characterizes turbulence in terms of **structure functions**, defined as correlation functions of velocity differences measured at different nearby locations in the flow (Temam (1976); McDonough (2004)). Before describing the most important results of the Kolmogorov's theory, we present below some relevant facts that lead to a statistical approach to turbulence.

For a physical phenomenon to be stable in space and time, it is not enough to verify the conservation laws, it must also be robust to small perturbations. In turbulence when the Reynolds number of a flow is greater than a certain critical value, there are instabilities caused by infinitesimal perturbations that can grow spontaneously, which are believed to be related to the coupling of the viscous term and the convective nonlinear terms in the constitutive equations. When the instabilities in the flow begin to appear, the mean flow is accompanied by turbulent fluctuations, a fact that leads to the loss of predictability in the measurements of fluid's velocity, i.e. the flow becomes a superposition of numerous random perturbations (Temam (1976)). However, we know that the Navier-Stokes equations are deterministic (Frisch (1995); Batchelor (1953); Livi and Vulpiani (2003)). So, it is widely conjectured that for a given initial condition there is a unique solution for all times and that it does not matter if the initial value is sharp or random.

There were some attempts to reconcile the experimental results in fluids with high Reynolds numbers and the constitutive relations from the perspective of the Reynolds averaged Navier Stokes (RANS) decomposition, where the values obtained from velocity measurements can be interpreted as being composed of a mean part and a fluctuating part (LESLIE (1973)). However, the resulting system of equations is not closed (closure problem) and therefore they are quite insoluble (Lesieur (1997)). So, given the need to find invariant measures of turbulence that could guarantee that the experimental results were reproducible, a new approach emerged in the first decades of the twentieth century, known as Taylor-Richardson-Kolmogorov phenomenology, which was based on Reynolds'

view of turbulence as a random process.

1.2 Statistical approach to turbulence

In 1922 Richardson (Richardson (1922)) introduced the concept of energy cascade to describe the transfer of kinetic energy from large, macroscopic scales of motion, where it is presumed to be the input of the flow, through successively smaller scales, ending with viscous dissipation (eddy viscosity) and conversion to heat (thermal energy). The concept of eddy viscosity was introduced by Boussinesq in 1877 (Boussinesq (1877)) and corresponds to the constant of proportionality between turbulent (Reynolds) stresses and mean (large-scale) strain rate, analogous to the mechanical viscosity in Newton's law (Temam (1976); Davidson (2004)). In 1925 Prandt used the concept of eddy viscosity to introduce "the mixing-length theory" (Prandtl (1925)), in which the parameter mixing length is defined as the distance over which a hypothesized turbulent eddy retains its identity. Taylor was one of the first to explicitly introduce the assumption that turbulence is a random phenomenon (Taylor (1935)). He employed a high level of mathematical rigor and introduced formal statistical methods, such as correlations, Fourier transforms and power spectra into the turbulence literature. We mention in passing that the energy cascade is often analyzed in terms of the dependence of the fluid's kinetic energy on Fourier wavenumbers, and in this context each wavenumber is associated with the size of a turbulent eddy (Temam (1976); Livi and Vulpiani (2003)). In Taylor's works the following new concepts were introduced:

- **The Taylor microscale** corresponds to length scales in the range between the integral scale and the dissipation scale.

- **The Taylor's frozen-flow hypothesis** states that in a turbulent flow for which the magnitude of the fluctuations is not too great, it is possible to deduce spatial turbulence quantities from time series measured at a single point in the flow.

- **Isotropic turbulence:** exhibits statistics that are independent of rotations and reflections.

- **Local isotropy** refers to isotropy only on small scales, identified by their (high) Fourier wavenumbers.

- **Homogeneous turbulence** is such that its statistical properties do not change with spatial translation, i.e., they do not change with position.

The works conducted by these researchers are considered as the preamble to the statistical description of turbulence. This perspective ultimately gained a prominent place in the literature through the intellectual contributions made by Kolmogorov and Oboukhov.

1.3 K41 and KO62 theory

The statistical theory of turbulence by Kolmogrov and Oboukhov employs the tools of dimensional analysis to derive functional relations between the scales that characterize the dynamics of the fluid. We present in the following section a brief description of these relevant scales.

1.3.1 *Turbulence's scales*

- **Macro-scale:** This is the scale associated with the largest eddies and we denote by U, L and T its characteristic velocity, length and time scales, which incidently coincide with the characteristic scales of the flow itself. The associated Reynolds number of the macro-scale is thus the same as that of the main flow. The features of these large eddies depend on the boundary conditions of the flow and may have a strong anisotropic character (dependence on spatial directions) (Batchelor (1953)).

- **Intermediate scales:** They correspond to scales below the macro-scale in which there is still no energy dissipation. We denote by u, l and t their characteristic velocity, length and the time scales respectively.

- **Micro-scale:** This is the smallest scale and it is where energy dissipation occurs. Its characteristic velocity, length and time scales are denoted by u_0, η and τ respectively. Unlike the macro-scale, these micro-scale eddies are quite isotropic in space.

Using this notation it is possible to construct a number of dimensionless ratios for the internal and dissipated specific energy, thus generating the corresponding Reynolds numbers for each scale. We start with the specific energy contained in large vortices (or eddies) per unit time, which is defined as

$$E_L = \frac{U^2}{2T} \rightarrow [E_L] \sim [U]^2[T]^{-1} \sim [U]^3[L]^{-1}, \tag{1.7}$$

On the other hand the specific energy dissipated per unit time on the macroscale is given by

$$\varepsilon_L \sim \nu \left(\frac{\partial U_i}{\partial x_j}\right)^2 \rightarrow [\varepsilon_L] \sim [\nu][U]^2[L]^{-2}, \tag{1.8}$$

thus the relation between internal energy and the dissipated energy is

$$\frac{[E_L]}{[\varepsilon_L]} \sim \frac{[U]^3[L]^{-1}}{[\nu][U]^2[L]^{-2}} \sim \frac{[U][L]}{[\nu]} \sim Re_L \gg 1. \tag{1.9}$$

This large Reynolds number implies that the macro-scale energy dissipation is negligible and therefore all its internal energy is transferred to the eddies of the intermediate scales

$$E_L \sim E_l \quad \rightarrow U^3 L^{-1} \sim u^3 l^{-1}. \tag{1.10}$$

Similarly, in the intermediate scale, the ratio of internal and dissipated energies generates the Reynolds number associated with that scale, thus

$$\frac{[E_l]}{[\varepsilon_l]} \sim \frac{[u]^3[l]^{-1}}{[\nu][u]^2[l]^{-2}} \sim \frac{[u][l]}{[\nu]} \sim Re_l \quad \rightarrow \quad Re_l = Re_L \left(\frac{l}{L}\right)^{4/3}. \tag{1.11}$$

Since the ratio of lengths is still significantly close to one, the Reynolds number associated with the intermediate scale is large and energy dissipation is still negligible. We may thus use the relations

$$E_L \sim E_l \sim E_\eta \quad \rightarrow \quad U^3 L^{-1} \sim u^3 l^{-1} \sim u_0^3 \eta^{-1}, \tag{1.12}$$

to estimate the internal energy per unit time of the microscale. For this subrange we have that the ratio between the energy in the cascade and the dissipated energy corresponds to

$$\frac{[E_\eta]}{[\varepsilon_\eta]} = \frac{[u_0]^3[\eta]^{-1}}{[\nu][u_0]^2[\eta]^{-2}} \sim Re_\eta \quad \rightarrow \quad Re_\eta = Re_L \left(\frac{\eta}{L}\right)^{4/3}. \tag{1.13}$$

By hypothesis the transported energy is of the same order as the dissipated energy, thus the above ratio is of the order of unity, which in turn implies

$$\frac{E_\eta}{\varepsilon_\eta} \sim 1 \quad \rightarrow \quad \frac{\eta}{L} \sim Re_L^{-3/4}. \tag{1.14}$$

This important equation directly relates the characteristic lengths of the microscale and the macroscale. In modern literature (Livi and Vulpiani (2003); McDonough (2004)), η is refered to as the microscale of Kolmogorov, at which all of the fluid's mechanic energy is dissipated, and whose associated Reynolds number is one.

1.3.2 *Kolmogorov 1941 theory*

Once the relevant scales of turbulence have been established, Kolmogorov's K41 theory presented two universality assumptions (Kolmogorov (1941c,b)) through which the so-called structure functions were constructed to establish relations for the moments of the distributions associated with the series of velocity increments between two separate points in the flow (Lagrangian turbulence) in terms of the relevant variables. The assumptions are listed below (Frisch (1995))

- **First universality assumption:** At very high, but not infinite, Reynolds number, all of the small-scale statistical properties are uniquely and universally determined by the length scale l, the mean dissipation rate (per unit mass) ε and the viscosity ν.

- **Second universality assumption:** In the limit of infinite Reynolds number, all small scale statistical properties are uniquely and universally determined by the length scale l and the mean dissipation rate ε.

Based on these two original hypotheses, experts in Kolmogorov's theory, such as as Frisch (Frisch (1995)), Yaglom (Yaglom (1948.)) and Batchelor (Batchelor (1953)), summarized K41 theory in terms of three basic hypothesis:

- $H1$. *In the limit of infinite Reynolds numbers, all the possible symmetries of the Navier-Stokes equation, usually broken by the mechanisms producing the turbulent flow, are restored in a statistical sense at small scales and away from boundaries.*

- $H2$. *Under the same assumptions as in $H1$, the turbulent flow is self-similar at small scales, i.e. it possesses a unique scaling exponent h such that.*

$$\delta\mathbf{u}(\mathbf{x}, \lambda\mathbf{l}) = \lambda^h \delta\mathbf{u}(\mathbf{x}, \mathbf{l}) \;\; \forall\lambda \in \Re_+, \;\; \mathbf{x} \in \Re^3 \tag{1.15}$$

  with increments $\mathbf{l}$ and $\lambda\mathbf{l}$ small compared with the integral scale.

- $H3$. *Under the same assumptions as in $H1$, the turbulent flow has a finite nonvanishing mean rate of dissipation ε per unit mass.*

The mean rate of energy dissipation ε, calculated from N-S equation (see appendix B), corresponds to

$$\varepsilon = 2\nu|\mathbf{S}|^2, \tag{1.16}$$

whose dimensions are $[\varepsilon] \sim [l]^2[t]^{-3}$. Using dimensional analysis rules and the Buckingham π theorem it is possible to estimate the structure functions, calculated as

$$S_p(l) = \langle \left([\vec{v}(\vec{x}+\vec{l}) - \vec{v}(\vec{x})] \cdot \hat{l} \right)^p \rangle = \langle (\delta v_l)^p \rangle. \tag{1.17}$$

In particular the K41 theory predicts that the average energy per unit mass associated with the velocity increments is given by

$$S_2(l) = \langle (\delta v_l)^2 \rangle = \langle E \rangle = C\varepsilon^{2/3} l^{2/3}, \tag{1.18}$$

where C is a universal constant. Equation (1.18) is known as the Kolmogorov's 2/3 law and it works very well in turbulent flows at very high Reynolds number. Incidently, applying the scale invariance hypothesis directly in $\delta\vec{v}(\vec{x}, \lambda\vec{l}) = \lambda^h \delta\vec{v}(\vec{x}, \vec{l})$, the value of the exponent h consistent with Kolmogorov's 2/3 law (Kolmogorov (1941c)) can is determined, thus

$$S_2(\lambda l) = \langle \left(\vec{v}(\vec{x}, \lambda\vec{l}) \cdot \vec{l} \right)^2 \rangle = C\varepsilon^{2/3} (\lambda l)^{2/3}, \tag{1.19}$$

where

$$\lambda^{2h} \langle (\delta v_l)^2 \rangle = C\varepsilon^{2/3} (\lambda l)^{2/3}, \tag{1.20}$$

it follows that the unique scaling exponent has the value $h = 1/3$ (Frisch (1995)). Relations for the structure functions of higher order can be found similarly, yielding

$$\langle \delta v_l^p \rangle = C_P (\varepsilon l)^{p/3} \quad (\eta \ll l \ll L). \tag{1.21}$$

In the particular case of the third-order structure functions of velocity increments, a linear relation with the distance, called the 4/5 law, is obtained with an exact value for the constant C_3

$$\langle \delta v_l^3 \rangle = -\frac{4}{5} \varepsilon l. \tag{1.22}$$

Another way to calculate the average energy contained by the system is through a spectral decomposition with a discrete Fourier representation of the periodic flow in a box of size l. Therefore, the velocity field may be expanded as a Fourier series

$$\vec{v}(\vec{x},t) = \sum_{n_1,n_2,n_3} \hat{v}(\vec{k},t)\exp(i\vec{k}\cdot\vec{x}), \tag{1.23}$$

where $\vec{k}$ is a vector with components k_i so that $\vec{k} = \{k_1,k_2,k_3\} = \left\{\frac{2\pi}{l}n_1, \frac{2\pi}{l}n_2, \frac{2\pi}{l}n_3\right\}$, with n_1, n_2 and n_3 being integers. we may define three ranges for the wavenumbers in this representation (McDonough (2004))

- **The production range** at low wavenumbers, about which nothing can be said in the present framework.
- **The inertial range** at intermediate wavenumbers, at which energy is shifted upwards towards higher wavenumbers without much production or dissipation taking place.
- **The dissipation range** at high wavenumbers, at which the energy put into the production range is finally destroyed.

Using an argument due to Obukhov (Obukhov (1941a,b)), one can estimate how the fluid's energy is distributed as a function of the wavenumber. We get

$$\langle E(k)\rangle = \int_k^\infty d\langle E\rangle = \int_k^\infty E(k)dk, \quad \text{where} \quad E(k)\sim k^{-n} \quad \text{for} \quad 1\leq n\leq 3, \tag{1.24}$$

therefore

$$\langle E(k)\rangle \sim \int_k^\infty k^{-n}dk \sim C_n k E(k). \tag{1.25}$$

Now using Kolmogorov's 2/3 law, we obtain

$$C_n k E(k) = C\varepsilon^{2/3} k^{-2/3} \quad \rightarrow \quad E(k) = C_K \varepsilon^{2/3} k^{-5/3}, \tag{1.26}$$

where C_K is the Kolmogorov constant. This is another important prediction of K41 theory and is known as the $k^{-5/3}$ energy spectrum of the inertial-range.

Contrary to what we might think of a homogeneous three-dimensional isotropic turbulent flow, the velocity fluctuations' amplitude is not distributed uniformly in space, feature that gives rise to a phenomenon called **internal intermittency** (Obukhov (1962); Landau and Lifshitz (1959); Kolmogorov (1962a)). It is an important statistical property of the flow that results from the local kinetic energy dissipation rate displaying relevant fluctuations about its mean value. This effect is not accommodated in Kolmogorov's 1941 theory, since it does not consider fluctuations of the variable ε. This critique became known as the Landau's objection and was one of the reasons that led to a reformulation of the K41 theory. Kolmogorov himself, with the help of previous work by Oboukhov, gave an answer to Landau's objection that became known as the KO62 theory, which will be discussed in the following subsection.

1.3.3 *The Kolmogorov Oboukhov Theory*

In 1961, at the Colloque International de Mecanique de la Turbulence in Marseille, Kolmogorov and Oboukhov presented their theory of intermittency (Kolmogorov (1962a); Obukhov (1962)), the KO62 theory. The new theory provides answers to the criticism raised by Landau, whose statement was translated into English as follows

Landau's Objection

It might be thought that the possibility exists of obtaining a universal formula, applicable to any turbulent flow, which should give $S_2(l)$ for all distances l that are small compared with L. In fact, however, there can be no such formula, as we see from the following argument. The instantaneous value of $\langle \delta v_l \rangle^2$ might in principle be expressed as a universal function of the

dissipation ε at the instant considered. When we average these expressions, however, an important part will be large eddies with size $\sim L$, and this variation is different for different flows. The result of the averaging therefore cannot be universal (Landau and Lifshitz (1959)).

This objection can be stated mathematically as follows. Assume that $N > 1$ experiments are made with different positive values of the mean dissipation rate, denoted by ε_i with $i = 1, \ldots, N$. The structure functions for the i-th flow (LESLIE (1973)) is given by

$$S_p^i(l) = C_P \varepsilon_i^{p/3} l^{p/3}. \tag{1.27}$$

Let us now construct a superensemble in order to accommodate the fluctuations in the N realizations of structure functions and dissipation rates. The superaveraged structure functions and dissipation rate are given respectively by

$$\langle S_p(l) \rangle = \frac{1}{N} \sum_{i=1}^{N} S_p^i(l), \quad \text{and} \quad \langle \varepsilon \rangle = \frac{1}{N} \sum_{i=1}^{N} \varepsilon_i. \tag{1.28}$$

Comparing the structure function obtained from the K41 theory, Eq. (1.21), with the superaveraged value above we obtain the following relation

$$\left(\frac{1}{N} \sum_{i=1}^{N} \varepsilon_i \right)^{p/3} = \frac{1}{N} \sum_{i=1}^{N} (\varepsilon_i)^{p/3}, \tag{1.29}$$

which is contradictory for all values of p, except for $p = 3$. To solve this, the KO62 theory proposes that the local energy dissipation $\varepsilon(\vec{x}, t)$, defined as the average of ε on a sphere of center $\vec{x}$ and radius r has a log-normal distribution **LN** (Kolmogorov (1962a,b)). With this assumption, the model predicts that the variance σ_r^2 of $\ln \varepsilon_r$ is given by

$$\sigma_r^2 = Q(\vec{x}, t) + \mu \ln \left(\frac{L}{r} \right), \tag{1.30}$$

where L is the integral scale of turbulence, $Q(\vec{x}, t)$ a function that depends on the large scales and μ is a universal constant, known as the **intermittency exponent** (Lesieur

(1997)). The surmise is supposed to be valid only for $r \ll L$. Using this model one can show that the structure functions are given by

$$S_n \sim \langle \varepsilon_r^{n/3} \rangle r^{n/3}, \tag{1.31}$$

where the moments for the local energy dissipation are[1]

$$\langle \varepsilon_r^p \rangle = \langle \varepsilon \rangle^p \exp\left(p(p-1)\frac{\sigma_r^2}{2} \right). \tag{1.32}$$

Using (1.30), it is possible to rewrite the above equation in terms of a derivative of order p

$$\langle \varepsilon_r^p \rangle = D_p \langle \varepsilon \rangle^p \left(\frac{L}{r} \right)^{\mu p(p-1)/2}, \tag{1.33}$$

where D_p is the derivative operator. In this notation the correlation function for the rate of energy dissipation is

$$\langle \varepsilon(\vec{x}+\vec{r},t)\varepsilon(\vec{x},t) \rangle = D_2 \langle \varepsilon \rangle^2 \left(\frac{L}{r} \right)^{\mu} = \frac{1}{2}\partial_r^2 (r^2 \langle \varepsilon(\vec{x},t)^2 \rangle), \tag{1.34}$$

while the second-order longitudinal structure function is given by

$$S_2(r,t) \sim \langle \varepsilon \rangle^{2/3} r^{2/3} \left(\frac{L}{r} \right)^{\mu/9}. \tag{1.35}$$

Its generalization to order n is straightforward

$$S_n \sim \langle \varepsilon \rangle^{n/3} r^{n/3} \left(\frac{L}{r} \right)^{\mu n(n-3)/18}. \tag{1.36}$$

The KO62 theory also generalizes the $k^{-5/3}$ energy spectrum law to the following law

$$E(k) \sim \langle \varepsilon \rangle^{2/3} k^{-5/3} (kL)^{-\mu/9}. \tag{1.37}$$

[1] For more details see Gurvich and Yaglom (1967) and Orszag (1970)

Gurvich and Yaglom (Gurvich and Yaglom (1967)) were able to provide a theoretical justification for the log-normal hypothesis of Oboukhov and Kolmogorov. Beginning with the integral length scale $L = l_0$, they defined a sequence of smaller length scales

$$l_1 = \alpha l_0; \ldots, l_j = \alpha^j l_0; \ldots; l_N = \alpha^N l_0. \tag{1.38}$$

The ratio α is small enough to ensure that, according to Kolmogorov's hypothesis, little or no energy will be transferred directly from an eddy of size l_j, to one of size l_{j+1} Therefore these eddies may be regarded as statistically independent. Furthermore, l_N is considered smaller than the Kolmogorov microscale η, and N is supposed to be large, implying that Re is very large indeed (Monin and Yaglom (2007)). Here, ε_j denotes the spatial average of $\langle \varepsilon \rangle = \bar{\varepsilon}$ over a box of side l_j, ε_0 may be identified with the average dissipation ε, while l_N is so small that ε_N does not differ appreciably from the instantaneous value of ε. We then have

$$\bar{\varepsilon} = \zeta_N \zeta_{N-1} \ldots \zeta_1 \varepsilon \tag{1.39}$$

and thus

$$\ln \bar{\varepsilon} = \ln \varepsilon + \sum_{j=1}^{N} \ln \zeta_j, \tag{1.40}$$

which shows that the random variable $\bar{\varepsilon}$ as a sum of independent random variables $\ln \zeta_j$ (Lesieur (1997)). If N is large enough, the central limit theorem assures us that the distribution of $\ln \bar{\varepsilon}$ must be normal or Gaussian, which implies a log-normal distribution for $\bar{\varepsilon}$.

More recently, using several features of Kolmogorov's theory such as energy cascade, intermittency and multiscale dynamics, Salazar and Vasconcelos (Salazar and Vasconcelos (2010)) introduced a dynamical stochastic model that accounted well for the heavy power law tails observed in experimental time series of velocity increments in turbulent flow. The log-normal distribution predicted by KO62 was found to be a limiting case. This theory, which we shall call the SV model, was the central motivation for the subjects

studied in this Thesis. However, before entering into the technical details of this Thesis' contributions, we want to present a brief chronological account of the Thesis' project.

1.4 A chronological description of the Thesis' project

1.4.1 *Stage 1*

In this part of the chapter, we want to contextualize the reader about the relevant facts that have motivated this research project, which was born from the idea to construct an extension to Generalized Hypergeometric Model (GHM) developed by Salazar and Vasconcelos (SV) (Salazar and Vasconcelos (2010, 2012); Salazar (2010)) and apply it to the eigenvalues' spectrum of closed ballistics cavities (better known as billiards) with mixed dynamics where the regular and chaotic universal regimes coexist (Abul-Magd *et al.* (2008); Prosen and Robnik. (1993); Prosen and Robnik (1994); Richter (1999)). The GHM is a hierarchical system of coupled stochastic differential equations, which have been proposed as a statistical model for describing turbulence in classical fluids, thus satisfying the symmetries of Navier Stokes equations (Frisch (1995); Salazar (2010)) in addition to obeying the principles of Kolmorov 1941 theory (K41) (Kolmogorov (1941c,b); Obukhov (1941a,b); Kolmogorov (1941d,a)) and being compatible with Kolmogorov-Obukhov 1962 (KO62) hypothesis (Obukhov (1962); Kolmogorov (1962a,b)).

Another reference model for this research has been the statistical superposition or superstatistics (SS) approach, which was introduced into physics by Beck et al. (Beck *et al.* (2005)). The SS approach establishes, through Bayes' theorem, the convolution between two types of statistics whose characteristic relaxation times are well separated so that one of the dynamics reaches a local equilibrium, while the other remains practically invariant. From this initial perspective, the GHM together with SS seemed to be suitable candidates to explain the deviations from Wigner-Dyson's (WD) statistics that are observed in the nearest neighbor spacing distribution (NNSD) of billiards with mixed dynamics. The WD distribution is a universal feature of chaotic dynamics in ballistic cavities. This hypothesis was strengthened after we came to know the research by Abul-

Magd, Richter, and et. al. (Abul-Magd *et al.* (2008)), which opened the possibility to explain through a dynamic model the integrable-chaotic transition from thus going beyond Brody's and Berry-Robnik distributions (Prosen and Robnik. (1993); Prosen and Robnik (1994); Mehta. (2004)). In (Abul-Magd *et al.* (2008)), the authors not only described the NNSD in cavities with mixed dynamics by means of the SS approach, but they also applied it to the eigenvector's probability density function (PDF) and some types of correlation functions. However, after analysing the results of reference (Abul-Magd *et al.* (2008)) in more detail, we perceived several problems may be related to the reduced number of eigenvalues and eigenvectors used to perform the statistic analysis. Even after being mindful of the enormous experimental difficulties that limit the measurement of a larger spectrum, we also noticed that the histograms had normalization problems and the fluctuations between neighboring bins were so great that many parametric families could make an acceptable fit. All these evidences combined with comments by Stöckmann (Stöckmann (2007)), who stated that the presence of antennas in resonant cavities could modify the NNSD in such a proportion that a cavity previously characterized as regular can change towards the chaotic regime, made us believe that a dynamical approach was needed to solve this problem.

In order to answer the questions raised by the subtleties that were not clarified in the literature of integrable-chaotic transition, we decided to perform some computational tests, and to do so we looked for efficient algorithms and available tool boxes. In that search we found the MPSpack MATLAB Toolbox, developed by Barnett and Betcke (Barnett and Betcke (2012)) and as one can find on their website is an algorithm designed to solve 2D Helmholtz scattering and eigenvalue problems via particular solutions and integral equations. In order to check the precision and power of this method, we ran a number of tests with the limaçon shape or Robnik's billiard.

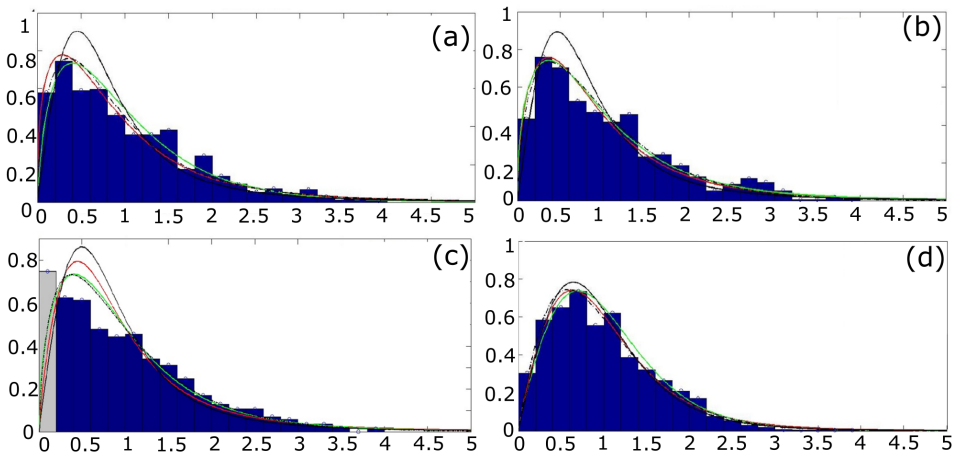

Figure 1.1: In blue: histogram of NNSD for Limaçon ((a),(b)) and Mushroom ((c),(d)) billiards with mixed dynamics. The black lines represent the predictions made by the SS model taken from the reference (Abul-Magd *et al.* (2008)). The colored lines correspond to the solution obtained through the Milstein method of a coupled set of stochastic differential equations (see appendix A). Our main interest here is to show the difficulty of establishing a statistical model when the number of data points is small.

Mathematically, this geometry is constructed from the coordinate transformation $x(\phi) = \cos\phi + \lambda\cos 2\phi$, $y(\phi) = \sin\phi + \lambda\sin 2\phi$, where the azimuth angle is defined in the domain $0 \leq \phi \leq 2\pi$, while the deformation parameter $0 \leq \lambda \leq 0.5$ controls the transition from the circular form ($\lambda = 0$) to the cardioid ($\lambda = 0.5$). In the literature (Richter (1999); Prosen and Robnik. (1993); Prosen and Robnik (1994); Gómez *et al.* (2005)) is more common to describe this billard in conformal notation according to the transformations $z(\phi) = \cos\phi + \imath\sin\phi$ and $\omega(\phi) = x(\phi) + \imath y(\phi) = z(\phi) + \lambda z^2(\phi)$. In figure 1.2 we show some eigenfunctions of the time-independent Schrödinger equation with Dirichlet boundary conditions applied to the limaçon billard. We made the acquisition of computed eigenvalues (3×10^4), in an attempt to make statistics to determine the form of the NNSD. Nevertheless, after unfolding the spectrum using Weyl's law (Heinz and Schreiber. (2002)), the results did not agree with those shown by the literature (Gómez *et al.* (2005)). One possible solution was to divide the spectrum according to the symmetry but it was not clear how to determine the procedure to execute such task. The

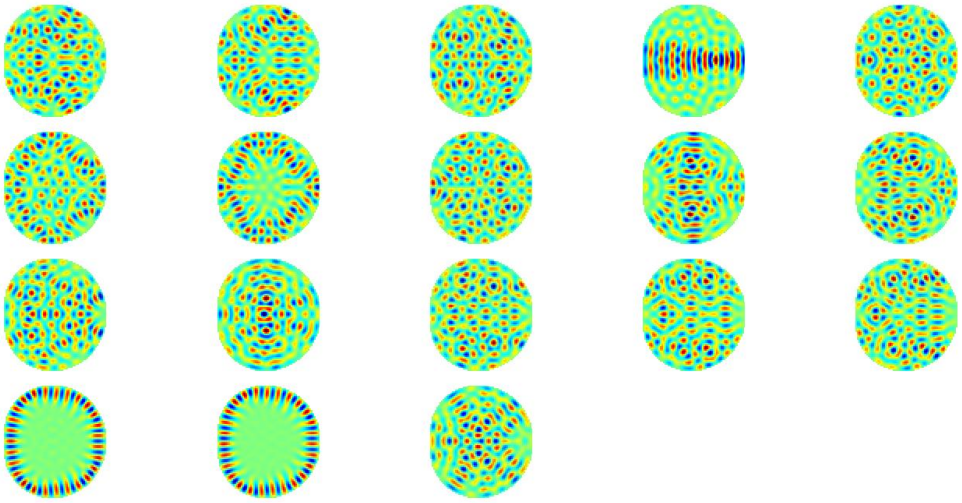

Figure 1.2: We show some modes of the Helmholtz equation's spectrum that is equivalent to the mathematical model of the time-independent Schödinger equation for the Limaçon billard with parameter $\lambda = 0.25$.

second option was to divide the geometry to break its symmetries, so using the MPSpack's tutorial (Barnett and Betcke (2012)) was designed a half limaçon billiard, but when performing this operation the toolbox presented errors to calculate large wave numbers. This led us to leave MPSpack and search another way to perform our own tests.

1.4.2 *Stage 2*

In this phase was considered the possibility to generate the cavities and the differential operators involved in our eigenvalues problem by using discrete differential geometry tools, particularly discrete exterior calculus (DEC). For that purpose, was used the Distmesh MATLAB Toolbox designed by Persson and Strang (Persson and Strang (2004); Persson (2004)) particularly useful. This tool set up a triangular mesh within a defined contour using Signed Distance Functions, in which the distance function can be computed by interpolation between values on a grid. DistMesh uses the Delaunay triangulation routine in MATLAB and restricts through its algorithm the formation of triangles with obtuse angles with the purpose of avoiding inconsistencies in the implementation of differential operators, which correspond to the operations on vertices, sides or faces over the original mesh or over the dual mesh whose vertices depending of the approach will be generated

in the circumcenters or barycentres of the first triangulation (Botsch *et al.* (2010); Crane (2005); Bobenko and Springborn. (2007)) (see figure (1.3)).

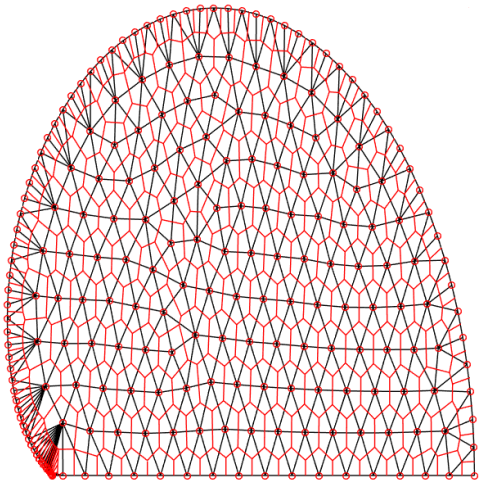

Figure 1.3: In black: Delaunay triangular mesh that excludes the formation of obtuse-angles. In red: barycentric hexagonal dual mesh applied to the Limaçon billiard

After generating the geometries, the next step was to construct the Laplace operator with Dirichlet boundary conditions for this mesh. In particular, during this work we followed the Peyré research (Peyré (2008)) for different reasons, including that he has implemented several mappings approach, such as (*i*) Conformal: no distortion in angles, (*ii*) Equilateral: no distortion in areas. With these DEC tools, the sparse matrix of the Laplace-Beltrami operator was constructed, which was diagonalize, and its eigenvalues were characterized based on two statistical parameters: (i) The Kullback Leibler distance δ_{LK} between the nearest neighbor spacing distribution of the spectrum and the universal Wigner-Dyson distribution and (ii) the exponent α in the tail of the power spectrum density $s(f) \sim 1/f^{\alpha}$. Results for flat billiards were consistent with previous works of the recent literature (Gómez *et al.* (2005)).

Working with conformal maps also allowed us to generate curvatures in the geometries and to diagonalize their corresponding Laplace-Beltrami operator (see appendix D). To

determine a possible dependence of the NNSD as a function of the curvature, an initially circular and plane geometry was considered and a deformation was created on its surface with controlled amplitude. The spectra were characterized via the measures mentioned above, the curvature acted as a kind of factor that produces a crossover from the integrable to the chaotic regimes, as described in Chapter Six.

1.4.3 *Stage 3*

Given the need to gain experience in the statistical analysis of complex systems, we followed as a parallel activity the research of Beck et al. (Beck *et al.* (2005)) and Guhr et al. (Schmitt *et al.* (2013)). These papers show the possibility of extracting an auxiliary data series (background series), which can be integrated numerically with the Gaussian kernel and reproduce the PDFs with heavy tails, which could be associated directly with the experimental data (signal). We tested this procedure using the same reference data used by Guhr and coworkers Schmitt *et al.* (2013), which were released to the public at (Standard and data from Yahoo! Finance (2013)). However, after performing several computational tests was perceived that the criterion to determine the background series (Abul-Magd *et al.* (2008); Beck *et al.* (2005); Schmitt *et al.* (2013)) sometimes does not recover the experimental signal after performing the numerical integration, which consists of the arithmetic average

$$P(x_i) = \frac{1}{N_\epsilon} \sum_{j=1}^{N_\epsilon} \frac{1}{\sqrt{2\pi\epsilon_j}} \exp\left(\frac{-x_i^2}{2\epsilon_j}\right) \tag{1.41}$$

of Gaussian distributions with variable variances. The variances were sampled from N_ϵ elements of the background series, which have obtained by computing the standard deviation of a running window from the signal data series.

We realized that the best way to generate the background series is by fixing the size of the running window such that after integrating with the Gaussian kernel, it produces the best fit to the experimental data. This is quite different form Guhr's procedure, in which the running window size are chosen by the criterion that a renormalized series, which is

obtained from subtracting the local mean from the original series and then dividing by the local standard deviation, recovers the Gaussian value for the kurtosis.

This new procedure, which is described in detail with examples in chapter three, has become a ubiquitous tool in this research, since it allowed us through a simple numerical integration to obtain the parametric family of distributions that have been found in the four complex systems characterized in this Thesis, which was supported by our theoretical model, the H-theory (Macêdo *et al.* (2017)) (see chapter two).

Our theoretical model, the H-theory, was constructed from an extension of the generalized hypergeometric model GHM developed by Salazar and Vasconcelos, which roughly can be summarized as a model to describe the emergence of distributions with heavy non-Gaussian tails through the stationary solution of a coupled system of stochastic differential equations.

1.4.4 *Stage 4*

At this stage the goal was to confirm the existence of a possibly large number of background scales, $N > 1$, from the experimental data of velocity increments ($u_{\delta_i}(j) = v(j + \delta_i - 1) - v(j - 1)$ with $\delta_i = 2^i$) of Eulerian turbulence in a jet of Hellium gas, supplied by Chabaud-Hábral et al. (Chabaud *et al.* (1994); Chanal *et al.* (2000)), which were analyzed previously by Salazar in (Salazar (2010)). We worked with the data for the Reynolds number $Re = 295,000$. In agreement with the SV approach, we found that the PDF of the smallest velocity increments normalized by its standard deviation, u_{δ_0}, had an optimal fit when five background scales were used, as shown in figure (1.4).

Another important feature in the SV approach is that the number of relevant scales in the background distribution decreases progressively when the statistics on normalized distributions u_{δ_i} are performed, for $\delta_i \to \{\delta_1, \delta_2, \delta_3, \delta_4, \dots\}$ until it recovers the integral scale, where the Gaussian distribution applies. The specific form in which this crossover occurred agreed with reference (Salazar (2010)) and did not seem to have any notable inconsistencies, since the GHM is a robust model that is based on assumptions and sym-

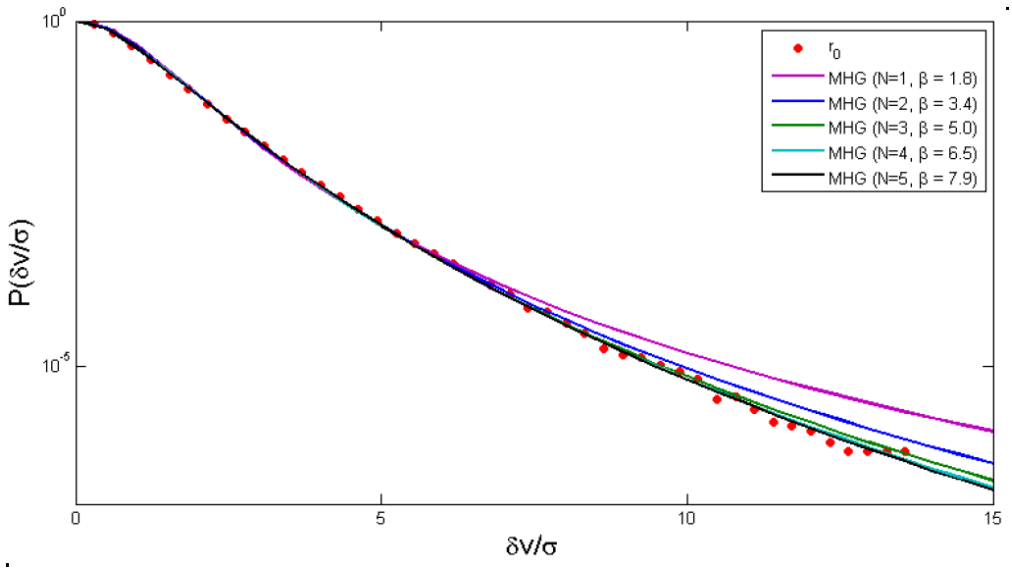

Figure 1.4: This figure, which has been taken from chapter 4 of reference (Salazar (2010)), justifies the existence of five background scales for the Eulerian turbulence with Reynolds number $Re = 295,000$.

metries underlying the Kolmogorov theory. So the arguments in the GHM appeared to be final, especially after we successfully fitted the hypergeometric functions ${}_NF_0$, corresponding to stationary solutions of the model, using the parameters set by Salazar for the Reynolds number $Re = 295,000$. However, for the sake of completeness, we decided to test if the other members of the three background families of the superstatistics model could also fit the PDF of the velocity increments, u_{δ_i}. The standard background distributions are

$$f(\varepsilon) = \begin{cases} \frac{(\beta\epsilon_0)^{\beta+1}}{\Gamma(\beta+1)}\varepsilon^{\beta}\exp\left(-\beta\varepsilon_0\varepsilon\right) & \text{Gamma class} \\ \\ \frac{(\beta\varepsilon_0)^{\beta+1}}{\Gamma(\beta+1)}\varepsilon^{-\beta-2}\exp\left(-\frac{\beta\varepsilon_0}{\varepsilon}\right) & \text{Inverse-Gamma class} \\ \\ \frac{1}{\varepsilon\sqrt{2\pi\sigma^2}}\exp\left(-\frac{(\ln\varepsilon-\mu)^2}{2\sigma^2}\right) & \text{Log-Normal class,} \end{cases}$$

and the composed distribution is obtained from

$$P(u) = \int_0^\infty \frac{1}{\sqrt{2\pi\varepsilon}} \exp\left(-\frac{u^2}{2\varepsilon}\right) f(\varepsilon) d\varepsilon. \tag{1.42}$$

We also noticed the existence of a direct correspondence between the moments of the marginal distribution $P(u)$ and the moments of $f(\varepsilon)$, also seen by Salazar (Salazar (2010)) in the inverse-gamma class, which is shown in table 1.1

	$\langle\varepsilon\rangle$	$\langle\varepsilon^2\rangle$	$\langle u^2\rangle$	$\langle u^4\rangle$
Gamma (G)	$\frac{\beta+1}{\beta\varepsilon_0}$	$\frac{(\beta+2)(\beta+1)}{(\beta\varepsilon_0)^2}$	$\langle\varepsilon\rangle_{(G)}$	$3\langle\varepsilon^2\rangle_{(G)}$
Inverse-Gamma (IG)	ε_0	$\frac{\beta\varepsilon_0^2}{(\beta-1)}$	$\langle\varepsilon\rangle_{(IG)}$	$3\langle\varepsilon^2\rangle_{(IG)}$
Log-Normal (LN)	$e^{\mu}e^{\sigma^2/2}$	$e^{2\mu}e^{2\sigma^2}$	$\langle\varepsilon\rangle_{(LN)}$	$3\langle\varepsilon^2\rangle_{(LN)}$

Table 1.1: Relations between the background's and signal's moments for the universal classes of the SS model, where $\langle x^n\rangle = \int x^n f(x)dx$.

Although Beck-Cohen-Swinney in (Beck *et al.* (2005)) perceived an essentially identical relation between the background and signal distributions (in their notation the background variable is the inverse of the variance) which was done defining the parameters $q := \frac{<\beta^{*2}>}{<\beta^{*}>^2}$ and $F = \frac{<u^4>}{<u^2>^2}$ and deriving the ratio $q = F/3$ for the superposition between the Gaussian and the log-normal distributions. They however never mentioned explicitly that this ratio is valid for all three universality classes (gamma, inverse-gamma and log-normal), nor did they mention that the $q = F/3$ ratio is strictly linked to having a Gaussian kernel in the superposition, therefore it is quite independent of the background family and it is also independent of whether the kernel probability distribution is conditioned by the variance ε or by its inverse β^*. They also did not establish direct relations between the signal and the background moments $\langle u^{2r}\rangle = \langle\beta^{*r}\rangle \prod_{k=1}^{r}(2k-1)$. Although this may seem an irrelevant fact, thanks to the fact that the signal's kustosis κ, or flatness F, is constant

when it is normalized by the standard deviation $\kappa(u) = \kappa(u/\sigma)$, the value of the background's variance can be directly deduced from the identity $\sigma^2(\varepsilon) =< \varepsilon^2 > -1 = \frac{\kappa(u)}{3} - 1$. Applying this simple procedure to the Eulerian turbulence data, we obtained excellent fits for the normalized velocity increments distributions u_{δ_i} for $\delta_i = \{1, 2, 4, 8, 16\}$. In this test we considered the following classes: (i) inverse-gamma, which gives the distribution

$$P_{IG}(u) = \frac{1}{\sqrt{2\pi\beta\epsilon_0}} \frac{\Gamma(\beta + 3/2)}{\Gamma(\beta + 1)} {}_1F_0\left(\beta + \frac{3}{2}, -\frac{u^2}{2\beta\epsilon_0}\right), \tag{1.43}$$

that we have called hypergeometric ${}_1F_0$ in agreement with the GHM, where β is the free parameter for the IG class in table 1.1; and (ii) the log-normal class, which gives the distribution

$$P(u) = \int_0^\infty \frac{\varepsilon^{-3/2}}{2\pi\sigma_{LN}} \exp\left(-\frac{u^2}{2\varepsilon}\right) \exp\left(-\frac{(\ln\varepsilon - \mu)}{2\sigma_{LN}^2}\right) d\varepsilon, \tag{1.44}$$

which does not have a defined name in literature, therefore we will refer to it in this chapter as $P(u)$. Using the kurtosis criterion for the $u(\delta_i)$ data series and fixing the free parameters using the relations in table 1.1, the best fits obtained are shown in figure (1.5).

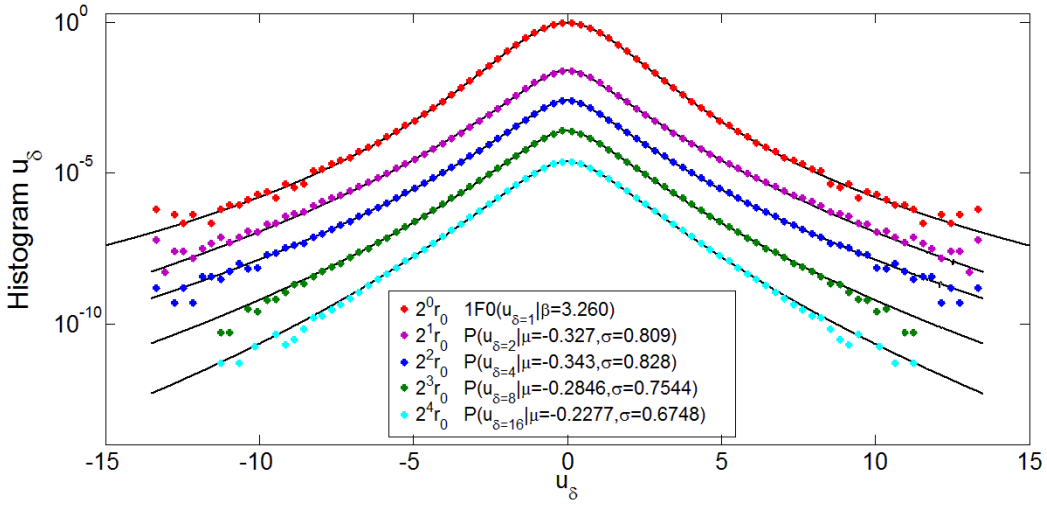

Figure 1.5: Normalized PDF for velocity increments u_{δ_i}, with $\delta_i = (1, 2, 4, 8, 16)$. In black lines: best fits made with the universal classes inverse-gamma and log-normal of the SS model.

These results were somewhat unexpected, since it puts in check the hypergeometric model (GHM) and contradicts in a first approximation the conclusion put forward by Salazar that according to figure (1.4) five background scales are necessary to obtain the best quantitative description of the u_{δ_0} PDF, which mathematically is the hypergeometric function

$$P_{IG}(u) = \frac{1}{\sqrt{2\pi\beta_1 \ldots \beta_5 \epsilon_0}} \prod_{i=1}^{5} \frac{\Gamma(\beta_i + 3/2)}{\Gamma(\beta_i + 1)} {}_5F_0\left(\beta_1 + \frac{3}{2}, \ldots, \beta_5 + \frac{3}{2}; -\frac{u^2}{2\beta_1 \ldots \beta_5 \epsilon_0}\right), \tag{1.45}$$

with parameters ($\beta_1 = \beta_2 = \beta_3 = \beta_4 = \beta_5 = 7.9$) and $\epsilon_0 = 1$. Using the generalized hypergeometric model (Salazar (2010)), equation (1.45) corresponds to the distribution generated by the superposition of five background scales

$$f_N(\varepsilon) = \int_0^\infty \ldots \int_0^\infty f(\varepsilon|\varepsilon_{N-1}) \ldots f(\varepsilon_1|\varepsilon_0) d\varepsilon_{N-1} \ldots d\varepsilon_1, \tag{1.46}$$

where to each scale one can associate a conditional distribution of the parametric family inverse gamma (IG)

$$f(\varepsilon_i|\varepsilon_{i-1}) = \frac{(\beta_i \varepsilon_{i-1})^{\beta_i+1}}{\Gamma(\beta_i + 1)} \varepsilon_i^{-\beta_i-2} \exp\left(-\frac{\beta_i \varepsilon_{i-1}}{\varepsilon_i}\right). \tag{1.47}$$

On the other hand, using the superstatistics model, we showed that is possible to fit with the same quality using a function ${}_1F_0$ with parameters $\beta_1 = 3.26$ and $\epsilon_0 = 1$ as shown in the black line that accompanies the red histograms at the top of figure (1.5). Also, we have identified that for distributions at different intervals δ_i greater than the measure's resolution; the superstatistics model produces an optimal fit using the log-normal class (LN) on the background. This distribution can also be constructed from the GHM in the limit as $N \to \infty$ and $\beta \to \infty$, with the finite variance condition $\sigma_{LN}^2 = N/\beta$

$$\lim_{N,\beta\to\infty} f_N(\varepsilon_N) = \frac{1}{\varepsilon\sqrt{2\pi\sigma_{LN}^2}} \exp\left(-\frac{(\ln\varepsilon - \mu)^2}{2\sigma_{LN}^2}\right). \tag{1.48}$$

The possibility of using superposition with LN distribution for velocity increases u_{δ_i} with $\delta_i = (2, 4, 8, 16)$, questioned the GHM hypothesis where there are a defined number of scales involved in the energy transfer process (cascades) as a function of δ_i. From these considerations, some interesting questions arose

- How many scales are involved in the dynamical process?
- How does the transition between classes take place as we move towards the integral scale?

We discovered a way to explain the u_{δ_i} PDF's behavior from the smallest scale ($\delta_0 = 1$) to larger scales, where the conditions of the central limit theorem are reestablished ($\sim \delta_{10} = 2^{10}$). The argumemnts will be presented in detail in chapter four.

1.4.5 *Stage 5*

In a transitional model, we removed the normalization condition from the standard deviation, so we let the central even moments ($\langle u_{\delta_i}^{2r} \rangle$) of the u distribution evolve as a function of δ_i. We considered as a starting point two popular stochastic volatility models in the financial market, the Heston and Hull-White models (Biró and Rosenfeld (2008); Dragulescu and Yakovenko. (2002); Vicente *et al.* (2006)). This SDE approach helped us improve our previous statistical analysis in two ways: (i) we now focus on time-lagged increment distributions, as opposed to marginal stationary distributions; (ii) we can account for long time-lagged Gaussian asymptotic behavior in the increment distributions by inserting time-dependence on some SDE parameters. The numerical solution of the SDE showed good qualitative agreement with experimental data on Eulerian turbulence of helium gas with $\mathrm{Re} = 295,000$.

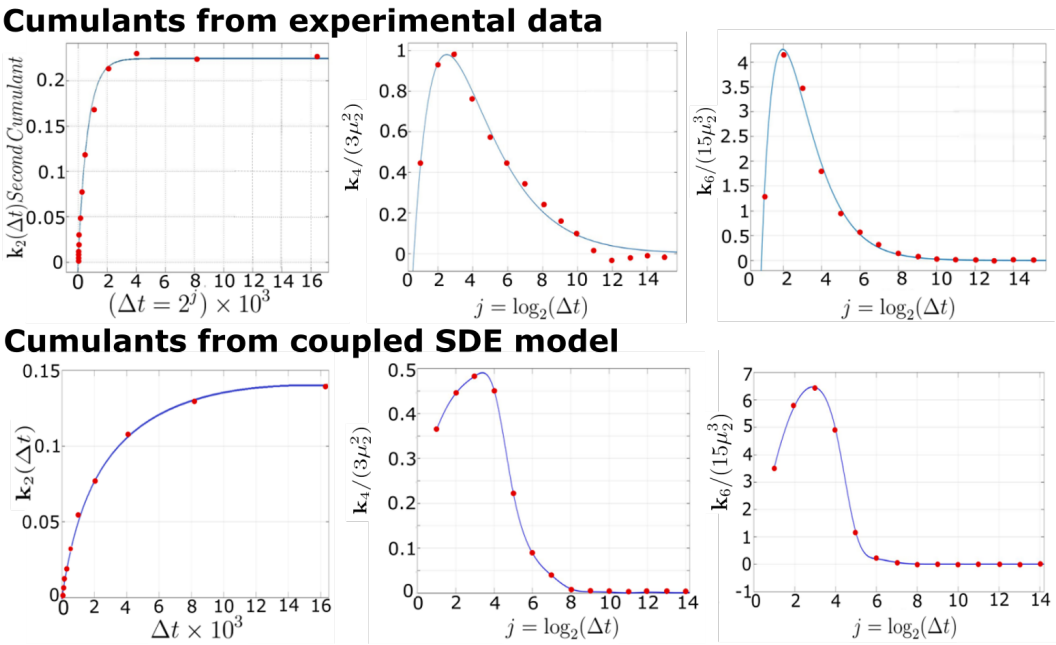

Figure 1.6: The coupled SDE describes qualitatively the cumulants behavior. However, the large number of free parameters in the model made it difficult to carry out a fit for the distribution of velocity increments u_{δ_i} (κ_i:i-th cumulant, μ_j: j-th central moment).

Although the results obtained with this numerical approach were interesting, the initial questions were still open. So, after an extended period of research we found a formalism that consistently describes the PDF's features of complex hierarchical systems similar to fluids with turbulent dynamics. The most satisfactory answer have been called the H theory, mainly because Fox H-functions forms the most general family that unifies the two classes of distributions with heavy tails: power law and stretched exponential (Macêdo *et al.* (2017)).

1.4.6 *Stage 6*

The most commonly studied statistical property of a time series is its histogram, which gives the shape of the probability density function. In the complex systems considered in this dissertation, the PDFs are sensitive to the scale of observation, or data acquisition, so that the forms associated with the central limit theorem (Gaussian, Lévy, Wigner-

Dyson) are obtained only on the integral scale, which is the largest scale of the system. In this perspective, the fluctuations in smaller scales can be relaxed until one reaches the local equilibrium exhibiting distributions that depend parametrically on variables that fluctuate in larger scales. Therefore, the signal's histogram obtained on the experimental detection scale, usually smaller than the integral scale, can be interpreted as a result of stochastic processes in which multiple spatial/temporal scales are coupled through a hierarchical structure. To describe in a more general context this type of behavior we proposed the formalism of H-theory, which generalizes the model GHM proposed by Salazar and Vasconcelos, in which the slow dynamics of the parameters that fluctuate in larger scales is obtained as a direct consequence of the validity of five basic principles: (i) Time-translations symmetry, (ii) local interactions, (iii) scale invariance, (iv) equilibrium condition and (v) unidirectional flow. The H-theory is a dynamic stochastic model that overcomes the other approaches' limitations in describing a temporal/spatial multiscale hierarchical system. It can also describe transitions between the two types of distributions with heavy tails, and with a joint fitting procedure it determines the number of scales for both the signal and the background of the complex system. This is an important feature, since if only the signal is fitted one gets an ambiguity, because model distributions with different values of the number of scales in the background produce fits with similar qualities.

2 The H-Theory

2.1 Introduction

Experimental time series of complex systems usually show large deviations from Gaussian statistics. It is common to assume a priori that the experimental time series is stationary, however, in general, the distributions may have time-dependence and if so it could be interpreted as fluctuations about some time-dependent mean (Livi and Vulpiani (2003)). There are two well-defined trends in the current literature to describe stationary time series of physical systems that differ substantially from Gaussian processes. In the first approach the time series is treated as the position of a particle undergoing an anomalous diffusive process, therefore its histogram or probability density function (PDF) corresponds to a Lévy distribution (Mantegna and Stanley (1994); Koponen (1995)). The physically undesirable consequence that such distributions have infinite variance is usually dealt with, a posteriori, by imposing some sort of truncation, generating the so-called truncated Lévy distributions. The second trend comes from the observation that in many cases the resulting heavy-tailed distributions can be accounted for by a superposition of statistics known as compounding [mathematics] or superstatistics [physics]. The basic assumption in a statistical superposition approach is the existence of two well separated time scales driving the dynamics, which would ultimately lead to a stationary solution where the short time distribution, due to the fast variables (the signal), is averaged over the long time slow variables (the background) distribution. Three universality classes have been found for the background distribution, which have been proposed on the basis of very general arguments, such as the central limit theorem for the sum or product of independent random variables. The three universal distributions are gamma, inverse-

gamma and lognormal. The empirical success of such a scheme is well described in the literature, as can be seen in examples ranging from turbulence in classical fluids (Beck *et al.* (2005)), microwave propagation through disordered cavities (Abul-Magd *et al.* (2008)) and price variations in financial time series (Schmitt *et al.* (2013)).

Albeit successful in describing the stationary distributions, or histograms, of the time series of many types of complex systems, statistical superposition cannot be considered a complete description since it offers no explanations to the other features of the stochastic process associated with the system's time series, such as correlation functions, noise power spectra and memory function. For that a dynamical approach is required. In the finance literature such approaches were put forward as stochastic volatility models, with the Heston (Heston (1993)) and Hull-White models (Hull and White (1987)) being the most popular. A basic assumption in the study of such models is the validity of the Chapman-Kolmogorov (CK) equation for the transition probability density associated with log-returns, defined as the logarithm of the ratio of prices separated by a time lag (Kleinert (2006)). The CK equation is basically a semigroup property that entails a scaling law relating, via convolution integrals, the probability distribution of log-returns at different time-scales. Experimental financial time series satisfy the CK equation with reasonably accuracy (Bouchaud and Potters (2000)). In the context of turbulence in classical fluids, a dynamical model has recently been put forward by Salazar and Vasconcelos (SV) (Salazar and Vasconcelos (2010)). It accommodates, through five physical requirements, two concepts introduced by Kolmogorov's approach to the onset of turbulence: the energy cascade, i.e. the energy transfer between spatial/temporal scales, and the phenomenon of intermittency, which accounts for stochastic changes in energy transfer rates. The underlying picture in Kolmogorov's theory is the hypothesis that at large Reynold's number big eddies are created spontaneously, which because of large inertia effects decay into smaller eddies in a series of events that go all the way down to the smallest scale where complete viscous dissipation takes place. The SV model consists basically in a set

of coupled stochastic differential equations for the rates of energy transferred between contiguous scales. For large scale separation, the stationary solution of the model for the distribution of velocity increments can be interpreted both as a multiscale extension of the superstatistical superposition approach and as dynamical derivation of the scaling hypothesis implied by the CK equation. The validity of the CK equation in the description of fully developed turbulence was independently verified in (Salazar and Vasconcelos (2010)). The main prediction of the SV model is a distribution of velocity increments given by a family of generalized hypergeometric functions, which contains a dimensionless integer parameter N and exhibits power law tails. Interestingly, the model predicts velocity increments with a Gaussian distribution for $N = 0$ and a t-Student (or q-Gaussian) distribution for $N = 1$. It is quite striking to observe that good agreement was found with experimental data on velocity increments distribution of Lagrangean turbulence and the generalized hypergeometric function with $N = 7$. The SV model accommodates two universality classes: the inverse-gamma and the log-normal models.

Notwithstanding the theoretical advances brought about by the SV model, three major problems remained: (i) the determination of the number of relevant time-scales N, (ii) the extraction of the background series from the experimental data and (iii) the extension to other universality classes, including the gamma class. In this work we shall address all three problems. We introduce a dynamical stochastic model, whose stationary solution extends the SV model to a large family of parametric distributions, which includes as particular cases the three standard universality classes of the statistical superposition approach. We show that both the signal and the background distributions can be represented in terms of Meijer's G-function and in some cases the more general Fox H-function. We also introduce a numerical procedure to extract from the time series of a given signal, the corresponding background distribution which reveals, besides the universality class, the number N of relevant time scales.

In the new dynamic model, described as a system of stochastic differential equations

(SDE), one assumes that distributions with heavy tails should be interpreted as the composition of various random sub-processes with well separated time scales that can reach a local equilibrium. Using the stationary solution of the model, we will characterize statistically the time series corresponding of complex dynamical systems through its probability density functions (PDF), in analogy with turbulence in a classical fluid. The main applications include (*i*) financial market returns, (*ii*) intensity increments of random fiber lasers, (*iii*) numerically calculated eigenvalues from the energy spectrum of resonant cavities with mixed dynamics and, (*iv*) velocity increments of Eulerian turbulence for He with Reynolds number $Re = 295,000$. In each case, the PDF associated presents large deviations from the Gaussian distribution, a fact that is assumed as a violation of the central limit theorem (CLT). In general, the Gaussian distribution is the result of a normal diffusive process, where the variance is a well-behaved function of time.

2.1.1 *The dynamical hierarchical model*

Consider an inhomogeneous non-equilibrium system in which a relevant observable, x, is described locally in a spatial or temporal cell by a conditional distribution function $P(x|\varepsilon)$, which contains a parameter, ε, that varies slowly from cell to cell according to some distribution $f(\varepsilon)$. The unconditional global distribution of x is then given by

$$P(x) = \int P(x|\varepsilon) f(\varepsilon) d\varepsilon. \tag{2.1}$$

The existence of at least two widely separated time scales in the dynamics of the system is a basic assumption for the validity of Eq. (2.1). In the statistical superposition approach, the form of $P(x|\varepsilon)$ is usually straightforwardly obtained from a large scale maximum entropy type of analysis, akin to equilibrium statistical mechanics. The choice of $f(\varepsilon)$, however, is a more subtle issue, which has been addressed in the literature by means of statistical fitting procedures. These studies led to a partial classification of complex non-equilibrium phenomena, regarding the choice of $f(\varepsilon)$, into three large universality classes: (i) gamma; (ii) inverse gamma and (iii) log-normal.

Although there has been much success in fitting distributions from superstatistical universality classes with experimental data, a stochastic dynamical model is an essential next step if the approach is required to make actual predictions and thus become a full fledged physical description. The dynamical model should, among other things, lay out the mechanisms underlying the emergence of the universality classes. We show below how to derive and extend the universality classes using stochastic differential equations (SDE). The proposed SDE is consistent with Kolmogorov's theory of turbulence and was constructed under five simple hypotheses, which can be enumerated as (i) the temporal translation symmetry, (ii) local interactions, (iii) scale invariance, (iv) equilibrium condition and (v) unidirectional flow. We show in figure 2.1 a pictorial description, which can be used as a complement to the more technical explanation that is presented in the following sections.

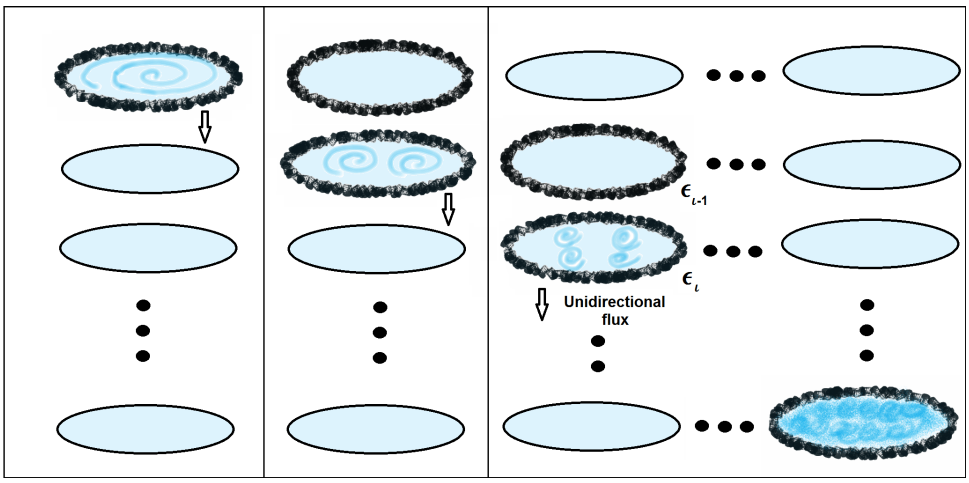

Figure 2.1: (i) The underlying picture in Kolmogorov's theory is the hypothesis that at large Reynold's number big eddies are created spontaneously, which because of large inertia effects decay into smaller eddies in a series of events that go all the way down to the smallest scale where complete viscous dissipation takes place. (ii) Hypothesis of local interactions: In the limit of infinite Reynolds number, the energy fluctuation of a scale i in the cascade is uniquely determined by their respective spatial scale and by the total energy's flow through this scale, represented by the difference $\varepsilon_i - \varepsilon_{i-1}$, between the outflow and incoming flow on this scale.

We start by considering a simple model for the signal at the observation time scale, which consists of a stochastic process with Langevin dynamics (Risken and Franck (1996)) given by

$$dx = -\zeta x dt + \sqrt{2\zeta\varepsilon_N} dV, \tag{2.2}$$

where, $\zeta = constant$, dV represents a Wiener process, and ε_N is a stochastic variable that has relaxed in the observation scale towards a local equilibrium (Born Oppenheimer hypothesis). In general, ε_N, with stationary distribution $f_N(\varepsilon_N)$, is the result of the composition with other scales $N-1$ random variables ε_i with well-separated time scales τ_i, $\tau_i \ll \tau_{i-1}$, so that the dynamic ε_i is described by a Langevin equation in which the terms of dissipation and fluctuations are a function of time and other relevant spatial/temporal scales in the system. We consider the general equation

$$d\varepsilon_i = F_i(\varepsilon_0, \ldots, \varepsilon_N, t)dt + G_i(\varepsilon_0, \ldots, \varepsilon_N, t)dW_i, \tag{2.3}$$

where the functional forms of $F_i(\varepsilon_0, \ldots, \varepsilon_N, t)$, $G_i(\varepsilon_0, \ldots, \varepsilon_N, t)$ and the total number of scales, N, will describe the PDFs associated with the time series of complex hierarchical systems. The choice of these functions has been made taking into account the cascade model of classical turbulence, as done in the SV model (Salazar (2010); Salazar and Vasconcelos (2010)). For that, we impose the following set of dynamical restrictions:

(i) Temporal translation symmetry

$$\partial_t F_i(\varepsilon_0, \ldots, \varepsilon_N, t) = 0 = \partial_t G_i(\varepsilon_0, \ldots, \varepsilon_N, t)$$

(ii) Local interactions

$$\begin{aligned} F_i(\varepsilon_0, \ldots, \varepsilon_N) &= F_i(\varepsilon_{i-1}, \varepsilon_i) \\ G_i(\varepsilon_0, \ldots, \varepsilon_N) &= G_i(\varepsilon_{i-1}, \varepsilon_i) \end{aligned}$$

(iii) Scale invariance

$$\begin{aligned} F_i(\lambda\varepsilon_{i-1}, \lambda\varepsilon_i) &= \lambda F_i(\varepsilon_{i-1}, \varepsilon_i) \\ G_i(\lambda\varepsilon_{i-1}, \lambda\varepsilon_i) &= \lambda G_i(\varepsilon_{i-1}, \varepsilon_i) \end{aligned}$$

(iv) Stationary condition

$$\varepsilon_i = \varepsilon_{i-1} \Rightarrow \left\langle \frac{d\varepsilon_i}{dt} \right\rangle = 0$$

(v) Unidirectional flux

$$Prob(\varepsilon_i < 0) = 0, \ \forall t, \ if \ \varepsilon_i(t=0) \geq 0$$

The most general form for the coefficients of equation (2.3) satisfying the five relations established above correspond to: $F_i(\varepsilon_0, \ldots, \varepsilon_N, t) = -\gamma_i(\varepsilon_i - \varepsilon_{i-1})$ and $G_i(\varepsilon_0, \ldots, \varepsilon_N, t) = \kappa_i \varepsilon_i^{\alpha} \varepsilon_{i-1}^{1-\alpha}$, where $\gamma_i, \kappa_i, \ \alpha$ are positive numbers. The physically reasonable values for the exponent α are those that lead to analytical functions in the diffusion coefficients of the associated Fokker-Planck equation, which are (i) $\alpha = 1$ which yields stationary distributions $f(\varepsilon_i|\varepsilon_{i-1})$ given by inverse gamma densities and (ii) $\alpha = 1/2$ which gives gamma densities for the stationary distributions. With this background, in the following sections we explicitly show how to get the probability density functions associated with the dynamical model.

2.2 Parametric Families

We start the formal mathematical presentation of the model with a simple case where the background's dynamics has a single scale $\varepsilon_N = \varepsilon_1 = \varepsilon$, which contains most of the universality classes treated in the current literature. In this case, the hierarchical model is restricted to two coupled Itô type stochastic differential equations

$$dx = -\zeta x dt + \sqrt{2\zeta\varepsilon} dV, \tag{2.4}$$

$$d\varepsilon = -\gamma(\varepsilon - \varepsilon_0)dt + \kappa g(\varepsilon) dW, \tag{2.5}$$

where dV and dW are independent Wiener processes, ζ, γ and κ are positive constants, and $g(\varepsilon) = \varepsilon_0^{1-\alpha}\varepsilon^{\alpha}$, where $\alpha = 1/2$ ($\alpha = 1$) for the gamma (inverse gamma) class. Furthermore, we admit well separated time scales, i.e. $\zeta \gg \gamma$.

Under this assumption, the Fokker-Planck equation associated with the Langevin equation (2.4) (for more details see Appendix C) has the form

$$\left[\partial_t - \zeta\partial_x x - \zeta\varepsilon\partial_x^2\right] P(x,t|\varepsilon) = 0, \tag{2.6}$$

whose stationary solution is obtained as

$$\left[x + \varepsilon\frac{d}{dx}\right] P(x|\varepsilon) = 0 \quad \Rightarrow \quad P(x|\varepsilon) = \frac{1}{\sqrt{2\pi\varepsilon}}\exp\left(-\frac{x^2}{2\varepsilon}\right), \tag{2.7}$$

corresponding to a Gaussian distribution conditioned by the variance ε, where this is a stochastic variable which behavior is described by equation (2.5) on large time scales. This feature causes the marginal distribution, $P(x)$, on the observation scale to exhibit heavy tails. So, is possible to determine that ε have a probability density function, $f(\varepsilon)$, which is the stationary solution of the Fokker-Planck equation (FPE)

$$\left[\partial_t - \gamma\partial_\varepsilon(\varepsilon - \varepsilon_0) - \frac{\kappa^2}{2}\partial_\varepsilon^2 g^2(\varepsilon)\right] f(\varepsilon,t) = 0. \tag{2.8}$$

The stationary solution satisfies[1]

$$\left[\beta(\varepsilon - \varepsilon_0) + \frac{d}{d\varepsilon}g^2(\varepsilon)\right] f(\varepsilon) = 0, \tag{2.9}$$

where $\beta = \frac{2\gamma}{\kappa^2}$ and $g(\varepsilon) = \varepsilon_0^{1-\alpha}\varepsilon^{\alpha}$. Substituting these values into (2.9), results in the ordinary differential equation

$$\frac{d}{d\varepsilon}(\varepsilon^{2\alpha} f(\varepsilon)) = -\beta(\varepsilon - \varepsilon_0) f(\varepsilon)\varepsilon_0^{2\alpha-2}, \tag{2.10}$$

[1]The reader should note that by taking the stationary solution of equation (2.8), it becomes independent of the time. So, it is possible to factorize one order of epsilon partial derivative, then the term to be derived corresponds to the left side of equation (2.9); this ordinary differential equation is in general equated to a constant, only that the probability density function ($f(\varepsilon)$) must be normalized. Therefore, we have to calibrate said constant in zero, to avoid the divergence of the $f(\varepsilon)$ PDF.

which can be solved via $F(\varepsilon) = \varepsilon^{2\alpha} f(\varepsilon)$, thereby

$$\frac{dF(\varepsilon)}{d\varepsilon} = -\beta \frac{(\varepsilon - \varepsilon_0)}{\varepsilon_0^{2-2\alpha} \varepsilon^{2\alpha}} F(\varepsilon). \tag{2.11}$$

This equation can be easily solved by separating variables, thus we get

$$\int \frac{dF(\varepsilon)}{F(\varepsilon)} = -\frac{\beta}{\varepsilon_0^{2-2\alpha}} \int \left(\frac{1}{\varepsilon^{2\alpha-1}} - \frac{\varepsilon_0}{\varepsilon^{2\alpha}} \right) d\varepsilon. \tag{2.12}$$

The explicit integration of (2.12) is best performed after discriminating the universality classes, which we do in the next subsections. The two classes are the gamma class ($\alpha = 1/2$) and the inverse-gamma class ($\alpha = 1$).

2.2.1 *Gamma class*

In this case, the exponent is $\alpha = 1/2$ and the integral (2.12) is reduced to

$$\ln F(\varepsilon) = -\frac{\beta\varepsilon}{\varepsilon_0} + \beta \ln \varepsilon + c_1, \tag{2.13}$$

which after returning to the original variable $f(\varepsilon)$ takes the form

$$F(\varepsilon) = c_2 \varepsilon^{\beta} \exp\left(-\frac{\beta\varepsilon}{\varepsilon_0} \right) \quad \Rightarrow \quad f(\varepsilon) = c_3 \varepsilon^{(\beta-1)} \exp\left(-\frac{\beta\varepsilon}{\varepsilon_0} \right), \tag{2.14}$$

where c_3 is obtained using the normalization condition $\int_0^\infty f(\varepsilon) d\varepsilon = 1$. The final result is

$$f(\varepsilon) = \frac{\beta^\beta}{\varepsilon_0^\beta \Gamma(\beta)} \varepsilon^{\beta-1} \exp\left(-\frac{\beta\varepsilon}{\varepsilon_0} \right), \quad \varepsilon > 0. \tag{2.15}$$

We have thus proved that for the particular case $\alpha = 1/2$ the stationary PDF associated with the equation (2.5) corresponds to the gamma distribution (2.15). The moments $\langle \varepsilon^{(r-1)} \rangle = \int_0^\infty d\varepsilon \varepsilon^{r-1} f(\varepsilon)$, are well defined through

$$\langle \varepsilon^{(r-1)} \rangle = \left(\frac{\beta}{\varepsilon_0} \right)^{1-r} \frac{\Gamma(\beta - 1 + r)}{\Gamma(\beta)}. \tag{2.16}$$

For positive and integer values of $r \in \mathbf{Z}^+$ we get the quantities commonly defined in statistics: mean, variance, kurtosis, etc., can be determined. However, the result obtained

in (2.16) will be used to show that the Gamma distribution can be understood as part of a general group of special functions known as the Meijer G-functions (Prudnikov *et al.* (1991); Meijer (1941)) that will be the cornerstone of our theoretical model. For this purpose we consider the Mellin Transform (see Appendix D) of the Meijer G-function $G_{p,q}^{m,n}(z)$, that is the usual way of defining this type of special functions (for more details see Mathai and Saxena (1973); Mathai (1993); Mathai *et al.* (2010))

$$\int_0^\infty dz z^{r-1} G_{p,q}^{m,n}\left(\begin{array}{c} (a_1),\ldots,(a_p) \\ (b_1),\ldots,(b_q) \end{array} \middle| \alpha z \right) = \alpha^{-r} \frac{\prod_{j=1}^{m}\Gamma(b_j+r)}{\prod_{j=m+1}^{q}\Gamma(1-b_j-r)} \frac{\prod_{j=1}^{n}\Gamma(1-a_j-r)}{\prod_{j=n+1}^{p}\Gamma(a_j+r)}. \tag{2.17}$$

Comparing equations (2.16) and (2.17), it becomes evident that the generalized relation for the moments of the gamma distribution, correspond to the Mellin transform of the Meijer G-function with parameters $m = q = 1$, $n = p = 0$, $\alpha = \beta/\varepsilon_0$, $\{a_j\} = $, $b_1 = \beta - 1$. Thus it is possible to rewrite the PDF (2.15) as

$$f(\varepsilon) = \frac{\beta}{\varepsilon_0 \Gamma(\beta)} G_{0,1}^{1,0}\left(\begin{array}{c} - \\ \beta - 1 \end{array} \middle| \frac{\beta\varepsilon}{\varepsilon_0} \right). \tag{2.18}$$

At this point, the use of the Meijer G-functions will be the mathematical tool that provides the possibility of having closed forms for the PDFs resulting from the multiscale superposition, as presented in the next sections. For now, the parametric dependence of the gamma distribution is shown in figure (2.2).

In this approach the value of the β parameter is central since it determines the shape of the gamma distribution, as shown in figure (2.2). Also, when working with experimental data series, the value of ε_0 is going to fix the background distribution's mean $\langle\varepsilon\rangle = \varepsilon_0 = 1$, so the parameter ε_0 will be previously known.

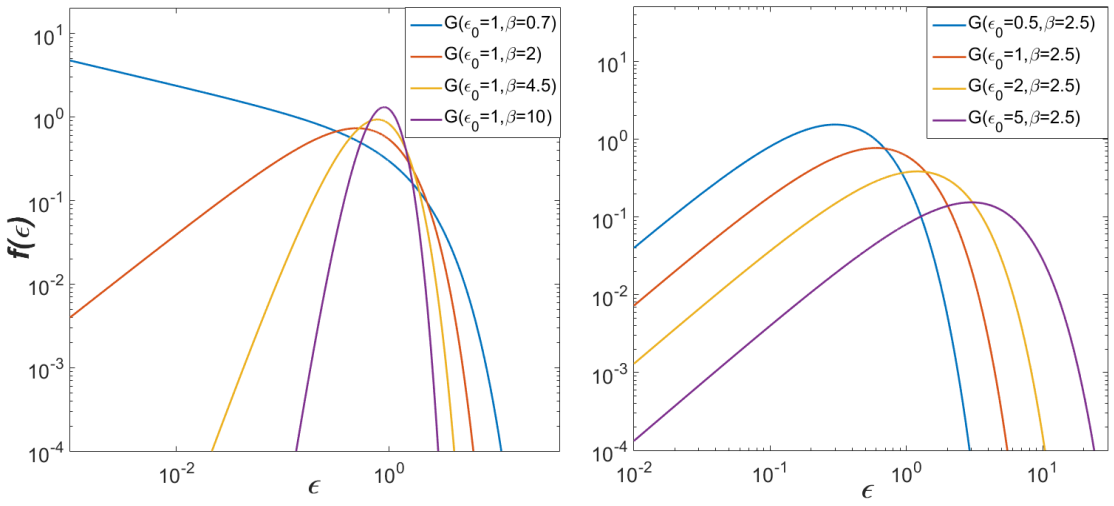

Figure 2.2: On the left we show how the β parameter controls the shape of the gamma distribution. On the right we show how the ε_0 parameter controls the distribution's mean for $\beta = constant$. In the figure's inset the values of the parameters, the letter G represents the initial of the word gamma.

2.2.2 *Inverse gamma classes*

The other possible case for the equation (2.12) corresponds to $\alpha = 1$. For this value, the integral takes the form

$$\ln F(\varepsilon) = -\beta \ln \varepsilon - \frac{\beta\varepsilon_0}{\varepsilon} + c_4, \tag{2.19}$$

which after returning to the original variable $f(\varepsilon)$ gives the distribution

$$F(\varepsilon) = c_5 \varepsilon^{-\beta} \exp\left(-\frac{\beta\varepsilon_0}{\varepsilon}\right) \quad \Rightarrow \quad f(\varepsilon) = c_6 \varepsilon^{-\beta-2} \exp\left(-\frac{\beta\varepsilon_0}{\varepsilon}\right). \tag{2.20}$$

Applying the normalization condition, we obtain the inverse-gamma density

$$f(\varepsilon) = \frac{(\beta\varepsilon_0)^{\beta+1}}{\Gamma(\beta+1)} \varepsilon^{-\beta-2} \exp\left(-\frac{\beta\varepsilon_0}{\varepsilon}\right), \quad \varepsilon > 0, \tag{2.21}$$

analogously to the previous case, the generalized equation for the moments of the distribution (2.21) is given by

$$\langle \varepsilon^{(r-1)} \rangle = \frac{1}{\beta\varepsilon_0\Gamma(\beta+1)} \left(\frac{1}{\beta\varepsilon_0}\right)^{-r} \Gamma(\beta+2-r). \tag{2.22}$$

Using the Mellin transform's property (2.17), we obtain the Meijer G-function with indexes $m = q = 0$, $n = p = 1$, while its coefficients are $\alpha = \frac{1}{\beta\varepsilon_0}$, $a_1 = -\beta - 1$, $a_j =$ for $j \neq 1$, $b_j =$ $\forall j$. With these values the inverse Gamma distribution becomes

$$f(\varepsilon) = \frac{1}{\beta\varepsilon_0\Gamma(\beta+1)} G^{0,1}_{1,0}\left(\begin{array}{c} -\beta-1 \\ \_\_\_\_ \end{array} \middle| \frac{\varepsilon}{\beta\varepsilon_0} \right). \tag{2.23}$$

The parametric dependence of the inverse gamma distribution (IG) is presented graphically in figure (2.3) . For this distribution, the β parameter controls its shape, while the ε_0 parameter is related to the distribution's mean. In fact for IG this parameter is strictly the mean $\langle \varepsilon \rangle = \varepsilon_0$. It must be remembered that the parameters β and ε_0 in each of the classes are different from each other $\beta_\gamma \neq \beta_{\bar{\gamma}}$ and $\varepsilon_0^{\gamma} \neq \varepsilon_0^{\bar{\gamma}}$.

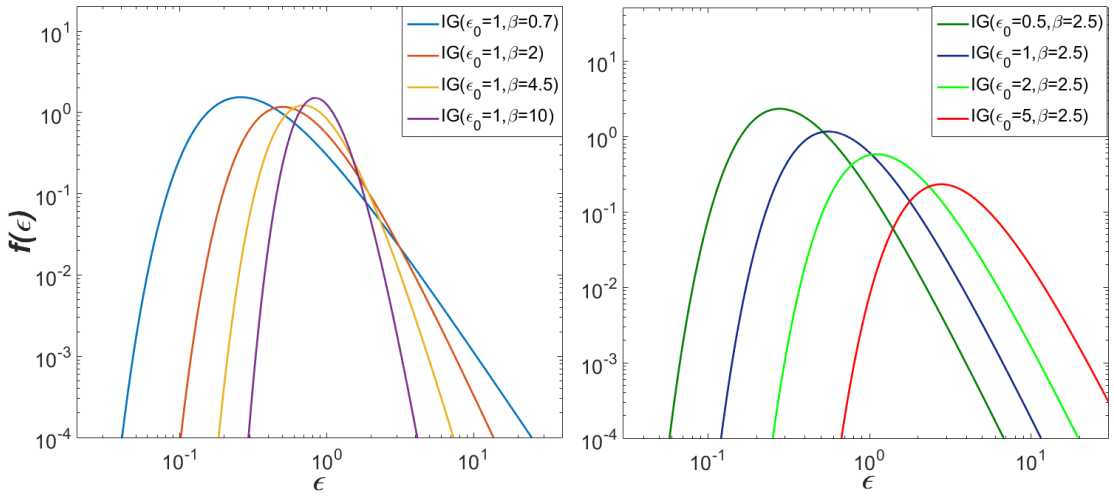

Figure 2.3: On the left we show how the β parameter controls the shape of the Inverse-Gamma distribution. On the right we show how the ε_0 parameter controls the distribution's mean for $\beta = constant$. In the figure's inset the values of the parameters, the letters IG represent the initials of the compound word Inverse-Gamma

After this introduction, where the expressions for the background's distributions with a single scale were written in terms of Meijer G-functions, we will now return to the physical model and treat the general case of N background scales.

2.3 The multiscale approach

In this section we shall derive the stationary solution of the systems of stochastic differential equations (2.24-2.25), which represents our dynamic model

$$dx = -\zeta x dt + \sqrt{2\zeta\varepsilon_N} dV, \tag{2.24}$$

$$d\varepsilon_i = -\gamma_i(\varepsilon_i - \varepsilon_{i-1})dt + \kappa_i g(\varepsilon_i|\varepsilon_{i-1})dW_i, \quad i = 1, \ldots, N. \tag{2.25}$$

The calculations proceed in two steps: (i) first, we admit well separated time scales, i.e. $\zeta \gg \gamma_N \gg \cdots \gg \gamma_i \gg \cdots \gg \gamma_1$ and obtain the joint distribution of background variables (stationary solution of the set of equations (2.25)), (ii) and second, under the same hypothesis, we determine the signal's distribution ($P(x)$) by calculating a weighted average of a Gaussian with variable variance ε_N . In other words, we derive the model's prediction for the unconditional stationary distribution in the observation scale $P(x)$.

In the unified notation each background variable ε_i in equation (2.25) has stationary distribution through its associated FPE and the classes are discriminated by means of the coefficient $g(\varepsilon_i|\varepsilon_{i-1}) = \varepsilon_{i-1}^{1-\alpha}\varepsilon_i^{\alpha}$, where $\alpha = 1/2$ ($\alpha = 1$) for the conditional gamma (conditional inverse gamma) class[2]

$$f(\varepsilon_i|\varepsilon_{i-1}) = \begin{cases} \frac{\beta_i^{\beta_i}}{\Gamma(\beta_i)} \frac{\varepsilon_i^{\beta_i - 1}}{\varepsilon_{i-1}^{\beta_i}} \exp\left(-\beta_i \frac{\varepsilon_i}{\varepsilon_{i-1}}\right) & \text{for } f(\varepsilon) \to \text{Gamma(G)} \\ \frac{(\beta_i \varepsilon_{i-1})^{\beta_i+1}}{\Gamma(\beta_i+1)} \varepsilon_i^{-\beta_i-2} \exp\left(-\beta_i \frac{\varepsilon_{i-1}}{\varepsilon_i}\right) & \text{for } f(\varepsilon) \to \text{Inverse-Gamma(IG)}. \end{cases}$$

[2]The exponents $\alpha = 1/2$ and $\alpha = 1$ are chosen to guarantee the analytical solution of the Fokker-Planck equation associated with the Langevin equation.

To determine the joint background distribution $f_N(\varepsilon_N)$, we first observe that the separation of time scales is equivalent to applying Bayes' theorem, so that the unconditional distribution that is being sought corresponds to the integral

$$f_N(\varepsilon_N) = \int d\varepsilon_{N-1} f(\varepsilon_N|\varepsilon_{N-1}) \ldots \int d\varepsilon_1 f(\varepsilon_1|\varepsilon_0). \tag{2.26}$$

It is necessary to decouple the multiple integrals on the conditional distributions and thus be able to calculate the Mellin transform of the background distribution (2.26). For this purpose we define new variables through the relation

$$\frac{\varepsilon_N}{\varepsilon_0} = \frac{\varepsilon_N}{\varepsilon_{N-1}} \frac{\varepsilon_{N-1}}{\varepsilon_{N-2}} \ldots \frac{\varepsilon_2}{\varepsilon_1} \frac{\varepsilon_1}{\varepsilon_0} = \zeta_N \zeta_{N-1} \ldots \zeta_2 \zeta_1. \tag{2.27}$$

The distributions of the new variables $g(\zeta_i)$ are obtained through

$$g(\zeta_i) = f(\varepsilon_i|\varepsilon_{i-1}) \frac{\partial \varepsilon_i}{\partial \zeta_i}\bigg|_{\varepsilon_{i-1}=const} \quad i = 1, \ldots, N. \tag{2.28}$$

Now the two types of classes, Gamma (G) and Inverse-Gamma (IG) are given by

$$g(\zeta_i) = \begin{cases} \frac{\beta_i^{\beta_i}}{\Gamma(\beta_i)} \zeta_i^{\beta_i - 1} \exp\left(-\beta_i \zeta_i\right) & \text{G} \\ \\ \frac{(\beta_i)^{\beta_i}}{\Gamma(\beta_i)} \zeta_i^{-\beta_i - 2} \exp\left(-\frac{\beta_i}{\zeta_i}\right) & \text{IG,} \end{cases}$$

it is now possible to independently calculate the right-hand integrals of (2.26) using a Mellin transform for each scale

$$\langle \zeta_i^p \rangle = \begin{cases} \frac{\Gamma(\beta_i + p)}{\beta_i^p \Gamma(\beta_i)} & \text{G} \\ \\ \beta_i^p \frac{\Gamma(\beta_i - p + 1)}{\Gamma(\beta_i + 1)} & \text{IG.} \end{cases}$$

So the joint Mellin's transform is simply the product of the transforms at each scale

$$\langle \zeta^{s-1} \rangle = \int_0^\infty d\zeta \zeta^{s-1} g(\zeta) = \begin{cases} \prod_{i=1}^N \frac{\Gamma(\beta_i + s - 1)}{\beta_i^{s-1} \Gamma(\beta_i)} & \text{G} \\ \\ \prod_{i=1}^N \beta_i^{s-1} \frac{\Gamma(\beta_i - s + 2)}{\Gamma(\beta_i + 1)} & \text{IG.} \end{cases}$$

The joint distribution for the multiple background scales regarding the Meijer G-functions is obtained using the property (2.17). Analogously to the procedure performed on a single scale

$$g(\zeta) = \begin{cases} \frac{\beta_1,\ldots,\beta_N}{\Gamma(\beta_1),\ldots,\Gamma(\beta_N)} G_{0,N}^{N,0}\left(\begin{array}{c} ---- \\ \beta_1 - 1,\ldots,\beta_N - 1 \end{array} \middle| \beta_1 \ldots \beta_N \zeta \right) & \text{G} \\ \\ \frac{(\beta_1,\ldots,\beta_N)^{-1}}{\Gamma(\beta_1+1),\ldots,\Gamma(\beta_N+1)} G_{N,0}^{0,N}\left(\begin{array}{c} -\beta_1 - 1,\ldots,-\beta_N - 1 \\ ---- \end{array} \middle| \frac{\zeta}{\beta_1 \ldots \beta_N} \right) & \text{IG.} \end{cases}$$

Through the relation $f_N(\varepsilon_N) = \frac{1}{\varepsilon_0} g(\zeta) = \frac{1}{\varepsilon_0} g\left(\frac{\varepsilon_N}{\varepsilon_0}\right)$ is returned to the distribution for original variable. It will prove useful to combine the above results for $f_N(\varepsilon_N)$ in a single formula using G-Meijer function. Let N_γ and $N_{\bar{\gamma}}$ be the number of gamma and inverse-gamma variables respectively, with the constraint $N_\gamma + N_{\bar{\gamma}} = N$, then

$$f_N(\varepsilon_N) = \omega \Omega_{\gamma\bar{\gamma}} G_{N_{\bar{\gamma}},N_\gamma}^{N_\gamma,N_{\bar{\gamma}}}\left(\begin{array}{c} \mathbf{a}_{\bar{\gamma}} \\ \mathbf{b}_\gamma \end{array} \middle| \omega \varepsilon_N \right), \tag{2.29}$$

where $\mathbf{a}_{\bar{\gamma}} = -\beta_1 - 1,\ldots,-\beta_{N_{\bar{\gamma}}} - 1$, $\mathbf{b}_\gamma = \beta_1 - 1,\ldots,\beta_{N_\gamma} - 1$ and

$$\omega = \prod_{j=1}^{N_\gamma} \beta_j \prod_{j=1}^{N_{\bar{\gamma}}} \frac{1}{\beta_j}, \tag{2.30}$$

$$\Omega_{\gamma\bar{\gamma}} = \prod_{j=1}^{N_\gamma} \frac{1}{\Gamma(\beta_j)} \prod_{j=1}^{N_{\bar{\gamma}}} \frac{1}{\Gamma(\beta_j + 1)} = \Omega_\gamma \Omega_{\bar{\gamma}}. \tag{2.31}$$

By convention, the β parameters are the same for each scale $(\beta_1 = \beta_2 = \cdots = \beta_N)_{\gamma\vee\bar{\gamma}}$, therefore, it is the primary interest of this dissertation to determine for the four systems (i) its parametric class, (ii) the scales number N, and (iii) the value of the corresponding β parameter. However, it is still premature to talk about how to make that choice. Since this chapter only introduces the theoretical model, and the effects that occur when changing the parameters β and N of the different classes. In that order of ideas, figure (2.4) shown several plots of the background composed of the class Gamma, represented by the equation (2.29). In figure (2.5) we plotted equation (2.29) for the inverse-gamma

class. It is important to note that although for these two classes the same values have been used for the parameters β and N, its effects on each family are different.

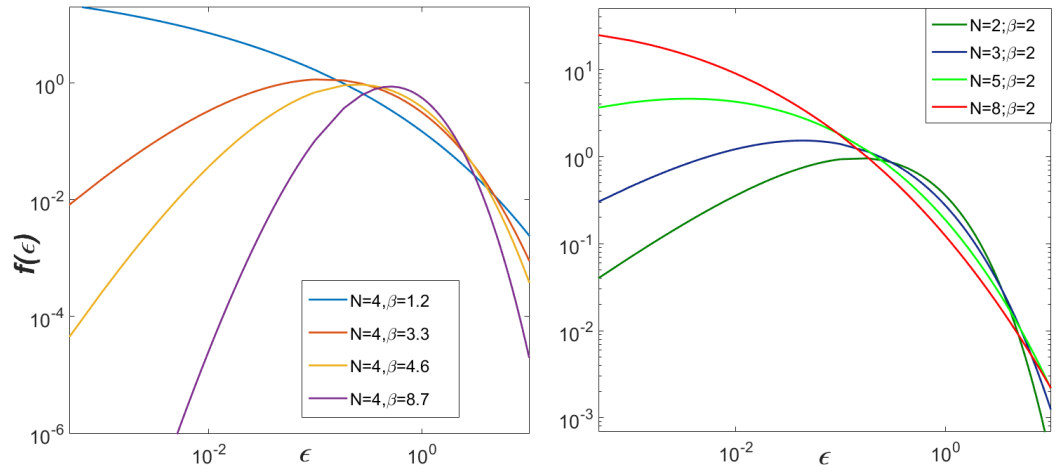

Figure 2.4: On the left we show how the β parameter controls the shape of the distribution setting the number of background's scales on $N = 4$. On the right we show the behavior of the distribution according to the scales' number given a parameter $\beta = constant$. In all cases the distribution has been plotted $f_N(\varepsilon_N)$ for the Gamma class (eq (2.29))

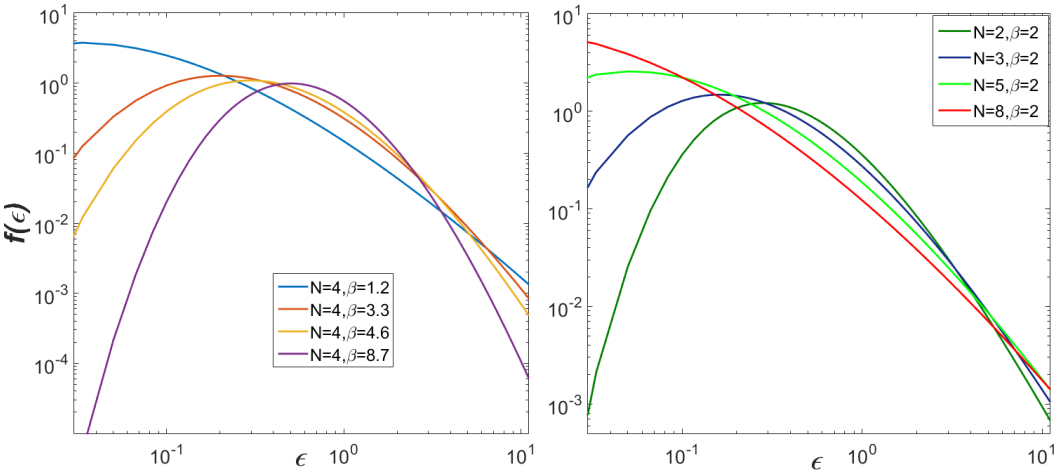

Figure 2.5: On the left we show how the β parameter controls the shape of the distribution setting the number of background's scales on $N = 4$. On the right we show the behavior of the distribution according to the scales' number given a parameter $\beta = constant$. In all cases the distribution has been plotted $f_N(\varepsilon_N)$ for the Inverse-Gamma class (eq (2.29))

Through these examples, we have given an overall idea of the type of distributions generated from stationary solutions of $f_N(\varepsilon_N)$. With this result, we can move to the second item stated at the beginning of this section, so in the following subsection, it will be explicitly described how to obtain the probability density function $P(x)$ for the observation scale.

2.3.1 *Marginal distribution*

In agreement with the hypothesis of large scales separations, the PDF ($P(x)$) of the experimental detection is the superposition of variables that fluctuate in smaller scales, and that relax until reaching a local equilibrium exhibiting background's distributions that depend parametrically on variables that range in the greater scales. Mathematically represented by the set of SDE (2.24, 2.25), we have already identified its stationary distributions in (2.7) and (2.29) separately, now just the superposition integral will be considered

$$P(x) = \int_0^\infty d\varepsilon_N P(x|\varepsilon_N) f_N(\varepsilon_N) = \frac{1}{\sqrt{2\pi}} \int_0^\infty \exp\left(-\frac{x^2}{2\varepsilon_N}\right) \varepsilon_N^{-1/2} f_N(\varepsilon_N) d\varepsilon_N, \tag{2.32}$$

which can be evaluated through the Mellin transform. To make such calculation, the following change of variable

$$y = \frac{x^2}{2\varepsilon_N} \quad \Rightarrow \quad x^2 = 2y\varepsilon_N \quad \Rightarrow \quad x^{s-1} = 2^{(s-1)/2} y^{(s-1)/2} \varepsilon_N^{(s-1)/2} \tag{2.33}$$

is made, and the transform of $P(x)$ takes the form

$$\underbrace{\int_0^\infty dx x^{s-1} P(x)}_{<x^{s-1}>} = 2^{(s-1)/2} \overbrace{\int_0^\infty dy y^{(s-1)/2} P(y)}^{<y^{(s-1)/2}>} \underbrace{\int_0^\infty d\varepsilon_N \varepsilon_N^{(s-1)/2} f(\varepsilon_N)}_{<\varepsilon_N^{(s-1)/2}>}, \tag{2.34}$$

where

$$P(y) = P(x|\varepsilon_N) \mid_{x=\sqrt{2\varepsilon_N y}} \frac{dx}{dy} = \frac{1}{\sqrt{4\pi y}} \exp(-y). \tag{2.35}$$

Sequentially the integrals on the right side of (2.34) are calculated, obtaining

$$\langle y^{(s-1)/2} \rangle = \frac{\Gamma\left(\frac{s}{2}\right)}{2\sqrt{\pi}}, \tag{2.36}$$

and

$$\langle \varepsilon_N^{(s-1)/2} \rangle = \begin{cases} \prod_{i=1}^{N} \beta^{(1/2-s/2)} \frac{\Gamma(\beta_i + s/2 - 1/2)}{\Gamma(\beta_i)} & \mathrm{G}(\gamma) \\ \\ \prod_{i=1}^{N} \beta_i^{(s/2-3/2)} \frac{\Gamma(\beta_i + 3/2 - s/2)}{\Gamma(\beta_i)} & \mathrm{IG}(\bar{\gamma}). \end{cases}$$

The second integral is expressed in terms of the two cases gamma and inverse gamma in concordance with the previous subsection, therefore Mellin transform to (2.34) also incorporates these two possibilities

$$\underbrace{\int_0^\infty dx x^{s-1} P(x)}_{<x^{s-1}>} = \begin{cases} \prod_{i=1}^{N} \frac{\beta_i^{1/2}}{\sqrt{8\pi}\Gamma(\beta_i)} \left(\frac{2}{\beta_i}\right)^{s/2} \Gamma\left(\frac{s}{2}\right) \Gamma\left(\beta_i - \frac{1}{2} + \frac{s}{2}\right) & \mathrm{G}(\gamma) \\ \\ \prod_{i=1}^{N} \frac{(2\beta)^{-3/2}}{\sqrt{\pi}\Gamma(\beta_i)} (2\beta_i)^{s/2} \Gamma\left(\frac{s}{2}\right) \Gamma\left(\beta_i + \frac{3}{2} - \frac{s}{2}\right) & \mathrm{IG}(\bar{\gamma}). \end{cases}$$

The purpose of this calculation is to determine the form of the distribution $P(x)$. For this we have used the following property on Fox H-function, that was taken from the reference Mathai *et al.* (2010)

$$\int_0^\infty dx x^{s-1} H_{p,q}^{m,n} \left(\begin{matrix} (a_1, A_1), \ldots, (a_p, A_p) \\ (b_1, B_1), \ldots, (b_q, B_q) \end{matrix} \middle| \alpha x \right) = \alpha^{-s} \frac{\prod_{j=1}^{m} \Gamma(b_j + B_j s)}{\prod_{j=m+1}^{q} \Gamma(1 - b_j - B_j s)} \frac{\prod_{j=1}^{n} \Gamma(1 - a_j - A_j s)}{\prod_{j=n+1}^{p} \Gamma(a_j + A_j s)}. \tag{2.37}$$

Using this identity we evaluated in the following subsubsections the two possible cases for $P(x)$, beginning with the Gamma class.

Signal's PDF for gamma class

By implementing property (2.37) for the Mellin transform of $P(x)$ of the gamma class by direct comparison it is recognized that $P(x)_\gamma$ corresponds to the Fox H-function with coefficients $m = q = N + 1$, $p = n = 0$, $a_j = A_j = \emptyset \ \forall \ \ j$, $b_1 = 0$, $b_j = \beta_{j-1} - 1/2$ for

$j = 2, ..., N+1$, $B_j = 1/2$ for $j = 1, \ldots, N+1$, and $\alpha = \sqrt{\frac{\prod_j \beta_j}{2}}$. Equation (2.37) takes the particular form

$$\int_0^\infty dx x^{s-1} H_{0,N+1}^{N+1,0}\left(\begin{array}{c} \\ (0,1/2),(\overline{\beta_1 - 1/2},1/2),\ldots,(\beta_N - 1/2,1/2) \end{array} \middle| \sqrt{\frac{\beta_1 \ldots \beta_N}{2}} x \right) = \prod_{i=1}^{N} \left(\sqrt{\frac{\beta_i}{2}}\right)^{-s} \Gamma\left(\frac{s}{2}\right) \Gamma\left(\beta_i - \frac{1}{2} + \frac{s}{2}\right).$$

We find

$$P(x) = \frac{\sqrt{\beta_1 \ldots \beta_N}}{2\sqrt{2\pi}\Gamma(\beta_1)\ldots\Gamma(\beta_N)} H_{0,N+1}^{N+1,0}\left(\begin{array}{c} \\ (0,1/2),(\overline{\beta_1 - 1/2},1/2)\ldots(\beta_N - 1/2,1/2) \end{array} \middle| \sqrt{\frac{\beta_1 \ldots \beta_N}{2}} x \right). \tag{2.38}$$

It is possible to eliminate the dependence of the parameters B_j, using the following identity

$$H_{p,q}^{m,n}\left(\begin{array}{c} (a_u, A_u) \\ (b_v, B_v) \end{array} \middle| z \right) = k H_{p,q}^{m,n}\left(\begin{array}{c} (a_u, kA_u) \\ (b_v, kB_v) \end{array} \middle| z^k \right). \tag{2.39}$$

Through (2.39) the function $H_{p,q}^{m,n}$ can be transformed into a Meijer G-function set corresponding to coefficients for which $B_j = 1$ (Prudnikov *et al.* (1991); Meijer (1941)), so $P(x)$ takes the final form

$$P(x) = \frac{\sqrt{\beta_1 \ldots \beta_N}}{\sqrt{2\pi}\Gamma(\beta_1)\ldots\Gamma(\beta_N)} G_{0,N+1}^{N+1,0}\left(\begin{array}{c} \\ (0),(\overline{\beta_1 - 1/2}),\ldots,(\beta_N - 1/2) \end{array} \middle| \frac{\beta_1 \ldots \beta_N x^2}{2} \right). \tag{2.40}$$

The asymptotic expansion of the function $G_{m,n}^{p,q}$, with $m = q = 0$ and $n = p = N+1$ Mathai and Saxena (1973), is given by

$$P_N(x) \sim x^{2\theta} \exp\left[-(N+1)(\omega x^2/2\epsilon_0)^{1/(N+1)}\right] \tag{2.41}$$

where $\theta = \left(\sum_{i=1}^N \beta_i - N\right)/(N+1)$ and $\omega = \prod_{j=1}^N \beta_j$. Due to this asymptotic behavior, this class will be denominated stretched exponential.

To have a clear image of the forms that take these functions, we have plotted in semilog scale the PDF (2.40), with the same parameters used in figure (2.4), so that (2.6) corresponds to $P(x) = \int_0^\infty P(x|\varepsilon_N) f_N(\varepsilon_N) d\varepsilon_N$, where the background's distributions $f_N(\varepsilon_N)$ are plotted in figure (2.4).

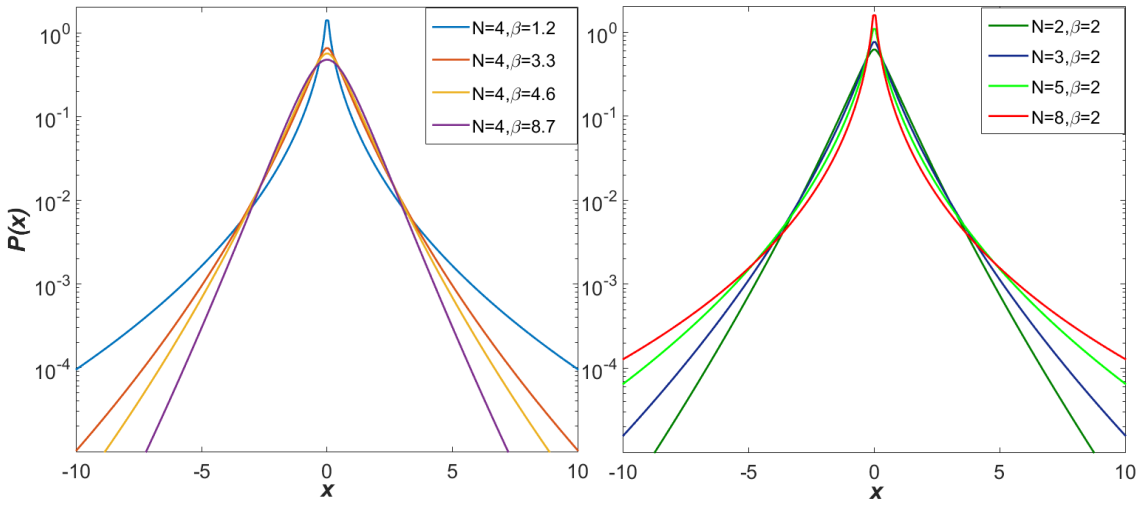

Figure 2.6: On the left we show how the β parameter controls the form of the distribution setting the number of background's scales on $N = 4$. On the right we show the behavior of the distribution according to the scales' number given a parameter $\beta = constant$. In all cases the distribution has been plotted $P(x)$ for the class stretched exponential (eq (2.40)).

Parametric distributions with heavy tails of the stretched exponential class have only been used in the current literature of complex systems for the case $N = 1$ (called K-distribution Jakeman and Pusey (1978)). So this work has made an original contribution to this area through the dynamic model called H theory, which supports the existence of this PDF's class in physical systems with chaotic dynamics. Specifically, in this thesis it has been calculated the spectrum of intensities in the random fiber laser (Chapter five), and the spectrum of the differences of the eigenvalues' spacing in ballistic cavities (Chapter seven) is characterized by this family.

Once has been established the probability density function of the signal $P(x)$ for the

stretched exponential class, an analogous calculation is made for the other class, which so far has been termed inverse-gamma because the form of conditional PDF $f(\varepsilon_i|\varepsilon_{i-1})$, partial solution of the SDE set (2.25) for the case $\alpha = 1$.

Signal's PDF for inverse gamma class

Applying the Mellin transform (2.37) into equation (2.42), is recognized by direct comparison that $P(x)_{\bar{\gamma}}$ corresponds to the Fox H-function with coefficients $m = q = 1$, $p = n = N$, $a_j = -\beta_j - 1/2$, $A_j = 1/2$ for $j = 1, ..., N$, $b_1 = 0$, $B_1 = 1/2$, $b_j = B_j = \emptyset$ for $j \neq 1$, and $\alpha = \sqrt{\frac{1}{2\prod_j \beta_j}}$.

$$\langle x^{s-1} \rangle_{\bar{\gamma}} = \prod_{i=1}^{N} \frac{(2\beta)^{-3/2}}{\sqrt{\pi}\Gamma(\beta_i)} (2\beta_i)^{s/2} \Gamma\left(\frac{s}{2}\right) \Gamma\left(\beta_i + \frac{3}{2} - \frac{s}{2}\right), \tag{2.42}$$

thus

$$\int_0^\infty dx x^{s-1} H_{N,1}^{1,N} \left(\begin{array}{c} (-\beta_1 - 1/2, 1/2), \ldots, (-\beta_N - 1/2, 1/2) \\ (0, 1/2) \end{array} \middle| \frac{x}{\sqrt{2\beta_1 \ldots \beta_N}} \right) = \prod_{i=1}^{N} (\sqrt{2\beta_i})^s \Gamma\left(\frac{s}{2}\right) \Gamma\left(\beta_i + \frac{3}{2} - \frac{s}{2}\right),$$

and $P(x)_{\bar{\gamma}}$ is the normalized function

$$P(x) = \frac{(2\beta_1 \ldots \beta_N)^{-3/2}}{\sqrt{\pi}\Gamma(\beta) \ldots \Gamma(\beta_N)} H_{N,1}^{1,N} \left(\begin{array}{c} (-\beta_1 - 1/2, 1/2), \ldots, (-\beta_N - 1/2, 1/2) \\ (0, 1/2) \end{array} \middle| \frac{x}{\sqrt{2\beta_1 \ldots \beta_N}} \right). \tag{2.43}$$

Now, the Fox H-function is transformed into a Meijer G-function using the identity (2.39), getting

$$P(x) = \frac{(\beta_1 \ldots \beta_N)^{-1/2}}{\sqrt{2\pi}\Gamma(\beta_1 + 1) \ldots \Gamma(\beta_N + 1)} G_{N,1}^{1,N} \left(\begin{array}{c} -\beta_1 - 1/2, \ldots, \beta_N - 1/2 \\ 0 \end{array} \middle| \frac{x^2}{2\beta_1 \ldots \beta_N} \right). \tag{2.44}$$

Expressing $P(x) \sim G_{p,q}^{m,n}$ has a significant operational advantage since several technical computing programs have the ability to plot and perform operations with the Meijer G-functions.

The PDF (2.44) can be directly connected to the multiscale aproach of generalized hypergeometric functions ${}_NF_0$, implemented by Salazar and Vasconcelos Salazar and Vasconcelos (2010); Salazar (2010), via the identity

$$G_{N,1}^{1,N}\left(\begin{array}{c} -\beta_1 - 1/2, \ldots, \beta_N - 1/2 \\ 0 \end{array} \middle| z \right) = \left(\prod_{i=1}^{N} \Gamma(\beta_i + 3/2) \right) {}_NF_0\left(\beta_1 + 3/2, \ldots, \beta_N + 3/2; \ ; -z\right), \tag{2.45}$$

where $z = \frac{x^2}{2\beta_1 \ldots \beta_N}$. For this model the asymptotic expansion corresponds to power-law tails

$$P(x) \sim \sum_{i=1}^{N} \frac{c_i}{x^{2\beta_i+3}}, \ \text{ for } \ |x| \to \infty, \tag{2.46}$$

where the c_i's are constants. Based on the asymptotic limit, this class will be called the power-law class.

To have a clear picture of the forms that take these functions, we have plotted in semilog scale the equation (2.44), with the same parameters used in figure (2.5), such that figure (2.7) corresponds to the PDF $P(x) = \int_0^\infty P(x|\varepsilon_N) f_N(\varepsilon_N) d\varepsilon_N$ for the signal, where the background's PDF $f_N(\varepsilon_N)$ have been plotted in figure (2.5).

This important class has allowed to characterize the velocity increments series of Helium gas modeled as Eulerian turbulence, and the series of intraday returns of the Ibovespa index with time interevents of $30s$ (Macêdo *et al.* (2017)). Systems that will be described in detail in chapter four.

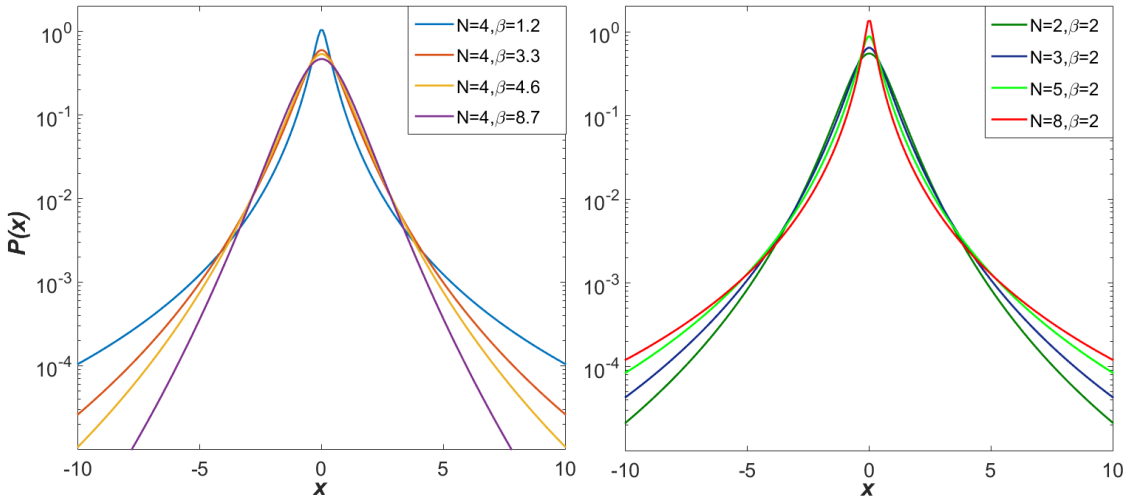

Figure 2.7: On the left we show how the β parameter controls the form of the distribution setting the number of background's scales on $N = 4$. On the right we show the behavior of the distribution according to the scales' number given a parameter $\beta = constant$. In all cases the distribution has been plotted $P(x)$ for the power-law class (eq (2.44)).

Unified representation for γ and $\bar{\gamma}$ classes

Working with the Meijer G-function representation allows unifying the two classes of parametric families presented so far, as was done with the background's distributions $f_N(\varepsilon_N)$ in the equation (2.29). Now the PDF $P(x)$ will have a single representation

$$P(x) = \frac{\omega^{1/2}\Omega_{\gamma\bar{\gamma}}}{\sqrt{2\pi}} G^{N_\gamma+1,N_{\bar{\gamma}}}_{N_{\bar{\gamma}},N_\gamma+1}\left(\begin{matrix} a_{\bar{\gamma}} + 1/2 \\ b_\gamma + 1/2, 0 \end{matrix} \middle| \frac{\omega x^2}{2} \right). \tag{2.47}$$

For particular cases: $N_\gamma = 0$, $N_{\bar{\gamma}} = 1$ the q-Gaussian distribution is obtained, whereas for $N_\gamma = 1$, $N_{\bar{\gamma}} = 0$ the exponentially damped K-distribution is established. Together with the Log-Normal distribution (corresponding to the limit $\lim_{N,\beta} \to \infty$) these are the three possible distributions in the current literature of the superstatistics model.

The following sections present other possible types of background's distributions for this SDE hierarchical model, which are described generically since so far we have not yet found physical systems in which those can be implemented, so its applications are still on

the waiting list.

2.3.2 *Probability density functions of the beta classes*

Since $f(\varepsilon)$ is a background distribution, i.e. it is generated from the dynamics of hidden, and in principle uncontrolled, degrees of freedom, we would like it to be as general as possible. With that in mind, we consider the possibility that the noise is bounded either above (beta class) or below (inverse beta class). The corresponding SDE is

$$d\varepsilon = -\gamma(\varepsilon - \bar{\varepsilon})dt + \kappa\sqrt{\varepsilon|1-\varepsilon|}dW, \tag{2.48}$$

where γ and κ are positive constants. Furthermore the constant $\bar{\varepsilon}$ satisfies $0 < \bar{\varepsilon} < 1$ for the beta class, and $0 < \varepsilon < 1$. The associated FPE is

$$\left\{\partial_t - \gamma\partial_\varepsilon(\varepsilon - \bar{\varepsilon}) - \frac{\kappa^2}{2}\partial_\varepsilon^2(\varepsilon(1-\varepsilon))\right\} f(\varepsilon, t) = 0. \tag{2.49}$$

Using its stationary form

$$\{\beta(\varepsilon - \bar{\varepsilon}) + d_\varepsilon\varepsilon(1-\varepsilon)\}\, f(\varepsilon) = 0, \tag{2.50}$$

where $\beta = 2\gamma/\kappa^2$, its solution can be found through substitution $F(\varepsilon) = \varepsilon(1-\varepsilon)f(\varepsilon)$

$$\frac{dF(\varepsilon)}{d\varepsilon} = -\beta(\varepsilon - \bar{\varepsilon})\frac{F(\varepsilon)}{\varepsilon(1-\varepsilon)}, \tag{2.51}$$

we find

$$F(\varepsilon) = \varepsilon^{\beta\bar{\varepsilon}}(1-\varepsilon)^{\beta(1-\bar{\varepsilon})}. \tag{2.52}$$

Returning to the original variable and normalizing, we get the beta distribution

$$f(\varepsilon) = \frac{\Gamma(\nu+\mu)}{\Gamma(\nu)\Gamma(\mu)}\varepsilon^{\nu-1}(1-\varepsilon)^{\mu-1}, \tag{2.53}$$

for $0 < \varepsilon < 1$, where $\nu = \beta\bar{\varepsilon}$ and $\mu = \beta(1-\bar{\varepsilon})$. We displayed graphically the parametric dependence of beta in the background's distribution (2.53) in figure (2.8)

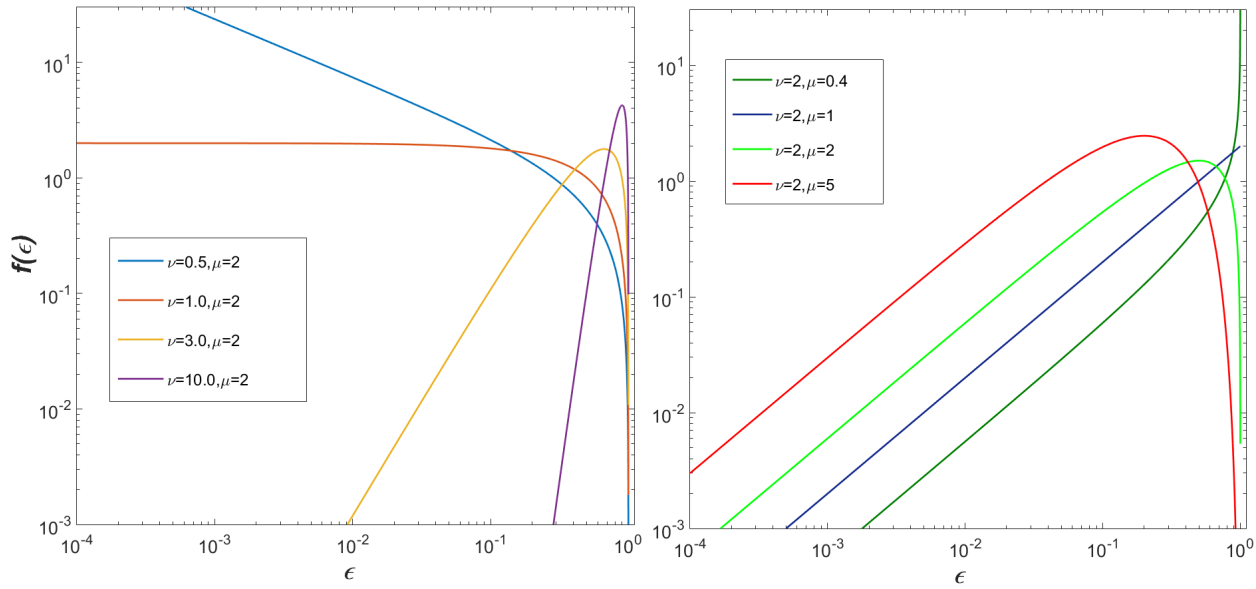

Figure 2.8: On the left we show how the ν parameter controls the form of the beta distribution, whereas the μ parameter is constant. Complementary to the right we show how the μ parameter controls the form of the beta distribution, whereas the ν parameter is constant

The beta PDF has a distribution associated with the inverse multiplicative of the background's variable ε which is described below.

The inverse-beta distribution

Define the random variable ζ as $\zeta = \frac{1}{\varepsilon}$. Its derivative is determined by Itô calculus as

$$d\zeta = -\frac{1}{\varepsilon^2}d\varepsilon + \frac{1}{\varepsilon^3}(d\varepsilon)^2. \tag{2.54}$$

Here, $d\varepsilon$ corresponds to the Langevin equation (2.48), so by direct substitution we get

$$d\zeta = -\frac{1}{\varepsilon^2}\left\{-\gamma(\varepsilon-\bar{\varepsilon})dt + \kappa\sqrt{\varepsilon(1-\varepsilon)}dW\right\} + \frac{1}{\varepsilon^3}\kappa^2\varepsilon(1-\varepsilon)\underbrace{(dW)^2}_{dt}. \tag{2.55}$$

Then, we proceed to organize the equation, separating the terms of fluctuation and dissipation

$$\frac{d\zeta}{\zeta} = \left(-\gamma\bar{\varepsilon}(\zeta - \frac{1}{\bar{\varepsilon}}) + \kappa^2(\zeta - 1)\right)dt + \kappa\sqrt{\zeta - 1}\underbrace{d\tilde{W}}_{-dW}. \tag{2.56}$$

Performing the necessary algebraic steps, the Langevin equation for the inverse beta is obtained

$$d\zeta = -\tilde{\gamma}\zeta(\zeta - \bar{\zeta})dt + \kappa\zeta\sqrt{\zeta - 1}d\tilde{W}. \tag{2.57}$$

The SDE (2.57) can be generically expressed as

$$d\varepsilon = -\gamma\varepsilon(\varepsilon - \bar{\varepsilon})dt + \kappa\varepsilon\sqrt{\varepsilon - 1}dW \tag{2.58}$$

and its asociated Fokker Planck equation is

$$\left\{\partial_t - \gamma\partial_\varepsilon(\varepsilon(\varepsilon - \bar{\varepsilon})) - \frac{\kappa^2}{2}\partial_\varepsilon^2(\varepsilon^2(\varepsilon - 1))\right\} f(\varepsilon, t) = 0, \tag{2.59}$$

with stationary form

$$\left\{\beta\varepsilon(\varepsilon - \bar{\varepsilon}) + d_\varepsilon(\varepsilon^2(\varepsilon - 1))\right\} f(\varepsilon) = 0, \tag{2.60}$$

where $\beta = 2\gamma/\kappa^2$. Its solution may be determined using the substitution $F(\varepsilon) = \varepsilon^2(\varepsilon - 1)f(\varepsilon)$

$$\frac{dF(\varepsilon)}{d\varepsilon} = -\beta\frac{\varepsilon - \bar{\varepsilon}}{\varepsilon(\varepsilon - 1)}F(\varepsilon), \;\; \Rightarrow \;\; F(\varepsilon) = (\varepsilon - 1)^{\beta(\bar{\varepsilon}-1)}\varepsilon^{-\beta\bar{\varepsilon}}. \tag{2.61}$$

Returning to the original variable and applying the normalization condition we deduced the inverse beta distribution as

$$f(\varepsilon) = \frac{\Gamma(\bar{\nu} + \bar{\mu})}{\Gamma(\bar{\nu})\Gamma(\bar{\mu})}\varepsilon^{-\bar{\nu}-1}(1 - \varepsilon^{-1})^{\bar{\mu}-1}, \tag{2.62}$$

for $\varepsilon > 1$, where $\bar{\nu} = \beta + 2$ and $\bar{\mu} = \beta(\bar{\varepsilon} - 1)$. In Figure (2.9) we present plots of inverse beta distribution, whose parameters were chosen by convenience.

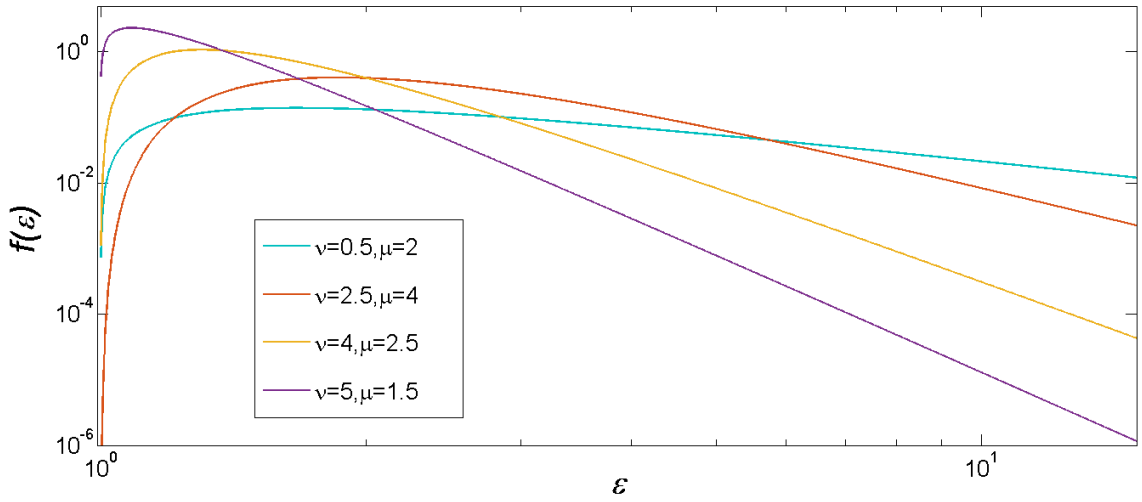

Figure 2.9: Plots of background's PDF $f(\varepsilon)$ for the inverse beta class, these parameters have been chosen conditioned that the Fox H-function associated with background and signal can be plotted. The reader should be aware that in the inset we used the notation $\mu \to \bar{\mu}$ and $\nu \to \bar{\nu}$.

It is important to note that due to the distribution's domain it's hard to execute the joint graphs for signal and background, for that reason, a set of restricted parameters has been chosen.

Just as for the gamma case, is possible to combine the above results in a single Meijer G-function. Let N_β and $N_{\bar{\beta}}$ be the number of beta and inverse-beta variables respectively, with the constraint $N_\beta + N_{\bar{\beta}} = 1$, then

$$f(\varepsilon) = \Omega_{\beta\bar{\beta}} G_{1,1}^{N_\beta, N_{\bar{\beta}}} \left(\begin{matrix} a_{\beta\vee\bar{\beta}} \\ b_{\beta\vee\bar{\beta}} \end{matrix} \middle| \varepsilon \right), \tag{2.63}$$

where $\beta \vee \bar{\beta} = \beta N_\beta + \bar{\beta} N_{\bar{\beta}}$. Furthermore, $a_\beta = \mu + \nu - 1$, $b_\beta = \nu - 1$, $a_{\bar{\beta}} = -\bar{\nu}$, $b_{\bar{\beta}} = -\bar{\nu} - \bar{\mu}$ and

$$\Omega_{\beta\bar{\beta}} = \prod_{j=1}^{N_\beta} \frac{\Gamma(\mu_j + \nu_j)}{\Gamma(\nu_j)} \prod_{j=1}^{N_{\bar{\beta}}} \frac{\Gamma(\bar{\mu}_j + \bar{\nu}_j)}{\Gamma(\bar{\nu}_j)} = \Omega_\beta \Omega_{\bar{\beta}}, \tag{2.64}$$

with $\nu_1 = \nu$, $\mu_1 = \mu$, $\bar{\nu}_1 = \bar{\nu}$ and $\bar{\mu}_1 = \bar{\mu}$.

PDF $P(x)$ for unified beta class signal

Using the Mellin transform properties for the Fox H-function, shown in previous sections a joint probability density function for the signal associated with the background distribution (2.63) is determined

$$P(x) = \frac{\Omega_{\beta\bar{\beta}}}{\sqrt{2\pi}} G_{1,2}^{N_\beta+1,N_{\bar{\beta}}} \left(\begin{array}{c} a_{\beta\vee\bar{\beta}} + 1/2 \\ b_{\beta\vee\bar{\beta}} + 1/2, 0 \end{array} \middle| \frac{x^2}{2} \right). \tag{2.65}$$

We will complete this development presenting graphs corresponding to the signal for classes β and $\bar{\beta}$, respecting the correspondence of parameters. The signal for the β class is the first case, shown in figure (2.10)

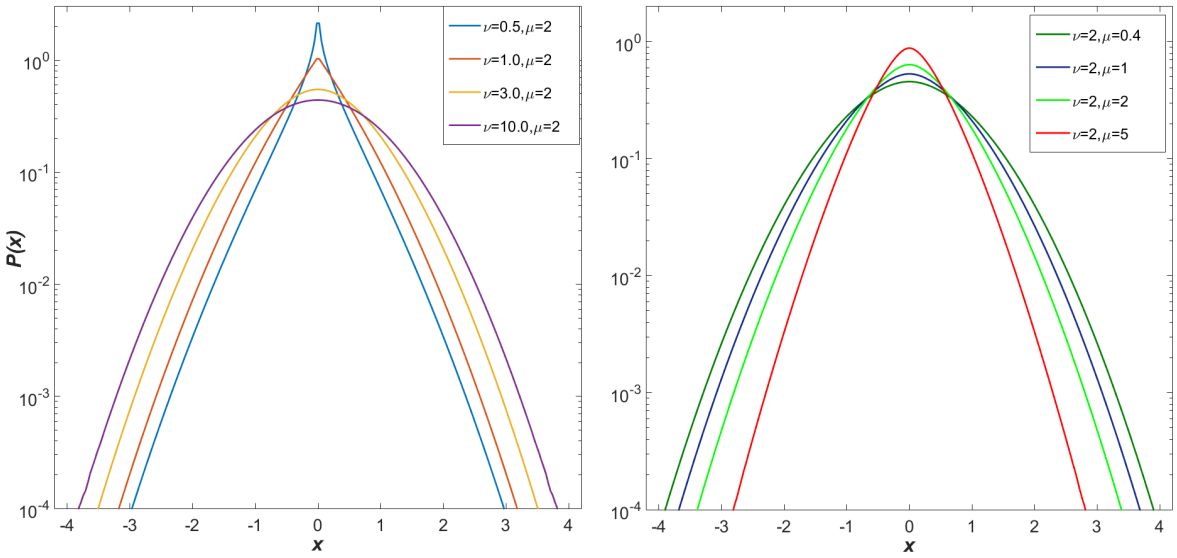

Figure 2.10: Plots of signal's PDF $P(x)$ for the beta class. On the left we show how the ν parameter controls the form of the beta distribution, whereas the μ parameter is constant. Complementary, on the right we show how the μ parameter controls the form of the beta distribution, whereas the ν parameter is constant

.

The asymptotic expansion for this class $N_\beta = 1$ and $N_{\bar{\beta}} = 0$, corresponds to

$$P(x) \sim x^{-2\mu} \exp\left(-\frac{x^2}{2}\right) [1 + O(x^{-2})], \quad (x \to \infty), \tag{2.66}$$

which is a truncated power law. In figure (2.11) curves of signal of the inverse beta class ($\bar{\beta}$) are shown

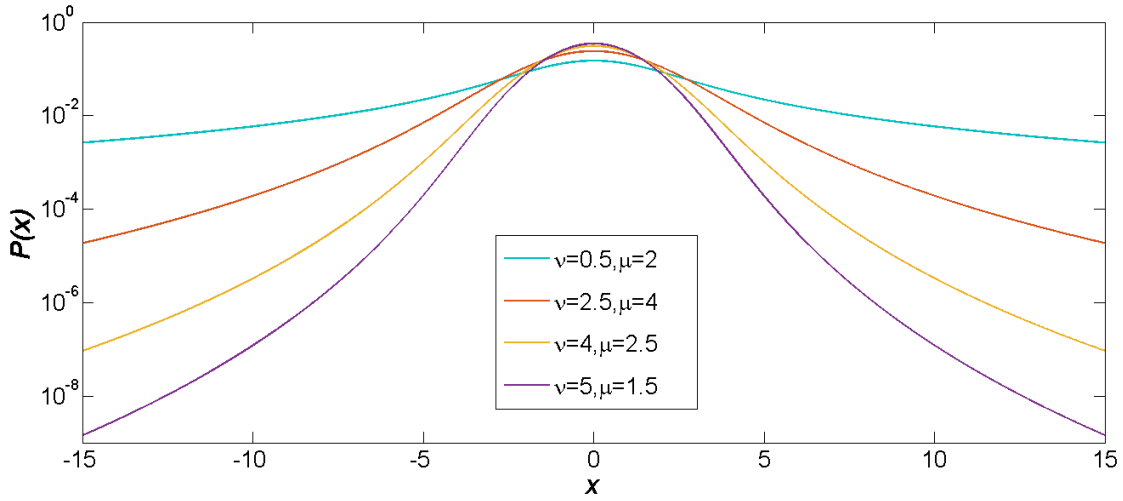

Figure 2.11: Plots of signal's PDF $P(x)$ for the inverse beta class. This graph uses the same parameters shown in the figure 2.9 for background's PDF.

Its asymptotic expansion $N_{\beta} = 0$ and $N_{\bar{\beta}} = 1$, corresponds to a power law

$$P(x) \sim x^{-2\bar{\nu}-1}, \quad (x \to \infty). \tag{2.67}$$

With these results, the presentation for the unified beta class is concluded.

2.3.3 *Generalized Gamma and Beta Classes*

The last extension at the level of a single background time scale is the introduction of the generalized gamma and beta distributions

Generalized gamma classes

In this case the SDE is

$$d\varepsilon = -\gamma(\varepsilon^r - 1)dt + \kappa\varepsilon^s dW, \tag{2.68}$$

where r, γ, κ are positive constants, dW is a Wiener process and $s = 1/2$ ($s = (1+r)/2$) for the gamma (inverse gamma) class. The stationary distribution for the gamma class is

$$f(\varepsilon) = \frac{r}{\Gamma(\beta/r)} \left(\frac{\beta}{r}\right)^{\beta/r} \varepsilon^{\beta-1} \exp\left(-\frac{\beta\varepsilon^r}{r}\right), \quad \text{where} \quad \beta = 2\gamma/\kappa^2. \tag{2.69}$$

As has been recurrent in this chapter, we plotted the parametric dependence of the function (2.69), as shown in figure (2.12), with $r \neq 1$, to distinguish the gamma distribution.

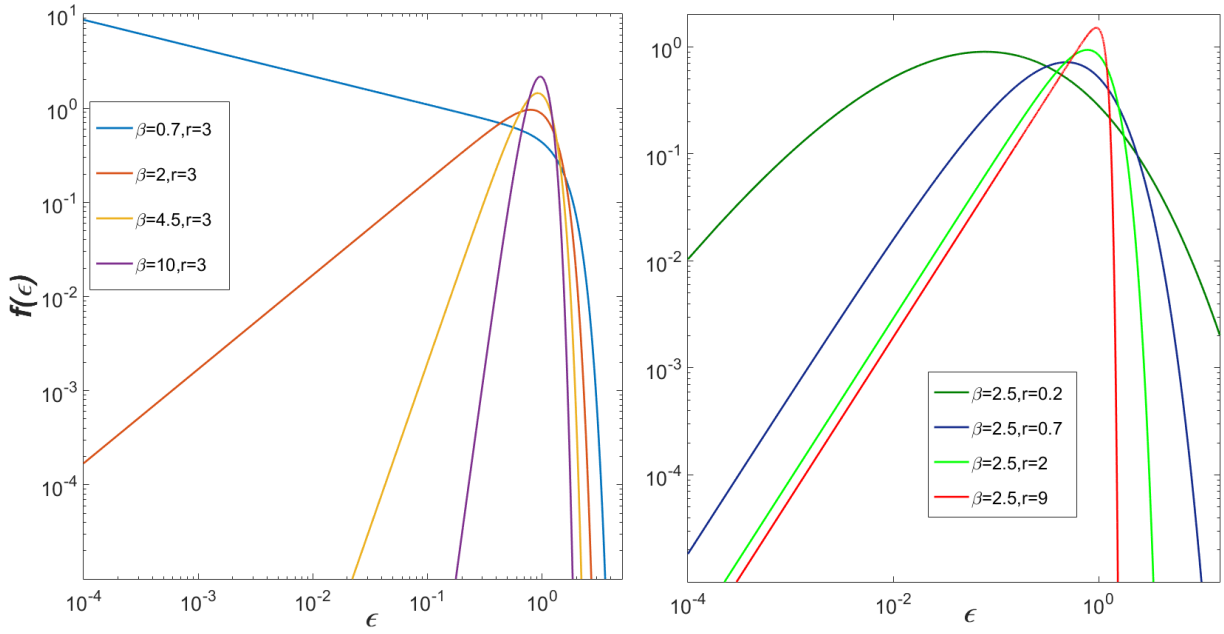

Figure 2.12: Plots of background's PDF $f(\varepsilon)$ for the generalized gamma class. On the left we show how the β parameter controls the form of the distribution, whereas the r parameter is constant. Complementary, on the right we show how the r parameter controls the form of the distribution, whereas the β parameter is constant.

Similarly the stationary distribution for the inverse generalized gamma class is

$$f(\varepsilon) = \frac{r}{\Gamma(\beta/r+1)} \left(\frac{\beta}{r}\right)^{\beta/r+1} \varepsilon^{-\beta-r-1} \exp\left(-\frac{\beta}{r\varepsilon^r}\right). \tag{2.70}$$

A general idea of the parametric dependency can be obtained from figure (2.13)

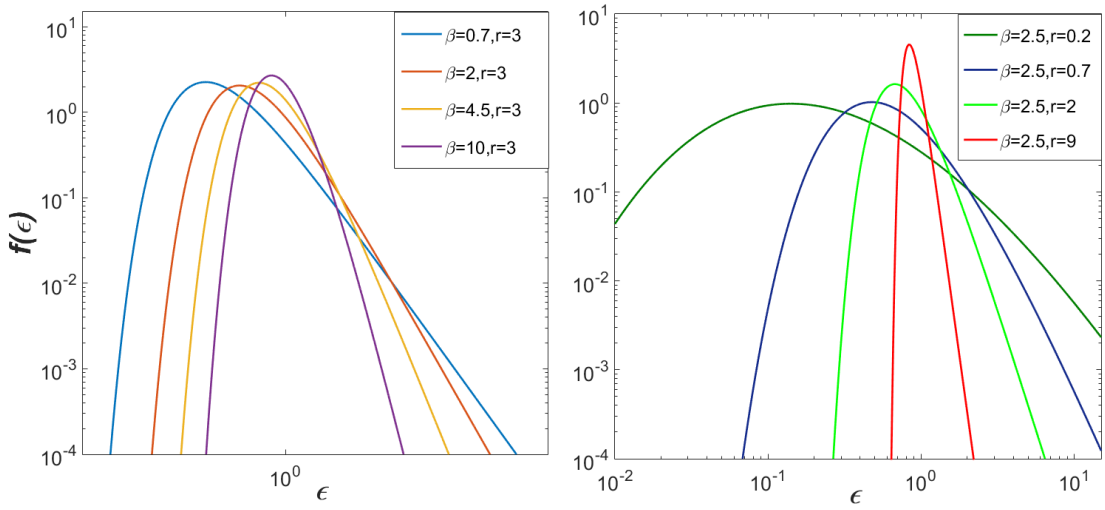

Figure 2.13: Plots of background's PDF $f(\varepsilon)$ for the generalized inverse gamma class. On the left we show how the β parameter controls the form of the distribution, whereas the r parameter is constant. Complementary, on the right we show how the r parameter controls the form of the distribution, whereas the β parameter is constant.

Generalized beta classes

The SDE in this case reads

$$d\varepsilon = -\gamma(\varepsilon^r - \bar{\varepsilon})dt + \kappa\sqrt{\varepsilon|1-\varepsilon^r|}dW, \quad \varepsilon > 1 \tag{2.71}$$

where r, γ, κ are positive constants and dW is a Wiener process. The stationary distribution for the beta class is

$$f(\varepsilon) = \frac{r\Gamma(\nu/r+\mu)}{\Gamma(\nu/r)\Gamma(\mu)}\varepsilon^{\nu-1}(1-\varepsilon^r)^{\mu-1}, \tag{2.72}$$

where $0 < \{\varepsilon, \bar{\varepsilon}\} < 1$, $\nu = \beta\bar{\varepsilon}$ and $\mu = \beta(1-\bar{\varepsilon})$. The parametric dependence is presented in the left part of figure (2.14).

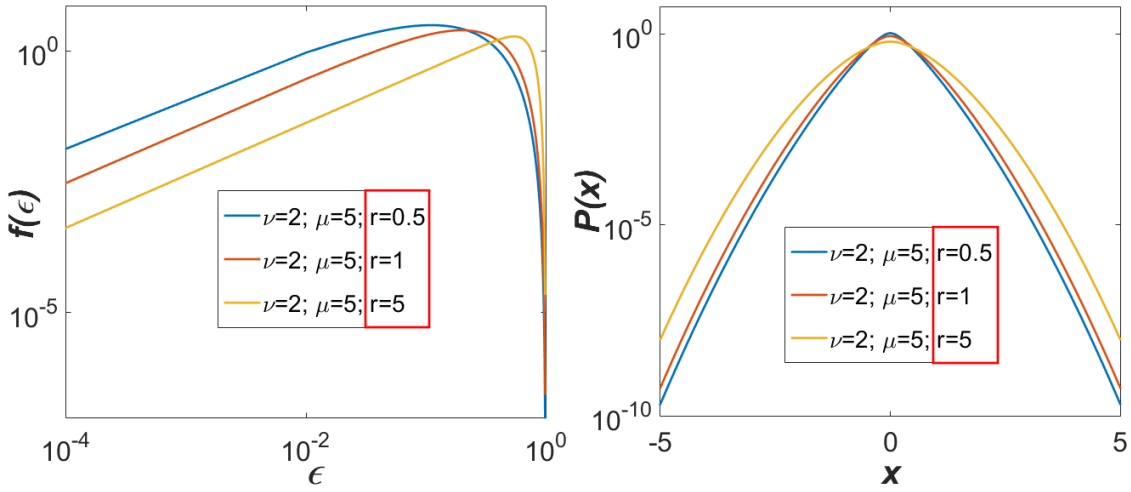

Figure 2.14: On the left plots of background's $f(\varepsilon) \sim H^{1,0}_{1,1}(\varepsilon)$ for the generalized beta class, equation (2.74). In this graph we show how the r parameter controls the form of the distribution. On the right we show plots of signal's PDF $P(x) \sim H^{2,0}_{1,2}(x^2)$ for the generalized beta class, equation (2.75) where $\omega = 1$, and $\Gamma_{\gamma\bar{\gamma}\beta\bar{\beta}} = \Gamma_{\beta}$, using the same parameters of the background

For inverse beta class we get

$$f(\varepsilon) = \frac{r\Gamma(\bar{\nu}/r + \bar{\mu})}{\Gamma(\bar{\nu}/r)\Gamma(\bar{\mu})}\varepsilon^{-\bar{\nu}-1}(1-\varepsilon^{-r})^{\bar{\mu}-1}, \tag{2.73}$$

where $\varepsilon, \bar{\varepsilon} > 1$, $\bar{\nu} = \beta + r$ and $\bar{\mu} = \beta(\bar{\varepsilon} - 1)$. In both cases, we defined $\beta = 2\gamma/\kappa^2$. Whose parametric dependence is shown in the left part of figure (2.15).

In the next section we give a unified description for the beta and inverse beta distributions, in terms of Fox H-functions. Also, we show the form of the probability density functions for the signal associated with the background distributions described in this segment of the manuscript.

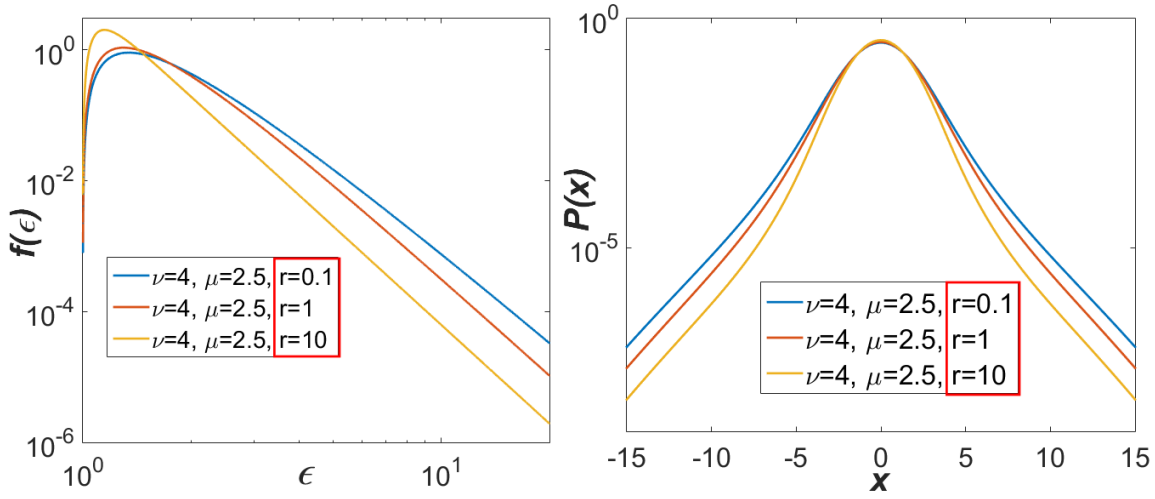

Figure 2.15: On the left plots of background's $f(\varepsilon) \sim H^{0,1}_{1,1}(\varepsilon)$ for the generalized inverse beta class, equation (2.74). In this graph we show how the r parameter controls the form of the distribution. On the right we show plots of signal's PDF $P(x) \sim H^{1,1}_{1,2}(x^2)$ for the generalized inverse beta class, equation (2.75) where $\omega = 1$, and $\Gamma_{\gamma\bar{\gamma}\beta\bar{\beta}} = \Gamma_{\bar{\beta}}$, using the same parameters of the background

2.4 Unified Fox H-function representation

Just as before, the expressions for the generalized gamma and generalized beta classes can be written in a single formula using Fox H-function and the constraint $N_\gamma + N_{\bar{\gamma}} + N_\beta + N_{\bar{\beta}} = 1$. Thus, we found

$$f(\varepsilon) = \omega\Omega_{\gamma\bar{\gamma}\beta\bar{\beta}} H^{N_{\gamma\beta},N_{\bar{\gamma}\bar{\beta}}}_{N_{\bar{\gamma}\beta\bar{\beta}},N_{\gamma\beta\bar{\beta}}} \left(\begin{matrix} (a,A)_{\bar{\gamma}\vee\beta\vee\bar{\beta}} \\ (b,B)_{\gamma\vee\beta\vee\bar{\beta}} \end{matrix} \middle| \omega\varepsilon \right), \tag{2.74}$$

where $N_{ij} = N_i + N_j$, $N_{ijk} = N_i + N_j + N_k$, $i \vee j \vee k = iN_i + jN_j + kN_k$, and $(x,X)_i = (x_i, X_i)$ for $i,j,k \in \{\gamma, \bar{\gamma}, \beta, \bar{\beta}\}$. Moreover, $\Omega_{\gamma\bar{\gamma}\beta\bar{\beta}} = \Omega_{\gamma\bar{\gamma}}\Omega_{\beta\bar{\beta}}$ and

$$\begin{aligned}
\omega &= \prod_{j=1}^{N_\gamma}\left(\frac{\beta_j}{r_j}\right)^{1/r_j}\prod_{j=1}^{N_{\bar\gamma}}\left(\frac{r_j}{\beta_j}\right)^{1/r_j}\\
\Omega_{\gamma\bar\gamma} &= \prod_{j=1}^{N_\gamma}\frac{1}{\Gamma(\beta_j/r_j)}\prod_{j=1}^{N_{\bar\gamma}}\frac{1}{\Gamma(1+\beta_j/r_j)}\\
\Omega_{\beta\bar\beta} &= \prod_{j=1}^{N_\beta}\frac{\Gamma(\mu_j+\nu_j/r_j)}{\Gamma(\nu_j/r_j)}\prod_{j=1}^{N_{\bar\beta}}\frac{\Gamma(\bar\mu_j+\bar\nu_j/r_j)}{\Gamma(\bar\nu_j/r_j)},
\end{aligned}$$

using the notation $\nu_1=\nu$, $\mu_1=\mu$, $\bar\nu_1=\bar\nu$, $\bar\mu_1=\bar\mu$, $\beta_1=\beta$ and $r_1=r$.In which it has been defined $a_{\bar\gamma}=-(\beta+1)/r$, $a_\beta=\mu+(\nu-1)/r$, $a_{\bar\beta}=1-(\bar\nu+1)/r$, $b_\gamma=(\beta-1)/r$, $b_\beta=(\nu-1)/r$, $b_{\bar\beta}=1-\bar\mu-(\bar\nu+1)/r$, and $A_i=1/r=B_i$ for $i\in\{\gamma,\bar\gamma,\beta,\bar\beta\}$. The superposition integral can now be readily calculated using properties of Fox H-function.

$$P(x)=CH^{N_{\gamma\beta}+1,N_{\bar\gamma\bar\beta}}_{N_{\bar\gamma\beta\bar\beta},N_{\gamma\beta\bar\beta}+1}\left(\begin{array}{l}(\tilde a,A)_{\bar\gamma\vee\beta\vee\bar\beta}\\(\tilde b,B)_{\gamma\vee\beta\vee\bar\beta},(0,1)\end{array}\middle|\frac{\omega x^2}{2}\right),\tag{2.75}$$

where $C=\omega^{1/2}\Omega_{\gamma\bar\gamma\beta\bar\beta}/\sqrt{2\pi}$, $\tilde a_i=a_i+1/(2r)$, $\tilde b_i=b_i+1/(2r)$ for $i\in\{\gamma,\bar\gamma,\beta,\bar\beta\}$.

Now, we plotted Eq. (2.75), for the four cases it represents (namely γ, $\bar\gamma$, β, and $\bar\beta$). Thus, in Fig. (2.16) we show the signal for the generalized gamma class, using the same background parameters, presented in previous sections. Similarly, figure (2.17) shows the signal for the generalized inverse gamma class.

The signal for generalized beta and generalized inverse beta class is shown in the right part of figures (2.14) and (2.15), respectively.

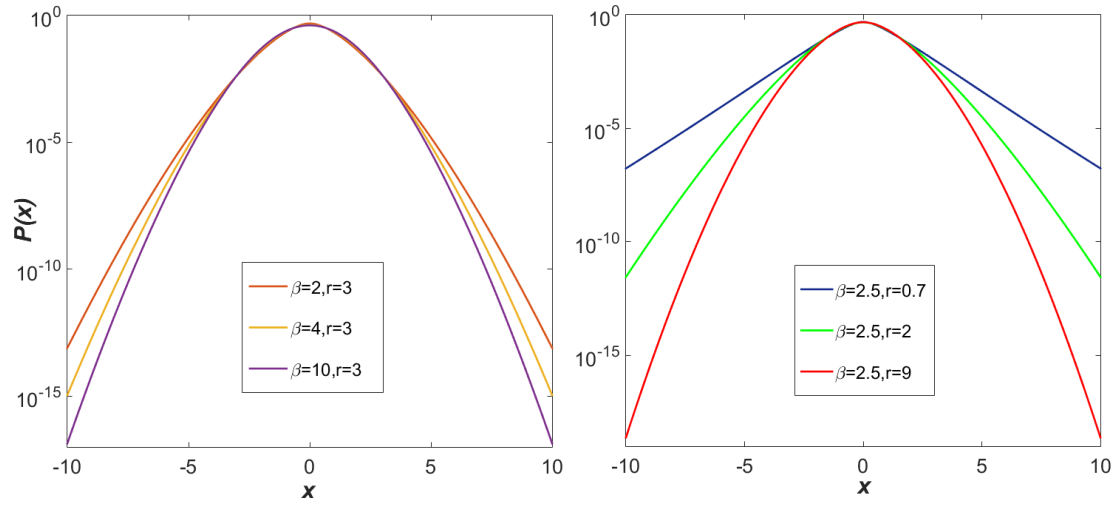

Figure 2.16: Plots of signal's PDF $P(x) \sim H^{2,0}_{0,2}(x^2)$ for the generalized gamma class, equation (2.75) where $\omega = (\beta/r)^{1/r}$, and $\Gamma_{\gamma\bar{\gamma}\beta\bar{\beta}} = \Gamma_{\gamma}$. On the left we show how the β parameter controls the form of the distribution, whereas the r parameter is constant. Complementary, on the right we show how the r parameter controls the form of the distribution, whereas the β parameter is constant.

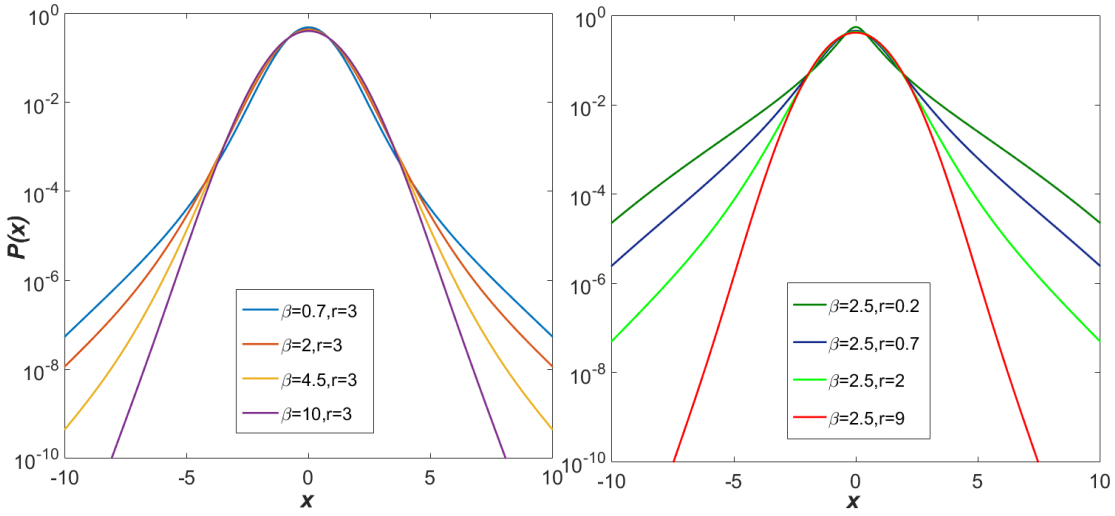

Figure 2.17: Plots of signal's PDF $P(x) \sim H^{1,1}_{1,1}(x^2)$ for the generalized inverse gamma class, equation (2.75) where $\omega = (r/\beta)^{1/r}$, and $\Gamma_{\gamma\bar{\gamma}\beta\bar{\beta}} = \Gamma_{\bar{\gamma}}$. On the left we show how the β parameter controls the form of the distribution, whereas the r parameter is constant. Complementary, on the right we show how the r parameter controls the form of the distribution, whereas the β parameter is constant.

2.5 Conclusions

We introduced a unified dynamical approach to describe statistical features of the time series of multiscale complex systems. The probability density of the corresponding time series is represented as a statistical superposition of a macroscopic variable with a large time scale and an arbitrary number of small time-scales background variables corresponding to effective internal degrees of freedom. We derived analytically a large family of background distributions from a dynamical model based on five simple physical constraints. We showed that this family of distributions has a simple representation in terms of Fox H-function which unifies and generalizes several results of the recent literature. A number of applications, including normal and anomalous diffusion with fluctuating background, were worked out in detail and explicit analytical expressions were derived.

3 Background series

3.1 Introduction

In the H-theory approach, we assume that the experimental data corresponds to a stationary series whose probability density function PDF is determined by

$$P(x) = \int_0^\infty P(x|\varepsilon_N) f_N(\varepsilon_N) d\varepsilon_N, \tag{3.1}$$

in which $P(x|\varepsilon_N)$ can be Gaussian[1]

$$P(x|\varepsilon_N) = \frac{1}{\sqrt{2\pi\varepsilon_N}} \exp\left(\frac{-x^2}{2\varepsilon_N}\right), \tag{3.2}$$

and $f_N(\varepsilon_N)$ is the PDF of the superposition of N background variables. To prove the theory, we need to know what is the time series associated with the background, whose superposition with a Gaussian kernel reproduces the PDF of the experimental data. To achieve this purpose, we developed a method that took as its starting point the results of reference (Schafer and Guhr (2010)). In this work, the data series of finantial returns $r(t)$, which initially presents deviations of the Gaussian (kurtosis $\kappa \neq 3$), is normalized as follows $\rho_n(t) = \frac{r(t)-\mu_n(t)}{\sigma_n(t)}$, where $\mu_n(t) = \langle r(t)\rangle_n$ is the local mean value and $\sigma_n(t) = \sqrt{\langle r^2(t)\rangle_n - \langle r(t)\rangle_n^2}$ corresponds to local standard deviation or financial language to the local volatility, and n is a number chosen such that the $\rho_n(t)$ PDF recovers the Gaussian form (kurtosis $\kappa = 3$). In the method developed in (Schafer and Guhr (2010)) the local variance series $(\sigma_n^2(t))$ provides the background distribution $f_N(\varepsilon_N)$. However, using this procedure sometimes we could not obtain by integration $(P(r) = \int P(r|\sigma^2) f(\sigma^2) d\sigma^2)$ the

[1] In general, the transition probability density function correspond to the PDF in the integral scale, which can be a Gaussian, Wigner-Dyson or Boltzmann distribution

reconstruction of the experimental PDF, as was also well documented in (xu and Beck (2016)). To solve this incongruence we have developed an alternative procedure to be described below.

3.2 The background series

From equation (3.1), which sets the connection between the marginal distribution $P(x)$ and background distribution $f_N(\varepsilon_N)$, one obtains the general relation between the moments $\langle x^{2r} \rangle$ and $\langle \varepsilon_N^r \rangle$

$$\langle x^{2r} \rangle = \langle \varepsilon_N^r \rangle \prod_{k=1}^{r} (2k-1) = \frac{2^r}{\sqrt{\pi}} \Gamma\left(r + \frac{1}{2}\right) \langle \varepsilon_N^r \rangle. \tag{3.3}$$

It is possible to simplify the procedure assuming that $P(x)$ has zero mean ($\langle x \rangle = \bar{x} = 0$) and unit variance ($\sigma^2 = 1$), whereby the central moments will satisfy $\mu_n(x) = \langle (x - \bar{x})^n \rangle = \langle x^n \rangle$, in particular the second moment is one ($\mu_2(x) = \sigma^2(x) = 1$), while the kurtosis defined as $\kappa(x) = \mu_4(x)/\mu_2^2(x)$ corresponds to the fourth central moment ($\kappa(x) = \mu_4(x) = \langle x^4 \rangle$). Once defined the first two nonzero central moments for $P(x)$ we can establish through equation (3.3) the value of the variance of ε_N

$$\mu_2(\varepsilon_N) = \sigma^2(\varepsilon_N) = \frac{\kappa(x) - 3}{3} = \frac{\gamma_2(x)}{3}, \tag{3.4}$$

since according to equation (3.3) the mean is one ($\langle \varepsilon_N \rangle = 1$). So, using equation (3.4) which corresponds to a theoretical criteria equivalent to applying Bayes theorem for conditional probability distributions, we construct an empirical extension of the experimental data series[2] $u(t)$. The following points are central to the method:

- We focus on the fluctuations or relative increases in the $u(t)$ series. Such variation can be calculated between first neighbors ($\tau = 1$), between second neighbors ($\tau = 2$) and so forth. In general we can define a variable $x(t) = u(t + \tau) - u(t)$ describing these fluctuations, so that the generic series $x(t)$ becomes our main object of study.

[2]Since this series is stationary the t parameter or time refers to the temporal sequence of data acquisition

- We work with a normalized series $x(t)$ with zero mean and unit standard deviation, which is obtained with the substitution

$$\frac{x(t) - \bar{x}(t)}{\sigma(x(t))} \to x(t). \tag{3.5}$$

- The procedure is based on dividing the normalized series $x(t)$ into intervals of size M and for each such interval compute a variance estimator

$$\varepsilon_M(t) = \frac{1}{M} \sum_{j=0}^{M-1} [x(t - j\delta t) - \bar{x}_M(t)]^2, \tag{3.6}$$

where $t = 1, 2, \ldots,$ length of the series, and $\bar{x}_M(t)$ represents local mean for M elements of the data series

$$\bar{x}_M(t) = \frac{1}{M} \sum_{j=0}^{M-1} [x(t - j\delta t)], \tag{3.7}$$

thus generating a new time series, based on a procedure that is known as running average.

- We numerically compound the $\varepsilon_M(t)$ distribution with Gaussian kernel, as suggested by (3.1), for various M, starting from the M value where the global variance of the time series $\varepsilon_M(t)$ ($\sigma^2(\varepsilon_M(t))$) is the nearest value of the third part of excess kurtosis of the time series $x(t)$ in agreement with the equation (3.4). Since such equation is an ideal mathematical relation, it that does not take into account the fact that the experimental series is finite. Therefore, the choice of the best value of M can be implemented by selecting the value for which the corresponding superposition integral, produce the best fit of the probability density function of the experimental data.

3.2.1 *Ilustrative examples*

In this section we show three examples that allowed us to test that the local variance series $\varepsilon_M(t)$ has a M value that can reproduce correctly the background series and its

associated $f_N(\varepsilon_N)$ distribution. In addition to this examples, we present a case in which the background series have N-scales with $N > 1$. Therefore, we want to realize a test via the local variance procedure to eventually separate the internal scales. It is equivalent to decoupled the background distribution f_N into two series, where one of them presents a single scale while the other has $N - 1$ scales.

3.2.2 *Extracting the inverse gamma distribution*

Since the marginal distribution (3.1), it can set up the PDF known as q-Gaussian, or ${}_1F_0$ hypergeometric function, corresponding to the standard function form of the Meijer G-function $G^{1,1}_{1,1}$

$$P(x;\beta_{\bar{\gamma}}) = \frac{1}{\sqrt{2\pi\beta_{\bar{\gamma}}}}\frac{\Gamma(\beta_{\bar{\gamma}}+3/2)}{\Gamma(\beta_{\bar{\gamma}}+1)}\left(1+\frac{x^2}{2\beta_{\bar{\gamma}}}\right)^{-(\beta_{\bar{\gamma}}+3/2)}, \tag{3.8}$$

integrating the Gaussian kernel (3.2), by the inverse gamma distribution with mean one

$$f_1(\varepsilon_1;\beta_{\bar{\gamma}}) = \frac{\beta_{\bar{\gamma}}^{\beta_{\bar{\gamma}}}}{\Gamma(\beta_{\bar{\gamma}})}\varepsilon_1^{-\beta_{\bar{\gamma}}-2}\exp\left(-\frac{\beta_{\bar{\gamma}}}{\varepsilon_1}\right) \tag{3.9}$$

and scale parameter $\beta_{\bar{\gamma}} = \beta_{i\gamma}$. Once we have been established the distributions of our interest, we present in two steps as the extraction scale procedure was applied to them:

- Computationally, we generated 1×10^6 pseudorandom numbers satisfying the PDF (3.8) with parameter $\beta_{\bar{\gamma}} = 20$.

- Now using the variance estimator ϵ_M, we want to determine a value of M such that its associated distribution corresponds to the equation (3.9) (with parameter $\beta_{\bar{\gamma}} = 20$).

In Figure (3.1) it can be observed the results of the computational test described above

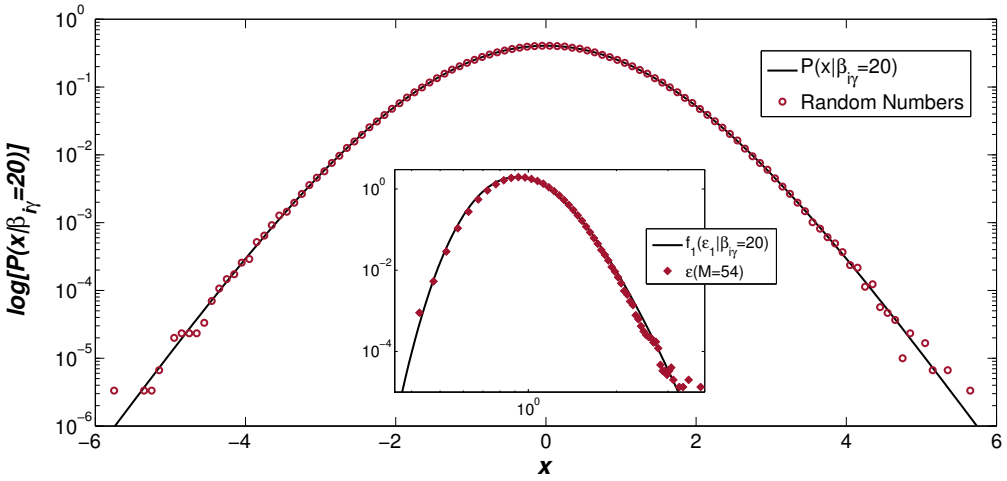

Figure 3.1: In this figure, we used a million of random numbers computer-generated, whose histogram (red dots) satisfies the PDF (3.8) for the signal. From that data set we reconstructed the background function (corresponding to the histogram of the inset), through the ε_M variance estimator.

In the external part of the figure the histogram generated by the pseudo random number satisfying the (3.8) PDF; while the figure's inset shows how the variance estimator ϵ_M with $M = 54$ reconstructs the inverse gamma background $f_1(\varepsilon_1; \beta_{\tilde{\gamma}})$, corresponding to the continuous line of the inset.

3.2.3 *Extracting the gamma distribution*

In a manner analogous to the process shown in subsection 3.2.2, now I applied the procedure to the superposition between the Gaussian kernel and a gamma distribution with mean one

$$f_1(\varepsilon_1; \beta_\gamma) = \frac{\beta_\gamma^{\beta_\gamma}}{\Gamma(\beta_\gamma)} \varepsilon_1^{\beta_\gamma - 1} \exp\left(-\beta_\gamma \varepsilon_1\right). \tag{3.10}$$

Such superposition is represented by the PDF

$$P(x; \beta_\gamma) = \frac{\sqrt{2}^{1-\beta_\gamma} \sqrt{\beta_\gamma}}{\sqrt{\pi}\Gamma(\beta_\gamma/2)} \sqrt{\beta_\gamma x^2}^{(\beta_\gamma - 1)/2} K_{\frac{\beta_\gamma - 1}{2}}\left(\sqrt{\beta_\gamma x^2}\right), \tag{3.11}$$

known as $K-$distribution (Schafer *et al.* (2015)), or the standard Meijer G-function $G^{2,0}_{0,2}$. In this example we generated one million pseudo-random numbers with (3.11) PDF, and

scale parameter $\beta_\gamma = 10$. The theoretical curve is the continuous black line of the external part of figure (3.2), while the circular markers coral colored to correspond to the histogram of computational data series

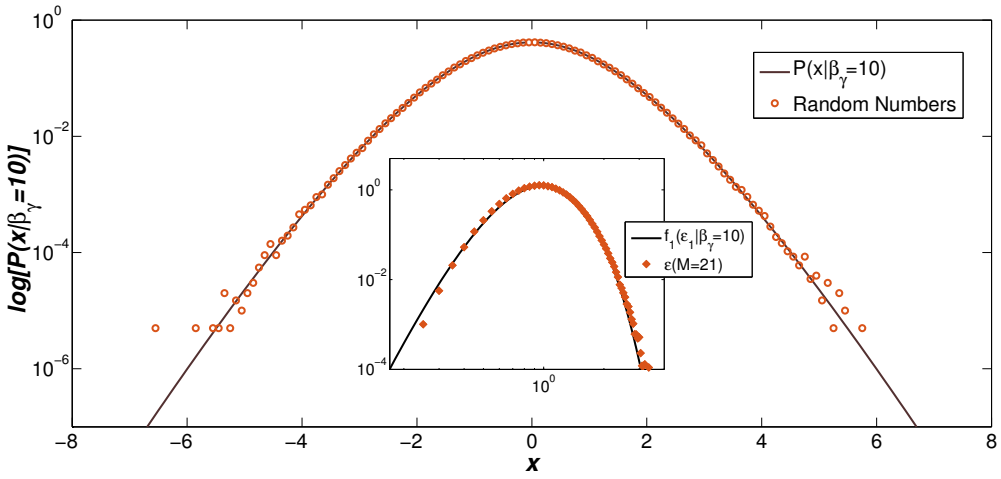

Figure 3.2: In this figure, we used one million of random numbers computer-generated, whose histogram (orange dots) satisfies the PDF (3.11) for the signal. From that data set we reconstructed the gamma background function (corresponding to the histogram of the inset), through the ε_M variance estimator.

The inset of figure (3.2) shows a test in which we found evidences that the estimator ε_M with $M = 21$ generates the auxiliary series such that its histogram fits very well with gamma distribution $f_1(\varepsilon; \beta_\gamma = 10)$, in agreement with the superposition hypothesis.

3.3 Background for beta class

Another important parametric distribution family that can be used as background series corresponds to the beta class $0 < \varepsilon < 1$. In this subsection, we want to emphasize the possibility of extracting the background series for superpositions between Gaussian kernel and beta $f_1(\varepsilon_1)$. However, it must note that due to the possible forms that can take the beta distribution

$$f_1(\varepsilon_1; \nu, \mu) = \frac{\Gamma(\nu + \mu)}{\Gamma(\nu)\Gamma(\mu)} \varepsilon_1^{\nu-1} (1 - \varepsilon_1)^{\mu-1}, \tag{3.12}$$

for different values of the parameters (ν, μ), we restrict your domain $\nu, \mu > 1$, particularly we worked with the values $\nu = 2$ and $\mu = 5$. Therefore, the PDF superposition (equation (3.1)) for this case, produce the Meijer G-function

$$P(x;\nu,\mu) = \frac{\Gamma(\mu+\nu)}{\sqrt{2\pi}\Gamma(\nu)} G^{2,0}_{1,2}\left(\begin{array}{c} \mu+\nu-1/2 \\ \nu-1/2, 0 \end{array} \middle| \frac{x^2}{2} \right), \tag{3.13}$$

which is plotted on semi-logarithmic scale in the continuous red line of figure (3.3). As has been recurrent in this chapter the black circular markers corresponds to the histogram of the pseudo-random numbers generated computationally

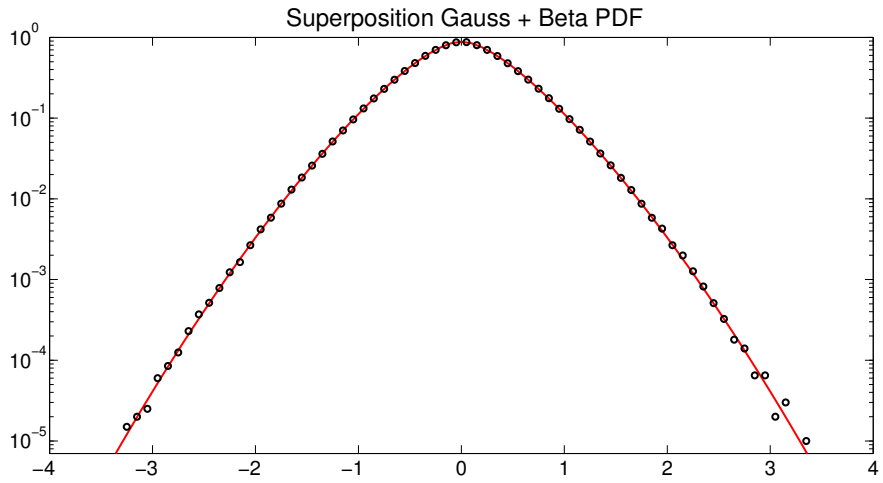

Figure 3.3: In agreement with the previous figures presented in this chapter, a million random numbers have been generated that satisfy the signal's PDF (3.13), which corresponds to a superposition between Gaussian kernel and beta distribution

The goal was to determine the value M for which the $\varepsilon_M(t)$ estimator presents the closest value to the mean and variance of the beta distribution $f_1(\varepsilon_1;\nu,\mu)$

$$\langle \varepsilon_1 \rangle = \bar{\varepsilon}_1 = \frac{\nu}{\nu+\mu} \quad \text{and} \quad \sigma^2(\varepsilon_1) = \frac{\mu\nu}{(\nu+\mu)^2(\nu+\mu+1)}. \tag{3.14}$$

In figure (3.4) it is shown both in linear and logarithmic scale the theoretical curve of the beta distribution and histogram of background series for the empirical estimator

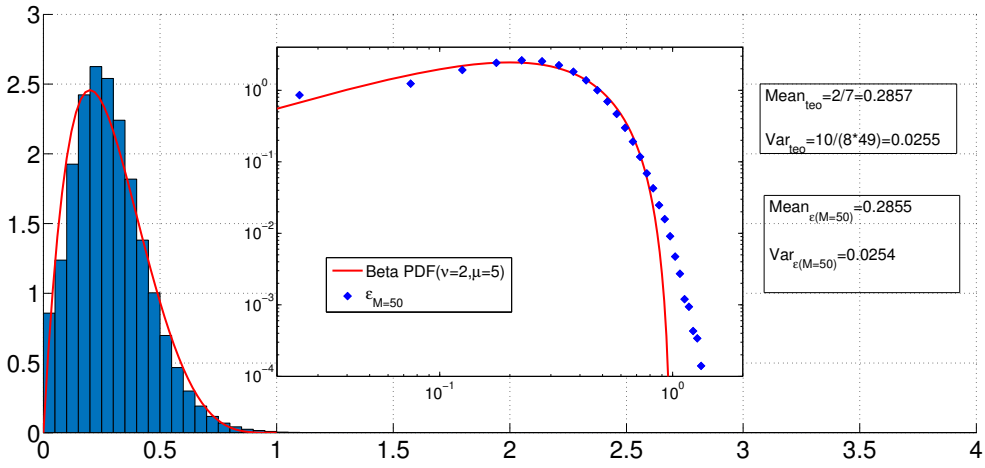

Figure 3.4: The blue histogram in normal scale (logarithmic scale in the inset) was obtained from the computational data series used in Figure (3.3). Through the variance estimator ε_M, the M value is the one for which the mean and variance are the closest to those theoretically stipulated.

with $M = 50$ whose mean and variance was the closest to the theoretical values (equation (3.14)).

It becomes clear that the empirical procedure for extracting background series sometimes is not accurate. For example, for this distribution the domain constraint must be taken into account $0 < \varepsilon < 1$. When the numerical integration between $\varepsilon_{M=50}$ and the Gaussian kernel is done, the PDF (3.13) is reconstructed in such a way that the difference between the two curves seems imperceptible at first glance. However, it should emphasized that the procedure has limited accuracy.

3.3.1 *Separating scales into the background*

This section presents briefly the hypothesis that the procedure for extracting background series could eventually decouple their scales, in case there is more than one. In particular, we worked with two scales of the parametric family inverse-gamma

$$f_2(\varepsilon_2; \beta_{1\bar{\gamma}}, \beta_{2\bar{\gamma}}) = \frac{(\beta_{1\bar{\gamma}}\beta_{2\bar{\gamma}})^{-1}}{\Gamma(\beta_{1\bar{\gamma}}+1)\Gamma(\beta_{2\bar{\gamma}}+1)} G^{1,1}_{1,1}\left(\begin{matrix} -\beta_{1\bar{\gamma}}-1, -\beta_{2\bar{\gamma}}-1 \\ \_\_\_ \end{matrix} \middle| \frac{\varepsilon_2}{\beta_{1\bar{\gamma}}\beta_{2\bar{\gamma}}} \right), \qquad (3.15)$$

with parameters $\beta_{1\tilde{\gamma}} = \beta_{2\tilde{\gamma}} = 7$ as it is shown by the continuos red line in the external part of figure 3.5

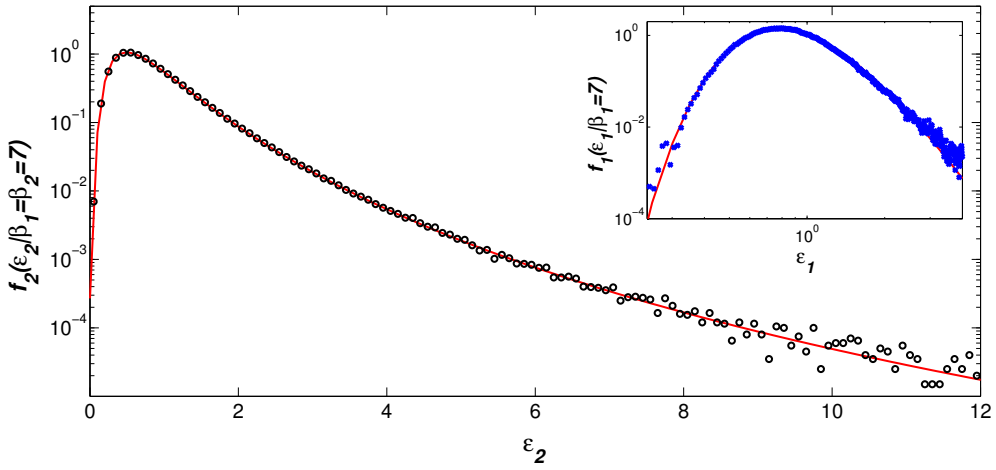

Figure 3.5: In this figure, the possibility of extracting scales within the joint background distribution is shown, particularly an inverse gamma distribution with two scales is plotted together with the histogram associated with the random numbers than satisfying such PDF. In the inset the corresponding separation is presented, i.e., it reconstructs with the variance estimator the inverse gamma distribution.

For this test, it was computationally generated pseudo-random numbers with probability density function $f_2(\varepsilon_2)$, whose histogram is represented by the circular black marker (fig. (3.5)). Once produced the data series was used the variance estimator ε_M to set the M value from which we obtained the inverse-gamma distribution with $\beta_{\tilde{\gamma}} = 7$. For $M = 130$. We found a series whose histogram is represented by the blue marker of internal figure (3.5). This result of the controlled test gives us the future possibility to extract subscales from the background series.

4 Applications of H-theory

4.1 Introduction

Since the proposal of Kolmogorov's theory, it is possible to identify two approaches for the description of turbulence, (i) **Eulerian**, in which structure functions corresponds to averages of velocity increments measured at nearby locations **r** into the fluid, and (ii) **Lagrangian turbulence**, related to changes in time (time lag τ) of the velocity increments (δv). This framework is relevant for stationary bodies exposed to turbulent flow conditions (Chevillard *et al.* (2005)). The statistics analysis of δv from one or the other approach can be connected through Taylor frozen turbulence hypothesis with the correspondence $U = r/\tau$ (Chabaud *et al.* (1994)), where U is the mean velocity.

In this chapter we present a statistical description through the hierarchical theory of stochastic equations applied to two complex systems: (i) turbulence in an axisymmetric jet with helium at low temperature (Chanal *et al.* (2000)), and (ii) intraday returns of the Ibovespa index with $30s$ (thirty-second) inter-event time. The probability density functions exhibit significant deviations from the Gaussian distribution on the experimental resolution scale.

This chapter presents the procedure to extract the auxiliary series for the background using the variance estimator ε_M, which satisfies the superposition hypothesis. Consecutively, it is established with a joint fitting the number of N background scales and the β shape parameter that characterize the PDFs, which are part of the Meijer G-function set.

4.2 Turbulence in classical fluids

From KO62 theory we can identify two dynamical mechanisms (i) **energy cascade**, understood as the transfer of energy between spatial/temporal scales, and (ii) **intermittency** that corresponds to fluctuations in the energy transfer rates between the scales. This model is consistent with the hypothesis of large Reynolds numbers, where large eddies that arise spontaneously decay by inertial effects in smaller eddies initiating a cascade of processes that ends in energy dissipation at the lower scales. Such premises support the existence of scales compounding, a fact that leads to the presence of heavy tails in the PDFs of the velocity increases in the turbulent regime.

In this section, we shall characterize by the Meijer G-functions, the probability density function of the series of 1.67×10^7 data corresponding to measurements made by B. Chabaud and co-workers (Chabaud *et al.* (1994)). The experiment is performed on an axisymmetric jet with helium at low temperature, whose Reynolds number to characterize is $Re = 295,000$. According to the authors of the experiment (Castaing *et al.* (1992)), the resolution frequency of the anemometer used as a sensor is $\tau^{-1} = 271.5$kHz. These measures are framed in the inertial range, assuming that the Reynolds number is the unique and universal parameter characterizing turbulence.

Experimental setup

After filtering and laminarizing, He gas goes through a convergent cone, 30 half angle, ending on a nozzle 2 mm in diameter. The jet then develops downwards in a cylindrical chamber of vertical axis, 12 cm in diameter (Fig. 4.1). A grid, 16 cm away from the nozzle, stabilizes the jet by breaking the largest eddies before they can interact with the walls. Helium then flows out of the cryostat to a recuperation tank (Chanal *et al.* (2000)).

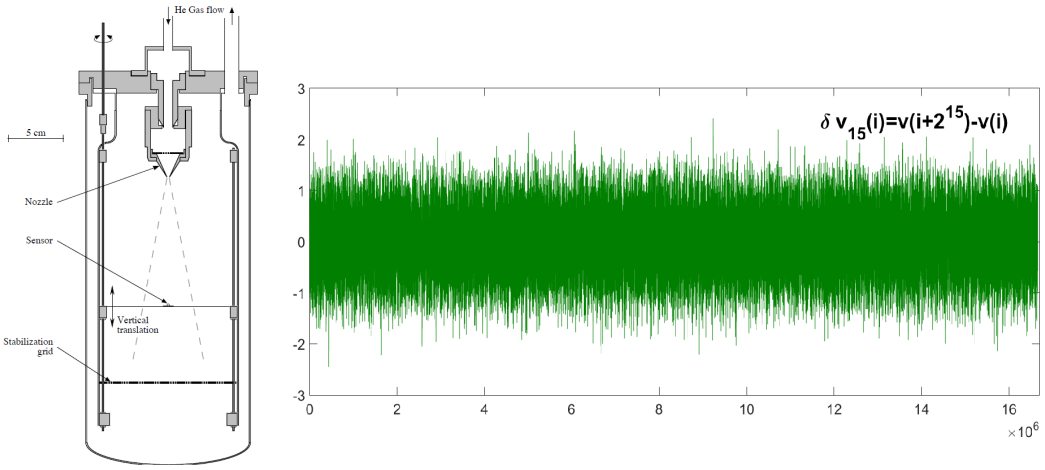

Figure 4.1: To the left is the experimental setup, consisting of (i) gas injection, (ii) laminarization honeycomb, (iii) nozzle, (iv) detector, (v) stabilization grid, (vi) pumping exit, and (vii) pressure measurement (Chabaud *et al.* (1994); Chanal *et al.* (2000)). In green is presented the series for the velocity differences δv between neighbors 2^{15}, where the Gaussian probability density function is recovered.

Our main objective is to determine the statistical behavior of PDFs associated with the data spectrum of velocity increments [1] $\delta v_\tau(t) = v(t+\tau) - v(t)$, as a function of experimental resolution time.

The PDFs of velocity increments are sensitive to the parameter $\tau_j = 2^j$. As evidence of this, the probability density functions (δv_{τ_j}) make a crossover from distributions with heavy tails for differences to first neighbors, until reaching a Gaussian behavior for differences between larger neighbors $\tau_j > 2^{10}$, as shown in Fig. (4.2).

It is possible to separate the standard deviation σ_j associated with each time lagged τ_j to characterize the tails of the PDFs. With such a procedure it is guaranteed to eliminate the dependence on the parameter which sets the mean of background functions, without losing the shape of the signal's tail. With this justification, we have performed the characterization of the series at different time delay using the normalized quantity $\delta v(\tau_j)/\sigma(\tau_j)$, written in discrete notation as

[1] Alternatively, a discrete notation is inserted where the velocity data fill a place in a vector v such that the data $v(i)$ corresponds to the ith position of the vector

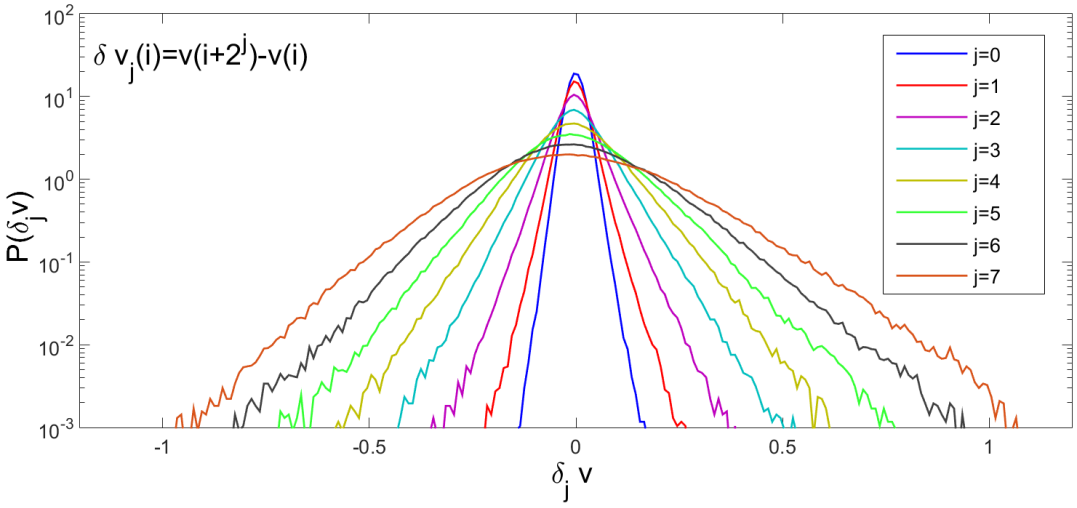

Figure 4.2: In this graph we are presenting the PDF of velocity increments as a function of the separation distance $\delta v_j(i) = v(i+2^j) - v(i)$ between the data. Here, the statistical moments associated with the PDFs has not been fixed, so it is possible to observe how the variance for each of the PDFs increases; Also the figures show the crossover in the tails. As the parameter j increases, the power law form in the tails is disappearing.

$$x(2^j) = \frac{\delta v_j(i)}{\sigma(\delta v_j)} = \frac{v(i+2^j) - v(i)}{\sigma(\delta v_j)}. \tag{4.1}$$

This form allows the direct implementation in the computer. On the other hand, since signal's PDF has zero mean and is normalized by the standard deviation, it is the kurtosis the first statistical indicator that characterizes the symmetrical part of the distributions

$$\kappa(\delta v_j) = \langle (\delta v_j)^4 \rangle = \frac{1}{N_j} \sum_{i=1}^{N_j} (\delta v_j(i))^4, \quad \text{where} \quad N_j = \text{length}(\delta v_j). \tag{4.2}$$

In agreement with the description made in chapter three, the functions have positive excess kurtosis $\gamma_2(\delta v_j) > 0$ for small j. Now with PDFs normalized by its standard deviation is presented in the figure (4.3) the discrete time lagged dependence noted by the value of j that measures the distance between events greater than the experimental resolution. Through this figure it becomes clear that these PDFs perform a crossover to Gaussian functions with $\gamma_2(\delta v_j) = 0$ for $j = 15$.

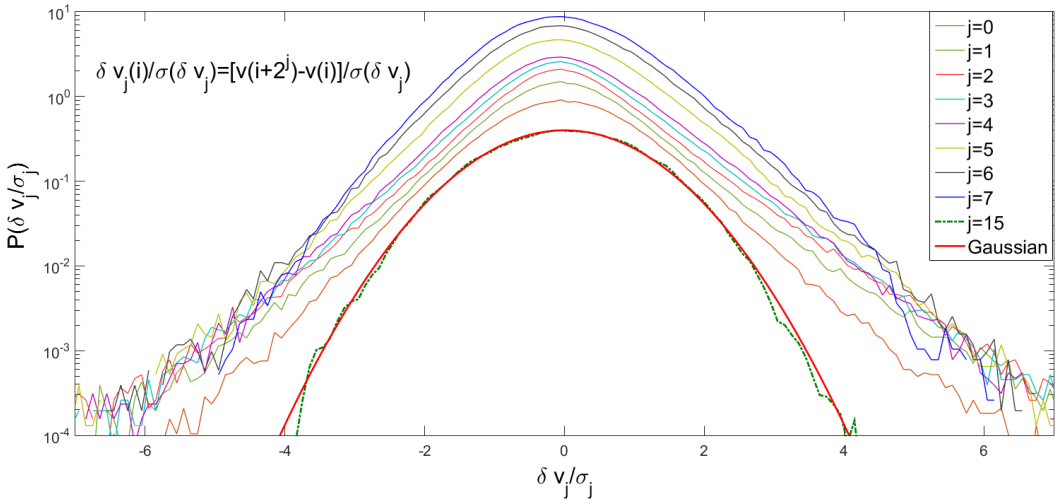

Figure 4.3: PDF's velocity increments doing crossover from heavy tailed to Gaussian distribution. Each curve is multiplied by a scale factor, with the purpose of obtaining a clear image of each one of them.

From the series of the velocity increments, the theoretical model of chapter two and the variance estimator described in chapter three, we proceed to determine the background auxiliary series. In principle, if gives detailed description of normalized velocity increments in the limit of the experimental resolution $j = 0$. Generally, this quantity is noted as $x = \frac{v(i+1)-v(i)}{\sigma(\delta v_0)}$. The time series (or data series) x is divided into intervals of size M called "windows." On each of these windows we calculated the mean and the variance, understood as the subtraction between the average of the square of the elements that make it up and the square of the local mean.

The value of the parameters M of the auxiliary series is chosen when the numerical integral composing the $\varepsilon_M(t)$-series and the Gaussian kernel has the least residue in comparison with the histogram of x, applying the least squares method. Excellent agreement is found for $M = 19$; see inset of Fig. (4.4(b)). The $\varepsilon_{(M=19)}$ corresponds to the background PDF $f_N(\varepsilon)$ equation (2.29), where by the asymptotic form of this and, the signal's PDF $P(x)$ type of power law (Fig.(4.4(a))) it is assumed[2] $N_\gamma = 0$ and $N_{\bar{\gamma}} = N$. Therefore, through the joint fit procedure for background and signal the number of scales for the power-law class is determined, as shown in figure 4.4.

[2]Tests were made to know if the Gamma class also provided good fitting for $P(x)$ using equation (2.40) and did not obtain satisfactory results

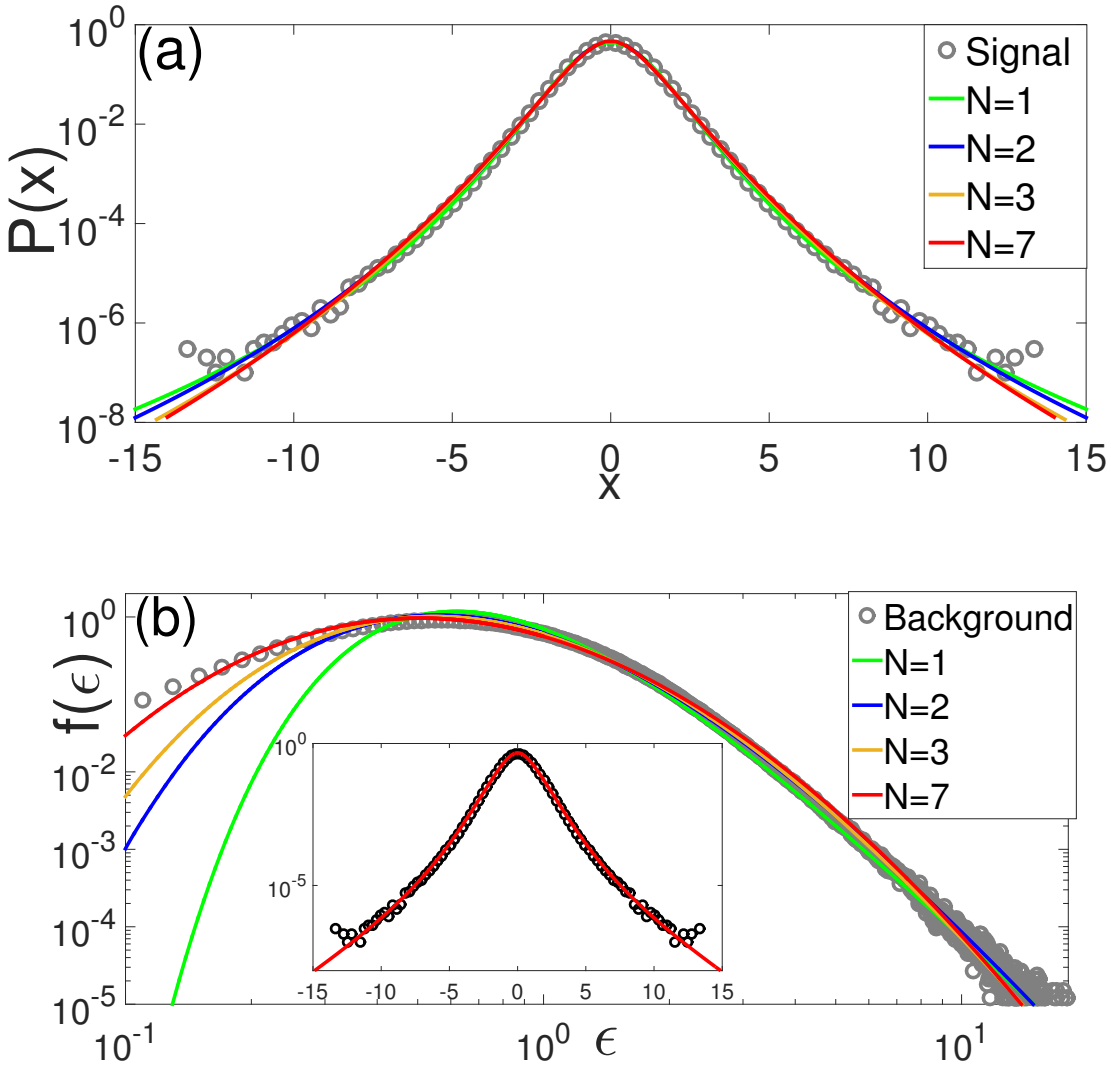

Figure 4.4: (Color line) (a)Experimental distribution for velocity increments (black dots) in a turbulent jet flow and model predictions (solid lines) for $N = 1$ and $\beta = 3.26$ (green), $N = 2$ and $\beta = 5.16$ (blue), $N = 3$ and $\beta = 7.47$ (Coral), $N = 7$ and $\beta = 15.5$ (red); (b) histogram (black dots) of the variance series $\varepsilon(t)$ and model predictions as in (a). Inset shows the superposition (red line) of $\varepsilon(t)$ with a Gaussian and the empirical distribution (black dots).

Several details of the procedure should be noted. There is a correspondence of colors between the scales N for the parts (a) and (b) of figure (4.4). For each curve with β parameters and N numbers of scales, it is has a good fit of the signal $P(x)$. This agreement happens because the Meijer G-functions perform an excellent fitting on the right side of the histogram of the background distribution $f(\varepsilon)$ (Fig. 4.4(b)), which controls the tail of the signal. On the other hand, the left side of the background controls the central part or signal body $(P(x))$. The signal probability density function does not have a very large excess kurtosis $(\gamma_2(x_{j=0}) < 2)$. Therefore, in this case, the body of $P(x)$ does not have a large deviation from the maximum of a Gaussian distribution. In general, to avoid multiple correspondences with Meijer G-functions for the PDFs we developed a joint fitting procedure for signal (Eq. (2.47)) and background (Eq. 2.29) that establishes an optimal fit of the two histograms. Taking into account both Figs. 4.4(a) and 4.4(b), we concluded that the solution with $N_{\bar{\gamma}} = 7$ and $\beta_{\bar{\gamma}} = 15.5$ gives the best overall fit to the turbulence data (Macêdo *et al.* (2017)).

Following, using this same procedure of extracting the background series and joint fitting have been established numerically (table 4.1) and graphically (figure (4.7)), the values for the PDF that satisfy the superposition hypothesis for the velocity increments to greater neighbors.

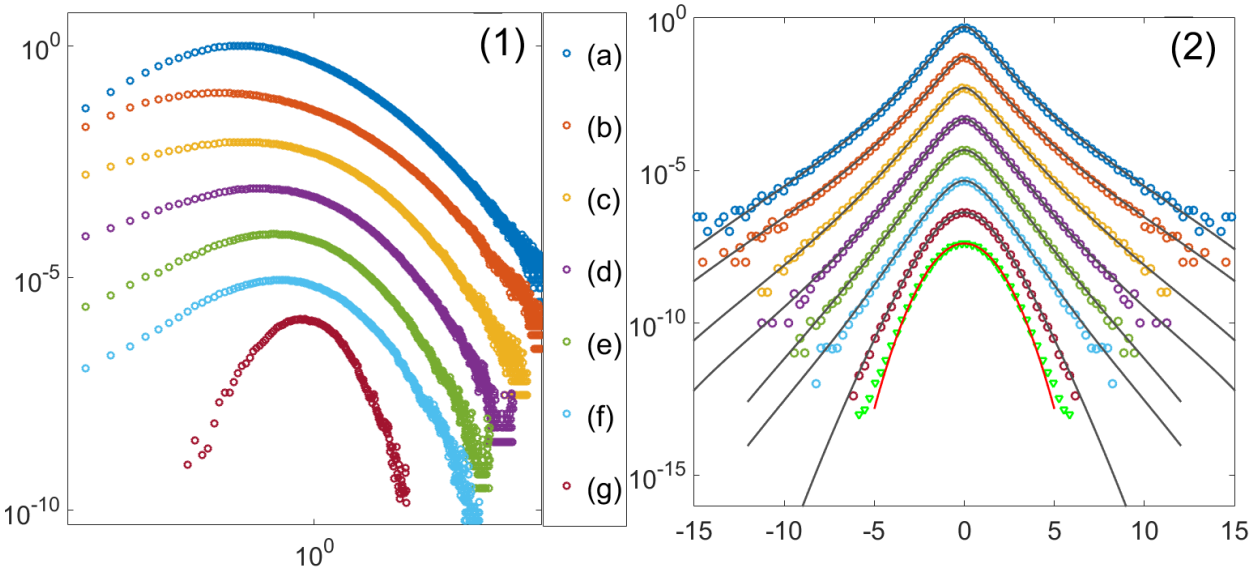

Figure 4.5: On the left: background's histograms of large neighbors. On the right: $x(2^j)$ signal's histograms and numerical integrals between the Gaussian kernel and its corresponding background's histogram, distinguished by color and letter as follows, $(a) : x(2^1), \ldots, (f) : x(2^6)$ and $(g) : x(2^9)$. Finally, in green the histogram for $x(2^10)$ is compared with the Gaussian distribution (in red)

.

The first step has been to extract the respective background series, where the size of the windows chosen is specified in table (4.1) and, its histograms have been plotted on the left side of the figure (4.5). Such histograms have been numerically integrated with the Gaussian kernel via Gauss-Laguerre quadrature to obtain the marginal distributions in continuous black lines that appear on the right side of figure 4.5. Once it has been corroborated that such auxiliary series guarantee the superposition, one proceeds to determine which is the parametric class that more accurately describes the background and signal distributions jointly.

The fit has been made in accordance with the following PDF feature for velocity increments as a function of the parameter τ_j. The measure of kurtosis for $\tau_2 = 2^2$ is maximum, from that value the tails of the PDF $P(x(\tau_j))$ begin to decrease, as described

in figure (4.6). Here we plotted values of the kurtosis excess relative to the central moments and cumulants $\frac{\gamma_2}{3} = \frac{k_4}{3\mu_2^2}$. Therefore using the form of the tails for the signals and the criterion of maximum kurtosis have been discriminated between the two types of universal classes before and after that maximum.

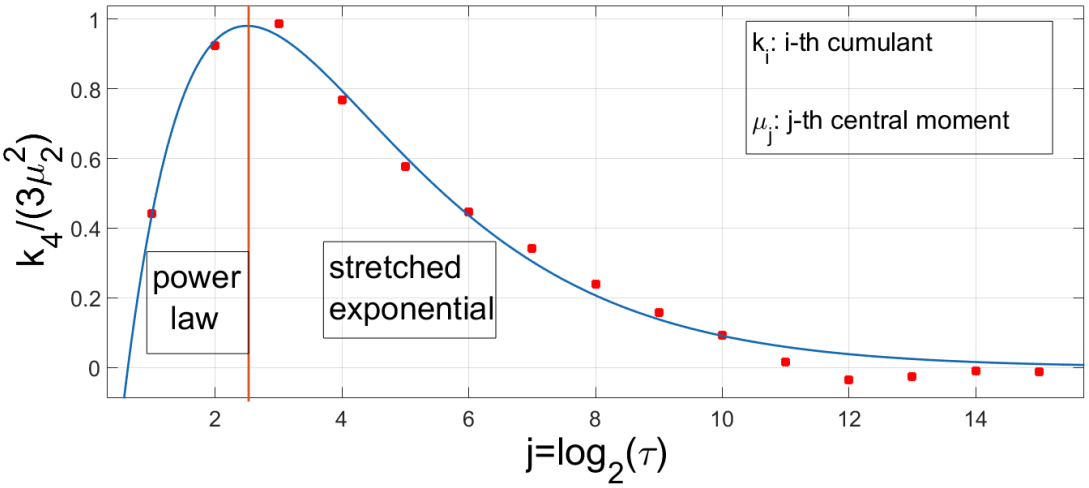

Figure 4.6: Behavior of the kurtosis excess for the signal $x(2^j)$ as a function of the j factor.

Before of the kurtosis maximum (τ_0 and τ_1), it has been determined by the shape of the background tails, that best fits are obtained by the power law class in the domain [0.1,15] for the background and, [-15,15] for the signal. After the kurtosis maximum, it has been determined that the best joint fits of signal and background are produced by the extended exponential class, using the same domain. Under this premise we have plotted the Meijer G-functions for signal and background shown in figure 4.7, where $2^1 \leq \tau_j \leq 2^9$.

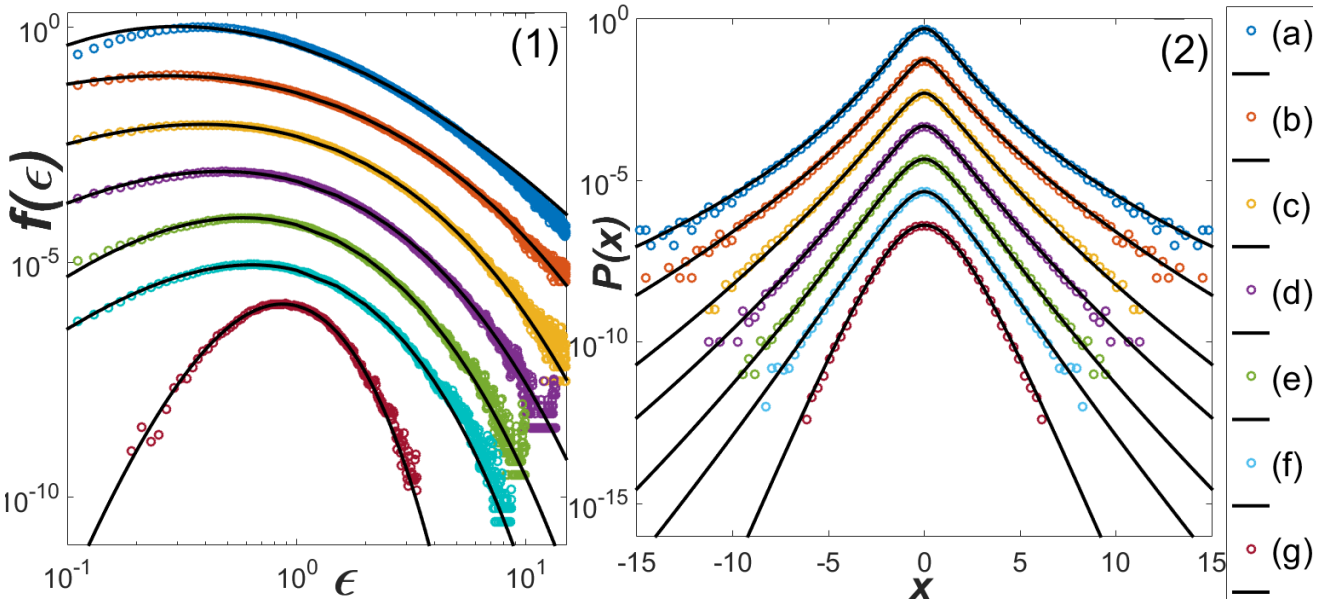

Figure 4.7: On the left: fitting with Meijer G-functions of background's histograms of large neighbors. On the right: fitting with Meijer G-functions of $x(2^j)$ signal's histograms. For both sides, the same parameters are used and a color correspondence is used as follows, $(a) : x(2^1), \ldots, (f) : x(2^6)$ and $(g) : x(2^9)$.

In summary, Table (4.1) presents the values of kurtosis, window's size M used in the variance estimator ε_M and, the values of the scales number N and shape β parameter for the two universal classes (power law $\bar{\gamma}$, and stretched exponential γ). These functions, represented by eqs (2.29, 2.47) were used for the fits of figure 4.7.

Perhaps the parameters listed in Table (4.1) are not definitive. Hypothetically, there could exist an alternate scenario where the two types of universal class have a set of parameters $N_{\gamma\vee\bar{\gamma}}$ and $\beta_{\gamma\vee\bar{\gamma}}$ that fit the background and the signal for each PDF as a function of τ_j with a certain accuracy. However, it should be noted that the ε_M variance estimator opens the possibility to infer from the auxiliary series the interscale dynamics, and that hierarchical theory provides the necessary and sufficient support to justify that non-Gaussianity is a consequence of the interaction with those intermediate scales.

2^j	$\kappa(x_j)$	$M \rightarrow \varepsilon_M$	$N_{\bar{\gamma}}$, $\beta_{\bar{\gamma}}$	N_{γ}, β_{γ}
2^0	4.3273	$M = 19$	$N_{\bar{\gamma}} = 7,\ \beta_{\bar{\gamma}} = 15.5$	_ _
2^1	5.7763	$M = 25$	$N_{\bar{\gamma}} = 6,\ \beta_{\bar{\gamma}} = 9.0$	_ _
2^2	5.9596	$M = 40$	_ _	$N_{\gamma} = 4,\ \beta_{\gamma} = 4.9$
2^3	5.3022	$M = 85$	_ _	$N_{\gamma} = 3,\ \beta_{\gamma} = 4.9$
2^4	4.7319	$M = 150$	_ _	$N_{\gamma} = 3,\ \beta_{\gamma} = 5.9$
2^5	4.3412	$M = 300$	_ _	$N_{\gamma} = 3,\ \beta_{\gamma} = 8.0$
2^6	4.0219	$M = 500$	_ _	$N_{\gamma} = 2,\ \beta_{\gamma} = 6.1$
2^9	3.2779	$M = 5000$	_ _	$N_{\gamma} = 2,\ \beta_{\gamma} = 18$
2^{10}	3.0463	$M =$ _ _	_ _	_ _

Table 4.1: In this table are presented: (i) The kurtosis values ($\kappa(x_j)$) for the normalized velocity increments $x_j = \frac{\delta v_j}{\sigma(\delta v_j)}$, for neighbors 2^j. (ii) The M boxes size with which the variance estimator was constructed ε_M. (iii) The universal classes' parameters used for the fit

4.3 Econophysics Aplications

Stock prices for companies quoted on the different stock exchanges are governed by supply, demand, market speculation, political events, natural events, etc. Such factors lead to the loss of the deterministic behavior of the history of its values at fixed time intervals. The analysis of the time series associated with the prices shows that it can be decomposed into two parts: one of trend (predictive behavior) and, a fluctuation part around the local trend or average of the series. Since the trend term is usually particular, the fluctuations are analyzed from the relative change between price values (S), also known as percentage changes PC and they are defined as

$$\frac{S(t_2) - S(t_1)}{S(t_1)}, \ldots, \frac{S(t_{i+1}) - S(t_i)}{S(t_i)}, \ldots, \frac{S(t_n) - S(t_{n-1})}{S(t_{n-1})}, \tag{4.3}$$

which are independent for $t_1 < \cdots < t_i < \cdots < t_n$ (Castaing *et al.* (2004)). The dynamics of the PC series was first investigated by Louis Bachelier as part of his PhD thesis titled *Théorie de la Spéculation*, which was a complete analysis of futures and options, based on the ideas of random fluctuations of stock prices (Bachelier *et al.* (2006)). Bachelier

considered price changes as being Gaussian distributed. However, modern approaches consider the log-prices as being Gaussian distributed, resulting in the geometric Brownian motion model of stock prices, developed by Fisher Black and Myron Scholes in 1973 (Black and Scholes (1973); Carinski and Kopp (2012)). The Black-Scholes model establishes an equation with Langevin dynamics for prices

$$\frac{dS(t)}{S(t)} = \mu dt + \sigma dW(t) \tag{4.4}$$

where μ is the drift parameter, σ is the volatility parameter (Castaing *et al.* (2004); Richmond *et al.* (2013); Hoffmann and Schreiber (2002)) and $dW(t)$ is the Wiener process, assumed as constant in this model. Another way of characterizing the fluctuations is through the logarithmic variation of the price (returns r_τ) ($r_\tau = \ln S(t) - \ln S(t-\tau)$), which shows remarkable similarities with the Brownian movement, such as self-similarity and linear growth of variance. A fact that can be shown from equation (4.4) using the variable change $r(t) = log(S(t))$ and the Itô lemma (Itô (1951))

$$dr = \frac{dS(t)}{S(t)} - \frac{dS^2(t)}{S^2(t)}, \tag{4.5}$$

where $dS(t)$ and $dS^2(t) = \sigma^2 S^2(t) dt$, are obtained through equation (4.4) using the rules $dt^2 = dt * dW(t) = 0$ and $dW^2(t) = dt$ (Oksendal (2003)), so by direct substitution one obtains

$$dr(t) = \left(\mu - \frac{\sigma^2}{2}\right) dt + \sigma dW(t), \tag{4.6}$$

where the probability density function $P(r,t)$, can be obtained through the Fokker-Planck equation

$$\frac{\partial P(r,t)}{\partial t} = -\left(\mu - \frac{\sigma^2}{2}\right) \frac{\partial P(r,t)}{\partial r} + \sigma^2 \frac{\partial^2 P(r,t)}{\partial r^2}. \tag{4.7}$$

The solution is obtained by Fourier transform, where one finds that $P(r,t)$ is a Gaussian distribution with mean $< r >= (\mu - \sigma^2/2)t$ and variance $< (r - < r >)^2 >= \sigma^2 t$, linearly

time dependent.

Although the hypothesis that the returns distribution is Gaussian provides the basis for the famous Black-Scholes (BS) theory, observational data from the financial market on scales of hours, minutes and even seconds have shown that associated PDFs have heavy tails with large deviations from the Gaussian distribution. Such deviations have been modeled by assuming that the volatility is a variable with stochastic dynamics. There are two outstanding models (*i*) Heston (Heston (1993)), and (*ii*) Hull White (Hull and White (1987)). In both models, the volatility (v) couples as multiplicative noise to the stochastic differential equation of the BS model

$$dx(t) = -a(v)dt + \sqrt{v}dW_1. \tag{4.8}$$

The relevant random variable is defined as $x(t) = \frac{S(t)}{S(0)} - \mu t$, while the drift coefficient is: $a(v) = v/2$ in the Itô scheme, or $a(v) = 0$ in the Stratonovich-scheme (Biró and Rosenfeld (2008)). The two models assume that volatility has a stochastic dynamic (eq. (4.9)), in which the drift terms are the same, whereas the diffusion coefficient denoted by $b(v)$ is the one that discriminates each one of them

$$dv = -\gamma(v - \theta)dt + b(v)dW_2, \tag{4.9}$$

where $b(v) = \kappa\sqrt{v}$ for the Heston model, and $b(v) = \kappa v$ for the Hull-White model.

It is clear that there is a correspondence between the Hull-White model and the generalized hypergeometric model (GHM) of Salazar and Vasconcelos (Salazar and Vasconcelos (2010, 2012); Salazar (2010)). In that innovative study, SV fitted the symmetrical part of the histograms through the asymptotic power law of hypergeometric functions ${}_NF_0$. These were extracted from the coupled SDE model

$$dx_\tau = \sqrt{\varepsilon_N}dW \tag{4.10}$$

$$d\varepsilon_i = -\gamma_i(\varepsilon_i - \varepsilon_{i-1})dt + \kappa_i \varepsilon_i dW_i \quad i = 1, \ldots, N. \tag{4.11}$$

In this model, ε plays the role of volatility, and intermittency emerges from the multiscale dynamics. In the unified theory (Macêdo *et al.* (2017))

$$d\varepsilon_i = -\gamma_i(\varepsilon_i - \varepsilon_{i-1})dt + \kappa_i \varepsilon_i^{\alpha} \varepsilon_{i-1}^{1-\alpha} dW_i, \quad i = 1, \ldots, N, \tag{4.12}$$

presented in chapter two, one can incorporate both the Hull-White and the GHM models. It is also possible to incorporate the single scale Heston model and generalizations thereof to N arbitrary scales.

4.3.1 *Intraday returns of the Ibovespa*

The H-theory, in combination with the procedure for the variance estimator, has allowed us to corroborate the superposition hypothesis in the PDFs corresponding to the series of the returns of IBOVESPA with inter-event time $\tau = 30s$. As described in previously sections, we can make a simultaneous fit of the background (Eq. (2.29)) and the signal (Eq. (2.47)) to determine the number of scales N involved in the overlap and the parameter β that characterizes it.

We analized quotes from the period of November 2002 to March 2004, corresponding to a total of about 53,000 data points. The background series was optimized at windows (or box) size $M = 5$, using the joint fitting, we have concluded that the best combined fit occurs for $N_{\bar{\gamma}} = 3$ and $\beta_{\bar{\gamma}} = 1.2$. The returns series for $\tau = 30s$ has a large kurtosis excess $\gamma_2(\tau = 30s) = 636.6578$, so one might think that it is necessary to have a very high number of background scales N to fit the signal's PDF. However, such fit can be made for all values of N, including $N = 1$ which generates a q-Gaussian distribution or ${}_1F_0$ with parameter $\beta = 0.15$ and, apparently there will always be a collection of parameters β that adjust the distribution as the number of scales increases. For example, in the characterization carried out by Salazar (Salazar (2010)), he used nine background scales,

which corresponds to the hypergeometric ${}_9F_0$ with parameters $\beta_j = 3$ for $j = 1, \ldots, 9$. So it must be emphasized that the joint fitting establishes a robust criterion for choosing the scales number in this returns series that is part of the group of complex multiscale systems.

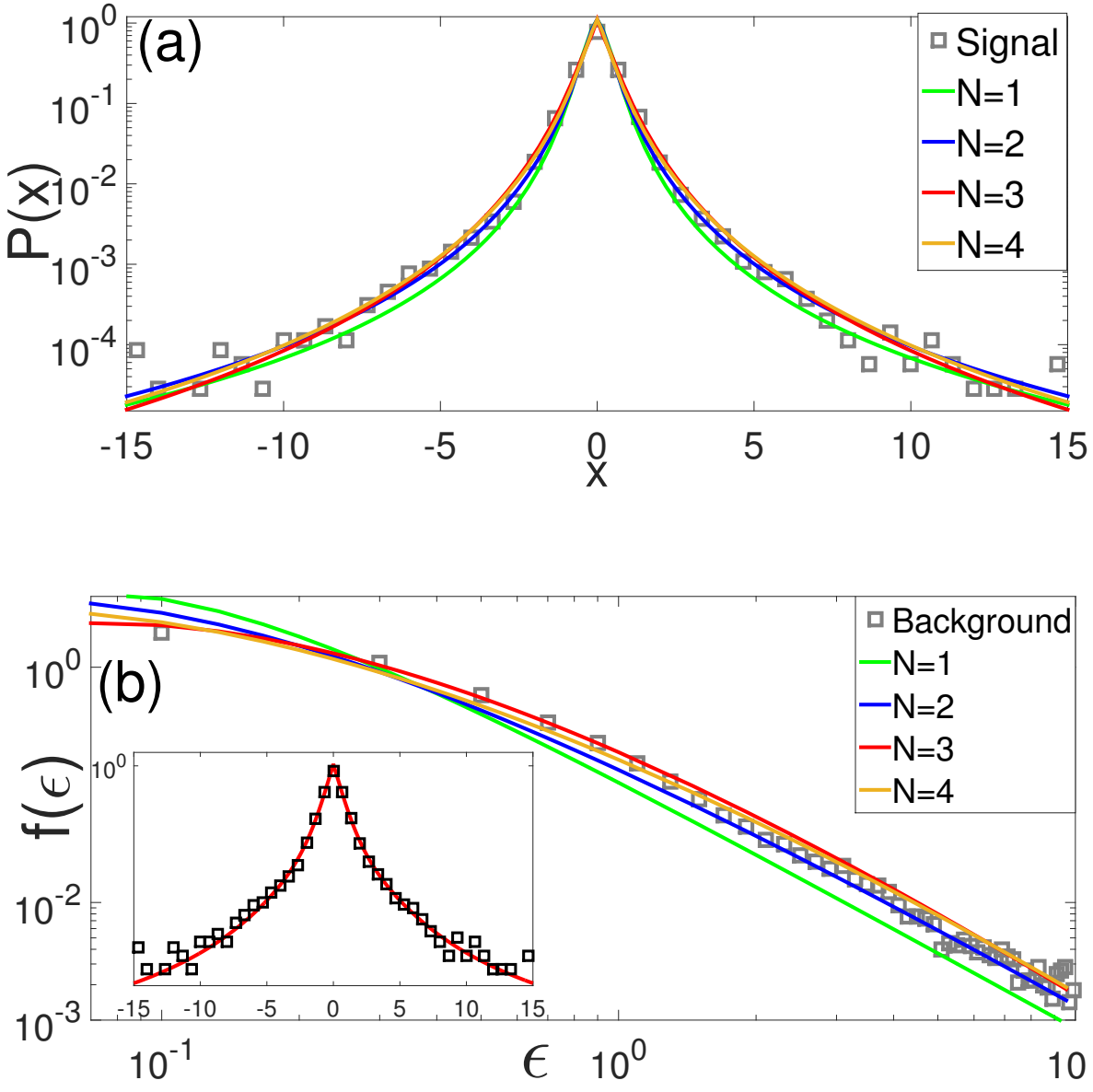

Figure 4.8: (Color line) (a) Empirical distribution of intraday returns of the Ibovespa index (black dots) and model predictions (solid lines) for $N = 1$ and $\beta = 0.15$ (green), $N = 2$ and $\beta = 0.5$ (blue), $N = 3$ and $\beta = 1.2$ (Coral), $N = 4$ and $\beta = 1.32$ (red); (b) histogram (black dots) of the variance series $\varepsilon(t)$ and model predictions as in (a). Inset shows the superposition (red line) of $\varepsilon(t)$ with a Gaussian and the empirical distribution (black dots).

4.4 Conclusions

Describing fluctuation phenomena in multiscale complex systems is an admittedly difficult task because (among other reasons) one does not usually have direct access to the interscale dynamics, and hence indirect inferences have to be made about its effect on the measured quantities. For instance, non-Gaussian statistics is usually seen as an evidence of complex interactions between scales, but a general dynamical framework to explain such deviations from Gaussianity has not yet been established. Here we have shown, from a rather minimal set of assumptions on the interscale stochastic dynamics, that there exist two general classes of heavy-tailed distributions for the statistics of multiscale fluctuations. The distributions in both classes are given in terms of the same family of special functions (Meijer G-function) but differ regarding the nature of the tail: power law and modified stretched exponential, respectively. Good agreement was found with experimental data on classical fluid turbulence as well as financial data-both sets of data analyzed here were shown to belong to the power-law class. Finally, the assumption of well separated time scales, albeit necessary for obtaining the analytical solutions presented here, is not essential for the validity of our dynamical model. If the relevant time scales are expected (say, from general grounds) to be of the same order, one could in principle solve numerically (Huy (2010)) the relevant system of stochastic differential equation to obtain the stationary distribution of the model.

Further development of the theory presented here and additional applications, including of the stretched-exponential class, will be discussed in forthcoming publications. Here we shall only note, as a concluding remark, that the distribution of intensity fluctuations in a random fiber laser can be described as a statistical mixture of Meijer G distributions with stretched exponential tails (Roa-González *et al.* (2017)).

5 Random lasers RL

5.1 Brief introduction

Scattering of light is a common phenomenon that occurs when the light is forced to change the propagation direction due to heterogeneity in a medium. In many applications scattering is treated as a detrimental (unwanted) effect. However, recent developments in the field of nanophotonics have shown that scattering in disordered media may have new functionalities, including an unexpected property of random lasers (Gu *et al.* (2015); Cao (2013); Wiersma (2008)).

A conventional laser (figure (5.1.a)) needs two essential elements: a material that generates gain through stimulated emission and an optical cavity that partially traps light. When the gain is greater than the losses, the system reaches the threshold, and there is laser radiation. The cavity then determines the modes, frequency, and directionality.

On the other hand, random lasers (figure (5.1.b)) differ from a conventional laser in the fact that the amplification of the feedback is not provided by a cavity formed by mirrors but by a scattering medium. Depending on the nature of the scattering medium (it may range from nanometers to several hundred nanometers), the disorder-induced dispersion can provide feedback on the intensity or feedback in the amplitude (Wiersma (2008)). Based on the feedback mechanisms, random lasers are classified into two categories: (i) random laser with incoherent and non-resonant feedback; (ii) random laser with coherent and resonant feedback (Cao (2013)). Over the years experiments have been performed with random lasers in different materials including semiconductors, organic films, liquid crystal, colloidal suspensions diluted in colorants, rare earth elements, biological tissues, quantum dots, among others. All these systems share the lack of directionality of the

emission due to having two-dimensional or three- dimensional geometry. The lack of directionality is due to random scattering and is also limited by the depth at which the pumping light penetrates the gain medium. Both, directionality and increased efficiency can be achieved if the scattering medium is placed inside a waveguide that transversely confines the light (de Matos *et al.* (2007); Burin *et al.* (2002)). In 2005, Shapira et al. (Shapira and Fischer (2005)) experimentally demonstrated that a set of identical but randomly spaced Bragg gratings could increase light localization and suggests that it could be used to obtain random lasers. More recently, Lizárraga et al. (Lizárraga *et al.* (2009)) used this scheme in an Er-doped fiber and effectively demonstrated random fiber lasers (RFLs).

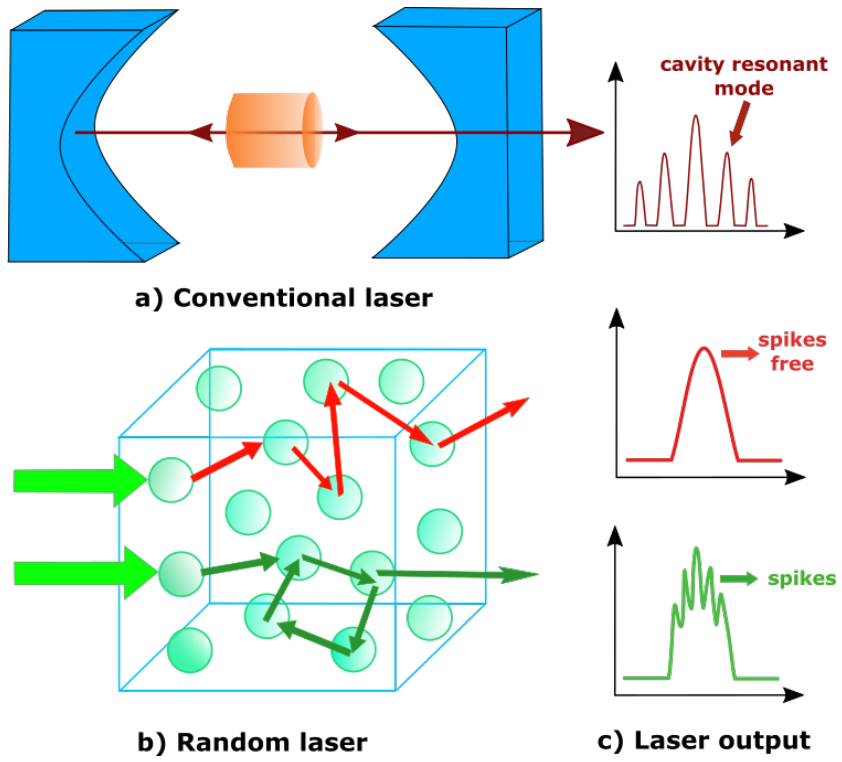

Figure 5.1: (a) A simplified scheme of the cavity used in a conventional laser. (b) Random laser cavity illustrating the incoherent feedback (red arrows) and coherent feedback (green arrows); (c) illustration of spectral outputs of a conventional laser and a random laser, where the spikes free correspond to incoherent feedback, whereas the coherent feedback is recognized by its spiky signature.

At present the statistical description of the output intensity spectrum for experiments with RL and RFL are modeled as a Gaussian distribution below the laser emission threshold. On the other hand, in the vicinity of the threshold, the distribution has heavy tails, which are modeled through a Lévy distribution with exponential truncation. Above the threshold, it is believed that the distribution of intensities recovers the conditions established by the central limit theorem (Lima *et al.* (2017); Uppu *et al.* (2012)). This behavior can be qualitatively justified by a recent analysis presented in (Raposo and Gomes (2015)), where the solution Lévy-type was obtained by a model with Langevin dynamics for the modes of the electromagnetic field. The model includes linear terms associated with the gain medium and radiation loss, plus nonlinear terms associated with the third-order susceptibility $\chi^{(3)}$.

Beyond this theoretical model, other researchers have shown that in the spectrum of output intensities using RFL (Gorbunov *et al.* (2015)), its PDFs are susceptible to variations of the control parameters, such as the pump power and the oscilloscope bandwidth. The susceptibility of intensity PDFs to measurement resolution is a good indicator of the possible existence of smaller scales that alter the shape of the signal (known as an intermittency effect).

Another relevant fact that led us to analyse an experiment with a large number of output intensities $I(t) > 1 \times 10^5$, is based on the fact that most reports with RL and RFL have been performed with an insufficient number of data, which makes it difficult to characterize intensities' PDFs through its tails (Lima *et al.* (2017); Uppu and Mujumdar (2014, 2013); Merrill *et al.* (2016)). However, the use of Lévy $\alpha-$ stable distributions, with characteristic function

$$P(k) = \exp\left\{-|ck|^{\alpha}[1 - i\beta sgn(k)\Phi] + ik\nu\right\}, \tag{5.1}$$

and asymptotic expansion $P(I) \sim I^{-1-\alpha}$, seems to be the accepted model, in spite of the inaccuracies that it brings the use few data points. In this statistical approach it is neces-

sary to incorporate an additional constraint ($P(I) = 0$ for $I > I_{max}$) that limits to finite values the second moment of the Lévy $\alpha-$stable distributions. This restriction is very important because the second-order moment gives information about the average energy density contained in the spectral series giving rise to functions of Lévy with exponential truncation $P(I) \sim I^{-1-\alpha} \exp(-\eta I)$. The analysis of the time series of intensities is done by setting the parameters (shape: $\alpha \in 0, 2$, skewness: $\beta \in [-1, 1]$, location $\nu \in (-\infty, \infty)$, scale: $c \in (0, \infty)$, $\Phi = \tan(\pi\alpha/2)$ for $\alpha \neq 1$, or $\Phi = -(2/k) \ln |k|$ for $\alpha = 1$) through its characteristic function (5.1). With this background, we wanted to know if the PDFs with heavy tails reported in Lima *et al.* (2017), in the vicinity of the laser emission threshold, could be modeled through the H-theory.

In colaboration with the photonic and biophotonic laboratory of DF-UPFE, we decided to carry out an experiment with the continuous-wave-pumped random fiber laser. In this system, the optical fiber used was doped with erbium, and fiber Bragg gratings scatterers were recorded which are randomly distributed in its length. We obtained output intensities in sufficient number to perform an optimal statistical characterization of the time series.

In other words, we wanted to know if the time series formed by the maxima of the output intensity, had features similar to other complex systems (as was presented in chapter four) that can be modeled under the assumptions of the H-theory. In particular, transfer of energy between different space/time scales and fluctuations in the energy transfer rates between contiguous scales. So in the present chapter we describe the results obtained with the experiment (Roa-González *et al.* (2017)).

5.2 Experimental setup

The experimental setup made by B. Lima and P.I.R. Pincheira, was described in references (Lima *et al.* (2017); Gomes *et al.* (2016)) and (Roa-González *et al.* (2017)). For completeness we present such configuration in the figure 5.2

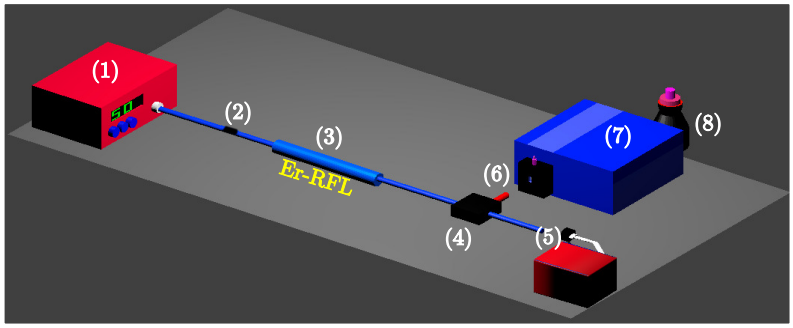

Figure 5.2: The experimental scheme used to obtain the spectrum of intensities. The figure was taken from the reference (Lima *et al.* (2017)) with the author's authorization. The elements used are detailed in table 5.1

(1)	Diode laser $1480nm$ CW
(2)	Connector between pumping and fiber Bragg gratings
(3)	Bragg gratings with random phase shifts written on a fiber doped with erbium
(4)	Wavelength-Division Multiplexing (WDM) $1480 - 1550$
(5)	Power meter to measure the output power P_{out} at 1480 nm
(6)	RFL emission out to spectrometer
(7)	Spectrometer
(8)	Liquid-N_2 cooled InGaAs CCD camera

Table 5.1: Laboratory elements used for experimental setup

Er-based random fiber laser. *The Er-RFL fabrication, including the fiber Bragg grating inscription, is detailed in (Gagné and Kashyap (2009)). It employs a polarization maintaining erbium-doped fiber from CorActive (peak absorption* $28dB/m$@1530 *nm,* $NA = 0.25$*, mode field diameter* $5.7\mu m$*), in which a randomly distributed phase error grating was written. Using this procedure, a very high number of scatterers (*$\gg 10^3$*) was implemented, improving the fiber randomness. A fiber length of 30 cm was used in the present work. The measured threshold from the FWHM analysis was* $P_{th} = (16.30 \pm 0.05)$ *mW. The Er RFL linewidth was limited by our instrumental resolution to* 0.1 *nm. We*

remark that the number of longitudinal modes in the Er-RFL, measured using a speckle contrast technique, is ~ 204 *(Gomes et al. (2016)). This finding corroborates the multimode character of the Er-RFL system.* (Lima *et al.* (2017); Roa-González *et al.* (2017))

Intensity measurements. *For the intensity fluctuations measurements, an extensive sequence of 150,000 output spectra was collected for each excitation power in the regimes below, near, and above threshold. The Er-RFL output was directed to a 0.1 nm resolution spectrometer with a liquid-*N_2 *CCD camera sensitive at 1540 nm. The spectra for each power were acquired with integration time 100 ms. We stress that the intensity fluctuations of the pump source, less than 5%, were not correlated with the RFL fluctuations analyzed here, as pointed out in (Gorbunov et al. (2015); Antenucci et al. (2015)) and also specifically in the present experimental setup*[1] *(Lima et al. (2017); Roa-González et al. (2017)).*

Now that some experimental details are known, in the following section we shall describe the characterization made of the spectrum of maximum output intensities via the power spectral density (or simply, the power spectrum), for the three regimes: below, near and above the threshold. Subsequently, we report the reasons why the characterization was made for the increments of intensity fluctuations with zero mean and normalized by its standard deviation. Also, we show the fits for the probability density functions in the three regimes, which has been performed in terms of a statistical mixture of Meijer G-functions for the regimes near and above the threshold, whereas below the threshold the PDF is Gaussian.

5.3 Power spectum

In general, it is possible to classify the time series associated with fluctuation phenomena through its power spectrum (PS), in the case of stationary series it can be obtained via Fourier transform of the correlation function using the Wiener-Khinchin the-

[1] The experiment described here is based and in many parts is similar to the published in the reference (Roa-González *et al.* (2017)).

orem (Risken and Franck (1996); Badii and Politi (1997)). There are different types of correlation $C(t)$ associated to complex systems, starting from uncorrelated process (or $\delta-$correlated) where $C(t) = 0$, which corresponds to statistically independent events, going through systems where their correlations show exponential decay, even processes where the decay of the correlation function is a power law, in which long-range memory manifests (Schroeder (1991); Weissman (1988)). If the conditions established by the Wiener-Khinchin theorem are satisfied, each type of correlation can be directly associated to a type of power spectrum. For example, for uncorrelated processes its PS is independent of the frequency. In contrast, if we have an exponential correlation due to an Ornstein-Uhlenbeck process, the power spectrum is associated with Lorentzian spectrum (Keizer (1987)). For systems with PS that can be interpreted as a superposition of infinitely many signals with low-frequency Lorentzian spectrum (Badii and Politi (1997); Weissman (1988)), colored noise[2] is generated with a dependence $1/f^{\alpha}$ directly associated to series with correlation $C(t) \sim t^{\alpha-1}$. There is a particular case where the power spectrum has exponent $\alpha = 0$ and is called white noise. If the white noise is integrated over time one obtains (brown)ian noise $1/f^2$ associated to integrable systems, while systems with chaotic dynamics have associated PS of the type $1/f$ called pink noise (see chapter six). Another important type is the black noise, which is associated with natural catastrophes such as earthquakes and corresponds to spectral exponents $\alpha > 2$ (Schroeder (1991); Cambel (1993)). Spectral exponents greater than two have also been reported in two-dimensional turbulence, where its PS is characterized by having two different types of exponent (or slope seen from the log-log scale) associated with double-cascade processes, and as shown below the power spectrum of the output intensities in the random fiber laser system in two of its regimes has double spectral exponent.

[2]The spectral power-law index α for the power spectrum has no relation to the shape parameter of the Lévy distribution.

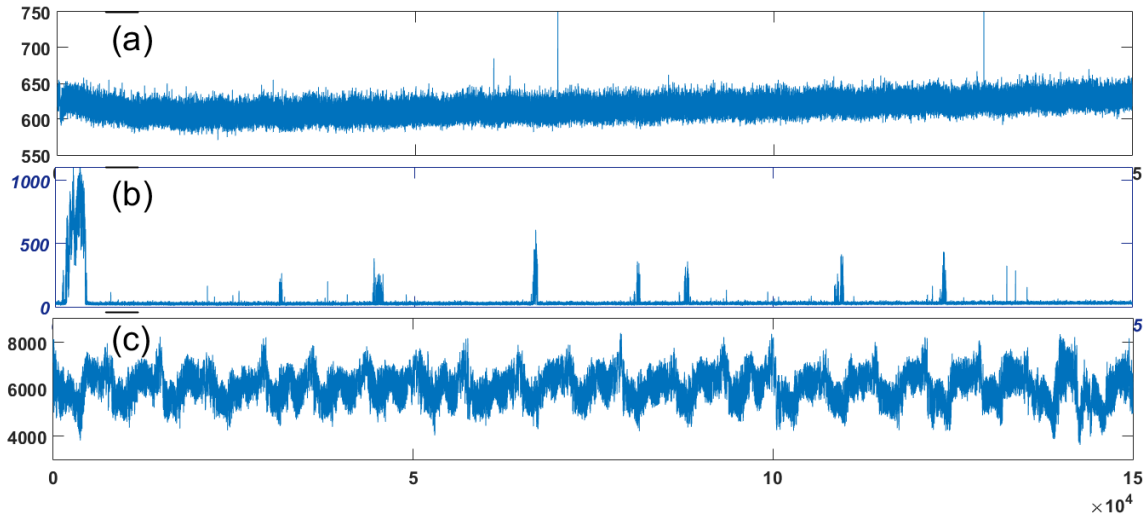

Figure 5.3: Time series for the output intensities, (a) below $P/P_{th} = 0.72$, (b) near $P/P_{th} = 0.99$, and (c) above $P/P_{th} = 2.92$ of lasing threshold.

Since the time series for the output intensities have a non-linear trend, as seen in the figure 5.3, we could not make a direct correspondence between correlations and PS, therefore only the spectral density for the three regimes, (i) below $P/P_{th} = 0.72$, (ii) near $P/P_{th} = 0.99$, and (iii) above $P/P_{th} = 2.92$ of threshold lasing[3] have been characterized.

Each time series (figure 5.3) were divided into windows (or boxes) of 256 elements, and 550 windows were taken without overlapping any element of the original series. Then using discrete Fourier transform

$$S(k) = \left| \sum_{n=1}^{L} I_n \exp\left(\frac{-2\pi i (n-1)(k-1)}{L} \right) \right|^2, \quad \text{where} \quad k = \frac{L}{2\pi} f, \tag{5.2}$$

the power spectrum was obtained for each of the 550 windows of size $L = 256$. These values were averaged, and, from this result, the logarithm for both the abscissa and ordinates was taken, which is plotted in the figure 5.4. Here k denotes the independent variable in the Fourier space, related to the frequency through equation (5.2).

[3]Where P_{th} denotes power threshold

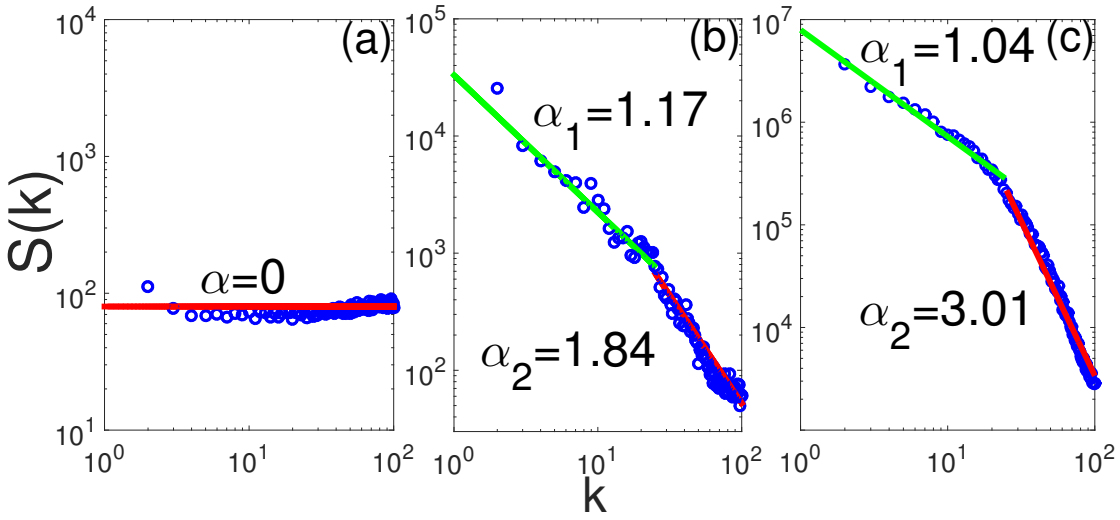

Figure 5.4: Power spectrum and turbulence in the intensity dynamics in Er-RFL. Log-log plots of the spectral density $S(k) \sim k^{-\alpha}$ of the time series of output intensities, in the regimes (a) below ($P/P_{th} = 0.72$), (b) near ($P/P_{th} = 0.99$), and (c) above ($P/P_{th} = 2.92$) threshold. Solid lines are power-law fits to the experimental data. The white noise ($\alpha = 0$) observed in (a) is consistent with statistically-independent non-turbulent Gaussian intensity fluctuations below threshold. The non-trivial double power-law behavior, indicated by red and green lines in (b) and (c), suggests the existence of turbulence in the Er-RFL dynamics both near and above the threshold.

The result for low frequencies shows that the first series (Fig.5.4.a, $P/P_{th} = 0.72$) corresponds to white noise, while near $P/P_{th} = 0.99$ and above $P/P_{th} = 2.92$ of the laser emission threshold, there is spectral density $S(k) \sim k^{-\alpha}$ with two exponent types, or slopes in log-log scale well-defined. This result may be related as an analog in the Kraichnan Leith Batchelor (KLB) theory (Burgess *et al.* (2015); Farazmand *et al.* (2011)), which predicts that for two-dimensional isotropic turbulence there are two inertial ranges, so due to the presence of an external force that injects energy into the system, two processes are simultaneously formed, the first called inverse cascade of energy, where the spectrum scaling as $E(k) \sim k^{-5/3}$, while in the second known as forward cascade of enstrophy inertial range, energy spectrum scaling as $E(k) \sim k^{-3}$. This analogy for the moment is a possibility since the results thrown by this experiment are surprising and are beyond the

approaches that the literature contemplates; so they are an open topic for research.

5.4 Mixture of multiscale distributions

In chapter two, we established the universal classes as stationary solutions of the stochastic dynamic model, which have been denominated (i) power law, and (ii) stretched exponential class. Now, we use one of them to characterize the PDF of 1.5×10^5 output intensities for the three regimes described in previous paragraphs. However, each spectrum presents fluctuations around a nonuniform mean (see figure 5.3). Also, the fluctuations' amplitude is so large than the variance associated to each of the three series would take great values. Therefore, we decided to remove the output intensities trend using the simplest possible way, using the relative increases between measures, as was done for the velocity increments series of chapter four. We shall consider a standardized central measure defined as

$$x(t) \equiv \delta I(t)/\sqrt{var(\delta I(t))}, \tag{5.3}$$

where $\delta I(t) = I(t+\tau) - I(t)$ represents the intensity fluctuations, and var denotes the variance of $\delta I(t)$ series. Thus, the series $x(t)$ in the insets of Figures (5.5), (5.6.a), and (5.7.a) guarantee a statistical description that only incorporates its fluctuating part.

Once the signal ($x(t)$) was established, its probability density function was obtained, and an attempt was made to make the direct fit with the classes of parametric families. As each of the regimes presented technical difficulties of different levels, these are reported separately.

The signal $x(t)$ before the threshold (figure 5.5) was the simplest to fit since its PDF corresponds to a Gaussian distribution, in agreement with previous descriptions made directly on the intensities series (Lima *et al.* (2017); Gomes *et al.* (2016)). So by the PDF ($P(x)$) and its spectral coefficient $\alpha = 0$, it is concluded that the series $x(t)$ below the threshold is composed of statistically independent events; i.e., in this regime, the

intensities fluctuations are in the integral scale.

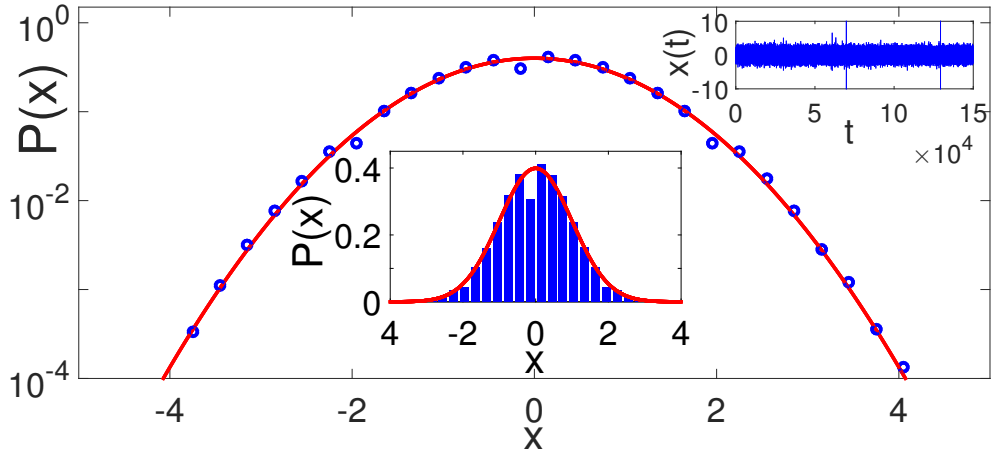

Figure 5.5: Gaussian distribution of intensity increments in Er-RFL and non-turbulent behavior below threshold. Semi-log plot of the distribution of experimental intensity increments x in the non-turbulent prelasing regime at $P/P_{th} = 0.72$ (dots) and best Gaussian fit (solid red line). Insets show the corresponding time series and the same plot in linear scale.

5.4.1 $P(x)$ *near the threshold*

The next step was to describe the signal $x(t)$ near the laser emission threshold $P/P_{th} = 0.99$, so after getting its histogram (figure (5.6.a)), immediately two things were perceived: (i) the signal is a distribution with heavy tails, visually linear on the semi-logarithmic scale, (ii) in the vicinity of $|x(t)| \sim 4$ the distribution presents a drastic change in its curvature forming a quasi-gaussian body i.e., a smooth curve that has the appearance of an inverted parabola in the semilog scale. This PDF presents a form that differs substantially from other distributions with heavy tails. So it was a priority to determine if this PDF could be described by the universal classes of the H-Theory by searching possible N scales and β parameters for the two families γ and $\bar{\gamma}$ that could eventually allow the fit. It was perceived that for large $N \geq 10$ the joint fit of the tail and the body of the distribution $P(x)$ improved. However, the theoretical curves showed a significant

deviation from the histogram of the experimental series in the vicinity of $x = 0$. To contribute to the solution, the background auxiliary series was extracted via the variance estimator ε_M with $M = 15$, whose histogram is plotted on the log-log scale in the part (b) of the figure 5.6. After numerically integrating this series (through the procedure described in chapter three) with the Gaussian kernel and, one obtaines the red curve of the inset of fig. (5.6.b), which fit with high performance the $x(t)$ histogram near of the threshold. So now it was clear that we should have a refined background fit to obtain a clear signal fit. Returning to work with the parameters previously found for the signal with $N \geq 10$ scales, now applied to the background, it became apparent that fits were deficient, so it was necessary to find an alternative solution.

From the visual features of the time series, it is always possible to get valuable information, so the signal $x(t)$ in the inset of the figure $(5.6.a)$ suggested the existence of two simultaneous mechanisms that generated the spectrum. The most active of them generates with small amplitudes ($|x(t)| \leq 4$) the greater data amount, while the other type of mechanism generates in smaller proportion great fluctuations. With this in mind, the first proposal was to realize a filter at $|x(t)| \leq 4$ that discriminates small ($|x(t)| \leq 4$) and large ($|x(t)| > 4$) events, in order to make an independent fit of the two truncated series. The idea was to find two Meijer G-functions $G_{p_1,q_1}^{m_1,n_1}(x)$ for ($|x(t)| \leq 4$) and $G_{p_2,q_2}^{m_2,n_2}(x)$ for ($|x(t)| > 4$), and try to establish continuity conditions $G_{p_1,q_1}^{m_1,n_1}(x)|_{x=4} = G_{p_2,q_2}^{m_2,n_2}(x)|_{x=4}$ and $\partial_x G_{p_1,q_1}^{m_1,n_1}(x)|_{x=4} = \partial_x G_{p_2,q_2}^{m_2,n_2}(x)|_{x=4}$. However, such separation was inadequate, mainly because there is not indication that a mechanism could produce only small or large intensities. Then, we looked for distributions that did not have a truncated domain, although the idea of the statistical mixture persisted.

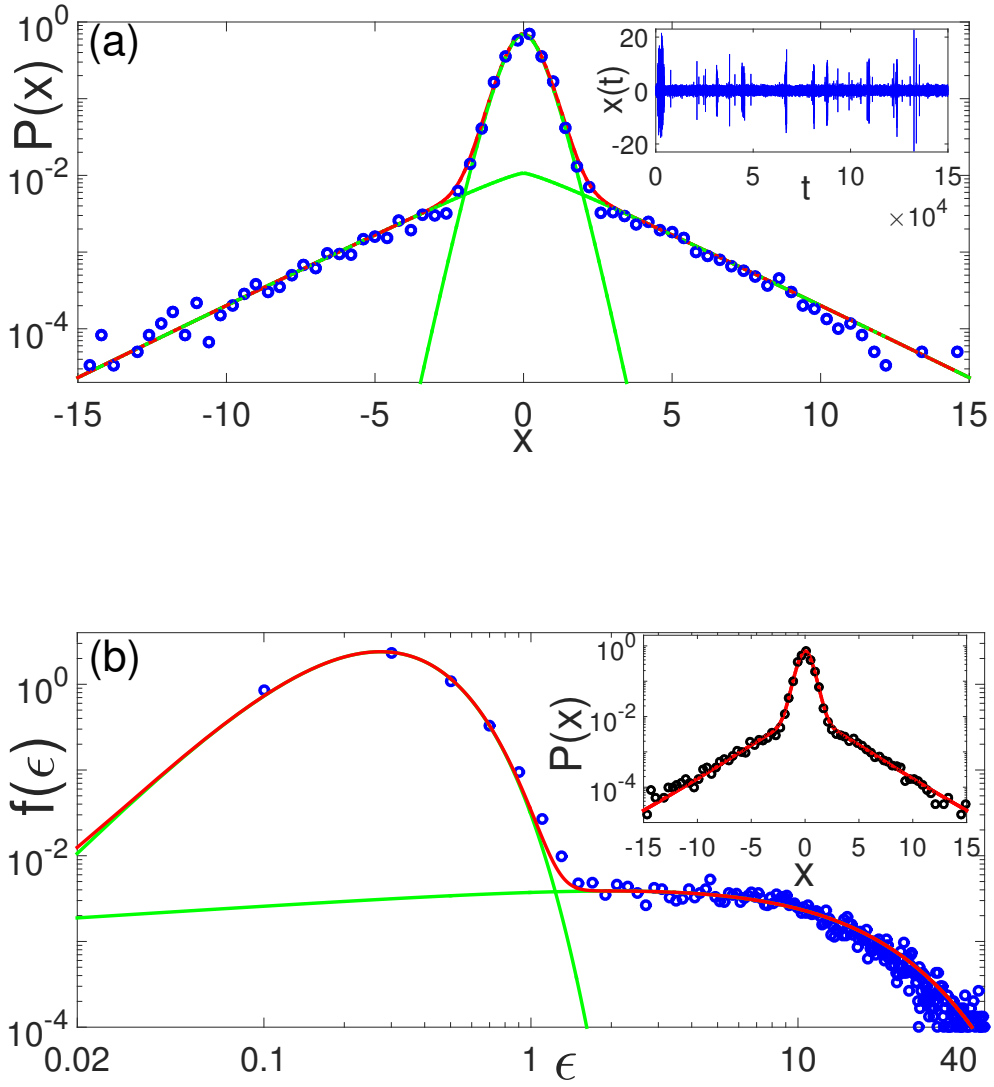

Figure 5.6: Statistical mixture of intensity increments in Er-RFL and turbulent behavior near the threshold. (a) Semi-log plot of the distribution of experimental intensity increments x at $P/P_{th} = 0.99$ (dots) and model prediction for the statistical mixture (solid red line). The mixture's K-distribution individual components are shown in dashed green lines. Inset shows the corresponding time series. A single time scale ($N = 1$), besides the largest macroscopic one, characterizes the turbulent behavior of the intensity fluctuations dynamics in Er-RFL near the threshold. (b) Log-log histogram of the variance series $\epsilon(t)$ (dots) and model prediction for the statistical mixture (solid red line), with same parameters as in (a). The mixture's individual components are shown in dashed green lines. Inset displays the compounding of $\epsilon(t)$ with a Gaussian (solid red line) and the experimental distribution (black dots).

An alternative was to make a filter for background distribution ε (see figure 5.6.b), with a cutoff in $\varepsilon = 1$, for which we discarded the data between $1 < \varepsilon < 3$, corresponding to the transition region between the two types of curvature. With these two series we performed independent fits for small ($\varepsilon \leq 1$) and large ($\varepsilon \geq 3$) events. Using least squares we obtained for the two cases an excellent correspondence with gamma distributions

$$f(\varepsilon) = \frac{\beta^{\beta}}{\varepsilon_0^{\beta}\gamma(\beta)}\varepsilon^{(\beta-1)}\exp\left(-\frac{\beta\varepsilon}{\varepsilon_0}\right), \tag{5.4}$$

with parameters $\beta = 4.21$, $\varepsilon_0 = 0.36$, and $\beta' = 1.2$, $\varepsilon_0' = 12.0$. To corroborate this possibility we performed a test in which we generated computationally random numbers that satisfy (5.4) with the parameters stipulated above in a proportion similar to the original series. The goal was to add two series with a total of 1×10^6 data, so was tried with a percentage of 85% to $f_{N=1}(\varepsilon|\beta, \varepsilon_0)$, and 15% to $f_{N=1}(\varepsilon|\beta', \varepsilon_0')$. Comparing the histogram of the statistical mixture with that of figure (5.6.b), it became apparent that they were close but not the same, so we attempted various weights p and $(1-p)$, to obtain two almost indistinguishable histograms using $p = 0.94$ of data associated with $f_{N=1}(\varepsilon|\beta, \varepsilon_0)$ and the remaining $(1 - p = 0.06)$ associate to $f_{N=1}(\varepsilon|\beta', \varepsilon_0')$. After this we compared the auxiliary series histogram directly with the analytic function

$$f_1(\varepsilon_1) = pf_1(\beta, \varepsilon_0; \varepsilon_1) + (1-p)f_1(\beta', \varepsilon_0'; \varepsilon_1). \tag{5.5}$$

This led to the red curve that fits the background of figure (5.6.b), while the green curves correspond to the components of the right-hand side of equation (5.5). Then, from H-theory, one deduces that the signal must correspond to the superposition integral

$$P_1(x) = \frac{1}{\sqrt{2\pi}}\int_0^{\infty}\exp\left(-\frac{x^2}{2\varepsilon_1}\right)\varepsilon_1^{-1/2}f_1(\varepsilon_1)d\varepsilon_1, \tag{5.6}$$

which produces a mixture of K-distributions of the type

$$P_1(x) = pP_1(\beta, \varepsilon_0; x) + (1-p)P_1(\beta', \varepsilon_0'; x), \tag{5.7}$$

with the same parameters used for the background (eq.(5.5)). This description reaffirms the validity of the model in the sense that nonlinearity and disorder in complex systems are manifested as universal features in the PDFs associated with its spectra. Simultaneously, it opens the possibility to several fundamental questions. For instance: what are the types of mechanisms that generate the statistical mixture in this system? For now, we speculated that the internal structure of the spectrum causing the statistical mixture is due to the spontaneous and stimulated emission composition that generates a correlated spectrum of output intensities.

5.4.2 $P(x)$ *above the threshold*

Finally, we shall make the statistical analysis the series $x(t)$ above the laser emission threshold ($P/P_{th} = 2.92$). To characterize the signal's PDF we have used the usual scheme. First, via the variance estimator we determined the background series, in this case, the window size that generated the best performance was $M = 22$, as shown in the inset of figure (5.7.b.)

At this point, it should be noted an important subtlety. Since the signal histogram (figure (5.7.a)) apparently fits well a K-distribution with parameter $\beta \sim 1$, there are two details that such description does not take into account: (i) the numerical integral with the background series in the vicinity of origin is a smooth curve, whereas the K-distribution generates a peak, (ii) using a K-distribution to fit the signal immediately assigns a Gamma distribution to the background, and that is the main flaw, since the background's histogram (figure 5.7.b.) does not fit this type of distribution. This is because about $\varepsilon \sim 10^{-1}$ the histogram's bins change their increasing tendency towards a soft decreasing behavior, then around $\varepsilon \sim 2$ the histogram changes its curvature again to go quickly towards zero[4]. In contrast, as have been shown in the second chapter, a gamma function or multiple coupled scales of them (see figure 2.4) only has one change in their curvature. Therefore, we intuitively knew that there was the possibility of having

[4]the previous description have been seen from the log-log scale

a background distribution resulting from the statistical mixture.

To consistently determine the assumption of a statistical mixture, it was necessary to do several tests, in which it was established that with $N = 6$, and a provisional combination of parameters was obtained an excellent joint fit for background and signal. Remembering that the number of scales in the background corresponds to the superposition integral

$$f_N(\varepsilon_N) = \int d\varepsilon_{N-1} \ldots \int d\varepsilon_1 f(\varepsilon_N|\varepsilon_{N-1}) \ldots f(\varepsilon_1|\varepsilon_0), \tag{5.8}$$

where $f(\varepsilon_i|\varepsilon_{i-1})$ is the conditioned Gamma distribution, so that when performing the integral (5.8) the joint distribution is obtained

$$f_N(\varepsilon_N) = \frac{\omega}{\varepsilon_0 \Gamma(\beta)} G_{0,N}^{N,0}\left(\begin{array}{c} - \\ \beta - \mathbf{1} \end{array} \middle| \frac{\omega \varepsilon_N}{\varepsilon_0} \right), \tag{5.9}$$

in which $\omega = \prod_{j=1}^{N} \beta_j$, and it has been introduced above the vector notation $\beta \equiv (\beta_1, \ldots, \beta_N)$ and $\Gamma(\mathbf{a}) \equiv \prod_{j=1}^{N} \Gamma(a_j)$.

The compounding integral for the signal distribution can be written as

$$P_N(x) = \frac{1}{\sqrt{2\pi}} \int_0^\infty \exp\left(-\frac{x^2}{2\varepsilon_N}\right) \varepsilon_N^{-1/2} f_N(\varepsilon_N) d\varepsilon_1, \tag{5.10}$$

where $f_N(\varepsilon_N)$ is given by (5.9). The integral (5.10) can also be evaluated using Mellin transforms, yielding

$$P_N(x) = \frac{\omega^{1/2}}{\sqrt{2\pi\varepsilon_0}\Gamma(\beta)} G_{0,N+1}^{N+1,0}\left(\begin{array}{c} - \\ \beta - \mathbf{1/2}, 0 \end{array} \middle| \frac{\omega x^2}{2\varepsilon_0} \right). \tag{5.11}$$

Therefore, using equations (5.9) and (5.11) with $N = 6$ I have determined the best parameters β, ϵ_0 and β', ϵ_0', besides the p weight value, via the statistical mixture of background distributions

$$f_6(\varepsilon_6) = p f_6(\beta, \varepsilon_0; \varepsilon_6) + (1-p) f_6(\beta', \varepsilon_0'; \varepsilon_6), \tag{5.12}$$

and signal, of the stretched exponential class

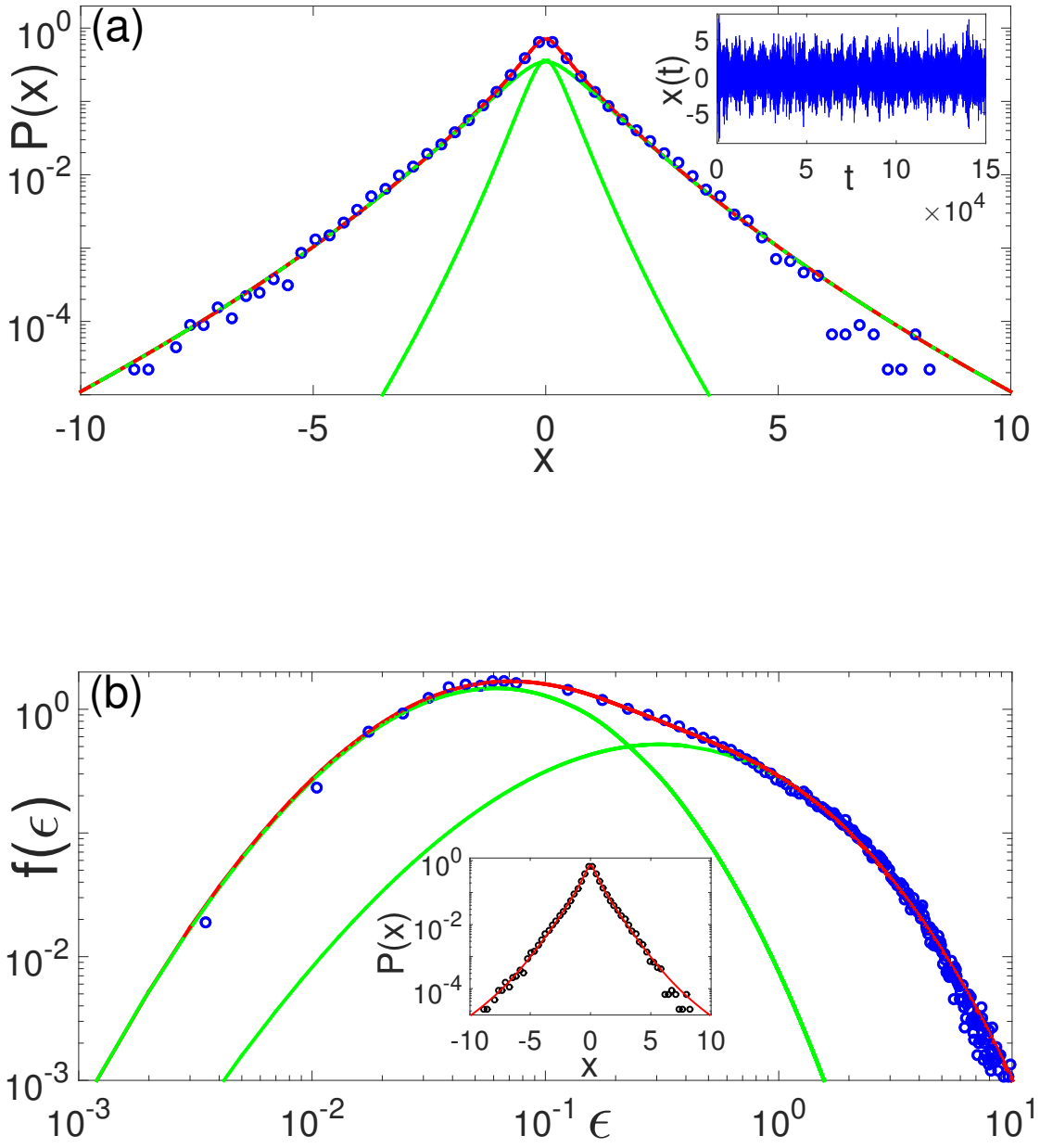

Figure 5.7: Statistical mixture of intensity increments in Er-RFL and multiscale turbulent cascade behavior above threshold. Description as in Fig. 5.6, but for the regime well above threshold, at $P/P_{th} = 2.92$. The expected raise in the number of relevant time scales upon increasing the excitation power, expressed in the statistical mixture of Meijer G-distributions with $N = 6$, is consistent with the multiscale turbulent cascade behavior of the intensity fluctuations dynamics in Er-RFL above threshold.

$$P_6(x) = pP_6(\beta, \varepsilon_0; x) + (1-p)P_6(\beta', \varepsilon_0'; x). \tag{5.13}$$

The obtained values were $p = 0.3$, $\beta = 8.3$, $\epsilon_0 = 0.19$, $\beta' = 6.5$ and $\varepsilon_0' = 1.3$. The statistical mixture was plotted as a red line in figure (5.7), while its components have been graphed in green. This statistical mixture allowed fine-tuning all regions (understood as near and far from the origin of the coordinate system) of the signal and background histograms.

5.5 Conclusions

In conclusion, we reported on the first observation of statistical signatures of turbulent emission in a cw-pumped one-dimensional RFL, with customized random Bragg grating scatterers. The distribution of intensity increments exhibits three qualitatively different forms as the excitation power is increased: it is Gaussian below threshold, it behaves as a statistical mixture of K-distributions near the threshold, and it is well described by a mixture of Meijer G-distributions with stretched exponential tails above threshold. A recently introduced hierarchical stochastic model, consistent with Kolmogorov's theory of turbulence, was used to interpret the experimental data (Roa-González *et al.* (2017)).

6 Ballistic cavities I

We studied the eigenvalue spectra of flat and curved ballistic cavities with mixed dynamics, where regular and chaotic behaviors coexist. The cavities considered have a shape control parameter driving a crossover from integrable to fully chaotic regimes. The cavities' eigenvalue spectra were obtained numerically using discrete exterior calculus. This technique allows a topology consistent implementation of the Laplace operator on a triangular mesh approximation of the system's surface. We propose a characterization of the eigenvalue spectrum based on three statistical parameters: (i) the Kullback Leibler distance δ_{LK} between the nearest neighbor spacing distribution of the spectrum and the universal Wigner-Dyson distribution, (ii) the burstiness parameter B, and (iii) the spectral exponent α in the tail of the power spectrum density $s(f) \sim 1/f^{\alpha}$. Results for flat billiards are consistent with previous works of the recent literature (Gómez *et al.* (2005)). For curved billiards, we found that by varying its curvature it is possible to induce a crossover from the integrable to the chaotic regimes. All results are shown in a δ_{LK} Vs α, and B Vs α, diagrams in an attempt to determine whether the crossover regimes are themselves new universality classes.

6.1 Introduction

Eigenvalues and eigenvectors of quantum billiards have been studied both experimentally using flat superconducting microwave resonators (Dietz and Richter (2015); Richter (1999); Graf *et al.* (1992)), and theoretically through various types of computational implementations and also analytically via solutions of integrable systems or via time independent perturbation theory within the limits established by Kolmogorov Arnold Moser

(KAM) theory (Li *et al.* (1998); Barnett and Betcke (2007); Heinz and Schreiber. (2002); Farantos (2014)). Most of these procedures aims at a statistical characterization of the cavities' eigenvalues and eigenvectors. From these studies it has been established that the statistical properties depend crucially on the shape of the cavity. For instance, the nearest neighbor spacing distributions (NNSD) of the eigenvalue spectra satisfies an exponential Poisson law for integrable systems, such as cavities with the shape of a circular disk, and a Wigner-Dyson (WD) type distribution for chaotic systems, such as a cavities bounded by a cardioid. Another example of a robust statistical signature of the cavities underlying dynamics is the power spectrum of the fluctuating part of the level spacing sequence, interpreted as a "time series". Integrable systems exhibit $1/f^2$ noise in the power spectrum, whereas chaotic systems are characterized by $1/f$ noise (Rangarajan and Ding (2000); Faleiro *et al.* (2004)). The robustness of these statistical signatures led to an essentially complete classification of chaotic and integrable systems based on the presence or absence of certain discrete symmetries, such as time-reversal and spin rotation.

Systems with mixed dynamics are however much more common and less understood. Their spectra have been studied, for instance, by varying the shape of billiards such that a smooth crossover between integrable and fully chaotic behaviours takes place by means of a simple control parameter. It has been found that the NNSD makes a transition from a Poisson to a Wigner Dyson distribution and that the corresponding power spectrum shows $1/f^{\alpha}$ noise, with $1 \leq \alpha \leq 2$ (Gómez *et al.* (2005)).

We want to establish a quantitative relation between the control parameter, which guides the transition from regular to chaotic, with the value of α spectral cofficient, and in turn determine a measure of the Kullback Leibler divergence of the NNSD associated with each value of the control parameter with respect to the Wigner Dyson distribution. The motivation for this characterization comes from the idea of trying to establish the existence of intermediate universality classes, for which there may not be enough to find the two measures described above. However, they are the ones that have shown more

susceptibility to change the value of the control parameter.

To fulfill this purpose, we have computationally generated three geometries with mixed dynamics. The first corresponds to Limaçon or Robnik-billiard described by the area under the curve of the conformal map $w = z + \lambda z^2$ (Prosen and Robnik. (1993); Prosen and Robnik (1994)), in which the control parameter λ ranges from $\lambda = 0$ the integrable-regular basis to chaotic regimen for $0.4 \leq \lambda \leq 0.5$. The second billiard corresponds to the mushroom billiard with triangular stem (Dietz *et al.* (2007); Abul-Magd *et al.* (2008)) (figure (6.2)), where the control parameter is the ratio r/R, being r the length of the stem, whereas R corresponds to the billiard radius, for this kind of geometry, the characterization has been done for the ratios $r/R = \left(\frac{1}{8}, \frac{1}{6}, \frac{1}{5}, \frac{1}{4}, \frac{3}{10}, \frac{1}{3}, \frac{2}{3}, \frac{7}{10}\right)$. Finally, we have worked with a circular billiard on which there has been applied a strain function $A\cos^2(\theta(x))$ generating the curved billiard of figure (6.11). In this case, the strain amplitude A is the control parameter.

Each billiard has been modeled through the stationary Schrödinger equation for a free particle, with Dirichlet boundary conditions. To construct the associated Laplacian and subsequent collection of eigenvalue energy spectrum, we have chosen discrete exterior calculus (Crane (2005); Desbrun *et al.* (2005)). This is a powerful and versatile computational method based on the idea of discrete operators of differential forms. We also used the Betti numbers of graph theory and its connectivity with simplicial De Rham complex (Frankel (1997)), which will be described in a practical and detailed form in the next section of this chapter. DEC is already used in graphical simulations (de Goes *et al.* (2015); Mohameda *et al.* (2016)) and animation (de Goes *et al.* (2016)) with great success. Applied to ballistic cavities DEC will provide the opportunity to study not only flat billiards but also allow the inclusion of other geometric properties, such as curvature. This has been implemented in the third type of billiard with mixed dynamics, as a result of the direct connection between the mean curvature and Laplace-Beltrami operator (Desbrun *et al.* (1999); Botsch *et al.* (2010); Lévy (2006)). DEC also offers the possibility of build-

ing other differential operators, such as the Dirac-Kahler operator (Eftimiades (2014)), or multi-harmonic operators (Panozzo and Jacobson (2014)). They will be further developed in future works.

There are some algorithms in the literature that use DEC (Bell and Hirani (2012); Eftimiades (2014); Panozzo and Jacobson (2014)). However, we have chosen to work based on two Matlab toolboxes Distmesh, (Persson and Strang (2004)) for generating geometries with mesh, and Toolbox-Graph (Peyré (2013)) to implement differential discrete forms operators. The combination of these toolboxes, together with independent work, involving the explicit construction of geometries and curvature, added to the implementation and verification of boundary conditions. Computational comparisons for flat billiards with normalized graph-theory and cotangent Laplace-Beltrami for the eigenvalues spectrum have been made (Peyré (2008)).

The eigenvalues were represented as a time series to which a local unfolding method is applied to obtain the NNSD distribution (Brody *et al.* (1981)). From this unfolding spectrum have been generated the δ_n-statistic (Gómez *et al.* (2005)). After that, using the iterative method of signal analysis known as Empirical Mode Decomposition the trend of δ_n-series have been removed (Huang *et al.* (1998); Morales *et al.* (2011)). On the new detrended series δ'_n, we applied the Fourier transform to obtain the mean power spectrum $< S(f) > \sim 1/f^{\alpha}$ (Gómez *et al.* (2005)), whose exponent is used as a measure to characterize each billiard.

6.2 Discrete exterior calculus DEC

A differential form or p-form corresponds to a covariant skew- symmetric tensor of rank p in the language introduced by Grassmann algebra (Frankel (1997)). The vector space of covariant p^{th} rank tensor will be denoted by $E^* \otimes E^* \otimes ... \otimes E^* = \otimes^p E^*$. Then if D is the total dimension of space, it is possible to define several operations over forms. For example: wedge product ($\wedge$), exterior differentiation (d), Hodge star ($\star$), codifferential (δ), sharp ($\#$) and flat ($\flat$) operator, those actions over the $p-$forms will be presented in

Table 6.1.

$\wedge$	$[(p)-form]\wedge[(q)-form]\rightarrow(p+q)-form;\,(p+q)\leq D$
d	$d:[(p)-form]\rightarrow(p+1)-form$
$\star$	$\star:[(p)-form]\rightarrow(D-p)-form$
$\delta:=d\star$	$\delta:[(p)-form]\rightarrow(p-1)-form$
$\#,\flat$	$\#,\flat:[(1)-form]\rightleftharpoons$ vector

Table 6.1: Applications of operators over $p-$forms in exterior calculus, where, $\wedge$ is the wedge or exterior product, d is the exterior differential, $\star$ is the Hodge star operator, δ is the codifferential, $\#$ Sharp operator, $\flat$ flat operator (For more details see reference (Frankel (1997))). D corresponds to the space dimension

In the continuous differential forms, the Laplace operator in D-dimensions is $\triangle f = (d+d\star)^2 f$, where g corresponds to space's metric. Now applied over a 0-form, this operator is reduced to equations (6.1-6.4) (Ivancevic (2011)).

$$\begin{aligned}
\triangle_g f = \star d\star df &= \star d\star(\partial_i f du^i) && (6.1)\\
&= \star d(\sqrt{|\det g|}\partial^i f d^{D-1}u_i) && (6.2)\\
&= \star[\partial_i(\sqrt{|\det g|})(\partial^i f)d^D u] && (6.3)\\
&= \frac{1}{\sqrt{|\det g|}}\partial_i(\sqrt{|\det g|}\partial^i f), && (6.4)
\end{aligned}$$

where $\partial^i = g^{ij}\partial_j$. This procedure reproduces the usual form of Laplace operator given by equation (6.5)

$$\triangle_g = -\frac{1}{\sqrt{|\det g|}}\sum_{i,j=1}^{n}\frac{\partial}{\partial u_i}\left(g^{ij}\sqrt{|\det g|}\frac{\partial}{\partial u_j}\right). \qquad (6.5)$$

On the other hand, our objective is not focused on the continuous version of differential forms, but on its discrete version (DEC), which is part of the algebraic topology and will be described by simplicial De Rham complex C_i, where $i = 1, ..., D-1$. This is the generic term to describe the mesh element of D-dimensions (Crane (2005); Frankel (1997);

Desbrun *et al.* (2008)). Each element of the mesh is named simplex, and computationally the largest dimension is $D = 3$, which corresponds to the so-called tets or tetrahedra.

In general, each geometry is built through a mesh that forms a set of vertices $\{v\}$, edges $\{e\}$, faces $\{f\}$ and tets $\{T\}$. The connectivity between tets and faces is determined by a 2-simplex C_2. Similarly, connectivity between faces and edges is made by a 1-simplex C_1. Finally, connectivity between edges and vertices is a 0-simplex C_0 (Desbrun *et al.* (2008)). DEC operators perform an hierarchical step from a C_p simplex to $C_{p\pm1}$, where the increase or decrease the range of the simplex depends on whether we are acting on the vector basis (dual basis of the simplex C_p) named chains $\frac{\partial}{\partial x^1}...\frac{\partial}{\partial x^n}$; or on $1-form$ basis $dx^1...dx^n$ for C^p simplex named cochains (Desbrun *et al.* (2008); de Goes *et al.* (2015)). The two types of basis satisfy the orthonormality relations $dx^i\left(\frac{\partial}{\partial x^j}\right) = \delta^i_j$. In the discrete case, the exterior differentiation d is the coboundary operator acting on cochains, which implies that d^p operating on a simplex C^p returns a C^{p+1} simplex, or simply $0 \leftarrow C^2 \overset{d^1}{\leftarrow} C^1 \overset{d^0}{\leftarrow} C^0 \leftarrow 0$. In contrast, the codifferential operator δ is the boundary operator ∂ acting on chains, so that ∂^p acting over simplex in dual basis C_p returns a C_{p-1}. The schematic action boundary operator is $0 \rightarrow C_2 \overset{\partial^2}{\rightarrow} C_1 \overset{\partial^1}{\rightarrow} C_0 \rightarrow 0$.

The simplex set depends on the way of implementing the mesh. It inevitably will influence the outcome of any procedure. One should not build a triangular mesh with obtuse angles, due to the occurrence of inconsistencies in circumcenters or barycenter positions in the 1-ring mesh or on dual cells, which may be in a position over the boundary of the geometry, a factor that contributes to errors in the calculation. There are three traditional ways of construction of cells (Botsch *et al.* (2010)) 1. The barycentric cell that connects the triangle barycenters with the edge midpoints. 2. Voronoi cell that replaces the triangle barycenters with triangle circumcenters. 3. Mixed Voronoi cells that replaces the circumcenter for obtuse triangles with the midpoint of the edge opposing the center vertex (v).

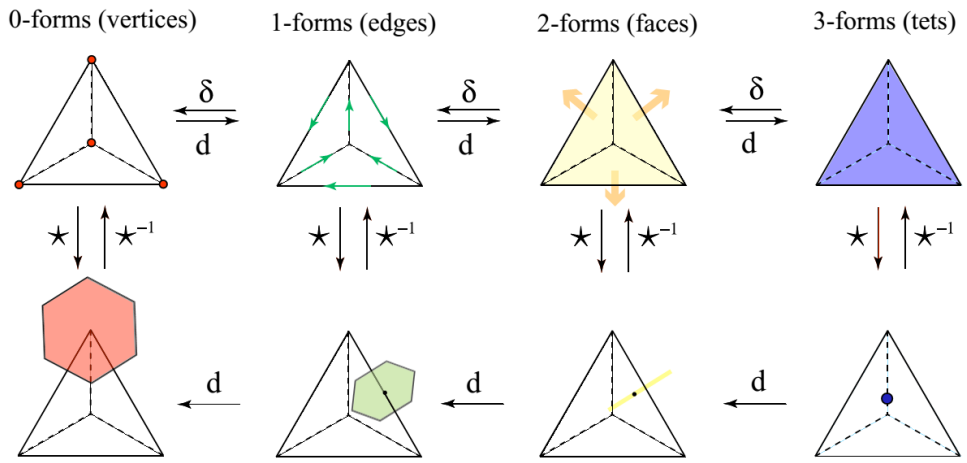

Figure 6.1: This figure was taken from the reference (Desbrun *et al.* (2008)) and presents schematically (i) the discrete exterior derivative, (ii) discrete codifferential operator, and (iii) discrete Hodge Star, via connections between vertices, sides, faces and tets.

For a robust mesh, we have worked with Distmesh (Persson and Strang (2004); Persson (2004)), a Matlab toolbox designed through an algorithm that combines a physical principle of force equilibrium in a truss structure with a mathematical representation of the geometry using signed distance functions. Through Distmesh we made the meshes for each of the geometries used in this chapter. The implementation can be explained using the illustrative example (see figure 6.2).

We have taken two triangles with a common edge, whose vertices are the set $\{X_i\}$, while its edges correspond to lowercase (a, b, c, d, e) and their faces Roman numerals I and II. On that configuration we defined the coboundary operator d^0 (Desbrun *et al.* (2005, 2008)), which for practical purposes is an ordered matrix of vertices (rows) with sides (columns), on each face (I, II) defined a direction of "movement", so that we have a binary assignment, zero or one depending on whether or not connection between a vertex and a edges. The $sign(\pm 1)$ is positive when it reaches the vertex and negative when out of it. Also we defined the boundary operator ∂_1, as the transpose of coboundary

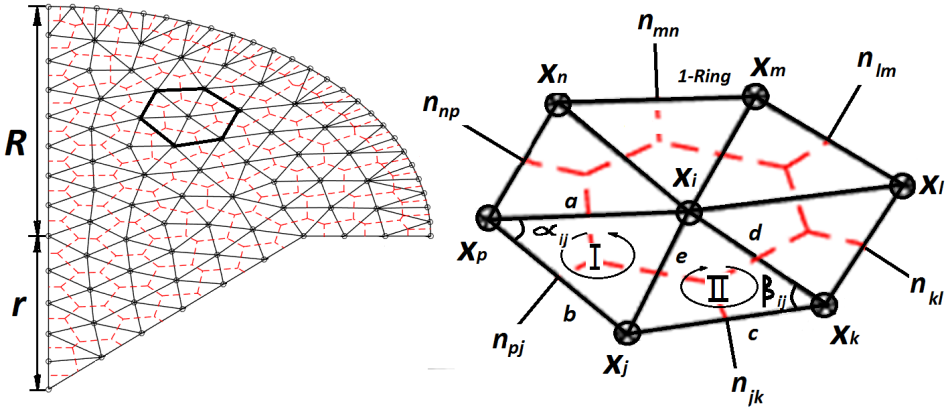

Figure 6.2: On the left (i) in black: Delaunay triangular mesh that excludes the formation of obtuse angles. (ii) In red: barycentric hexagonal dual mesh applied to Mushroom billiard with triangular stem. On the right we show a zoom of the bold hexagon of the left side, where the common vertex for the six triangles is called X_i. This vertex is taken as a reference to construct the Laplace operator whose procedure have been detailed in Appendix E. So, in this approach to each vertex is associated a primary hexagonal cell that allows the construction of the differential operator.

operator $\partial^1 = (d^0)^T$. The non normalized Laplace operator to the 0-form corresponds to the noncommutative product $L = \partial^1 d^0$ equation (6.6). This formulation can be connected directly with graph laplacian theory, which defines an degree diagonal matrix D, which counts the number of connections to each vertex to the edges, and an adjacency matrix A that through a binary assignment (Peyré (2008)) describes whether a particular vertex is directly connected to another on one edge. In graph approach, non-normalized laplacian is defined as $L = D - A$, equation (6.7). Performing the operations in equations (6.6) and (6.7), it becomes clear that the two forms are equivalent and produce the same type of laplacian equation (6.8).

$$L = \partial^1 d^0 = \begin{pmatrix} -1 & 0 & 0 & -1 & 1 \\ 1 & -1 & 0 & 0 & 0 \\ 0 & 1 & 1 & 0 & -1 \\ 0 & 0 & -1 & 1 & 0 \end{pmatrix} \begin{pmatrix} -1 & 1 & 0 & 0 \\ 0 & -1 & 1 & 0 \\ 0 & 0 & 1 & -1 \\ -1 & 0 & 0 & 1 \\ 1 & 0 & -1 & 0 \end{pmatrix} \tag{6.6}$$

$$L = \underbrace{\begin{pmatrix} 3 & 0 & 0 & 0 \\ 0 & 2 & 0 & 0 \\ 0 & 0 & 3 & 0 \\ 0 & 0 & 0 & 2 \end{pmatrix}}_{D} - \underbrace{\begin{pmatrix} 0 & 1 & 1 & 1 \\ 1 & 0 & 1 & 0 \\ 1 & 1 & 0 & 1 \\ 1 & 0 & 1 & 0 \end{pmatrix}}_{A} \tag{6.7}$$

$$L = \begin{pmatrix} 3 & -1 & -1 & -1 \\ -1 & 2 & -1 & 0 \\ -1 & -1 & 3 & -1 \\ -1 & 0 & -1 & 2 \end{pmatrix} \tag{6.8}$$

To normalize the Laplacian $L \to \bar{L}$, in the graph approach it is sufficient to obtain the square root of the inverse matrix degree $\bar{L} = D^{-1/2}LD^{-1/2}$. The weights are called combinatorial (Peyré (2008)), depending only on the topology (vertex, edge). In general this local normalized operator can be written as $\bar{L} = D^{-1/2}(D-W)D^{-1/2}$, where W is the weight matrix with elements ω_{ij} and $D = diag_i(d_i)$, related to weight functions through $d_i = \sum_j \omega_{ij}$. We have used conformal weights $\omega_{ij} = \cot(\alpha_{ij}) + cot(\beta_{ij})$, which generate the operator known as Laplace-Beltrami, as a generalization of the Laplacian from flat spaces.

$$\triangle(f_i) := \frac{1}{2A_i} \sum_{x_j \in N_1(x_i)} (\cot \alpha_{i,j} + \cot \beta_{i,j}) (f_j - f_i), \tag{6.9}$$

where α_{ij} and β_{ij} are the two angles opposite to the $e-$edge in the two triangles figure (6.2), and $N_1(i)$ is the set of 1-ring neighbor vertices of vertex X_i (Desbrun *et al.* (2008)). Such weights are called conformal because they preserve angles mesh, and they minimize deformation in the sense that they minimize the Dirichlet energy (Botsch *et al.* (2010)). It relates directly to the integral of mean curvature equation (6.10) over mixed Voronoi cell A_M, for each triangle of the mesh (Desbrun *et al.* (1999); Crane (2005)). The triangle itself defines the local surface metric

$$\int_{A_M} K(f) dA = \frac{1}{2} \sum_{x_j \in N_1(x_i)} (\cot \alpha_{i,j} + \cot \beta_{i,j}) (f_j - f_i). \tag{6.10}$$

Computational methods for obtaining the weights of the laplace operator can be found in reference (Peyré (2008)) and detailed implementation in *toolbox_graph* for Matlab (Peyré (2013)). It has been the computational tool used to obtain the spectrum with more than twenty thousand levels for the Laplacian with conformal-weights in each of the geometries described in the following sections.

6.3 Statistics for billiards with mixed dynamics

We must calibrate the unfolding method of the energy spectrum obtained through the eigenvalues of the sparse-laplacian matrix with conformal weights. We wanted to consider two geometries extensively documented in the literature. The first geometry corresponds to a quarter circle (regular-integrable system), while the second corresponds a quarter Bunimovich billiard (chaotic system) (see figure 6.3). Over each mesh geometry, we have been applied Dirichlet boundary conditions.

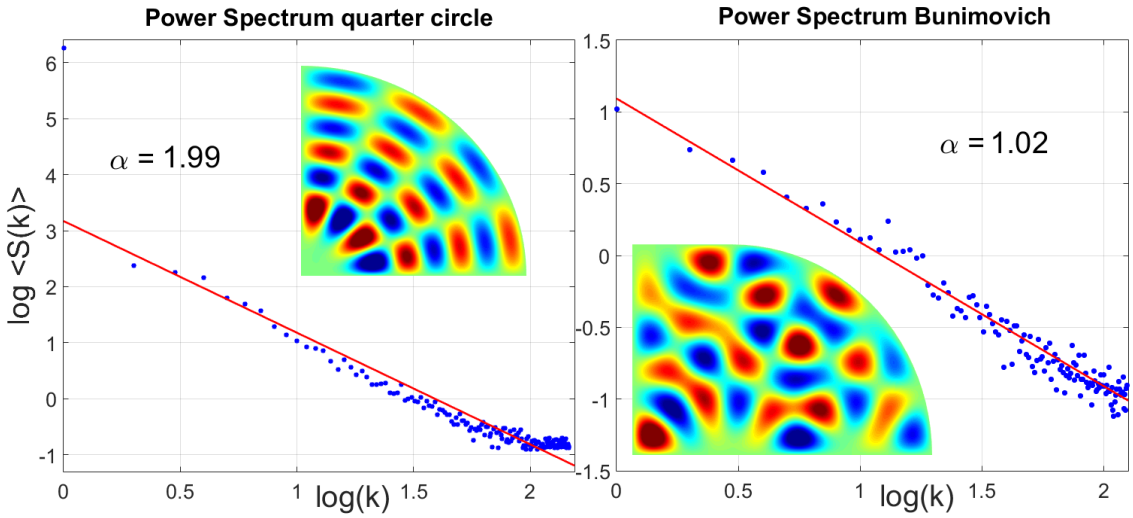

Figure 6.3: On the left: the quarter of circumference known as regular billiard. On the right: chaotic billiard of Bunimovich. These two geometries have been used to calibrate the procedure for obtaining the spectral exponent α, from the discrete Fourier transform series of δ'_n. In the two cases, we have averaged 25 series of 256 data. In agreement with the current literature, the power spectrum is of the form $\langle s(k) \rangle \sim k^{-\alpha}$, with exponent $\alpha = 2$ in the regular case and $\alpha = 1$ for the chaotic cavity.

The Weyl law is the usual way to unfolding billiard's eigenvalue spectrum. In this approach the spectrum with M elements is organized as $E_1 < E_2 < ... < E_i < ... < E_M$. Then, using the cumulative distribution function, defined as $CDF(E) = N(E) = \#\{n|E_n < E\}$, it is possible to decompose this CDF in two parts $N(E) = \bar{N}(E) + \tilde{N}(E)$, a trend part $\bar{N}(E)$ and fluctuating part $\tilde{N}(E)$. The trend part is established via $\bar{N}(E) = \frac{AE}{4\pi} + \frac{L\sqrt{E}}{4\pi} + C$, where A coefficient is the billiard's area and L is the billiard's perimeter (Bohigas (1991)). This method was designed for flat two-dimensional geometries. However, in this chapter, we shall describe curved billiards, as a crossover mechanism between regularity and chaos. So, we want to employ a different unfolding method (Brody *et al.* (1981)) to be able to work directly with the spectrum as a time series, thus applying signal analysis tools, which are independent of the geometric features of the systems.

After organizing the spectral data $E_1 < E_2 < ... < E_i < ... < E_M$, we have normalized the energy spectral series, dividing by the smallest eigenvalue $\lambda_1 < \lambda_2 < ... < \lambda_i < ... < \lambda_M$ $\lambda_1 = 1$ and $\lambda_i = Ei/E_1$. We have used local unfolding equation (6.11) to calculate the unfolded eigenvalues ϵ_i, a practical procedure employed in other applications (Brody *et al.* (1981); Voultsidou and Herrmann (2009)).

$$\epsilon_{i+1} = \epsilon_i + \frac{\lambda_{i+1} - \lambda_i}{D_i}, \tag{6.11}$$

where D_i in Equation (6.12) corresponds to the local mean with free parameter d.

$$D_i = \frac{1}{d} \sum_{j=i-d}^{i} (\lambda_{j+1} - \lambda_j). \tag{6.12}$$

The local unfolding aims to convert the same magnitude order the $\{\lambda_i\}$ spacing series, because if we defined directly the spacing $\Delta\lambda_i = \lambda_{i+1} - \lambda_i$, it holds that $\Delta\lambda_I \gg \Delta\lambda_J$, when the index I is close to the first eigenvalues, and the J index is close to last eigenvalues in the $\{\lambda_i\}$ series. On the other hand, if from the unfolding series $\{\epsilon_i\}$ we formed the spacing series $s_i = \epsilon_{i+1} - \epsilon_i$, with mean one $< s >= 1$, $\{s_i\}$ is scale invariant $s_I \sim s_J$. It is crucial to keep in mind that the unfolding method may lead to different statistical

characterizations as reported in (Abuelenin and Abul-Magd (2012)), and although the NNSDs appear to be invariant to the unfolding methods, other measures such as power spectrum are highly susceptible.

From the approach of quantum spectrum as a time series (Santhanam *et al.* (2006)), we have introduced the δ_n statistic defined by equation (6.13), corresponding to fluctuating part of spectrum,

$$\delta_n = \sum_{i=1}^{n}(s_i - < s >) = \epsilon_{n+1} - \epsilon_1 - n. \tag{6.13}$$

The main goal of using the δ_n statistic has been to build the mean power spectrum $< S(k) >$ (Gómez *et al.* (2005)). According to reference (Morales *et al.* (2011)) it is posibble to construct a new detrended fluctuation δ'_n, subtracting the trend $\delta'_n = \delta_n - r^{(m)}$, where $r^{(m)}$ is the m^{th} residue of iterative method Empirical Mode Decomposition (EMD) (Huang *et al.* (1998)). EMD is an adaptive method based in the Hilbert-Huang transform (Yang *et al.* (2012)). This method proposes the expansion and decomposition of the data in terms of intrinsic mode functions (IMFs) the components it outputs should separate phenomena occurring on different time scales.

The δ'_n statistic fluctuations can be used to determine the exponent of the power spectrum $S(k)$, given by

$$S(k) = \left| \frac{1}{\sqrt{M}} \sum_{n=1}^{M} \delta'_n \exp\left(\frac{-2i\pi nk}{M}\right) \right|^2. \tag{6.14}$$

Power-law behavior of $< S(k) > \sim 1/k^{\alpha}$ is only an approximation, valid without taking into account the highest frequencies of the spectrum (Gómez *et al.* (2005); Morales *et al.* (2011)).

The results obtained for the mean power spectrum were $< S(k) > \sim \frac{1}{k^{\alpha}}$, with $\alpha = 1.99$ for regular-integrable system (quarter circle billiard), and $\alpha = 1.02$ for the chaotic system (Bunimovich billiard). This test was a way to calibrate the computational method and thus make us confident to apply it to the study of billiards with mixed dynamics that will

be presented in the next section.

6.3.1 *Measures for $P(s)$ crossover*

In this section we present the Kullback-Leibler distance (KLD) δ_{LK} (Kullback and Leibler (1951)) and Burstiness parameter (Goh and Barabási (2008)). We have chosen then as measures to characterize the crossover from Poisson statistics to Wigner-Dyson of the nearest neighbor spacing distribution $P(s)$ for the three geometries: Limaçon, Mushroom, and curved billiard. By definition

$$\delta_{LK}(Cp_j) = \frac{\sum_i P_{WD} \log\left(\frac{P_{WD}}{P_{ob}(Cp_j)}\right)}{\sum_i P_{WD} \log\left(\frac{P_{WD}}{P_{ob}(Cp_{min})}\right)}, \tag{6.15}$$

which corresponds to a normalized measure that compares the distance between the $(P_{ob}(Cp_i))$ PDF associated with the spacing spectrum for each geometry with respect to the Wigner-Dyson (P_{WD}) PDF. $P_{ob}(Cp_{min})$ is the farthest PDF for each geometry from the WD. In other words, is the PDF or smallest deformation parameter value

$$P_{ob}(Cp_{min}) = \{P_{ob}(\lambda)|_0, P_{ob}(r/R)|_0, P_{ob}(A)|_{0.03}\},$$

for which the geometry is integrable or close to it.

Another way to characterize the PDF $P(s)$ for unfolded spacing spectrum s (s is an inter-event time IET) for billiards has been done by measuring the deviations from Poisson distribution by the Burstiness parameter, which is defined in the bounded range (-1,1), where $B = 1$ correspond inter-event time take place highly bursty, $B = 0$ neutral, and $B = -1$ regulate. The Burstinnes coefficient

$$B = \frac{\sigma(s) - < s >}{\sigma(s) + < s >} \tag{6.16}$$

is expressed in terms of standard deviation $\sigma(s)$ and mean $< s >$ of NNSD. For the billiards there are two references measures for B parameter. Poisson NNSD, where its Burstiness coefficient is $B_{Poi} = 0$, and Wigner-Dyson distribution, for which this value

correspond to $B_{WD} = -0.3134$. We have characterized the crossover between these two extreme values for each of the parameters $\{\lambda_j, (r/R)_j, A_j\}$ that control of the geometry.

In the next subsections we characterize each of the geometries, showing the values of the measures $\delta_{LK}(Cp_j)$, $B(Cp_j)$ and $\alpha(Cp_j)$. Using these criteria we propose a law of corresponding states.

Limaçon or Robnik Billiards

The limaçon-billiard or Robnik-billiard is a system described by the area under of the conformal map curve $w = z + \lambda z^2$ (Prosen and Robnik. (1993); Prosen and Robnik (1994)). This geometry changes from an integrable-regular for $\lambda = 0$, to an entirely chaotic cardioid billiard $\lambda = 0.5$, making a transition to $0 < \lambda < 0.5$ where limaçon-billiard has mixed dynamics. We have worked with eight λ values, which are shown in figure (6.4). The primary purpose is to characterize the transition to the chaotic regime according to table (6.2) values.

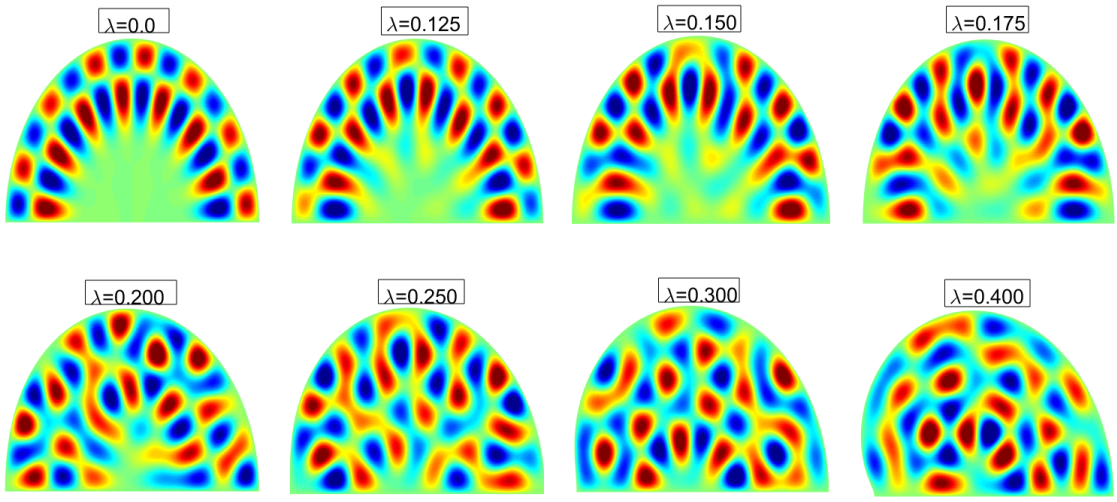

Figure 6.4: In this figure, we show the eight values of the control parameter λ over which the energy eigenvalues spectrum was determined. Here the reader can perceive the parametric dependence of a stationary function used as a reference.

λ	$\delta_{LK}(\lambda)$	$\|B(\lambda)\|$	$\alpha(\lambda) - 1$
0	1	0.0356	0.99 ± 0.07
0.125	0.6244	0.1078	0.85 ± 0.10
0.150	0.5025	0.1341	0.74 ± 0.10
0.175	0.1800	0.2154	0.62 ± 0.09
0.200	0.0287	0.2789	0.48 ± 0.07
0.250	0.0175	0.2895	0.24 ± 0.10
0.300	0.0088	0.2962	0.16 ± 0.10
0.400	0.0068	0.3056	0.03 ± 0.11

Table 6.2: Numerical values of the three statistical measures obtained via the energy spectrum associated with each control parameter (λ).

The values of the Kullback-Leibler distance were obtained from the histograms for the NNSD of figure (6.5), with bin width 0.1 in the interval of $[0.05, 4.05]$. On the other hand, the values of the Burstiness parameter were obtained through its time series, while the values of the spectral exponents have been extracted from the Fourier transform of the δ'_n-set, as shown in figure (6.6).

The $\alpha(\lambda)$ values have been approximated in the second decimal place, in agreement with value obtained in reference (Gómez *et al.* (2005)). So this geometry has been used mainly to calibrate the computational algorithms used in all stages of this description, beginning with the DEC, passing through the unfolding of the energy levels, continuing with the utilization of the EMD to obtain the $\delta-$statistic and finally take its discrete Fourier transform.

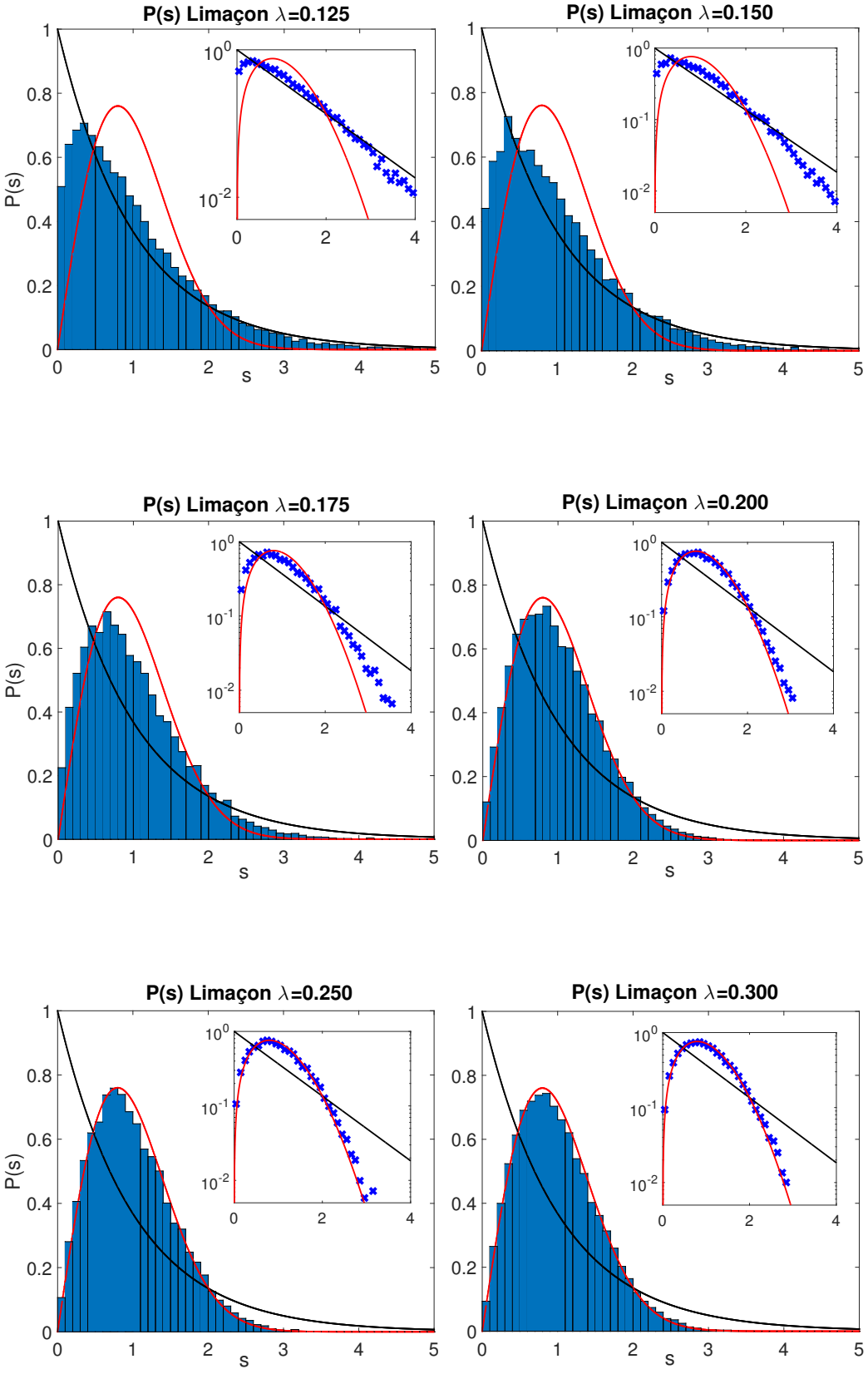

Figure 6.5: In blue: Histograms of NNSD for six of the eight parameters λ that have been used for the description of the Limaçon billard. The red line represents the Wigner-Dyson distribution, while the black line corresponds to the Poisson distribution. In the inset of each one, we have plotted the PDFs in semilogarithmic scale.

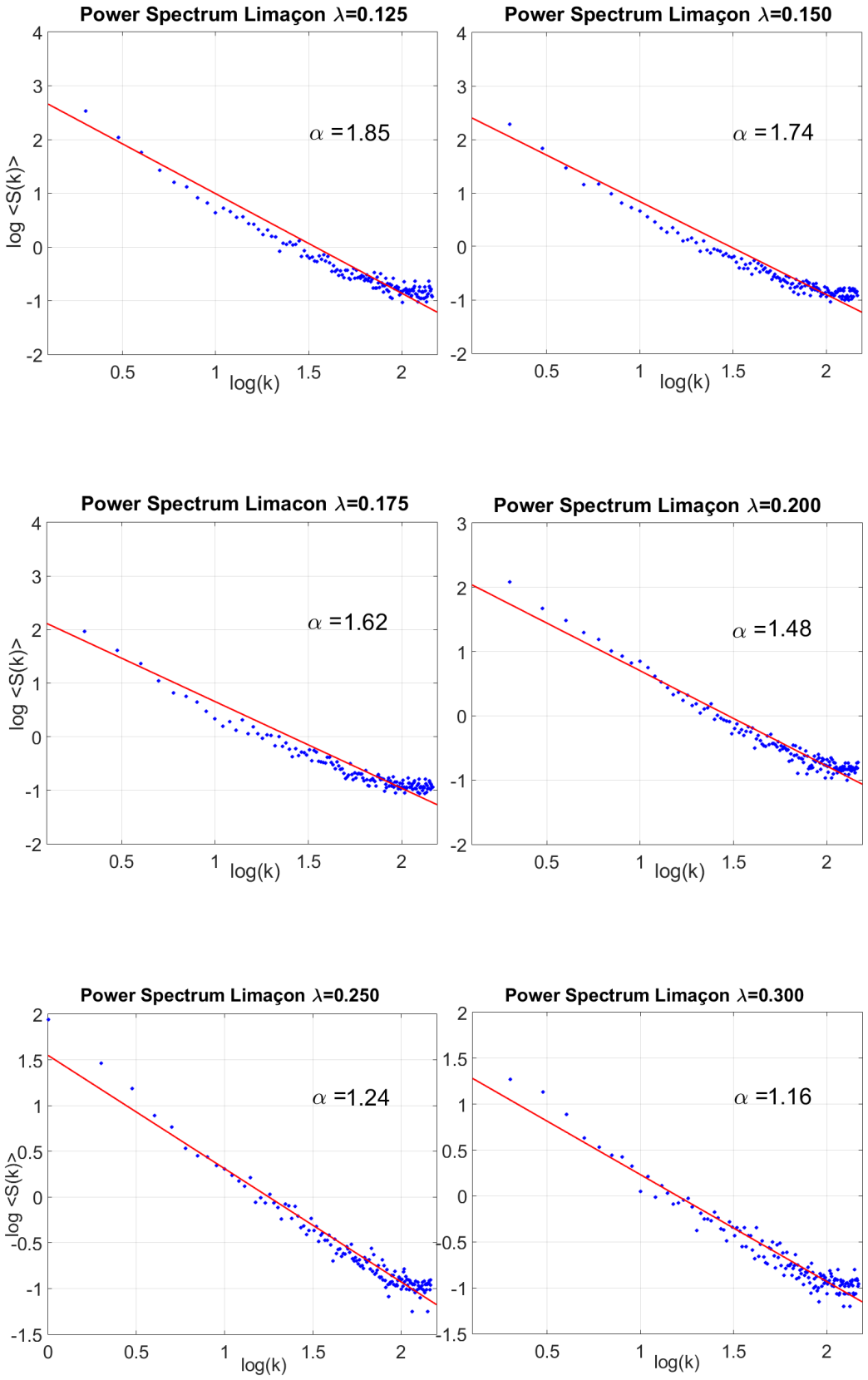

Figure 6.6: The blue dots represent the power spectrum, in six of the eight λ parameters that have been used for the description of the Limaçon billard. The red line in each subfigure represents the best linear fit made through least squares, where the slope corresponds to its α spectral exponent.

After acquiring a certain degree of experience with the characterization of Limaçon billard, we continued the investigation of DEC applied to cavities that present mixed dynamics. Therefore, we decided to describe the mushroom with triangular stem, that is a geometry with similar dynamics features to exhibited by the Limaçon.

Mushroom

This billiard, called the triangular stem mushroom, presented in figure (6.7), has been experimentally characterized as a resonant microwave cavity for the coefficients $r = 1/3$ and $r = 2/3$ in the reference (Abul-Magd *et al.* (2008)). However, this interesting paper presents a small number of energy levels, making it difficult to establish a measure of the deviation of its NNSD from the Wigner-Dyson distribution. So, we were looking for a more detailed statistical description using computational simulation through the DEC method. Starting from the regular geometry stemless ($r = 0$) for the quarter circle, we evaluated eight ratios more ($r/R = (1/8, 1/6, 1/5, 1/4, 3/10, 1/3, 2/3, 7/10)$), where r is the stem length while R is the radius of the circular part (see figure (6.2)). For each of the coefficients r/R corresponding to the control parameter, about 2.5×10^4 eigenvalues were extracted, which were sorted ascendingly and unfolded according to the previously established procedure.

Once we determined the time series for the spacing energy levels. The values of the three statistical measures $\delta_{LK}(P_{WD}|P(r/R))$, $|B(r/R)|$ and $\alpha(r/R)$ were stipulated, as shown in table 6.3.

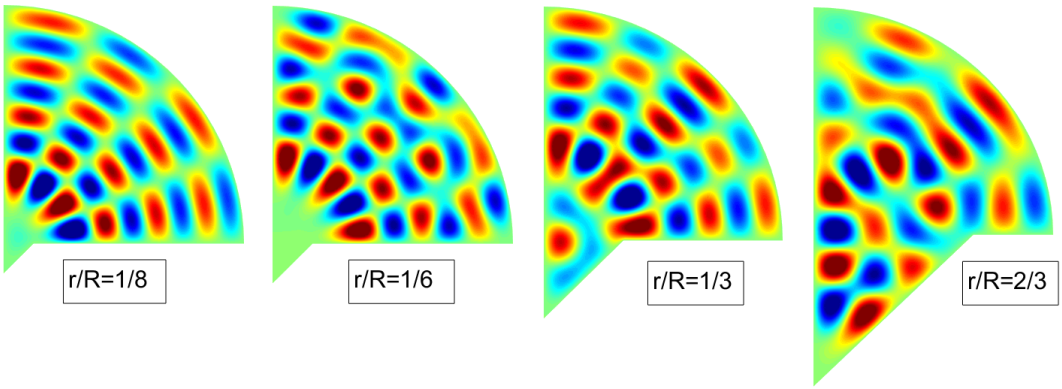

Figure 6.7: In this figure, we show the four of the nine values of the control parameter r/R over which the energy eigenvalues spectrum was determined. Here the reader can perceive the parametric dependence of a stationary function used as a reference.

r/R	$\delta_{LK}(r/R)$	$\|B(r/R)\|$	$\alpha(r/R)-1$
0	1	0.0356	0.99 ± 0.07
1/8	0.8186	0.0665	0.93 ± 0.07
1/6	0.6860	0.0967	0.82 ± 0.08
1/5	0.5980	0.1122	0.77 ± 0.08
1/4	0.3797	0.1603	0.69 ± 0.07
3/10	0.1215	0.2385	0.65 ± 0.08
1/3	0.0210	0.2839	0.47 ± 0.09
2/3	0.0132	0.2938	0.24 ± 0.10
7/10	0.0034	0.3058	0.15 ± 0.09

Table 6.3: Numerical values of the three statistical measures obtained via the energy spectrum associated with each control parameter (r/R).

In agreement with the statistical measures of the Mushroom Billard, figures 6.8, 6.9 and 6.10, shows via its nearest neighbor spacing distribution and its spectral coefficient, that is possible to reach the full chaotic regime by increasing the control parameters value.

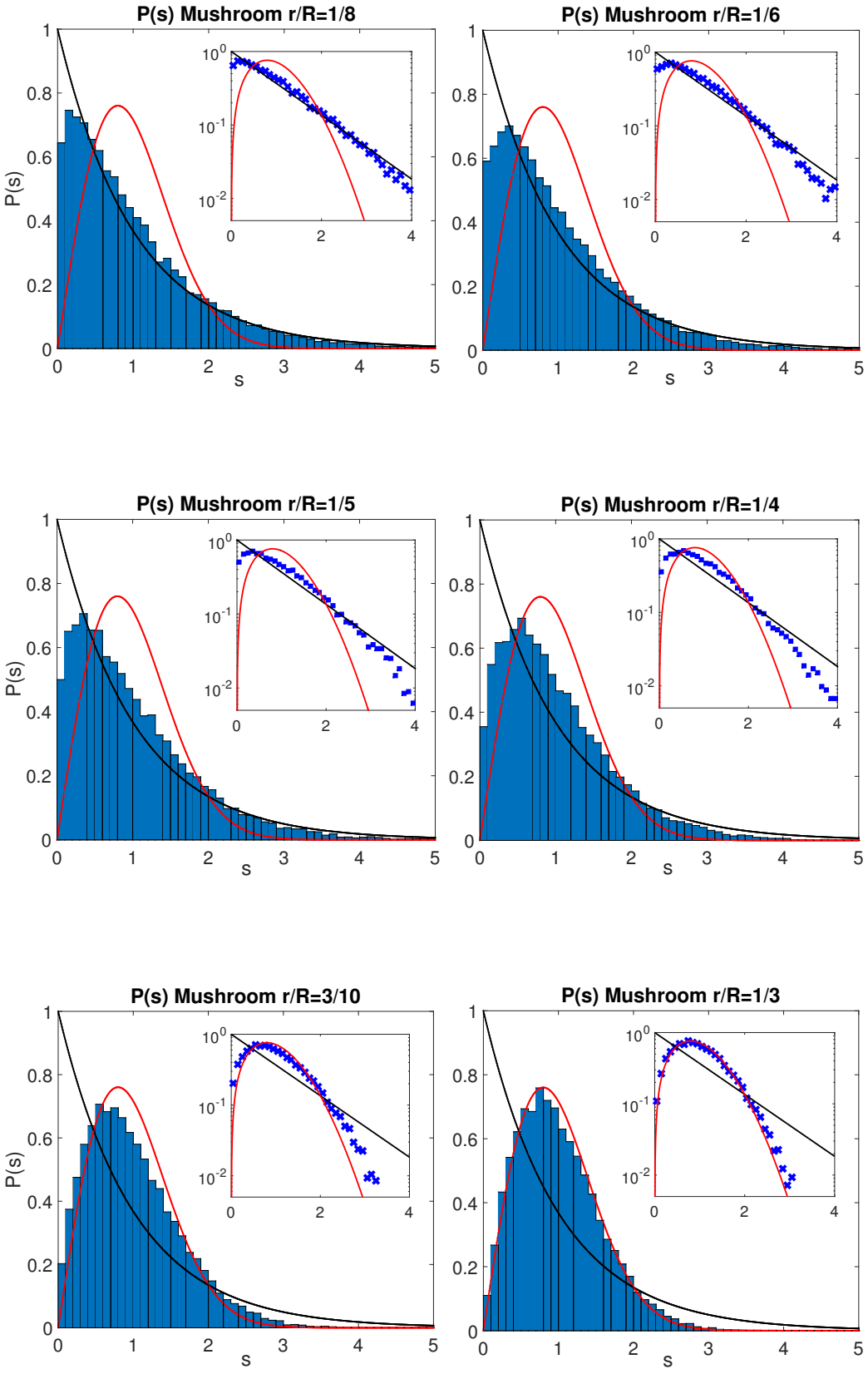

Figure 6.8: In blue: Histograms of NNSD for six of the nine parameters r/R that have been used for the description of the Mushroom billard. The red line represents the Wigner-Dyson distribution, while the black line corresponds to the Poisson distribution. In the inset of each one, we have plotted the PDFs in semilogarithmic scale.

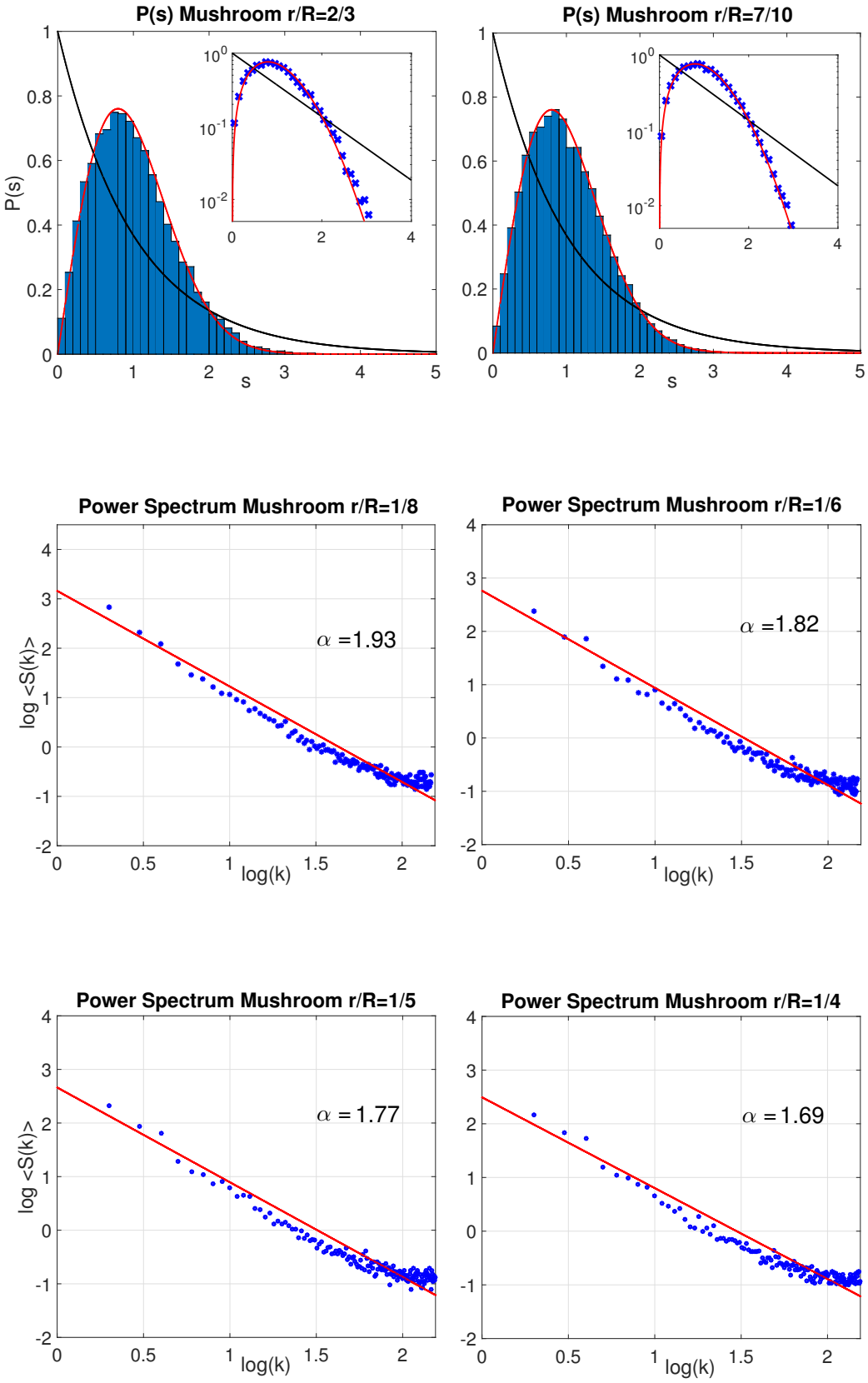

Figure 6.9: In the first row, the two NNSDs for the larger r/R control parameters, are shown. The second and third row shows the power spectrum and its corresponding linear fit, for the four smaller r/R parameters, not including zero.

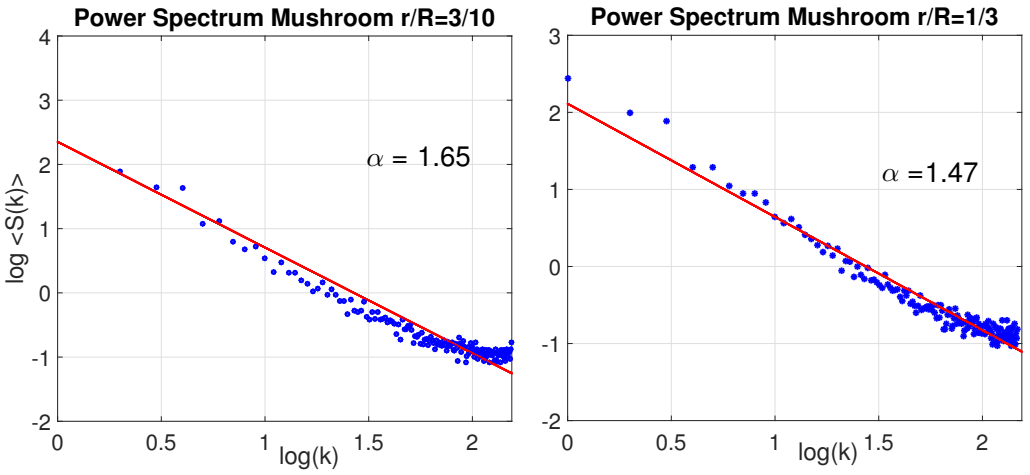

(b)
b

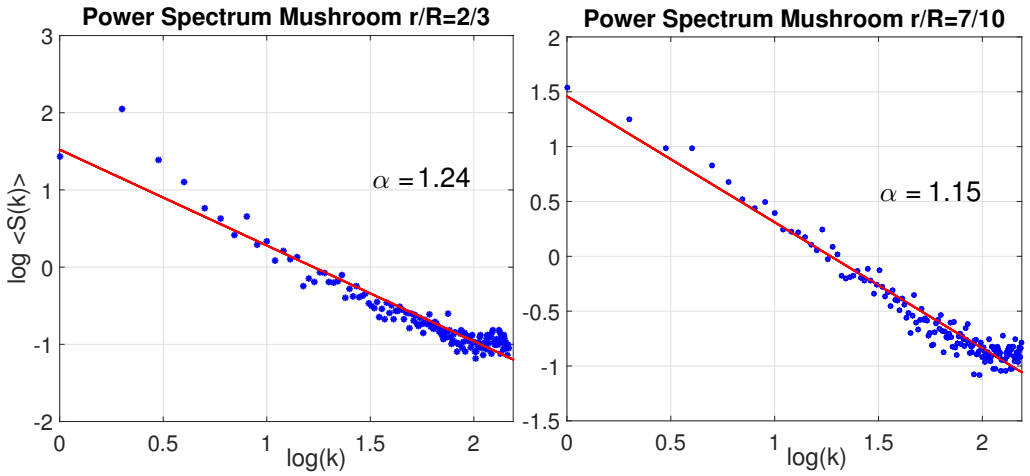

Figure 6.10: The power spectrum and its corresponding linear fit, for the four larger r/R parameters

Curved billiards

In this section we describe how a surface curvature on a geometry, which is in principle integrable-regular, produces a crossover to the chaotic regime. Using the advantages of conformal maps (Peyré (2008)), we performed an initial deformation, which changes in a controlled manner the vertices of the mesh, through a $A\cos^2(\theta(x))$ function, as shown in figure (6.11). On the new configuration a conformal transformation is applied to recover the flat surface, and the spectrum of the Laplace-Beltrami operator is calculated.

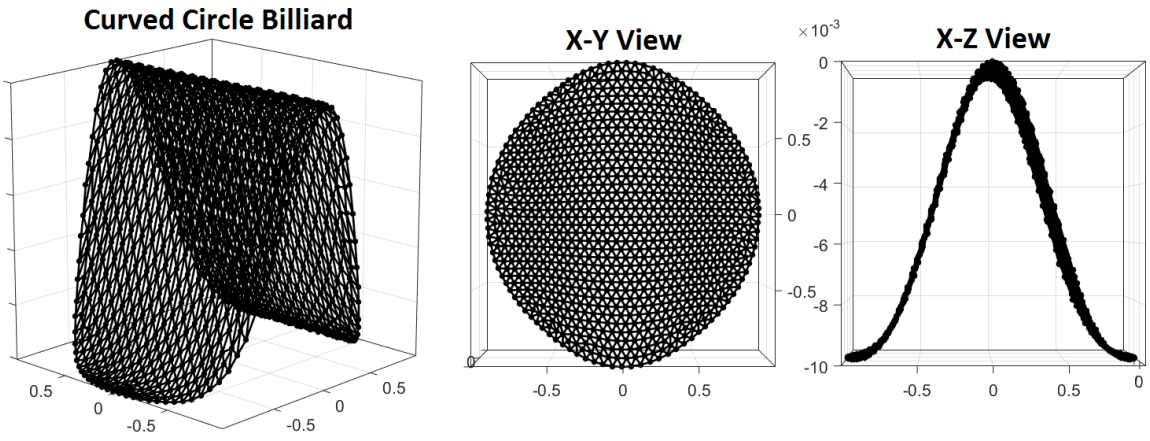

Figure 6.11: On the left: isometric projection of the curved billiard. On the center: its top view (plane $(x-y)$). On the right: its side view (plane $(x-z)$)

There are an arbitrary number of choices for the curvature's shape. Therefore, it is premature to say that all of them will cause a change of the eigenvalues spectrum. In this case, we are interested in finding a functional form connecting the dynamic regime and the geometric deformations in billiards. The control parameter in this geometry corresponds to the deformation amplitude A. We have worked with nine different amplitude values, as shown in Table 6.4. In a way analogous to the characterizations made for the other billiards, this system exhibit a dependence on the control parameter A, and the statistical

measures $\delta_{LK}(P_{WD}|P_{ob}(A))$, $|B(A)|$ and $\alpha(A)$.

A	$\delta_{LK}(A)$	$\|B(A)\|$	$\alpha(A)-1$
0.03	1	0.1587	0.68 ± 0.06
0.07	0.3362	0.1920	0.61 ± 0.06
0.1	0.1806	0.2179	0.52 ± 0.06
0.2	0.1712	0.2273	0.43 ± 0.07
0.3	0.1530	0.2318	0.40 ± 0.06
0.4	0.1281	0.2427	0.31 ± 0.06
0.5	0.1201	0.2473	0.27 ± 0.07
0.9	0.0857	0.2614	0.24 ± 0.06
1.9	0.0321	0.2895	0.14 ± 0.10

Table 6.4: Numerical values of the three statistical measures obtained via the energy spectrum associated with each control parameter (A), for the curved billiard.

For this geometry, the crossover from the integrable to the chaotic regime is not clear, even though the control parameter increases to a value that almost doubles the radius of the primary disk ($A = 1.90$). i.e., for each of the cases, the eigenvalue spectra still indicate the presence of mixed dynamics according to the three statistical measures used. We could speculate on the multiple reasons for this behavior, beginning by attributing them to the possible presence of very close spacings because the billiard was not divided to avoid the repetition of eigenvalues by reflection symmetry. In this sense, the attempt to characterize the transition between universal regimes due to the surface curvature of the billiard remains open and will be a topic of future research.

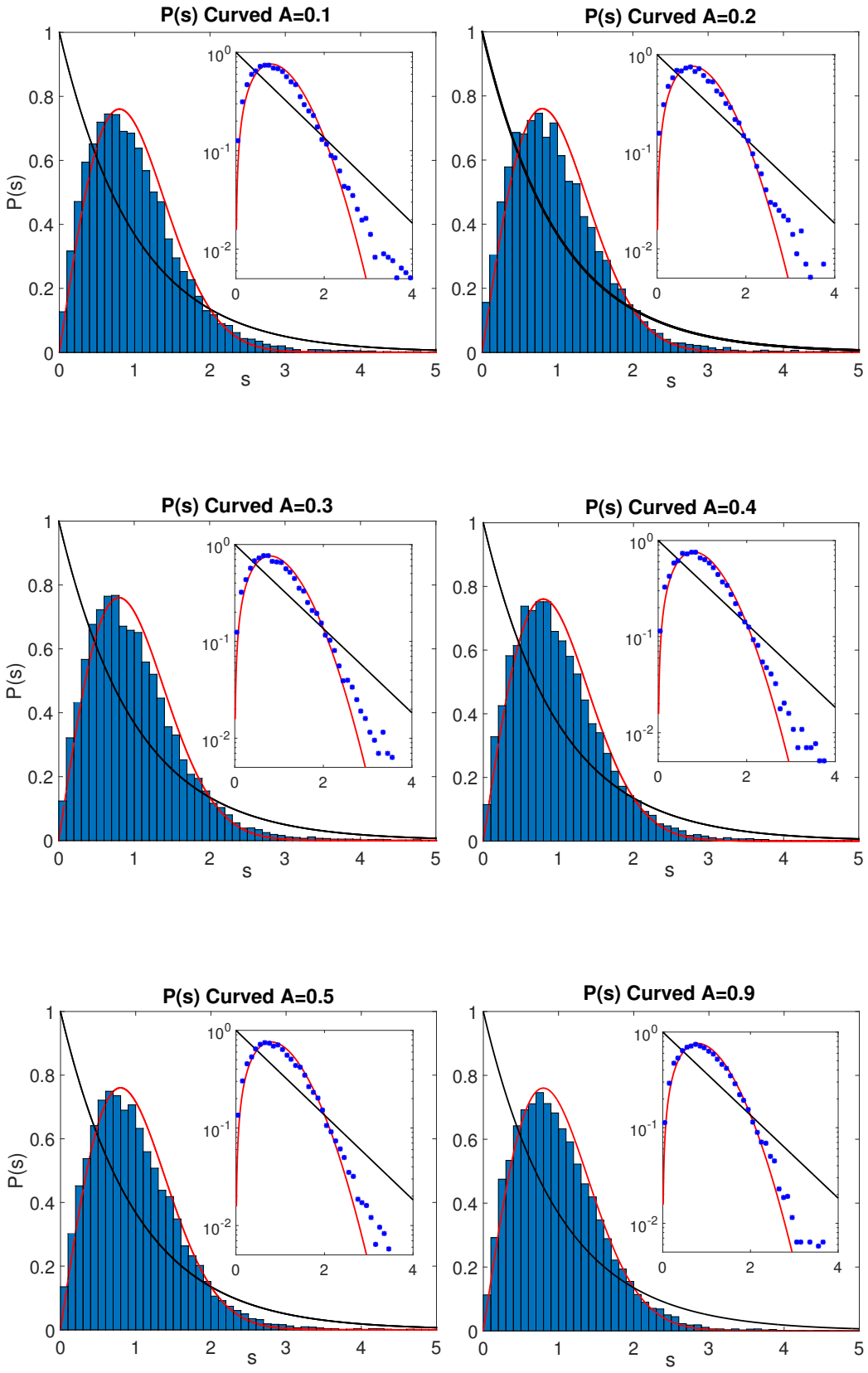

Figure 6.12: In blue: Histograms of NNSD for six of the nine parameters A that have been used for the description of the curved billard. The red line represents the Wigner-Dyson distribution, while the black line corresponds to the Poisson distribution. In the inset of each one, we have plotted the PDFs in semilogarithmic scale.

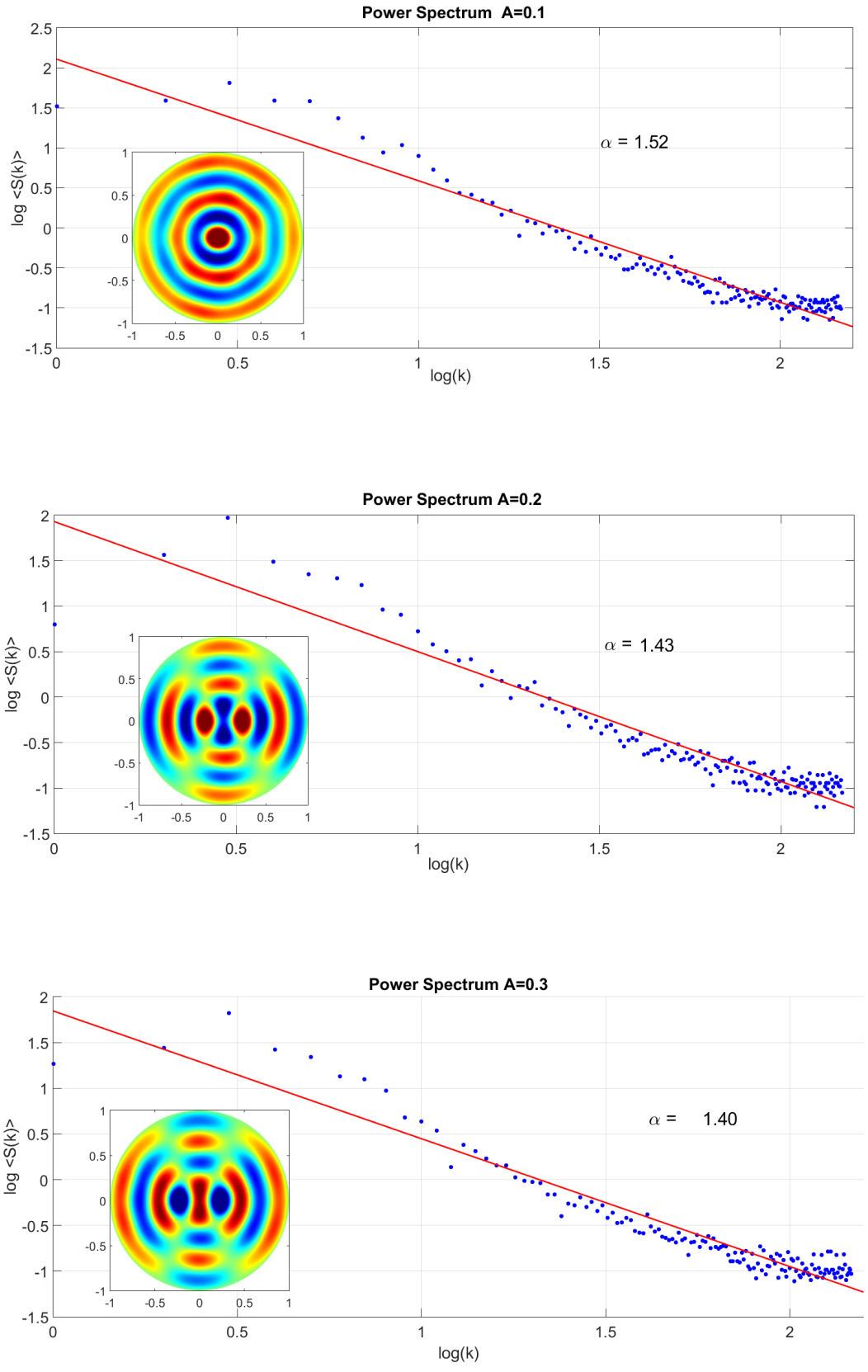

Figure 6.13: The blue dots represent the power spectrum for the parameters $A = 0.1$, $A = 0.2$, and $A = 0.3$, of the curved billiard. The red line in each subfigure represents the best linear fit made through least squares, where the slope corresponds to its α spectral exponent.

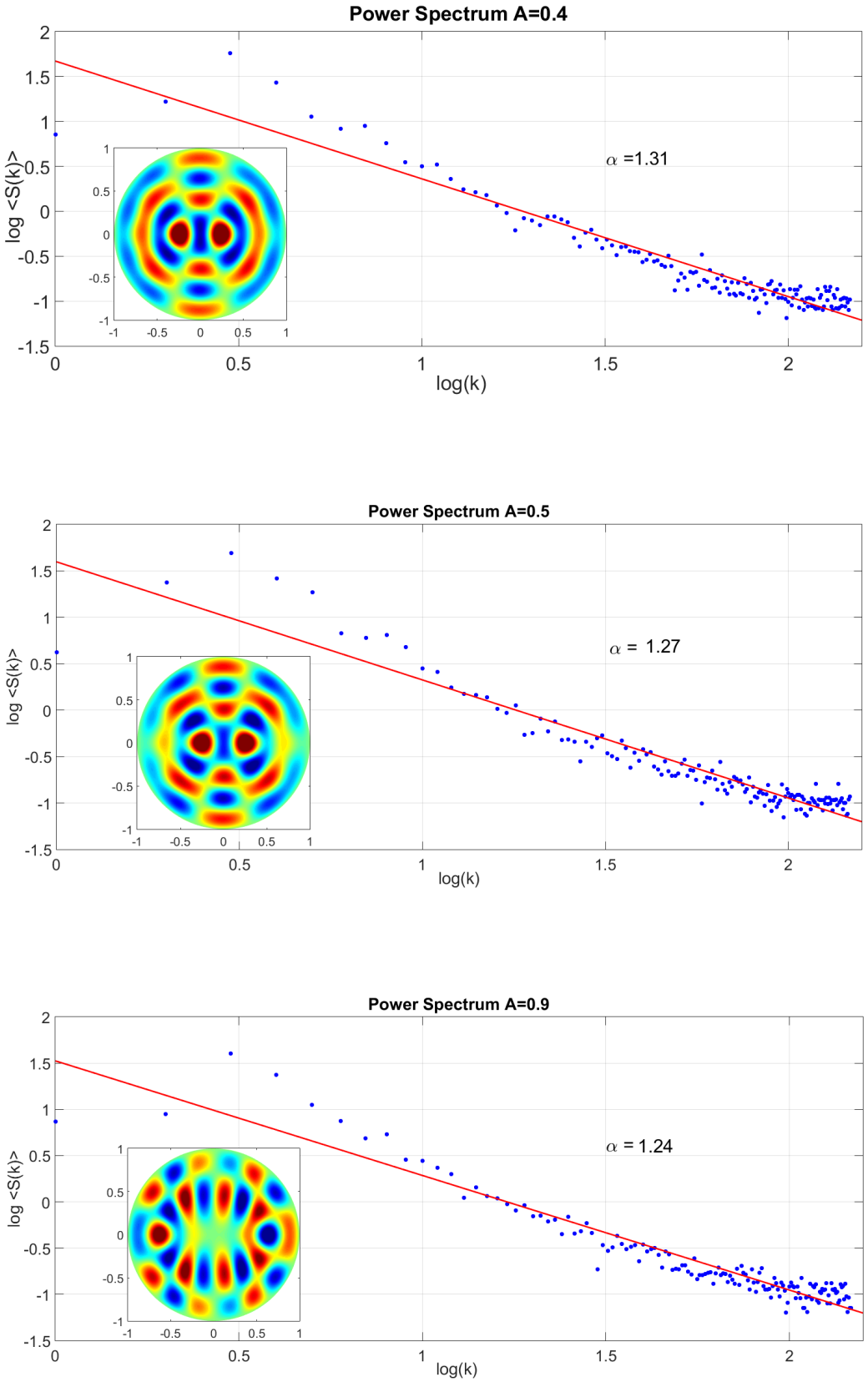

Figure 6.14: The blue dots represent the power spectrum for the parameters $A = 0.4$, $A = 0.5$, and $A = 0.9$, of the curved billiard. The red line in each subfigure represents the best linear fit made through least squares, where the slope corresponds to its α spectral exponent.

Finally, we made two graphs which are intended to show that billiards make similar crossovers, described through the statistical measures that characterize each one. The first chart (see figure (6.15)) shows a law of corresponding states between the spectral coefficient and the Burstiness parameter, while in the second graph (see figure (6.16)) we see a correspondence between the Kullback-Leibler distance and spectral coefficient. In both cases, the curves have been fitted simultaneously for the three billiards using a stretched exponential function $y = A\exp\left(Bx^C\right)$, where the plotted variables and its fitting parameters are displayed in the caption of each figure.

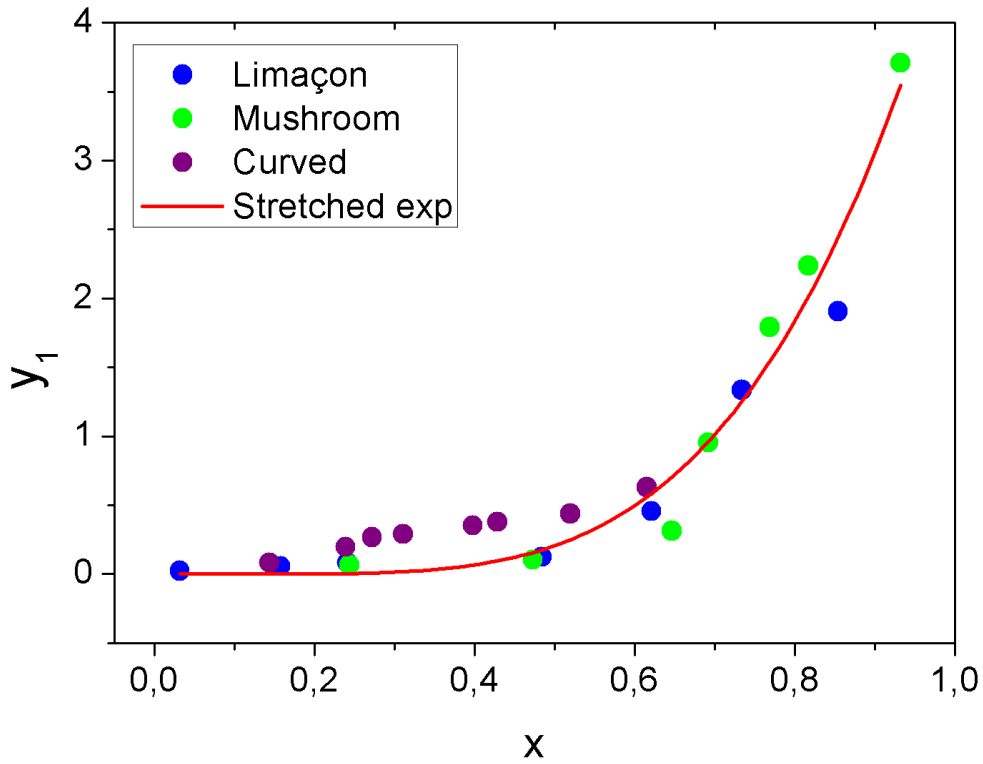

Figure 6.15: The abscissa axis represents the relation $x = \alpha - 1$ for the spectral coefficient; while in the ordinates axis shows the relation $y_1 = \frac{1-B}{B}$ for the burstiness parameter. Here the data for the three billiards (i)Limaçon (blue), (ii) Mushroom (green), and (iii) Curved (violet), have been fitting via the stretched exponential function $y = A\exp\left(Bx^C\right)$, with coefficients $A = 1.57 \times 10^8$, $B = -17.31$, $C = -0.24$.

From figures (6.15) and (6.16) we see that the Kullback-Leibler distance and Burstiness parameter, are for the cavities described in this chapter redundant measures. Therefore,

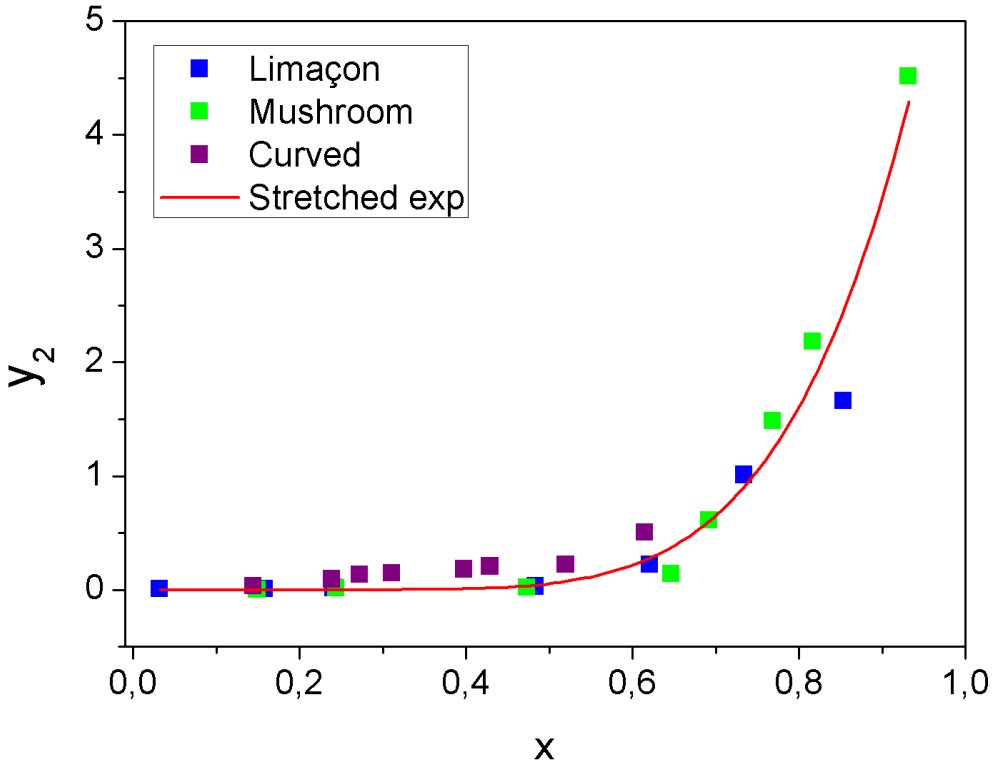

Figure 6.16: The abscissa axis represents the relation $x = \alpha - 1$ for the spectral coefficient, while in the ordinates axis shows the relation $y_2 = \frac{\delta_{LK}}{(1-\delta_{LK})}$ for the Kullback-Leibler distance. Here the data for the three billiards (i)Limaçon (blue), (ii) Mushroom (green), and (iii) Curved (violet), have been fitting via the stretched exponential function $y = A \exp\left(Bx^C\right)$, with coefficients $A = 4.15 \times 10^8$, $B = -17.95$, $C = -0.34$.

with only one of them is sufficient to characterize the histograms' deviations of each billiard according to its respective control parameter Cp. Also, these figures show that the curved billiard does not appear to have the same tendencies.

In the next chapter we shall use the H-theory to obtain the dynamic model for the transition from the integrable to the chaotic regime of the Limaçon and Mushroom geometries.

7 Ballistic cavities II

7.1 Abstract

In this chapter, we present the connection of the method of stochastic differential equations with two ensembles of the random matrices theory, (i) Gaussian Diagonal Ensemble GDE, and (ii) Gaussian Orthogonal Ensemble GOE. In particular, the case where the Hamiltonian corresponds to a real symmetric matrix 2×2 generates the Wigner-Dyson stationary distribution, which characterize the NNSD in the chaotic regime. So, in the first approach, the probability density functions are the result of the superposition between a Wigner-Dyson distribution conditioned by its variance, which couples under the hypothesis of large-scale separations with a background distribution of class (i) Inverse-Gamma, and (ii) Gamma. In this way, one provides dynamical support for the work done by Abul-Magd, Dietz, Friedrich, and Richter in (Abul-Magd *et al.* (2008)). After presenting the generalities of the dynamic model, it is established that the superposition with the gamma class describes the crossover from Poisson to Wigner- Dyson. This distribution has been used to make the fit of the spectra for the energy levels spacing of Limaçon and Mushroom billiards that were introduced in the previous chapter.

The second approach of the chapter emerges as another original idea of this research, where we perform a second-order statistics for the energy spectrum. The main advantage of this description is that it uses symmetric distributions where a Boltzmann distribution characterizes the regular regime (see figure 7.1), and the crossover is made via the K-distribution until it reaches the Gaussian distribution describing the full chaotic regime. With the purpose of calibrating the ends of the transition, the GDE and GOE ensembles have been computationally generated, as shown in figures (7.1.I.c) and (7.1.II.c), where

the red lines correspond to the fits of the theoretical model developed for the second-order statistics.

7.2 Introduction

Classically a billiard is a system where a free particle is confined to a flat surface, and each time it reaches the boundary there is an elastic collision characterized by a symmetrical reflection to the normal of the point where the shock occurred. This system, which is apparently simple, began to have relevance in physics when

On Friday 27 April 1900, at the Royal Institution of Great Britain, Lord Kelvin delivered a lecture entitled "The 19th-century clouds over the dynamical theory of heat and light." In which he said: without exception, the average kinetic energy of any component of the motion of the inertial center is, according to the Boltzmann-Maxwell doctrine, equal to $\frac{1}{3i}$ *of the whole average kinetic energy of the system. The general Boltzmann-Maxwell doctrine includes the proposition, even in those cases in which it is not deducible algebraically from the equality of the* $3i$ *energies.* (Kelvin (1901))

On that memorable date, Lord Kelvin presented the results of the experiment he made with his assistant Anderson using two types of billiard, the first with a triangular geometry and the second with a flower shape (see reference (Kelvin (1901)). Through the measurements made in these, he concluded that the long temporary measures for the components of the velocity in each case did not coincide, opening the possibility of the violation to the Ergodic hypothesis (Nakamura and Harayama (2004)).

Billiards were introduced in physics with this event, and have been for more than a century a tool used to characterize dynamics of a system as a function of its trajectories. Thus, from the classical approach these systems are divided into (i) integrable systems, are characterized by their Hamiltonian admits n independent integrals of motion in involution. In other words, these systems are integrable if the equations of motion can be

solved for any set of initial conditions by quadratures, where the Poisson bracket between these, or between each of the quadratures and the Hamiltonian are zero [1]. (ii) Chaotic, corresponding to geometries in which the paths diverge to small changes in initial conditions, that is, are systems where for a single initial condition the object moving inside the cavity can cover all possible values of the kinematic variables on which is formed the phase space. (iii) There is a third class, where stable orbits coexist, robust to small perturbations and unstable very vulnerable to them, to such a class is called billiards with mixed dynamics.

On the other hand, with the evolution of quantum mechanics in the twentieth century, the scientists began to study increasingly complex systems, whose be impossible to solve analytically, it made necessary the appearance of a different approach. Thus, in the late 1950s, the random matrices theory was born, which in its beginning was formulated to give an interpretation to the behavior of highly excited levels in heavy nuclei where the shell model is not applicable. This theory emerged from the works by Wigner (Wigner (1955)), Dyson (Dyson (1962a,b,c, 1963)) and Metha (Mehta. (2004); Metha (1960); Metha and M.Gaudin (1960)), where the Hamiltonian of the nucleus is described as a matrix whose elements are represented by a random variable, considering as the only constraint between its elements, the symmetries of the system that is wanted to study. In current physics, this theory is used to explain disordered systems and its symmetries are established by the Cartan's classification (Caselle and Magnea (2004)). In this approach, ten classes are recognized, subdivided into three Wigner-Dyson classes, three chiral classes, and four to the Bogoliubov-de Gennes classes (Macedo-Junior and Macêdo (2006); Mirlin *et al.* (2010)). Random Matix Theory is a huge set of information, so in this chapter, we are going to restrict only to the Gaussian Orthogonal Ensemble GOE, and to a particular case called Gaussian Diagonal Ensemble GDE, to show the connection that these two collectivities have with the billiards and its spectrum.

Through the rapid technological advances of recent decades, the study of matter in

[1] The above is not the only definition of integrability, but it is useful to get an idea about this condition

the sub-micrometer scale has become a relatively common event. In such systems where the laws of quantum mechanics are prevalent, scientists have discovered a large number of phenomena that a century ago were unimaginable. For example, small structures have been made with semiconductor heterojunctions quantum dots, where the resistance behavior has been characterized as a function of the electric and/or magnetic field applied (Marcus *et al.* (1992)). Through them it was perceived that this dependency is not deterministic, i.e., the resistance presents rapid fluctuations by modifications of the applied field. Moreover, it become evident that the behavior of these fluctuations depends on the geometry of the quantum dot. Experiments have also been conducted with so-called quantum corrals (Crommie *et al.* (1995, 1993)), and ballistic cavities in superconductors (Abul-Magd *et al.* (2008); Dietz and Richter (2015)), with the purpose of studying the local properties electrons confined in a two-dimensional geometry modeled as a nearly free electron gas.

The scientific community perceived with these and previous experiments that the energy spectra of resonant two-dimensional cavities described by quantum mechanics and the billiards of balls outlined by the classical approach share several characteristics which can be introduced as correspondences since the set of quantum numbers can be attributed to the motion constants (Nakamura and Harayama (2004)). From this point of view, there is a discussion of the existence of integrability when the quantum numbers of the system present intersections due to interaction with external fields, a fact that for example generates energy level crossing. Such interpretation has a correspondence with the topological approach made by Liouville for classical systems, where the intersection of the manifolds is the trajectories of the phase space. Also, if over a system described by the wave mechanics that is initially integrable is applied a non-integrable perturbation, may be partially (mixed chaotic systems) or wholly, destroyed (full chaotic systems) the motion constants. So the repulsion appears between nearby energy levels and introduces the concept of quantum chaos, which is tentatively defined as a study of the semiclassical

behavior of systems whose classical motion exhibits a high dependence on the initial conditions.

The absence of predictability in the values that take the quantum numbers of these systems, implied that the statistical approach made by the RMT gained great importance as it can describe with high precision the probability density function of its energy spacing spectrum. Using this preamble, in this chapter, we shall characterize the crossover of the energy spectrum of cavities that start in the integrable, nearest neighbor spacing distributions are described through the Gaussian Diagonal Ensemble GDE, which is a collective composed of diagonal and real matrices, i.e., its elements are statistically independent and correspond directly to their eigenvalues.

In the opposite case, when avoided energy level crossing is imposed, that the probability distribution is invariant under temporal inversion and real symmetric transformations $P(H)dH = P(H')dH'$, where $H' = KH^{\dagger}K^{-1} = KHK^{-1}$, and $K^{*}K = 1$. So, the probability density function can only depend on the powers of the trace of H. In this approach, it is assumed that the matrix elements are not correlated $P(H_{11}, \ldots, H_{mm}) = P(H_{11}) \ldots P(H_{mm})$. Thus, the PDF that satisfies these conditions is a Gaussian of the form $P(H) = C \exp\left(-ATr(H) - BTr(H^2)\right)$. This collective, in the RMT, is one of the three Wigner-Dyson classes and is called the Gaussian Orthogonal Ensemble (GOE).

In the simplest case, the Hamiltonian corresponds to a symmetric 2×2 matrix, and we want to describe the dynamics of the spacing of its energies $s = E_2 - E_1$, and the stationary solution. We generically designated its elements as $H_{ij} = x_{ij}$, and each of them presents Langevin dynamics

$$dx_{11} = -x_{11}dt + \sqrt{2\varepsilon_1}dW_{11}(t) \tag{7.1}$$

$$dx_{22} = -x_{22}dt + \sqrt{2\varepsilon_1}dW_{22}(t) \tag{7.2}$$

$$dx_{12} = -x_{12}dt + \sqrt{\varepsilon_1}dW_{12}(t). \tag{7.3}$$

The previous system of equations can be expressed in a compact notation through

$$dx_i^{(\alpha)} = -\sum_{j=1}^{N} \gamma_{ij} x_j^{(\alpha)} dt + \sqrt{f_{(i)}\varepsilon_M} dW^{\alpha}(t). \tag{7.4}$$

We want the dynamics of the system to be expressed in terms of its eigenvalues. So, according to the symmetry of the ensemble, an orthonormal transformation is applied to diagonalize the Hamiltonian

$$\begin{pmatrix} x_{11} & x_{12} \\ x_{12} & x_{22} \end{pmatrix} = \begin{pmatrix} \cos\theta & \sin\theta \\ -\sin\theta & \cos\theta \end{pmatrix} \begin{pmatrix} E_1 & 0 \\ 0 & E_2 \end{pmatrix} \begin{pmatrix} \cos\theta & -\sin\theta \\ \sin\theta & \cos\theta \end{pmatrix}. \tag{7.5}$$

Through this transformation of coordinates we obtain the relations

$$x_{11} = E_1 \cos^2\theta + E_2 \sin^2\theta \tag{7.6}$$

$$x_{22} = E_1 \sin^2\theta + E_2 \cos^2\theta \tag{7.7}$$

$$x_{12} = (E_2 - E_1) \sin\theta \cos\theta, \tag{7.8}$$

where its inverse transformation corresponds to

$$E_1 = x_{11} \cos^2\theta + x_{22} \sin^2\theta - x_{12} \sin 2\theta \tag{7.9}$$

$$E_2 = x_{11} \sin^2\theta + x_{22} \cos^2\theta + x_{12} \sin 2\theta \tag{7.10}$$

$$\tan 2\theta = \frac{2x_{12}}{x_{22} - x_{22}}. \tag{7.11}$$

Stochastic dynamics for energy eigenvalues is expressed according to the conditions established by the Itô lemma, as a Taylor series of the second order

$$f(x + dx, y + dy, z + dz) = \sum_{j=0}^{\infty} \left[\frac{1}{j!} \left(dx \frac{\partial}{\partial x} + dy \frac{\partial}{\partial y} + dz \frac{\partial}{\partial z} \right)^j f(x, y, z) \right]. \tag{7.12}$$

Therefore, the derivatives of the equations (7.9) and (7.10) are written as

$$dE_i = \sum_{j=1}^{3} \left[dx_j \frac{\partial E_i}{\partial x_j} + \frac{1}{2} \left((dx_j)^2 \frac{\partial^2 E_i}{\partial x_j^2} \right) \right], \tag{7.13}$$

where the Wiener processes satisfies the orthonormal conditions $dW_{ij}(t)dW_{kl}(t') = \delta_{ik}\delta_{jl}\delta(t-t')dt$; which implies, $(dx_{11})^2 = (dx_{22})^2 \sim 2\varepsilon_1 dt$, $(dx_{12})^2 \sim \varepsilon_1 dt$ and $dx_{11}dx_{22} = dx_{11}dx_{12} = dx_{22}dx_{12} = 0$. Using these conditions we get

$$dE_1 = -\left(E_1 + \frac{\varepsilon_1}{E_2 - E_1}\right)dt + \sqrt{2\sigma}dW_1 \tag{7.14}$$

$$dE_2 = -\left(E_2 + \frac{\varepsilon_1}{E_1 - E_2}\right)dt + \sqrt{2\sigma}dW_2. \tag{7.15}$$

The noise terms in these equations are related to the original variables through

$$\sqrt{2\sigma}dW_1 = \sqrt{2\varepsilon_1}\cos^2\theta dW_{11} + \sqrt{2\varepsilon_1}\sin^2\theta dW_{22} - \sqrt{\varepsilon_1}\sin 2\theta dW_{12} \tag{7.16}$$

$$\sqrt{2\sigma}dW_2 = \sqrt{2\varepsilon_1}\sin^2\theta dW_{11} + \sqrt{2\varepsilon_1}\cos^2\theta dW_{22} + \sqrt{\varepsilon_1}\sin 2\theta dW_{12}, \tag{7.17}$$

thus the Langevin equations system for energies can be written in compact notation as

$$dE_i = -\left(E_i - \sum_{j\neq i}\frac{\varepsilon_1}{E_i - E_j}\right)dt + \sqrt{2\varepsilon_1}dW_i. \tag{7.18}$$

Now, we define $s \equiv E_2 - E_1$, with the constraint $E_2 \geq E_1$ i.e. $s \geq 0$. Subtracting the two equations from the system (7.18) gives the stochastic differential equation for the spacing of the energies

$$ds = -\left(E_2 + \frac{\varepsilon_1}{(-s)}\right)dt + \left(E_1 + \frac{\varepsilon_1}{s}\right)dt + \sqrt{2\varepsilon_1}(dW_2 - dW_1), \tag{7.19}$$

associated with Dyson's Brownian motion

$$ds = \left(-s + \frac{2\varepsilon_1}{s}\right)dt + \sqrt{2\tilde{\sigma}}dW, \tag{7.20}$$

where $\tilde{\sigma} = 2\varepsilon_1$. Therefore,

$$ds = \overbrace{\left(-s + \frac{2\varepsilon_1}{s}\right)}^{D^{(1)}(s)}dt + 2\sqrt{\varepsilon_1}dW. \tag{7.21}$$

The stochastic differential equation (7.21) establishes the dynamics of the integral scale, with the associated Fokker-Planck equation

$$\frac{\partial P(s,t)}{\partial t} = \left[-\frac{\partial}{\partial s}\left(-s + \frac{2\varepsilon_1}{s} \right) + 2\varepsilon_1 \frac{\partial^2}{\partial s^2} \right] P(s,t), \tag{7.22}$$

that is in agreement with the reference (Risken and Franck (1996)). It has the general stationary solution

$$P_{eq}(s) = C \exp\left(-\Phi(s)\right). \tag{7.23}$$

It is necessary to determine the potential function $\Phi(s)$, via its relation to the drift coefficient

$$\frac{d\Phi(s)}{ds} = -\frac{1}{2\varepsilon_1} D^{(1)}(s), \tag{7.24}$$

which is obtained by direct integration

$$\Phi(s) = \frac{s^2}{4\varepsilon_1} - \ln s. \tag{7.25}$$

In this way, after establishing the normalization constant, the equation (7.23) becomes

$$P_{eq}(s|\varepsilon_1) = \frac{s}{2\varepsilon_1} \exp\left(-\frac{s^2}{4\varepsilon_1} \right), \tag{7.26}$$

for the case where ε_1 is constant, it is determined through the normalization condition that its value is $\varepsilon_1 = \frac{1}{\pi}$, yielding the Wigner-Dyson distribution.

On the other hand, as was presented in Chapter Six, neither the Wigner-Dyson distribution nor the Poisson distribution, can fit the probability density functions in billiards with mixed dynamics. However, Poisson and WD do describe the ends of the transition. So that in the following sections two approaches will be presented based on the conditions of the H theory. The PDFs produced by these models, fit with high precision each of the histograms for the billiards Limaçon and Mushroom previously presented.

In figure (7.1) we show the histograms for (i) the energy spectrum $P(E)$, (ii) the spacing spectrum (NNSD), and (iii) the spectrum of spacing increments $P(x)$. We considered both the Gaussian diagonal and orthogonal ensembles, and we defined the variable $x_i \equiv (s_i - s_{i-1})/\sigma(x)$ for nearest neighbor increments of level spacing, with the aim of performing second-order statistics for the energy levels, and $\sigma(x)$ is the standard deviation.

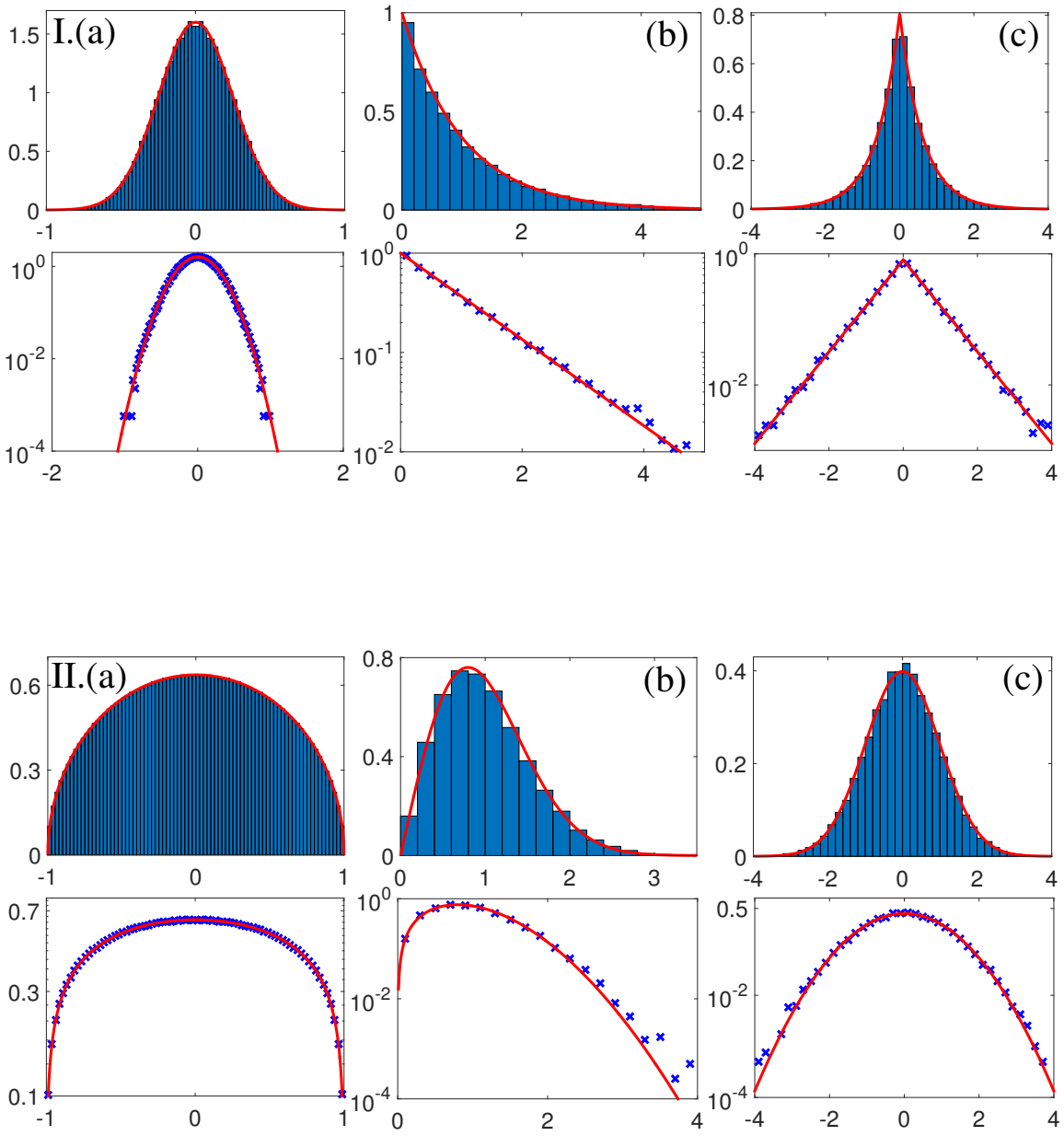

Figure 7.1: Simulations of the Gaussian Diagonal Ensemble (GDE) are shown in I. The panels show the average level density ((a) leftmost), the NN level spacing distribution ((b) centre) and the distribution of NN increments of level spacings ((c) rightmost) in linear (upper) and semi-log (lower) scales The theoretical curves, shown as red lines, are the Gaussian distribution with zero average and unit variance ((a) leftmost), the Poisson law ((b) centre) and the Boltzmann distribution ((c) rightmost). In part II. simulations of the Gaussian Orthogonal Ensemble (GOE). Just as before, the panels show the average level density ((a) leftmost), the NN level spacing distribution ((b)centre) and the distribution of NN increments of level spacings ((c)rightmost) in linear (upper) and semi-log (lower) scales. The red lines are the Wigner semicircle law ((a) leftmost), the Wigner-Dyson distribution ((b) centre) and the Gaussian distribution with zero average and unit variance ((c)rightmost).

7.3 Dynamic model applied to NNSD

In this approach, we propose that the deviations of the nearest neighbors spacing distribution (NNSD) in the observation scale are due to the superposition between the larger scale of the system with Langevin dynamics

$$ds = \left(-s + \frac{2\varepsilon_N}{s}\right) dt + 2\sqrt{\varepsilon_N} dW, \tag{7.27}$$

and the internal variables that characterize the slowly changing background

$$d\varepsilon_i = -\gamma_i(\varepsilon_i - \varepsilon_{i-1})dt + \kappa_i \varepsilon_i^{\alpha} \varepsilon_{i-1}^{1-\alpha} dW_i, \quad i = 1, \ldots, N. \tag{7.28}$$

Since the billiard spacing spectra have about 2.5×10^4 data, their histograms show trend loss beyond $P(s) > 1 \times 10^{-3}$. For this reason, a single background scale is sufficient to account for the deviation of its PDFs. Then the background dynamics given by the equation (7.28), is restricted to $i = 1$. Where background stationary distributions are (i) inverse-gamma for $\alpha = 1$, and (ii) gamma for $\alpha = 1/2$. It using this information, we proceed to determine the marginal distribution of the model

$$P(s) = \frac{1}{2} \int_0^{\infty} \frac{s}{\varepsilon_1} \exp\left(-\frac{s^2}{4\varepsilon_1}\right) f(\varepsilon_1) d\varepsilon_1, \tag{7.29}$$

the integral (7.29) is evaluated under the large scales separation assumption, where the kernel of integration corresponds to the conditional PDF (7.26) which is the stationary solution of the equation (7.27). Whereas $f(\varepsilon_1)$ may correspond in principle to an inverse-gamma distribution ($\bar{\gamma}$) or gamma (γ), cases presented separately in the following subsections.

7.3.1 *Inverse-Gamma Class*

In this part of the manuscript, the marginal distribution (7.29) is determined, when the background is the inverse-gamma class (stationary solution of Eq. (7.28) for $\alpha = 1$)

$$f(\varepsilon_1) = \frac{(\beta\varepsilon_0)^{\beta+1}}{\Gamma(\beta+1)}\varepsilon_1^{-\beta-2}\exp\left(-\frac{\beta\varepsilon_0}{\varepsilon_1}\right). \tag{7.30}$$

The signal's PDF (7.29) is calculated, through the Mellin transform, where the change of variable $s = \sqrt{4\varepsilon_1 y}$ for the kernel (7.26) is made. So by raising to power $(r-1)$, the previous equation takes the form $s^{r-1} = 2^{r-1}y^{(r-1)/2}\varepsilon_1^{(r-1)/2}$. We thus have equation

$$\underbrace{\int_0^\infty ds s^{r-1}P(s)}_{<s^{r-1}>} = 2^{r-1}\overbrace{\int_0^\infty dy y^{(r-1)/2}P(y)}^{<y^{(r-1)/2}>}\underbrace{\int_0^\infty d\varepsilon_1\varepsilon_1^{(r-1)/2}f(\varepsilon_1)}_{<\varepsilon_1^{(r-1)/2}>}, \tag{7.31}$$

where the distribution $P(y)$ is constructed through the change of variable

$$P(y) = \left(P(s|\varepsilon_1)|_{s=\sqrt{4\varepsilon_1 y}}\right)\underbrace{\sqrt{\frac{\varepsilon_1}{y}}}_{(ds/dy)} = \exp(-y), \tag{7.32}$$

while the moments of order $(r-1)/2$, expressed on the right side of the equation (7.31), are

$$\langle y^{(r-1)/2}\rangle = \Gamma\left(\frac{r+1}{2}\right) \tag{7.33}$$

$$\langle\varepsilon_1^{(r-1)/2}\rangle = \frac{1}{\sqrt{\beta\varepsilon_0}\Gamma(\beta+1)}\left(\frac{1}{\beta\varepsilon_0}\right)^{-\frac{r}{2}}\Gamma\left(\beta+\frac{3}{2}-\frac{r}{2}\right). \tag{7.34}$$

Therefore, the substitution of these results into Eq. (7.31) produces

$$\underbrace{\int_0^\infty ds s^{r-1}P(s)}_{<s^{r-1}>} = \frac{1}{2\sqrt{\beta\varepsilon_0}\Gamma(\beta+1)}\left(\frac{1}{2\sqrt{\beta\varepsilon_0}}\right)^{-r}\Gamma\left(\frac{r+1}{2}\right)\Gamma\left(\beta+\frac{3}{2}-\frac{r}{2}\right). \tag{7.35}$$

Using the properties of Mellin transform for the Fox H-function

$$\int_0^\infty ds s^{r-1}H_{p,q}^{m,n}\left(\begin{array}{c}(a_1,A_1),\ldots,(a_p,A_p)\\(b_1,B_1),\ldots,(b_q,B_q)\end{array}\middle|\alpha s\right) = \alpha^{-r}\frac{\prod_{j=1}^m\Gamma(b_j+B_jr)}{\prod_{j=m+1}^q\Gamma(1-b_j-B_jr)}\frac{\prod_{j=1}^n\Gamma(1-a_j-A_jr)}{\prod_{j=n+1}^p\Gamma(a_j+A_jr)}, \tag{7.36}$$

by direct comparison with the equation (7.35) we get

$$\int_0^\infty ds s^{r-1} H_{1,1}^{1,1}\left(\begin{array}{c} (-\beta-1/2,1/2) \\ (1/2,1/2) \end{array} \middle| \frac{s}{2\sqrt{\beta\varepsilon_0}} \right) = \left(\frac{1}{2\sqrt{\beta\varepsilon_0}}\right)^{-r} \Gamma\left(\frac{r+1}{2}\right) \Gamma\left(\beta+\frac{3}{2}-\frac{r}{2}\right). \tag{7.37}$$

The marginal distribution (7.29), expressed as function of the above result, corresponds to the Fox H-function

$$P(s) = \frac{1}{2\sqrt{\beta\varepsilon_0}\Gamma(\beta+1)} H_{1,1}^{1,1}\left(\begin{array}{c} (-\beta-1/2,1/2) \\ (1/2,1/2) \end{array} \middle| \frac{s}{2\sqrt{\beta\varepsilon_0}} \right). \tag{7.38}$$

Equation (7.38) can be reduced to a Meijer G-function, through the property

$$H_{p,q}^{m,n}\left(\begin{array}{c} (a_u,A_u) \\ (b_v,B_v) \end{array} \middle| z \right) = k H_{p,q}^{m,n}\left(\begin{array}{c} (a_u,kA_u) \\ (b_v,kB_v) \end{array} \middle| z^k \right), \tag{7.39}$$

It produces as a final result the probability density function

$$\boxed{P(s) = \frac{1}{\sqrt{\beta^3\varepsilon_0}\Gamma(\beta)} G_{1,1}^{1,1}\left(\begin{array}{c} (-\beta-1/2) \\ (1/2) \end{array} \middle| \frac{s^2}{4\beta\varepsilon_0} \right).} \tag{7.40}$$

Now, we can determine the relation between the parameters β and ε_0, for the PDF to have a unit average, through equation (7.37)

$$\int_0^\infty sP(s)ds = 2\sqrt{\frac{\varepsilon_0}{\beta}} \left(\frac{\Gamma(3/2)\Gamma(\beta+1/2)}{\Gamma(\beta)} \right), \tag{7.41}$$

when equation (7.41) has value one, the parameter ε_0 becomes

$$\boxed{\varepsilon_0 = \frac{\beta}{4}\left(\frac{\Gamma(\beta)}{\Gamma(3/2)\Gamma(\beta+1/2)} \right)^2.} \tag{7.42}$$

The PDF (7.40) has been plotted for several β parameters and is shown in figure (7.2). These curves are compared with the Wigner-Dyson (WD) (black line) distribution. Here, it becomes visible that at the asymptotic limit $\beta \to \infty$ the distributions (7.40) become a WD. On the other hand, and as far as it was tested, $P(s)$ fails to describe the Poisson distribution.

We have thus established that this kind of superposition is not the most appropriate to characterize the crossover from Poisson to WD that present the energy spacings of the billiards with mixed dynamics. However, as shown in the following section, the compounding with the Gamma distribution allow describing all cases, regular, mixed, and full-chaotic.

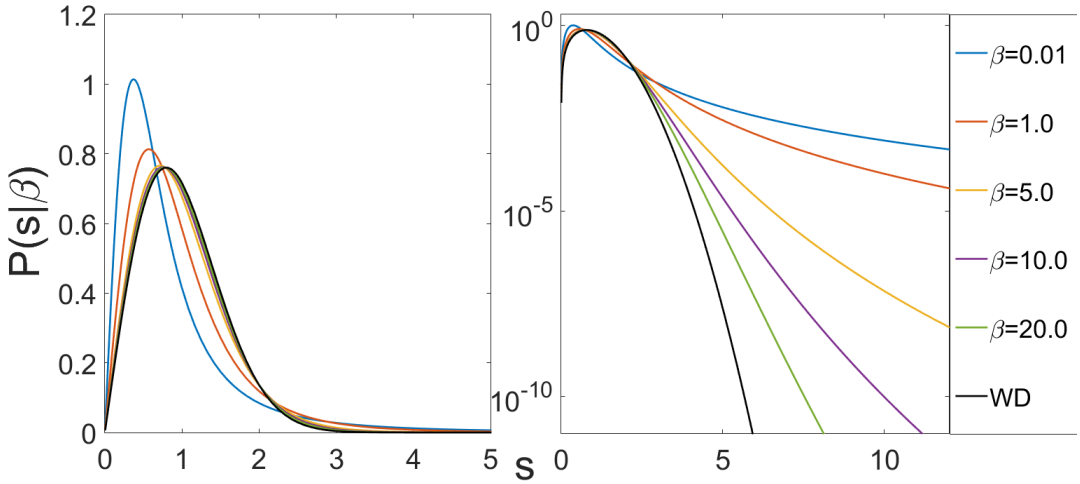

Figure 7.2: On the left, in regular scale is presented the dependence of Equation (7.40) for the β values demarcated at the right end of the figure. On the right side, the same curves have been plotted on a semi-logarithmic scale to see in detail the tails shape of this distribution. In both cases, the Wigner-Dyson PDF has been plotted in black as a reference.

7.3.2 *Gamma Class*

In this subsection, we determine the signal's probability density function form (7.29) for the case in which the background ($f(\varepsilon)$) is a gamma distribution

$$f(\varepsilon_1) = \frac{\beta^\beta}{\varepsilon_0^\beta \Gamma(\beta)} \varepsilon_1^{\beta-1} \exp\left(-\frac{\beta\varepsilon_1}{\varepsilon_0}\right). \tag{7.43}$$

The first step is to find the Mellin transform for the exponent $(r-1)/2$ of equation (7.43)

$$\langle \varepsilon_1^{r/2-1/2} \rangle = \frac{\beta^\beta}{\varepsilon_0^\beta \Gamma(\beta)} \int_0^\infty d\varepsilon_1 \varepsilon_1^{r/2+\beta-3/2} \exp\left(-\frac{\beta\varepsilon_1}{\varepsilon_0}\right) = \left(\frac{\beta}{\varepsilon_0}\right)^{1/2-r/2} \frac{\Gamma(\beta + r/2 - 1/2)}{\Gamma(\beta)}. \tag{7.44}$$

Then, using the result of equation (7.44), the Mellin transform for the marginal distribution 7.29) take the form

$$\underbrace{\int_0^\infty ds s^{r-1} P(s)}_{<s^{r-1}>} = \frac{1}{2\Gamma(\beta)} \sqrt{\frac{\beta}{\varepsilon_0}} \left(\frac{1}{2}\sqrt{\frac{\beta}{\varepsilon_0}}\right)^{-r} \Gamma(1/2 + r/2)\Gamma(\beta - 1/2 + r/2). \tag{7.45}$$

Direct comparison between equations (7.36) and (7.45), we obtain the parametric relations $\alpha = \frac{1}{2}\sqrt{\frac{\beta}{\varepsilon_0}}$, $b_1 = \beta - 1/2$, $B_1 = 1/2$, $b_2 = 1/2$, $B_2 = 1/2$, and $a_j = A_j = \emptyset \ \forall \ \ j$. Therefore, the Mellin transform (7.45) can be written as the Fox H-function

$$\int_0^\infty ds s^{r-1} H_{0,2}^{2,0}\left(\begin{matrix} \\ (\beta - \overline{1/2}, 1/2), (1/2, 1/2) \end{matrix} \middle| \frac{s}{2}\sqrt{\frac{\beta}{\varepsilon_0}} \right) = \left(\frac{1}{2}\sqrt{\frac{\beta}{\varepsilon_0}}\right)^{-r} \Gamma(\beta - 1/2 + r/2)\Gamma(1/2 + r/2). \tag{7.46}$$

The marginal distribution for this class is

$$P(s) = \frac{1}{2\Gamma(\beta)} \sqrt{\frac{\beta}{\varepsilon_0}} H_{0,2}^{2,0}\left(\begin{matrix} \\ (\beta - \overline{1/2}, 1/2), (1/2, 1/2) \end{matrix} \middle| \frac{s}{2}\sqrt{\frac{\beta}{\varepsilon_0}} \right). \tag{7.47}$$

This PDF can be reduced to a G-Meijer function via the identity (7.39)

$$\boxed{P(s) = \frac{1}{\Gamma(\beta)} \sqrt{\frac{\beta}{\varepsilon_0}} G_{0,2}^{2,0}\left(\begin{matrix} \\ (\beta - \overline{1/2}), (1/2) \end{matrix} \middle| \frac{\beta s^2}{4\varepsilon_0} \right).} \tag{7.48}$$

Equation (7.46), for the case $r = 2$, sets the mean of the distribution

$$\langle s \rangle = \frac{2}{\Gamma(\beta)} \sqrt{\frac{\varepsilon_0}{\beta}} \Gamma(3/2)\Gamma(\beta + 1/2), \tag{7.49}$$

where the constraint (7.50) satisfies the unit average

$$\boxed{\varepsilon_0 = \frac{\beta}{4} \left(\frac{\Gamma(\beta)}{\Gamma(3/2)\Gamma(\beta + 1/2)}\right)^2.} \tag{7.50}$$

Equation (7.48) allows to describe the PDFs for two universal regimes, integral and chaotic, in addition to the crossover between them. Since, as shown in figure (7.3), for the value of $\beta = 0.5$ (light blue curve) the distribution (7.48) is a Poisson distribution, whereas for the asymptotic limit $\beta \to \infty$ converges to the Wigner-Dyson, which corresponds to the black curve of figure (7.3). From this result, we can fit the histograms' NNSD of the billiards Limaçon and Mushroom.

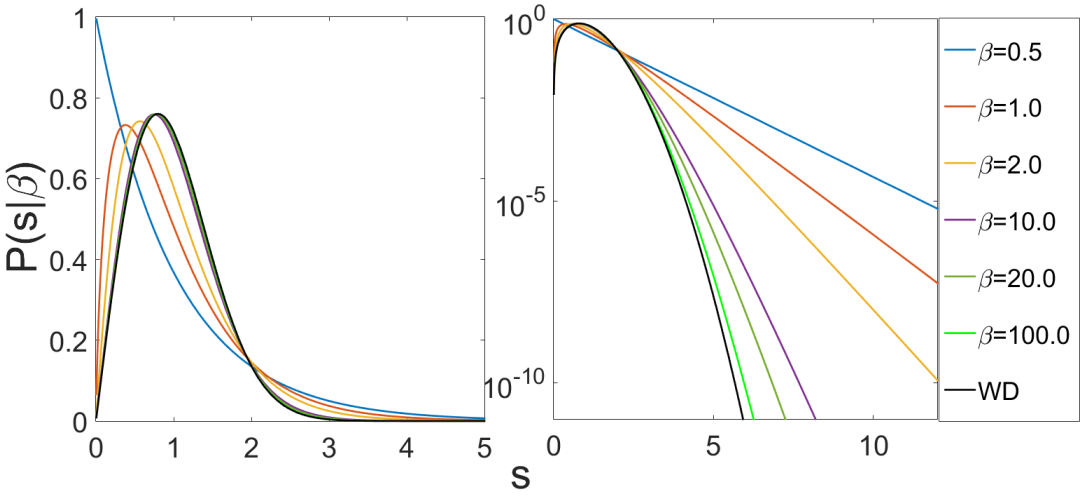

Figure 7.3: On the left, in regular scale is presented the dependence of Equation (7.48) for the β values demarcated at the right end of the figure. On the right side, the same curves have been plotted on a semi-logarithmic scale to see in detail the tails shape of this distribution. In both cases, the Wigner-Dyson PDF has been plotted in black as a reference.

7.4 Fits for NNSD of Limaçon Billiard

In figure (7.4), we show the histograms of the spacing spectrum and its corresponding fit for the eight values of the control parameters λ of the Limaçon billiard. (i) In linear scale where it stands out the body of the distributions (upper part), and (ii) in semi-log scale, it is seen in detail its tails (bottom). The fits have been made through Poisson distribution (red first line) for $\lambda = 0.0$, the Wigner-Dyson PDF (last red line) for $\lambda = 0.4$ and the PDF (7.48) (black lines) for the remaining intermediate parameters.

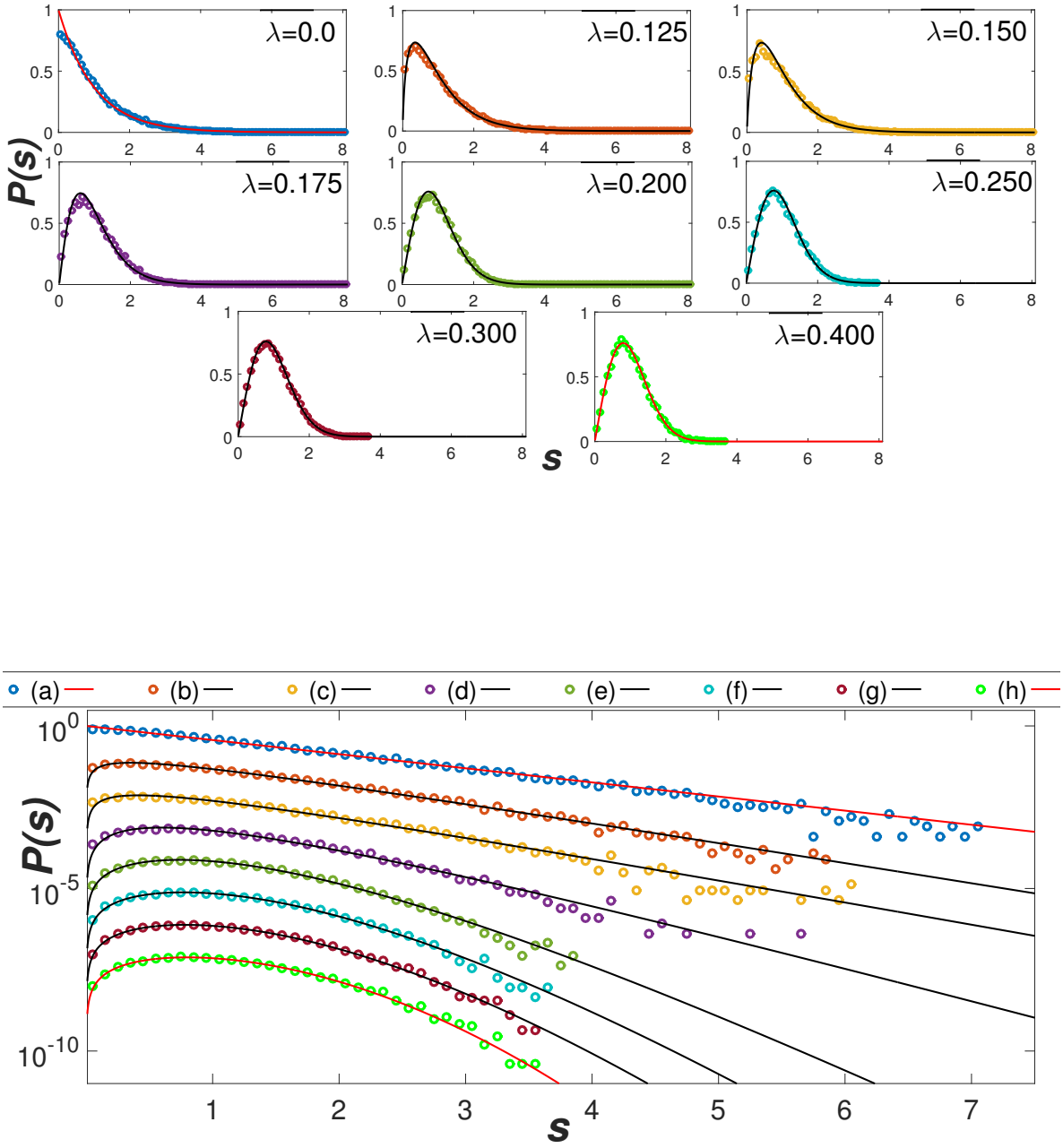

Figure 7.4: Using Equation (7.48) we have fitted the NNSD's histograms for the eight values of the control parameter λ of the Limaçon billiard. So, in the upper part, the graphs are shown in linear scale, while at the bottom they are in semilogarithmic scale, in this case, each of them has been multiplied by a factor of 0.1 on the previous one. The fits have been made through Poisson distribution (red first line, case (a)) for $\lambda = 0.0$, the Wigner-Dyson PDF (last red line, case (h)) for $\lambda = 0.4$ and the PDF (7.48) (black lines, with $\beta = 0.92$: case (b), $\beta = 1.1$: case (c), $\beta = 2.35$: case (d), $\beta = 8.5$: case (e), $\beta = 17$: case (f), $\beta = 30$: case (g)) for the remaining intermediate parameters.

7.5 Fits for NNSD of Mushroom Billiard

In a manner analogous to the procedure performed for the billiard of Limaçon, in this section, we show in figure (7.5) the histograms of the spacing spectrum and its corresponding fits for the nine values of the control parameter r/R of the Mushroom billard. (i) On the linear scale (upper part), and (ii) on the semi-log scale (bottom). The fits have been made through Poisson distribution (red first line) for $r/R = 0$, the Wigner-Dyson PDF (last red line) for $r/R = 7/10$ and the PDF (7.48) (black lines) for the remaining intermediate parameters.

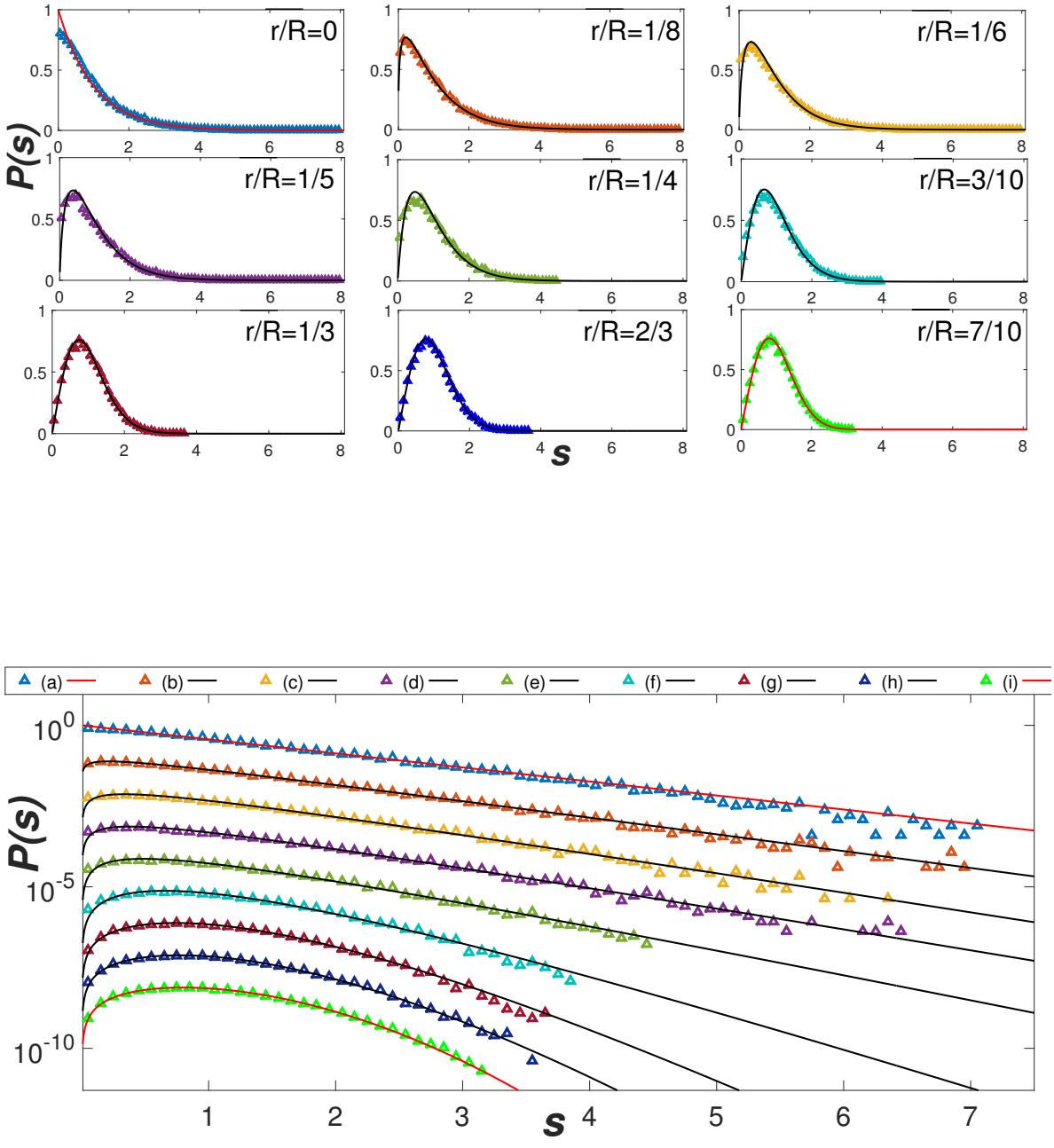

Figure 7.5: Using Equation (7.48) we have fitted the NNSD's histograms for the nine values of the control parameter r/R of the Mushroom billiard. So, in the upper part, the graphs are shown in linear scale, while at the bottom they are in Semi-logarithmic scale, in this case, each of them has been multiplied by a factor of 0.1 on the previous one. The fits have been made through Poisson distribution (red first line, case (a)) for $r/R = 0.0$, the Wigner-Dyson PDF (last red line, case (i)) for $r/R = 7/10$ and the PDF (7.48) (black lines, with $\beta = 0.68$: case (b), $\beta = 0.89$: case (c), $\beta = 1.0$: case (d), $\beta = 1.4$: case (e), $\beta = 3.4$: case (f), $\beta = 9$: case (g), $\beta = 20$: case (h)) for the remaining intermediate parameters.

.

7.6 Nearest neighbor increments of level spacings

Let $\{s_i\}_{i\in\mathbf{N}}$ be the discrete stochastic process of unfolded level spacings. For a finite time series of length N, it defines the marginal distribution as

$$P(s) = \frac{1}{N}\sum_{i=1}^{N}\langle\delta(s-s_i)\rangle\,,$$

the form of $P(s)$ depends on the system's dynamics. Integrable systems obey a Poisson law

$$P_I(s) = e^{-s} \tag{7.51}$$

and are well described by the Gaussian diagonal ensemble (GDE), whereas quantum chaotic systems follow the Wigner-Dyson distribution of the Gaussian orthogonal ensemble (GOE) of random matrix theory,

$$P_C(s) = \frac{\pi}{2}s\exp\left(-\frac{\pi s^2}{4}\right). \tag{7.52}$$

A number of interpolating distributions have been proposed in the literature (Prosen and Robnik (1994); Reichl (2004)) for systems with mixed dynamics, but none were derived from a full-fledged statistical description, such as GDE or GOE.

In the study of turbulence and mathematical finance, it is common to consider the statistics of increments, e.g. velocity increments in turbulent flow and log-returns in finance. Their statistics are generally called second-order statistics. Here, we consider a special case of second order statistics by defining the stochastic process of nearest neighbor(NN) increments of level spacings $\{x_i\}_{i\in\mathbf{N}}$, where $x_i = (s_{i+1}-s_i)/\sigma$. The marginal distribution is defined as usual

$$P(x) = \frac{1}{N}\sum_{i=1}^{N}\langle\delta(x-x_i)\rangle\,,$$

which can be written in terms of the joint distribution of consecutive level spacings $P(s_1, s_2)$

$$P(x) = \int_0^\infty ds_1 \int_0^\infty ds_2 P(s_1, s_2)\delta.(x - (s_2 - s_1)/\sigma)$$

For integrable systems we may use the fact that there is no level repulsion and thus $P_I(s_1, s_2) = P_I(s_1)P_I(s_2)$. Therefore

$$\begin{aligned} P_I(x) &= \int_{-\infty}^\infty \frac{dk}{2\pi} \int_0^\infty ds_1 \int_0^\infty ds_2 e^{-s_1-s_2} e^{ik(x-(s_2-s_1)/\sigma)} \\ &= \int_{-\infty}^\infty \frac{dk}{2\pi} \frac{\sigma^2 e^{ikx}}{k^2+\sigma^2} \\ &= \frac{\sigma}{2} e^{-\sigma|x|}, \end{aligned}$$

which is the Boltzmann distribution. In this approach, the crossover PDF between the regular-integrable regime for the chaotic is given by the marginal

$$P(\beta; x) = \int_0^\infty d\varepsilon P(x|\varepsilon) f(\beta; \varepsilon), \tag{7.53}$$

the conditional distribution associated with the largest scale of the system corresponds to the Gaussian

$$P(x|\varepsilon) = \frac{1}{\sqrt{2\pi\varepsilon}} \exp\left(-\frac{x^2}{2\varepsilon}\right), \tag{7.54}$$

while the background corresponds the Gamma distribution with unitary average

$$f(\beta; \varepsilon) = \frac{\beta^\beta}{\Gamma(\beta)} \varepsilon^{\beta-1} e^{-\beta\varepsilon}, \quad \varepsilon > 0. \tag{7.55}$$

The superposition integral, according to the procedure shown in this document generates the PDF for the signal

$$\boxed{P(\beta; x) = \frac{\beta^{1/2}}{\sqrt{2\pi}\Gamma(\beta)} G_{0,2}^{2,0}\left(\begin{array}{c} - \\ \beta - 1/2, 0 \end{array} \middle| \frac{\beta x^2}{2} \right).} \tag{7.56}$$

Thus, by setting the free parameter in $\beta = 1$, the marginal (7.56) takes the form of the Boltzmann distribution

$$P_I(x) = P(1;x) = \frac{1}{\sqrt{2}} e^{-\sqrt{2}|x|}, \tag{7.57}$$

which describes the second-order statistics for the regular integral regime. On the other hand, when we take the limit of the free parameter going to infinity, it recoveres the Gaussian distribution that characterizes the chaotic regime

$$P_C(x) = \lim_{\beta\to\infty} P(\beta;x) = \frac{1}{\sqrt{2\pi}} e^{-x^2/2}. \tag{7.58}$$

In figures (7.6) and (7.7) we show the histograms for nearest neighbor (NN) increments of level spacings of the Limaçon and Mushroom billiards respectively. The integrable regimes corresponds to the minimum value of the control parameter. It is zero for the two billiards, and is represented by the fourth disc, whose histograms are plotted in the central part of figures (7.6) and (7.7) (in blue balls), fit by the Boltzmann distribution (Eq. (7.57)), in green (blue) Limaçon (Mushroom). The full chaotic regime is reached in each case for the largest value of the control parameter, whose histogram corresponds to the $x-$shaped markers of the central part of figures (7.6) and (7.7), fitted by the Gaussian distribution, equation (7.58). The intermediate parameters associated with mixed dynamics have been adjusted by the red dotted lines, amplified in the inset of the right part of each figure, where each histogram are in the insets of the left and lower part.

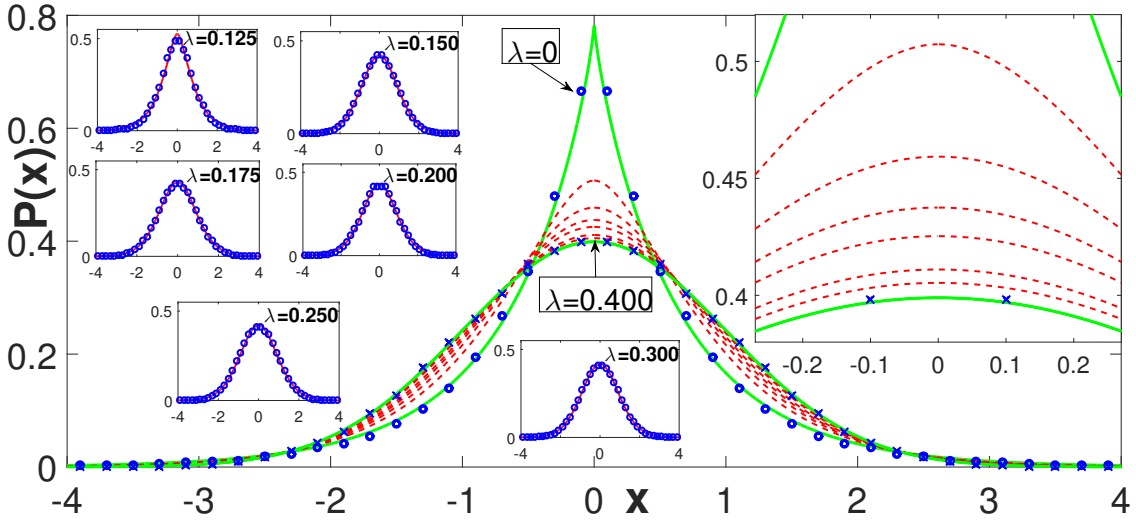

Figure 7.6: Using Equation (7.56) we have fitted the NN increments of level spacings histograms for the eight values of the control parameter λ of the Limaçon billiard. The fits have been made through Boltzmann distribution (green line for $\lambda = 0.0$), the Gaussian PDF (green line for $\lambda = 0.400$) and the PDF (7.56) (dashed red lines, with $\beta = 2.05$: for $\lambda = 0.125$, $\beta = 6.80$: for $\lambda = 0.150$, $\beta = 5.90$: for $\lambda = 0.175$, $\beta = 5.40$: for $\lambda = 0.200$, $\beta = 7.40$: for $\lambda = 0.250$, $\beta = 8.60$: for $\lambda = 0.300$) for the remaining intermediate parameters.

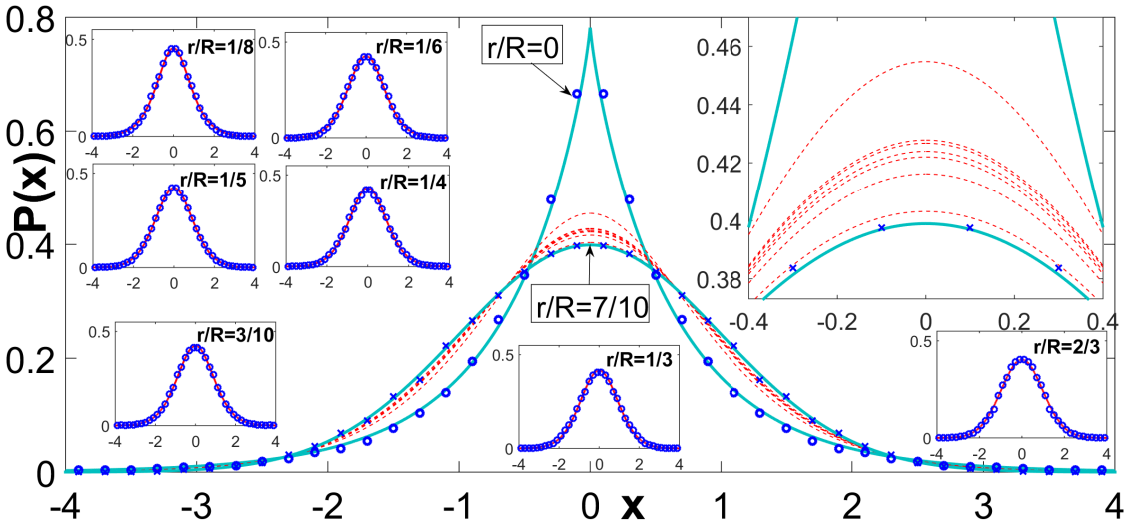

Figure 7.7: Using Equation (7.56) we have fitted the NN increments of level spacings histograms for the nine values of the control parameter r/R of the Mushroom billiard. The fits have been made through Boltzmann distribution (light blue line for $r/R = 0.0$), the Gaussian PDF (light blue line for $r/R = 7/10$) and the PDF (7.56) (dashed red lines, with $\beta = 3.20$: for $r/R = 1/8$, $\beta = 5.90$: for $r/R = 1/6$, $\beta = 7.00$: for $r/R = 1/5$, $\beta = 5.70$: for $r/R = 1/4$, $\beta = 6.50$: for $r/R = 3/10$, $\beta = 9.20$: for $r/R = 1/3$, $\beta = 35.8$: for $r/R = 2/3$, for the remaining intermediate parameters.

7.7 Conclusions

We characterized the eigenvalue spectra of two families of quantum billiards with mixed dynamics, where regular and chaotic behaviors may coexist, the Limaçon and the Mushroom shaped billiards. These families were defined with a shape control parameter that drives a crossover from regular to fully chaotic regimes. The fluctuations in each spectrum were analysed by treating them as a time series with the level order playing the role of time.

We determined that in general the probability density function of the nearest neighbors spacing distribution is represented as a statistical superposition of a large time-scale conditional Wigner-Dyson distribution weighted by the gamma distribution that characterizes the slowly changing background, where the dynamics of the system is formulated as a hierarchical stochastic model.

We found in the nearest neighbor spacing increments distribution ($P(x)$) a smooth crossover from the Boltzmann distribution in the regular limit to a Gaussian distribution in the chaotic regime. In the intermediate region, where mixed dynamics takes place, the nearest neighbor spacing increments is found to be well described by a $K-$ distribution (Jakeman and Pusey (1978)).

8 Conclusions and perpectives

8.1 Conclusions

The H-theory, as it has been termed the formalism resulting from this research work, has proved to be versatile and robust for describing the dynamics of the hierarchical complex systems. This model is a direct consequence of five basic principles: (i) temporal translational symmetry, (ii) local interactions, (iii) scale invariance, (iv) equilibrium condition, and (v) unidirectional flow. Via this approach, we have characterized the PDFs for the signal in the experimental detection scale, which were interpreted as the result of stochastic processes in which multiple spatial/temporal scales are coupled through a hierarchical structure.

In this manuscript, starting with the second chapter, the universal classes, its asymptotic behavior and its parametric dependencies have been shown in detail. Using the Mellin transform, the probability density functions for the multi-scale approach have been established. The solutions have been written via the Fox H-functions, which in most cases have been simplified to Meijer G-functions. Later, in Chapters four, five and seven we have shown valuable and innovative applications.

In chapter three it was established that the variance estimator that allows the decoupling of the background from the signal, and guarantees the validity superposition hypothesis. This procedure has been extended in chapters four and five as a fundamental tool to characterize the experimental series (i) of the velocity measurements in a turbulent fluid, (ii) output intensities of the erbium random fiber laser, and (iii) the returns series

with thirty seconds inter-event time of Ibovespa São Paulo Index.

Through a joint fitting procedure, for the signal and background, we eliminated the ambiguity that several distributions can describe the same data series Macêdo *et al.* (2017). This was a crucial contribution made by this formalism, since it allows to establish in systems that present PDF with heavy tails, the parametric family associated with the stationary distribution of its time series, the number of background scales and its parameter values. We remark that all applications detailed in this thesis, are sensitive to the scale of observation, or data acquisition, so that the forms associated with the central limit theorem (Gaussian, Wigner-Dyson) are obtained only in the scale Integral, which is the largest scale of the system.

The H-theory, was used in chapter four, to characterize the entire transition of the velocity increments spectrum $\delta v_\tau(t) = v(t+\tau) - v(t)$, of the Eulerian turbulence experiment made by B. Chabaud and et al, from the experimental resolution scale ($\tau = 2^0$), to the integral scale ($\tau > 2^{10}$).

In the erbium random fiber laser system described in chapter five, I have presented together with the co-authors of paper Roa-González *et al.* (2017) for the first time in the literature, relations between the output intensities spectrum and two-dimensional turbulence, such as a double spectral density coefficient $1/f^\alpha$. We also established for the first time in this type of systems the existence of statistical mixture for probability density functions, which are of the stretched exponential class. On the other hand, by the form of the distributions shown in reference Burgess *et al.* (2015), gives some evidence of the connection between the statistical mixture and the Kraichnan-Leith-Batchelor similarity theory, which could be the focus of future work.

In chapters six and seven, the energy spacing spectra of resonant cavities with mixed dynamics were analyzed via discrete exterior calculus, which is a powerful tool that esta-

blishes a direct correspondence between the continuous operators and its discrete version. This implementation has allowed us to begin the investigation of the curvature effects in the spectrum of resonant cavities through conformal transformations which preserve the angles of the mesh.

Using the stochastic differential equations model presented in chapter seven, which is framed in the H-theory domain, we have presented a theory for describing the crossover from the integral to the chaotic regime. Such models can be used in any system that presents similar transitions, such as spin chains and random networks, among others.

8.2 Perpectives

Working on this research project offered me several valuable experiences, among which I highlight the opportunity to corroborate through experimental data a theoretical model. So as far as possible, I would like to keep this trend, via the optical experiments to delve between the connections of random lasers, turbulence, and spin glasses.

The discrete exterior calculus also opens many possibilities and connections, in the short term, I want to resume the investigation of the curvature effect on the spectral series of the cavities. Also, I want to simulate through DEC the Navier-Stokes equations confined in two-dimensional and three-dimensional geometries, to characterize the spectrum for velocity increments.

The DEC also offers the possibility to simulate other physical phenomena in closed or open geometries, which generate a spectral series associated with different ensembles of random matrix theory, research that has already begun to be carried out by my adviser in collaboration with researchers from the CIN of the UFPE and the mathematics department of UFRPE. A project that I want to integrate soon.

References

Abuelenin, S. and Abul-Magd, A. (2012). Efficient of unfolding on the spectral statistics of adjacency matrices of complex networks. **12**.

Abul-Magd, A., Dietz, B., Friedrich, T. and Richter, A. (2008). Spectral fluctuations of billiards with mixed dynamics: From time series to superstatistics. **77**.

Antenucci, F., Conti, C., Crisanti, A. and Leuzzi, L. (2015). General phase diagram of multimodal ordened and desordened lasers in closed and open cavities. **114**.

Bachelier, L., (Translated, with Commentary by), Davis, M. and Etheridge, A. (2006). Louis bachelier's theory of speculation: The origins of modern finance. **1**.

Badii, R. and Politi, A. (1997). Complexity hierarchical structures and scaling in physics. **1**.

Barnett, A. and Betcke, T. (2012). Mpspack user manual. **1**.

Barnett, A. H. and Betcke, T. (2007). Quantum mushroom billiards. **17**.

Batchelor, G. K. (1953). The theory of homogeneous turbulence. **1**.

Beck, C., Cohen, E. D. and Swinney, H. (2005). From time series to superstatistics. **72**.

Bell, N. and Hirani, A. N. (2012). Pydec: Software and algorithms for discretization of exterior calculus. **1**.

Biró, T. and Rosenfeld, R. (2008). Microscopic origin of non-gaussian distributions of financial returns. **387**.

Black, F. and Scholes, M. (1973). The pricing of options and corporative liabilities. **81 (637-654)**.

Bluman, G. W. and Anco, S. C. (2002). Symmetry and integration methods for differential equations. **154**.

Bobenko, A. I. and Springborn., B. A. (2007). A discrete laplace-beltrami operator for simplicial surfaces. **1**.

Bohigas, O. (1991). Random matrix theories and chaos dynamics. **1**.

Botsch, M., Kobbelt, L., Pauly, M., Alliez, P. and Lévy, B. (2010). Polygon mesh processing. **1**.

Bouchaud, J. P. and Potters, M. (2000). Theory of financial risk and derivative pricing. **1**.

Boussinesq, J. (1877). Essai sur la théorie des eaux courantes. **23**.

Brody, T. A., Flores, J., French, J. B., Mello, P. A., Pandey, A. and Wong, S. M. (1981). Random matrix physics: spectrum and strength fluctuations. **53**.

Burgess, B. H., Scott, R. K. and Shepherd, T. G. (2015). Kraichnan leith batchelor similarity theory and two-dimensional inverse cascades. **767**.

Burin, A. L., Ratner, M. A., Cao, H. and Chang, S. H. (2002). Random laser in one dimension. **88**.

Cambel, A. B. (1993). Applied chaos theory: A paradigm for complexity. **1**.

Cao, H. (2013). Lasing in random media. **13**.

Carinski, M. and Kopp, E. (2012). The black-scholes model. **1**.

Caselle, M. and Magnea, U. (2004). Random matrix theory and symmetric spaces. **394**.

Castaing, B., Chabaud, B. and Hébral, B. (1992). Hot wire anemometer operating at cryogenic temperatures. **63**.

Castaing, B., Chabaud, B. and Hébral, B. (2004). Monte carlo methods in financial engineering. **1**.

Chabaud, B., Naert, A., Peinke, J., Chillà, F., Castaing, B. and Hébral., B. (1994). Transition toward developed turbulence. **24**.

Chanal, O., B.Chabaud, B.Castaing and Hébral., B. (2000). Intermentetency in a tubulent low temperature gaseous helium jet. **17**.

Chevillard, L., Roux, S. G., Lévêque, E., Mordant, N., Pinton, J. F. and Arnéodo, A. (2005). Intermittency of velocity time increments in turbulence. **95**.

Crane, K. (2005). Discrete differential geometry: An applied introduction presented at siggraph'05. **1**.

Crommie, M. F., Lutz, C. P. and Eigler, D. M. (1993). Confinement of electrons to quantum corrals on a metal surface. **2**.

Crommie, M. F., Lutz, C. P., Eigler, D. M. and Heller, E. J. (1995). Waves on a metal surface and quantum corrals. **2**.

Davidson, P. A. (2004). Turbulence an intruduction for scientists and engineers. **1**.

Desbrun, M., Meyer, M., Schröder, P. and Barr., A. (1999). Implicit fairing of irregular meshes using diffusion and curvature flow. **1**.

Desbrun, M., Hirani, A. N., Leok, M. and Marsden., J. E. (2005). Discrete exterior calculus. **1**.

Desbrun, M., Kanso, E. and Tong, Y. (2008). Discrete differential forms for computational modeling–discrete differential geometry (287-324). **1**.

Dietz, B. and Richter, A. (2015). Quantum and wave dynamical chaos in superconducting microwave billiards. **25**.

Dietz, B., Friedrich, T., Miski-Oglu, M., Richter, A. and Schafer, F. (2007). Spectral properties of bunimovich mushroom billiards. **75**.

Dragulescu, A. and Yakovenko., V. (2002). Probability distribution of returns in the heston model with stochastic volatility. **2**.

Dyson, F. (1962a). Statistical theory of the energy levels of complex systems. i. **3**.

Dyson, F. (1962b). Statistical theory of the energy levels of complex systems. ii. **3**.

Dyson, F. (1962c). Statistical theory of the energy levels of complex systems. iii. **3**.

Dyson, F. (1963). Statistical theory of the energy levels of complex systems. iv. **4**.

Eftimiades, A. (2014). Kahler: An implementation of discrete exterior calculus on hermitian manifolds. **1**.

Faleiro, E., Gómez, J. M. G., Molina, R. A. and L. Muñoz, J. R., A. Relaño (2004). Theoretical derivation of $1/f$ noise in quantum chaos. **93**.

Farantos, S. C. (2014). Nonlinear hamiltonian mechanics applied to molecular dynamics theory and computational methods for understanding molecular spectroscopy and chemical reactions. **1**.

Farazmand, M. M., Kevlahan, N. K. R. and Protas, B. (2011). Controlling the dual cascade of two-dimensional turbulence. **668**.

Frankel, T. (1997). The geometry of physics: an introduction. **1**.

Frisch, U. (1995). Turbulence: the legacy of an kolmogorov. **1**.

Gagné, M. and Kashyap, R. (2009). Demonstration of a 3 mw threshold er-doped random fiber laser based on a unique fiber bragg grating. **17**.

de Goes, F., Desbrun, M. and Tong, Y. (2015). Vector field processing on triangle meshes. **1**.

de Goes, F., Desbrun, M., Meyer, M. and DeRose, T. (2016). Subdivision exterior calculus for geometry processing. **33**.

Goh, K. I. and Barabási, A. L. (2008). Burstiness and memory in complex systems. **81**.

Gomes, A., Lima, B., Pincheira, P. I. R., Moura, A., Gagné, M., Raposo, E. P., de Araújo, C. B. and Kashyap, R. (2016). Glassy behavior in a one-dimensional continuous-wave erbium-doped random fiber laser. **94**.

Gómez, J. M. G., no, A. R., Retamosa, J., Faleiro, E., Salasnich, L., čar, M. V. and Robnik, M. (2005). $1/f^{\alpha}$ noise in spectral fluctuations of quantum systems. **94**.

Gorbunov, O. A., Sugavanam, S. and Churkin, D. V. (2015). Intensity dynamics and statistical properties of random distributed feedback fiber laser. **40**.

Graf, H. D., Harney, H. L., Lengeler, H., Lewenkopf, C. H., Rangacharyulu, C., Richter, A., Schardt, P. and Weidenmuller, H. A. (1992). Distribution of eigenmodes in a superconducting stadium billiard with chaotic dynamics. **69**.

Gu, F. L. B., Gomes, A., Yong, K. T., Wen, S. and Prasad, P. N. (2015). Lasing in nanocomposite random media. **10**.

Gurvich, A. S. and Yaglom, A. M. (1967). Breakdown of eddies and probability distributions for small-scale turbulence. **10**.

Heinz, K. and Schreiber., H. M. (2002). Computational statistical physics from billiards to monte carlo. **1**.

Heston, S. L. (1993). A closed-form solution for options with stochastic volatility with applications to bond and currency options. **6(2)**.

Hoffmann, K. H. and Schreiber, M. (2002). Computational statistical physics: From billiards to monte carlo. **1**.

Huang, N. E., Shen, Z., Long, S. R., Wu, M. C., Shih, H. H., Zheng, Q., Yen, N. C., Tung, C. C. and Liu, H. H. (1998). The empirical mode decomposition and the hilbert spectrum for nonlinear and non-stationary time series analysis. **454**.

Hull, J. and White, A. (1987). The pricing of options on assets with stochastic volatilities. **42**.

Huy, T. (2010). Latent factor commodity models: filtering and estimation. **1**.

Itô, K. (1951). On stochastic differential equations. **1**.

Ivancevic, V. G. (2011). Undergraduate lecture notes in de rham hodge theory. **1**.

Jakeman, E. and Pusey, P. N. (1978). Significance of k distributions in scattering experiments. **40**.

Keizer, J. (1987). Statistical thermodynamics of nonequilibrium processes. **3**.

Kelvin, L. (1901). Nineteenth century clouds over the dynamical theory of heat and light. **1**.

Kleinert, H. (2006). Path integrals in quantum mechanics, statistics, polymer physics and financial markets. **1**.

Kloeden, P. and Platen, E. (1999). Numerical solution of stochastic differential equations. **1**.

Kolmogorov, A. (1941a). Decay of isotropic turbulence in an incompressible viscous fluid. **31**.

Kolmogorov, A. (1941b). Energy dissipation in locally isotropic turbulence. **32**.

Kolmogorov, A. (1941c). Local structure of turbulence in an incompressible fluid at very high reynolds numbers. **30**.

Kolmogorov, A. (1941d). Logarithmically normal distribution of the size of particles under fragmentation. **31**.

Kolmogorov, A. (1962a). Précisions sur la structure locale de la turbulencê dans un fluide visqueux aux nombres de reynolds élevés (in french and russian). **1**.

Kolmogorov, A. (1962b). A refinement of previous hypotheses concerning the local structure of turbulence in a viscous incompressible fluid at high reynolds number. **13(1)**.

Koponen, I. (1995). Analytic approach to the problem of convergence of truncated lévy flights towards the gaussian stochastic process. **52**.

Kullback, S. and Leibler, R. (1951). On information and sufficiency. **22**.

Landau, L. D. and Lifshitz, E. M. (1959). Fluid mechanics translated by j. b. sykes and w. h. reid from original russian published in 1944. **1**.

Lesieur, M. (1997). Turbulence in fluids 3rd rev. **3**.

LESLIE, D. C. (1973). Developments in the theory of turbulence. **1**.

Li, B., Robnik, M. and Hu, B. (1998). Relevance of chaos in numerical solutions of quantum billiards. **57**.

Lima, B. C., Gomes, A. S., Pincheira, P. I., Moura, A. L., Gagné, M., Raposo, E. P., Araújo, C. B. D. and Kashyap, R. (2017). Observation of lévy statistics in one-dimensional erbium-based random fiber laser. **34**.

Livi, R. and Vulpiani, A. (2003). The kolmogorov legacy in physics. **2**.

Lizárraga, N., Puente, N. P., Chaikina, E. I., Leskova, T. A. and Méndez, E. R. (2009). Single-mode er-doped fiber random laser with distributed bragg grating feedback. **17**.

Lévy, B. (2006). Laplace-beltrami eigenfunctions: Towards an algorithm that understands geometry. **5**.

Macedo-Junior, A. and Macêdo, A. (2006). Brownian-motion ensembles of random matrix theory: A classification scheme and an integral transform method. **752**.

Macêdo, A., Roa-González, I., Salazar, D. and Vasconcelos, G. (2017). Universality classes of fluctuation dynamics in hierarchical complex systems. **95**.

Mantegna, R. N. and Stanley, H. E. (1994). Stochastic process with ultraslow convergence to a gaussian: The truncated lévy flight. **73**.

Marcus, C. M., Rimberg, A. J., Westervelt, R. M., Hopkins, P. F. and Gossard, A. C. (1992). Conductance fluctuations and chaotic scattering in ballistic microstructure. **69**.

Mathai, A. and Saxena, R. (1973). Generalized hypergeometric functions with applications in statistics and physical sciences. **1**.

Mathai, A. M. (1993). A handbook of generalized special functions for statistical and physical sciences. **1**.

Mathai, A. M., Saxena, R. and Haubold, H. J. (2010). The h-function theory and applications. **1**.

de Matos, C. J. S., de S. Menezes, L., Brito-Silva, A. M., Martinez Gámez, M. A., Gomes, A. S. L. and de Araújo, C. B. (2007). Random fiber laser. **99**.

McDonough, J. M. (2004). Introductory lectures on turbulence. **1**.

Mehta., M. L. (2004). Random matrices, 3rd edition. **1**.

Meijer, C. S. (1941). Multiplikationstheoreme für di funktion $g_{p,q}^{m,n}(z)$. **44**.

Merrill, J. W., Cao, H. and Dufresne, E. R. (2016). Fluctuations and correlations of emission from random lasers. **93**.

Metha, M. L. (1960). On the statistical properties of the level-spacings in nuclear spectra. **18**.

Metha, M. L. and M.Gaudin (1960). On the density of eigenvalues of a random matrix. **18**.

Mirlin, A., Evers, F., Gornyi, I. and Ostrovsky, P. M. (2010). Anderson transitions: Critically, symmetries and topologies–50 years of anderson location. **1**.

Mohameda, M. S., Hirani, A. N. and R.Samtaney (2016). Discrete exterior calculus discretization of incompressible navier stokes equations over surface simplicial meshes. **312**.

Monin, A. S. and Yaglom, A. M. (2007). Statistical fluid mechanics, volume ii: Mechanics of turbulence. **2**.

Morales, I. O., Landa, E., Stránský, P. and Frank, A. (2011). Improved unfolding by detrending of statistical fluctuations in quantum spectra. .

Nakamura, K. and Harayama, T. (2004). Quantum chaos and quantum dots. **1**.

Obukhov, A. M. (1941a). Sound scattering in a turbulent flow. **30**.

Obukhov, A. M. (1941b). Spectral energy distribution in a turbulent flow. **32**.

Obukhov, A. M. (1962). Some specific features of atmospheric turbulence. **67**.

Oksendal, B. (2003). Stochastic differential equations: An introduction with applications. **1**.

Orszag, S. A. (1970). Indeterminacy of the moment problem for intermittent turbulence. **13, 2211**.

Panozzo, D. and Jacobson, A. (2014). libigl tutorial. **1**.

Persson, P. O. (2004). Mesh generation for implicit geometries. **1**.

Persson, P. O. and Strang, G. (2004). A simple mesh generator in matlab. **46(2)**.

Peyré, G. (2008). Numerical mesh processing, course notes. **1**.

Peyré, G. (2013). gpeyre/matlab-toolboxes. **1**.

Prandtl, L. (1925). Bericht über untersuchungen zur ausgebildeten turbulenz. **5**.

Prosen, T. and Robnik., M. (1993). Energy level statistics in the transition region between integrability and chaos. **26**.

Prosen, T. and Robnik, M. (1994). Semiclassical energy level statistics in the transition region between integrability and chaos: transition from brody-like to berry-robnik behaviour. **27**.

Prudnikov, A. P., Brychkov, Y. A. and Marichev, O. L. (1991). Evaluation of integrals and the mellin transform. **39**.

Rangarajan, G. and Ding, M. (2000). Integrated approach to the assessment of long range correlation in time series data. **61**.

Raposo, E. P. and Gomes, A. S. (2015). Analytical solution for the lévy-like steady-state distribution of intensities in random lasers. **91**.

Reichl, L. E. (2004). The transition to chaos: Conservative classical systems and quantum manifestation. **1**.

Reynolds, O. (1894). On the dynamical theory of incompressible viscous fluids and the determination of the criterion. **56**.

Richardson, L. F. (1922). Weather prediction by numerical process. **1**.

Richmond, P., Mimkes, J. and Hutzler, S. (2013). Econophysics and phycical economics. **1**.

Richter, A. (1999). Playing billiards with microwaves — quantum manifestations of classical chaos. **1**.

Risken, H. and Franck, T. (1996). The fokker-planck equation methods of solution and applications. **1**.

Roa-González, I., Lima, B., Pincheira, P., Brum, A., Macêdo, A., Vasconcelos, G. L., de S. Menezes, L., Raposo, E. P. and Gomes, A. S. (2017). Turbulence hierarchy in a random fiber laser. **31**.

Salazar, D. and Vasconcelos, G. (2010). Stochastic dynamical model of intermittency in fully developed turbulence. **82**.

Salazar, D. and Vasconcelos, G. (2012). Multicanonical distribution: Statistical equilibrium of multiscale systems. **86**.

Salazar, D. S. P. (2010). Modelo dinâmico hierárquico estocástico para intemitência em turbulência e em outros sistemas complexos. **1**.

Santhanam, M. S., Bandyopadhyay, J. N. and Angom, D. (2006). Quantum spectrum as a time series: Fluctuation measures. .

Schafer, R. and Guhr, T. (2010). Local normalization: Uncovering correlations in non-stationary financial time series. **389**.

Schafer, R., Barkhofen, S., Guhr, T., Stockmann, H. J. and Kuhl, U. (2015). Compounding approach for univariate time series with nonstationary variances. **92**.

Schmitt, T., Chetalova, D., Schäfer, R. and Guhr., T. (2013). Non-stationarity in financial time series: Generic features and tail behavior. **103**.

Schroeder, M. (1991). Fractals, chaos, power laws: Minutes from an infinite paradise (ch. 5). **1**.

Shapira, O. and Fischer, B. (2005). Localization of light in a random-grating array in a single-mode fiber. **22**.

Standard and data from Yahoo! Finance (2013), P. . (2013). Url http://finance.yahoo.com. **1**.

Stöckmann, H. J. (2007). Quantum chaos an introduction. **1**.

Sutera, S. P. and Skalak, R. (1977). The history of poiseuille's law. **25**.

Tanner, R. and Waiters, K. (1998). Rheology: An historical perspective. **7**.

Taylor, G. I. (1935). Statistical theory of turbulence. **151**.

Temam, R. (1976). Turbulence and navier stokes equations. **1**.

Uppu, R. and Mujumdar, S. (2013). Dependence of the gaussian-lévy transition on the disorder strength in random lasers. **87**.

Uppu, R. and Mujumdar, S. (2014). Lévy exponents as universal identifiers of threshold and critically in random lasers. **90**.

Uppu, R., Tiwari, A. and Mujumdar, S. (2012). Identification of statistical regimes and crossovers in coherent random laser emission. **37**.

Vicente, R., de Toledo, M., Leite, V. and Caticha, N. (2006). Underlying dynamics of typical fluctuations of an emerging market price index: The heston model from minutes to months. **361**.

Voultsidou, M. and Herrmann, J. M. (2009). Significance estimation in fmri from random matrices – handbook of research on advance tecniques in diagnostic imaging and biomedical applications. **1**.

Weissman, M. B. (1988). $1/f$ noise and other slow, nonexponential kinetics in condensed matter. **60**.

Wiersma, D. S. (2008). The physics and applications of random lasers. **4**.

Wigner, E. P. (1955). Characteristic vectors of bordered matrices with infinite dimensions. **1**.

xu, D. and Beck, C. (2016). Transition from lognormal to χ^2-superstatistics for financial time series. **1**.

Yaglom, A. M. (1948.). Homogeneous and isotropic turbulence in a viscous compressible fluid. .

Yang, Z., Bingham, C., Ling, B. W. K., Gallimore, M., Stewart, P. and Zhang, Y. (2012). Trend extraction based on hilbert-huang transform. **8**.

Zohuri, B. (2016). Dimensional analysis beyond the pi theorem. **1**.

A Coupled SDEs for spacing energy levels

Coupled stochastic equations to energy levels spacing in the ballistic cavities with mixed dynamics have been characterized by a set of three matrix equations which each equation represent one input for GOE $2X2$ $x_i^{(\alpha)}$ where $i = \{11, 12, 22\}$ and $\alpha = 1, 2$, the elements of each vector are coupled through γ matrix. It will generate the time series for energy spacing levels $S = \sqrt{(x_{11}^{(2)} - x_{22}^{(2)})^2 + 4x_{12}^{(2)}}$.

$$\begin{pmatrix} dx_i^{(1)} \\ dx_i^{(2)} \end{pmatrix} = -\begin{pmatrix} \gamma_{11} & \gamma_{12} \\ \gamma_{21} & \gamma_{22} \end{pmatrix} \begin{pmatrix} x_i^{(1)} \\ x_i^{(2)} \end{pmatrix} dt + \sqrt{f_{(i)}\epsilon_1(t)} \begin{pmatrix} dW_i^{(1)} \\ dW_i^{(2)} \end{pmatrix}. \tag{A.1}$$

The variance evolution in this model is associated with the $\epsilon_M(t)$ coefficient which corresponds to greater scale at hierarchy. In this section we have taken the particular case $M = 1$, this single scale for variance is characterized by time ζ_1 who satisfies the condition $\zeta_1 \ll 1 < \lambda$. Condition that establishes the separation of scales between $S(t)$ and ϵ_1 evolution.

$$d\epsilon_1 = -\zeta_1(\epsilon_1 - \epsilon_0)dt + k_1\epsilon_1 dW_{\epsilon_1}(t). \tag{A.2}$$

Our goal is to determine the stationary PDF solution for spacing $S = \sqrt{(x_{11}^{(2)} - x_{22}^{(2)})^2 + 4x_{12}^{(2)}}$ corresponding to system solution. Using the Milstein's method for coupled stochastic equations. To implement this computational method, we must discretize the equations (A.1-A.2), which can be written generically as (A.3) equation.

$$dX_t^l = a^l(t, X_t)dt + \sum_{k=1}^{m} b^{l,k}(t, X_t)dW_t^k. \tag{A.3}$$

Equation (A.3) has a iterative solution with fixed hopping Δt, given by Milstein method

$$X_t^l = X_{t-1}^l + a^l(t-1, X_{t-1})\Delta t + \sum_{k=1}^{m} b^{l,k}(t-1, X_{t-1})\Delta W_{t-1}^k + \sum_{k_1=1}^{m}\sum_{k_2=1}^{m} L^{k_1} b^{l,k_2}(t-1, X_{t-1}) I_{(k_1,k_2)}\Delta t, \tag{A.4}$$

where L^{k_1} is a differential operator for discretized variables $L^{k_1} = \sum_r b^{r,k_1}\frac{\partial}{\partial x_r}$, and $I_{(k_1,k_2)}$ corresponds to the Itô integrals for multiplicative white noise associated with the product of two Wiener processes.

A.1 Milstein method

Milstein method is in general used for solving stochastic differential equations of the form:

$$dX_t^i = a^i(t, X_t)dt + \sum_{j=1}^{m} b^{i,j}(t, X_t)dW_t^j. \tag{A.5}$$

Equation (A.5) has a iterative solution with fixed hopping Δt, given by Milstein method Kloeden and Platen (1999); Huy (2010) as follows

$$X_t^i = X_{t-1}^i + a^i(t-1, X_{t-1})\Delta t + \sum_{j=1}^{m} b^{i,j}(t-1, X_{t-1})\Delta W_{t-1}^j + \sum_{j_1=1}^{m}\sum_{j_2=1}^{m} L^{j_1} b^{i,j_2}(t-1, X_{t-1}) I_{(j_1,j_2)}\Delta t, \tag{A.6}$$

where $I_{(j_1,j_2)}$ represent the integrals of multiplicative white noise, whose results depends on the approach taken either Itô or Stratanovich, and indexes j_1, j_2.

$$I_{(j_1,j_2)} = \int_{t_n}^{t_{n+1}} \int_{t_n}^{s_1} dW^{j_1} dW^{j_2}. \tag{A.7}$$

Since the diagonal case, i.e. when $j_1 = j_2$ integrals in the two approaches differ by the factor $\frac{\Delta t}{2}$, in our case we have worked with the Itô approach, which has the form:

$$I_{(j_1,j_1)} = \frac{1}{2}\left((\Delta W^{j_1})^2 - \Delta t\right) = J_{(j_1,j_1)} - \frac{1}{2}\Delta t. \tag{A.8}$$

If the indexes are different $j_1 \neq j_2$ integrals in the two approaches are the same but the result greatly increases the difficulty of implementing such a result in the computer code, because it obeys a power series of the form:

$$\begin{aligned} I_{(j_1,j_2)} = J^p_{(j_1,j_2)} = \Delta t \left(\frac{1}{2}\Xi_{j_1}\Xi_{j_2} + \sqrt{\rho_p}(\mu_{j_2,p}\Xi_{j_1}) \right) \\ + \frac{\Delta t}{2\pi} \sum_{r=1}^{p} \frac{1}{r} \left(\psi_{j_1,r}(\sqrt{2}\Xi_{j_2} + \nu_{j_2,r}) - \psi_{j_2,r}(\sqrt{2}\Xi_{j_1} + \nu_{j_1,r}) \right), \end{aligned} \tag{A.9}$$

where $\Xi_j, \psi_{j,r}, \nu_{j,r}, \mu_{j,r}$ are all independent $N(0:1)$ Gaussian random variables proportional to $\frac{1}{\sqrt{\Delta t}} dW^j$, further the coefficient ρ_p is also a series of the form:

$$\rho_p = \frac{1}{12} - \frac{1}{2\pi^2} \sum_{r=1}^{p} \frac{1}{r^2} \tag{A.10}$$

For the purposes of computer code we have taken only the first term of each of the series $p = 1$, since advance different tests were made adding more terms of the series. However, we did not observe significant changes in the results for the systems discussed here. In contrast, when all terms of the series of r is obviated the results were not satisfactory because it differed noticeably from the theoretical curves for the tests performed.

B Dissipation rate of Navier Stokes equations

The dissipation of turbulent energy requires an equation to represent the turbulent kinetic energy. This is usually achieved by the so-called Reynolds decomposition, where the instantaneous flow is described by a time averaged variable Φ and a fluctuating variable ϕ.

$$\tilde{\phi} = \Phi + \phi \quad \rightarrow \quad \Phi \equiv \frac{1}{T}\int_{t_0}^{t_0+T} \tilde{\phi} dt \tag{B.1}$$

$$\rho\frac{\partial \vec{v}}{\partial t} + \rho(\vec{v}\cdot\vec{\nabla})\vec{v} = -\vec{\nabla}p + \mu\nabla^2\vec{v} \tag{B.2}$$

$$\vec{\nabla}\cdot\vec{v} = 0, \tag{B.3}$$

where the quantities to decompose into two parts are the velocity and the pressure

$\vec{v} = \{v_1, v_2, v_3\} = \sum_{i=1}^{3} v_i \hat{e}_i$

$\vec{\nabla} = \sum_{i=1}^{3} \hat{e}_i \frac{\partial}{\partial x_i}$ $\nabla^2 = \sum_{i=1}^{3} \frac{\partial^2}{\partial x_i^2}$

$v_i \rightarrow \tilde{v}_i = V_i + v_i$, $p \rightarrow \tilde{p} = P + p$. Introducing these variables into the Navier-Stokes equation, we get

$$\rho\left(\frac{\partial}{\partial t}(V_i + v_i) + (V_j + v_j)\frac{\partial}{\partial x_j}(V_i + v_i)\right) = -\frac{\partial}{\partial x_j}(P + p) + \mu\frac{\partial^2}{\partial x_j^2}(V_i + v_i). \tag{B.4}$$

Performing the multiplications indicated in the above equation

$$\frac{\partial V_i}{\partial t} + \frac{\partial v_i}{\partial t} + V_j\frac{\partial V_i}{\partial x_j} + V_j\frac{\partial v_i}{\partial x_j} + v_j\frac{\partial V_i}{\partial x_j} + v_j\frac{\partial v_i}{\partial x_j} = -\frac{1}{\rho}\frac{\partial}{\partial x_j}(P + p) + \nu\frac{\partial^2}{\partial x_j^2}(V_i + v_i). \tag{B.5}$$

Using equation (B.5), I proceed to take the average of each of the terms, which are noted by the bar at the top

$$\begin{aligned}\overline{v_i\frac{\partial V_i}{\partial t}}+\overline{v_i\frac{\partial v_i}{\partial t}}+\overline{v_iV_j\frac{\partial V_i}{\partial x_j}}+\overline{v_iV_j\frac{\partial v_i}{\partial x_j}}+\overline{v_iv_j\frac{\partial V_i}{\partial x_j}}+\overline{v_iv_j\frac{\partial v_i}{\partial x_j}}\\ =-\overline{\frac{v_i}{\rho}\frac{\partial}{\partial x_j}(P+p)}+\overline{\nu v_i\frac{\partial^2}{\partial x_j^2}(V_i+vi)},\end{aligned} \tag{B.6}$$

where the velocity parts (trend and fluctuating) satisfying the following relations

- $\overline{V}=V$
- $\overline{v}=0$
- $\overline{vV}=\overline{v}\overline{V}=0$
- $\overline{vv}\neq 0$
- $\overline{v_i\frac{\partial v_i}{\partial t}}=\overline{\frac{\partial \frac{1}{2}v_iv_i}{\partial t}}=\frac{\partial k}{\partial t}$ where $k=\frac{1}{2}\overline{v_iv_i}$
- $\overline{\nu v_i\frac{\partial^2}{\partial x_j^2}(V_i+v_i)}=\overline{\nu v_i\frac{\partial^2}{\partial x_j^2}(v_i)}=\nu\frac{\partial^2\left(\frac{1}{2}v_i^2\right)}{\partial x_j^2}-\nu\frac{\partial v_i}{\partial x_j}\frac{\partial v_i}{\partial x_j}$

Using the results of the previous items, it is possible to write the Navier-Stokes equation as a function of the average kinetic energy

$$\frac{\partial k}{\partial t}+V_j\frac{\partial k}{\partial x_j}+\overline{v_iv_j}\frac{\partial V_i}{\partial x_j}+\frac{\partial}{\partial x_j}\left(\frac{1}{2}\overline{v_iv_iv_j}\right)=-\frac{1}{\rho}\frac{\partial}{\partial x_j}\left(\overline{v_ip}\right)+\nu\frac{\partial^2 k}{\partial x_j^2}-\nu\overline{\frac{\partial v_i}{\partial x_j}\frac{\partial v_i}{\partial x_j}}, \tag{B.7}$$

when is simplified the equation (B.7) gives

$$\frac{\partial k}{\partial t}=-\overline{v_iv_j}\frac{\partial V_i}{\partial x_j}-\nu\overline{\frac{\partial v_i}{\partial x_j}\frac{\partial v_i}{\partial x_j}}. \tag{B.8}$$

Equation (B.8) allows identifying the mean rate of energy dissipation

$$\varepsilon=\nu\overline{\frac{\partial v_i}{\partial x_j}\frac{\partial v_i}{\partial x_j}}=2\nu\overline{s_{ij}s_{ij}} \tag{B.9}$$

C Connection between Langevin and Fokker-Planck equations

This appendix shows the connection between the Fokker-Planck equation and the Langevin equation. The Fokker-Planck equation is understood as the second-order expansion of the Kramers-Moyal equation (KME) (Risken and Franck (1996)). The KME can be deduced in different ways, in particular, we use the relation with Bayes' theorem, where the purpose is to determine the probability density function PDF a posteriori $W(x, t+\delta t)$ from integration of the product between the transition PDF $P(x, t+\delta t|x', t)$ and the a priori PDF $W(x'|t)$, given by

$$W(x, t+\delta t) = \int P(x, t+\delta t|x', t)W(x'|t)dx'. \tag{C.1}$$

We express the moments of transition probability density function of equation (C.1) as

$$M_n(x't, \delta t) = \langle[\xi(t+\delta t) - \xi(t)]^n\rangle|_{\xi(t)=x'} = \int (x-x')^n P(x, t+\delta t|x', t)dx, \tag{C.2}$$

now, using the Fourier transform, we set the characteristic function of the $P(x, t+\delta t|x', t)$ as a Taylor series for its moments

$$C(u, x', t, \delta t) = \int_{-\infty}^{\infty} \exp(iu(x-x'))P(x, t+\delta t|x', t)dx = 1 + \sum_{n=1}^{\infty} \frac{(iu)^n M_n(x't, \delta t)}{n!}, \tag{C.3}$$

so that when we taking the inverse Fourier transform we obtain

$$P(x, t+\delta t|x', t) = \frac{1}{2\pi}\int_{-\infty}^{\infty} \exp(-iu(x-x'))\left[1 + \sum_{n=1}^{\infty} \frac{(iu)^n M_n(x't, \delta t)}{n!}\right] du. \tag{C.4}$$

Once this procedure has been performed, we use the following properties for the Dirac delta function

$$\frac{1}{2\pi}\int_{-\infty}^{\infty}(iu)^n \exp(-iu(x-x'))du = \left(-\frac{\partial}{\partial x}\right)^n \delta(x-x') \tag{C.5}$$

and

$$\delta(x-x')f(x') = \delta(x-x')f(x),$$

where through the above properties we establish

$$P(x,t,+\delta t|x',t) = \left[1+\sum_{n=1}^{\infty}\frac{1}{n!}\left(-\frac{\partial}{\partial x}\right)^n M_n(x,t,\delta t)\right]\delta(x-x'). \tag{C.6}$$

We now assume that the moments M_n can be expanded into a Taylor series with respect to δt Risken and Franck (1996)

$$\frac{M_n(x,t,\delta t)}{n!} = D^{(n)}(x,t)\delta t + O((\delta t)^2), \tag{C.7}$$

by taking into account only the linear terms in δt we thus have

$$\frac{\partial W(x,t)}{\partial t} = \sum_{\nu=1}^{N}\left(-\frac{\partial}{\partial x}\right)^{\nu} D^{(\nu)}(x,t)W(x,t); \quad \infty > N \geq 2. \tag{C.8}$$

Relation (C.8) is known as the Kramers-Moyal equation. The goal now is to determine the form of the coefficients $D^{(n)}(x,t)$ associated with the Langevin equation (C.9), given by

$$\frac{d\xi}{dt} = A(\xi,t) + B(\xi,t)\Gamma(t), \tag{C.9}$$

where the term $\Gamma(t)$ is white noise, which satisfies the following properties $\langle\Gamma(t)\rangle = 0$; $\langle\Gamma(t)\Gamma(t')\rangle = 2\delta(t-t')$. We obtain by integrating equation (C.9)

$$\xi(t+\delta t) - x = \int_t^{t+\delta t} dt_1 A\left(\xi(t_1),t_1\right) + \int_t^{t+\delta t} dt_1 B\left(\xi(t_1),t_1\right)\Gamma(t_1). \tag{C.10}$$

We proceed to expand the drift coefficient and the noise amplitude regarding the stochastic variable

$$A\left(\xi(t_1),t_1\right) = A(x,t_1) + \frac{\partial A(\xi(t_1),t_1)}{\partial \xi(t_1)}|_{\xi(t_1)=x}\left(\xi(t_1)-x\right) + \ldots, \tag{C.11}$$

$$B\left(\xi(t_1),t_1\right) = B(x,t_1) + \frac{\partial B(\xi(t_1),t_1)}{\partial \xi(t_1)}|_{\xi(t_1)=x}\left(\xi(t_1)-x\right) + \ldots. \tag{C.12}$$

We substitute relations (C.11) and (C.12) in equation (C.10), to obtain

$$\begin{aligned}\xi(t+\delta t)-x = &\int_t^{t+\delta t} dt_1 \left(A(x,t_1) + \frac{\partial A(\xi(t_1),t_1)}{\partial \xi(t_1)}|_{\xi(t_1)=x}\left(\xi(t_1)-x\right)\right)\\ &+\int_t^{t+\delta t} dt_1 \left(B(x,t_1) + \frac{\partial B(\xi(t_1),t_1)}{\partial \xi(t_1)}|_{\xi(t_1)=x}\left(\xi(t_1)-x\right)\right)\Gamma(t_1) + \ldots.\end{aligned}$$

We use iteration over the terms $(\xi(t_1)-x)$, then we produce

$$\begin{aligned}\xi(t+\delta t)-x = &\int_t^{t+\delta t} dt_1 A(x,t_1) + \int_t^{t+\delta t} dt_1 \frac{\partial A(\xi(t_1),t_1)}{\partial \xi(t_1)}|_{\xi(t_1)=x}\int_t^{t_1} dt_2 A(x,t_2)\\ &+\int_t^{t+\delta t} dt_1 \frac{\partial A(\xi(t_1),t_1)}{\partial \xi(t_1)}|_{\xi(t_1)=x}\int_t^{t_1} dt_2 B(x,t_2)\Gamma(t_2) + \ldots\\ &+\int_t^{t+\delta t} dt_1 B(x,t_1)\Gamma(t_1) + \int_t^{t+\delta t} dt_1 \frac{\partial B(\xi(t_1),t_1)}{\partial \xi(t_1)}|_{\xi(t_1)=x}\int_t^{t_1} dt_2 A(x,t_2)\Gamma(t_1)\\ &+\int_t^{t+\delta t} dt_1 \frac{\partial B(\xi(t_1),t_1)}{\partial \xi(t_1)}|_{\xi(t_1)=x}\int_t^{t_1} dt_2 B(x,t_2)\Gamma(t_2)\Gamma(t_1)\ldots\end{aligned}$$

We take the averages of the previous equation

$$\begin{aligned}\langle \xi t+\delta t\rangle = &\int_t^{t+\delta t} dt_1 A(x,t_1) + \int_t^{t+\delta t}\int_t^{t_1}\left(\frac{\partial A(\xi(t_1),t_1)}{\partial \xi(t_1)}|_{\xi(t_1)=x}\right)A(x,t_2)dt_2dt_1 + \ldots\\ &+\int_t^{t+\delta t} dt_1 \left(\frac{\partial B(\xi(t_1),t_1)}{\partial \xi(t_1)}|_{\xi(t_1)=x}\right)\int_t^{t_1} dt_2 B(x,t_2)2\delta(t_2-t_1) + \ldots,\end{aligned}$$

and using property $\langle \Gamma(t)\Gamma(t')\rangle = 2\delta(t-t')$ is obtained

$$\langle \xi t + \delta t \rangle = \int_t^{t+\delta t} dt_1 A(x,t_1) + \int_t^{t+\delta t} \int_t^{t_1} \left(\frac{\partial A(\xi(t_1),t_1)}{\partial \xi(t_1)} |_{\xi(t_1)=x} \right) A(x,t_2) dt_2 dt_1 + \ldots$$
$$+ \int_t^{t+\delta t} dt_1 \left(\frac{\partial B(\xi(t_1),t_1)}{\partial \xi(t_1)} |_{\xi(t_1)=x} \right) B(x,t_1) + \ldots$$

In the limit $\delta t \to 0$, we thus arrive at

$$D^{(1)}(x,t) = A(x,t) + \left(\frac{\partial B(\xi(t),t)}{\partial \xi(t)} |_{\xi(t)=x} \right) B(x,t). \tag{C.13}$$

Now, through the relation $\langle [\xi(t+\delta t) - \xi(t)]^n \rangle |_{\xi(t)=x'} = M_n(x't,\delta t) \sim (n!) D^{(n)}(x,t)\delta t$. We take the averages on the square of the Langevin equation, thus we find that the coefficient $D^{(2)}(x,t)$ is given by

$$D^{(2)}(x,t) = \frac{1}{2} \lim_{\delta t \to 0} \frac{1}{\delta t} \int_t^{t+\delta t} \int_t^{t+\delta t} dt_1 dt_2 B(x,t_1) B(x,t_2) 2\delta(t_1 - t_2) = B^2(x,t), \tag{C.14}$$

taking into account only the linear variations in δt the higher order coefficients $D^{(n)}(x,t)$ for $n \geq 3$ are zero. The previous feature leads us that the Langevin equation (C.9) having a Kramers-Moyal expansion only up to second order. Therefore, we have a direct correspondence with the Fokker-Plank equation, so during the present manuscript, it becomes recurrent to associate with each Langevin equation a Fokker-Planck equation.

D Mellin Transform

D.1 Mellin Transform

Starting from the gamma function definition

$$\Gamma(s) = \int_0^\infty e^{-x} x^{s-1} dx, \tag{D.1}$$

and using its inverse representation, we obtain the exponential function

$$e^{-x} = \frac{1}{2\pi i} \int_{c-i\infty}^{c+i\infty} \Gamma(s) x^{-s} ds. \tag{D.2}$$

Expanding the function as a Dirichlet series

$$\varphi(s) = \sum_{n=1}^{\infty} \frac{a_n}{n^s}, \tag{D.3}$$

and introducing a one $\left(1 = \frac{\Gamma(s)}{\Gamma(s)}\right)$ to convenience, to later expand the numerator in the integral representation of the gamma function

$$\varphi(s) = \sum_{n=1}^{\infty} \frac{a_n \Gamma(s)}{\Gamma(s) n^s} = \sum_{n=1}^{\infty} \frac{a_n}{\Gamma(s)} \int_0^\infty \frac{e^{-x} x^{s-1} dx}{n^s}, \tag{D.4}$$

from equation (D.5), it is possible to identify that the term in parentheses is e^{-nx}

$$\varphi(s) = \sum_{n=1}^{\infty} \frac{a_n}{\Gamma(s)} \int_0^\infty \underbrace{\left(\frac{1}{2\pi i} \int_{c-i\infty}^{c+i\infty} \Gamma(s) (nx)^{-s} ds \right)}_{e^{-nx}} x^{s-1} dx. \tag{D.5}$$

Equation (D.5) can be organized by commutating summation and integral to identify the serial expansion of the $f(x)$ function

$$\varphi(s) = \frac{1}{\Gamma(s)} \int_0^\infty \underbrace{\left(\sum_{n=1}^{\infty} a_n e^{-nx} \right)}_{f(x)} x^{s-1} dx, \tag{D.6}$$

this way we get the Mellin Transform

$$\varphi(s) = \frac{1}{\Gamma(s)} \int_0^\infty f(x) x^{s-1} dx, \tag{D.7}$$

and the inverse Mellin Transform

$$f(x) = \frac{1}{2\pi i} \oint_C \varphi(s) x^{-s} ds \tag{D.8}$$

E Laplace-Beltrami operator

This appendix is a summary of the ideas to build the Laplace-Beltrami operator. In particular we are interested in the displacements of each vertex $f_i = f(x_i)$ (which in the language of differential forms corresponds to a $0-form$). Let us assume that the three-vertices of a reference triangle, which Cartesian coordinates are $(\mathbf{x}_i, \mathbf{x}_j, \mathbf{x}_k)$, where $\mathbf{x}_i = (x_i, y_i)$, for any type of displacement generated on triangulation conforms angles should be preserved. This condition can be satisfied if a shift to the coordinates of the barycenter is made. i.e. relative to this triangle may be considered as weights, B_i, B_j, B_k, subject to the normalization condition $\sum_{\delta=1}^{3} B_\delta = 1$. We want to determine the barycentric coordinates of $\mathbf{x} = (x, y)$

$$\mathbf{x} = \frac{B_i\mathbf{x}_i + B_j\mathbf{x}_j + B_k\mathbf{x}_k}{B_i + B_j + B_k}, \tag{E.1}$$

with the constraint $B_i = 1 - B_j - B_k$. From the vector equation (E.1) for barycenter, we can establish two vector functions equivalent

$$\underbrace{\begin{pmatrix} x - x_i \\ y - y_i \end{pmatrix}}_{f(x,y)} = \underbrace{\overbrace{\begin{pmatrix} x_j - x_i & x_k - x_i \\ y_j - y_i & y_k - y_i \end{pmatrix}}^{T} \begin{pmatrix} B_j \\ B_k \end{pmatrix}}_{f(B_j,B_k)}, \tag{E.2}$$

where equation (E.3) establishes the inverse relation

$$\begin{pmatrix} B_j \\ B_k \end{pmatrix} = \underbrace{\frac{1}{2A}\begin{pmatrix} y_k - y_i & x_i - x_k \\ y_i - y_j & x_j - x_i \end{pmatrix}}_{T^{-1}} \begin{pmatrix} x - x_i \\ y - y_i \end{pmatrix}. \tag{E.3}$$

Once determined the shape of the $f(x,y)$, for our reference triangle, we want to establish two main sets of Laplacian operations associated with the set of neighbors to vertrice $\mathbf{x_i}$. The first set of operations determines the gradient $\nabla f(x,y) \rightarrow \nabla f(B_j, B_k)$.

$$\nabla(f) = \begin{pmatrix} \frac{\partial f}{\partial x} \\ \frac{\partial f}{\partial y} \end{pmatrix} = \begin{pmatrix} \frac{\partial B_j}{\partial x}\frac{\partial f}{\partial B_j} + \frac{\partial B_k}{\partial x}\frac{\partial f}{\partial B_k} \\ \frac{\partial B_j}{\partial y}\frac{\partial f}{\partial B_j} + \frac{\partial B_k}{\partial y}\frac{\partial f}{\partial B_k} \end{pmatrix} \tag{E.4}$$

$$\nabla(f) = \begin{pmatrix} \frac{\partial B_j}{\partial x} \\ \frac{\partial B_j}{\partial y} \end{pmatrix} \frac{\partial f}{\partial B_j} + \begin{pmatrix} \frac{\partial B_k}{\partial x} \\ \frac{\partial B_k}{\partial y} \end{pmatrix} \frac{\partial f}{\partial B_k} \tag{E.5}$$

Derivatives defined in Equation (E.5), are obtained from the equation (E.3), thus giving the final gradient form.

$$\nabla f = \frac{1}{2A}\begin{pmatrix} y_k - y_i \\ x_i - x_k \end{pmatrix}(f_j - f_i) + \frac{1}{2A}\begin{pmatrix} y_i - y_j \\ x_j - x_i \end{pmatrix}(f_k - f_i) \tag{E.6}$$

Introducing the notation $(\mathbf{x_k} - \mathbf{x_i})^{\perp} = R^{\perp}(\mathbf{x_k} - \mathbf{x_i})$, whose corresponds to a orthogonal positive rotation (equation(E.7)) of vector Botsch *et al.* (2010) $(\mathbf{x_k} - \mathbf{x_i}) = \begin{pmatrix} x_k - x_i \\ y_k - y_i \end{pmatrix}$, which corresponds to the direction joining the vertices k and i, each determined by the coordinates $\mathbf{x_k}$ and $\mathbf{x_i}$ of triangle

$$R^{\perp} = \underbrace{\begin{pmatrix} \cos\theta & \sin\theta \\ -\sin\theta & \cos\theta \end{pmatrix}}_{\theta=\pi/2} = \begin{pmatrix} 0 & 1 \\ -1 & 0 \end{pmatrix} \tag{E.7}$$

So the gradient in E.6 can be written in compact notation as E.8.

$$\nabla f = (f_j - f_i)\frac{(\mathbf{x_k} - \mathbf{x_i})^{\perp}}{2A} + (f_k - f_i)\frac{(\mathbf{x_i} - \mathbf{x_j})^{\perp}}{2A} \tag{E.8}$$

Once set ∇f, we have built the Laplacian associated, through the theorem of Gauss Ostrogadsky where the normal vectors over which the integration is performed are shown in Figure (6.2), and can be build through the set of orthogonal rotations opposite sides of first neighbors of vertex coordinate $\mathbf{x}_i$.

$$\int_{A_i} \triangle f dA' = \int_{\partial A_i} \nabla f \cdot \mathbf{n} ds' \cong \sum_{\gamma,\delta} \nabla f_{i\gamma\delta} \cdot \mathbf{n}_{\gamma\delta} \tag{E.9}$$

In other words there is a set of triangles having the vertex $\mathbf{x_i}$ in common, this set is called 1-ring of x_i, consisting of six vertices that form the hexagon's area A_i, so that the integral of equation (E.9), has a discrete form composed of of the inner product sum between the gradient of each triangle and normal vector associated at 1-ring. Taking our triangle reference, the inner product has the form

$$\begin{aligned}\nabla f_{ijk} \cdot \mathbf{n}_{jk} = (f_j - f_i)\frac{(\mathbf{x_k} - \mathbf{x_i})^{\perp} \cdot (\mathbf{x_k} - \mathbf{x_j})^{\perp}}{2A} \\ +(f_k - f_i)\frac{(\mathbf{x_i} - \mathbf{x_j})^{\perp} \cdot (\mathbf{x_k} - \mathbf{x_j})^{\perp}}{2A},\end{aligned}$$

where A is the triangle area.

$$A = \frac{1}{2}|\mathbf{x_k} - \mathbf{x_j}||\mathbf{x_i} - \mathbf{x_j}| \sin(\alpha_{ik}) = \frac{1}{2}|\mathbf{x_k} - \mathbf{x_j}||\mathbf{x_k} - \mathbf{x_i}| \sin(\beta_{ij}). \tag{E.10}$$

Producing the final result:

$$\nabla f_{ijk}\mathbf{n}_{jk} = \frac{1}{2}[cot(\beta_{ij})(f_j - f_i) + cot(\alpha_{ik})(f_k - f_i)]. \tag{E.11}$$

When making the same operations on the other five triangles which 1-ring members for i vertex, we get

$$\nabla f_{ikl}\mathbf{n}_{kl} = \frac{1}{2}[cot(\beta_{ik})(f_k - f_i) + cot(\alpha_{il})(f_l - f_i)] \tag{E.12}$$

$$\nabla f_{ilm}\mathbf{n}_{lm} = \frac{1}{2}[cot(\beta_{il})(f_l - f_i) + cot(\alpha_{im})(f_m - f_i)] \tag{E.13}$$

$$\nabla f_{imn} \cdot \mathbf{n}_{mn} = \frac{1}{2}[cot(\beta_{im})(f_m - f_i) + cot(\alpha_{in})(f_n - f_i)] \tag{E.14}$$

$$\nabla f_{inp} \cdot \mathbf{n}_{np} = \frac{1}{2}[cot(\beta_{in})(f_n - f_i) + cot(\alpha_{ip})(f_p - f_i)] \tag{E.15}$$

$$\nabla f_{ipj} \cdot \mathbf{n}_{pj} = \frac{1}{2}[cot(\beta_{ip})(f_p - f_i) + cot(\alpha_{ij})(f_j - f_i)] \tag{E.16}$$

Associating terms, we get:

$$\int_{A_i} \triangle f dA = \frac{1}{2} \sum_{x_\gamma \in A_1(x_i)} (\cot \alpha_{i,\gamma} + \cot \beta_{i,\gamma}) (f_\gamma - f_i) \tag{E.17}$$

Thus the discrete average of the Laplace-Beltrami operator of a function f at vertex $\mathbf{x}_i$ is given by

$$\triangle f(x_i) := \frac{1}{2A_i} \sum_{x_\gamma \in N_1(x_i)} (\cot \alpha_{i,\gamma} + \cot \beta_{i,\gamma}) (f_\gamma - f_i) \tag{E.18}$$